Locking the Advanced LIGO Gravitational Wave Detector: with a focus on the Arm Length Stabilization Technique

Alexa Staley

Submitted in partial fulfillment of the
requirements for the degree of
Doctor of Philosophy
in the Graduate School of Arts and Sciences

COLUMBIA UNIVERSITY

2015

ABSTRACT

Locking the Advanced LIGO Gravitational Wave Detector: with a focus on the Arm Length Stabilization Technique

Alexa Staley

The Advanced LIGO gravitational wave detectors have recently achieved a new milestone. The two detector network is now operational and is being tuned for sensitivity. Currently, the state of the art detectors are the most sensitive ground-based interferometers to date and are closer than ever to the reality of a gravitational wave detection.

For many years, there has been a worldwide effort to directly detect gravitational waves, a phenomena that was predicted in Einstein's theory of general relativity. A direct detection would further validate Einstein's theory, but more importantly would provide a novel approach to studying the universe and the elusive physics of gravity beyond Einstein's theory.

However, none of this would be possible without the success of the arm length stabilization scheme. This recently demonstrated technique, which will be the focus of this thesis, is a critical step required to get the LIGO interferometers operational. This scheme is unique to the advanced generations of detectors and is extremely valuable for such a complex instrument. As part of my research, I characterized, modeled, and helped design this important technique. I was also a part of a small team that brought the LIGO Hanford interferometer to its operational point for the first time.

For astrophysical reasons, the goal of Advanced LIGO's design is to measure a gravitational strain as small as $4 \times 10^{-24}/\sqrt{Hz}$, requiring a length resolution of approximately 10^{-19} m. This high sensitivity demands multiple optical cavities to enhance the response of the interferometer. The interferometer is a Michelson interferometer geometry consisting of two 4km arm cavities,

whose differential length is measured by the phase change of a resonating infrared laser at the gravitational wave readout port. The Michelson interferometer is enhanced by Fabry-Perot arm cavities, a power recycling cavity, and a signal extraction cavity. The Fabry-Perot arm cavities effectively increase the arm lengths by two orders of magnitude. Meanwhile, the power recycling cavity is used to enhance the circulating power within the interferometer, and the signal extraction cavity is used to enhance the optical response at the gravitational-wave readout.

Besides the increased design sensitivity of Advanced LIGO, a crucial requirement for a gravitational wave detection will be a high duty cycle. As an example, a worldwide Advanced LIGO network of five detectors, each with an 80% up-time, would only produce about 30% network up-time. A deterministic, robust, and fast sequence to transition the interferometer from an uncontrolled to a controlled state is mandatory. Advanced LIGO has five longitudinal degrees of freedom which must be controlled in order for the interferometer to be operational. However, all degrees of freedom are strongly coupled making this a traditionally challenging process. The state of the arm cavities can completely alter the state of the dual-recycled Michelson interferometer. Active feedback control is required to operate these instruments and keep the cavities locked on resonance. The optical response is highly non-linear until a good operating point is reached. The linear operating range is between 0.01% and 1% of a fringe for each degree of freedom. The resonance lock has to be achieved in all five degrees of freedom simultaneously, making the acquisition difficult. Furthermore, the cavity linewidth seen by the laser is only $\sim$1 Hz which is four orders of magnitude smaller than the linewdith of the free running laser. To mitigate several of these critical problems, a new arm length stabilization technique was introduced to the lock sequence. The arm length stabilization technique utilizes two additional green lasers that are brought into resonance in each arm cavity. This effectively decouples the arm cavities from the rest of the interferometer. While the main infrared beam is kept off resonance from the arm cavity, a modulation technique utilizing third harmonics locks the central dual-recycled Michelson interferometer. In the final step, both arm cavities are slowly tuned onto resonance, nominal sensors are used, and full lock is achieved.

To ensure a high duty cycle for Advanced LIGO and confirm repeatability of the locking sequence, a detailed study and characterization of the arm length stabilization technique was conducted. A model of the scheme and a noise budget was developed. The model was beneficial while designing and implementing the scheme for the first time at the Advanced LIGO observatories. Meanwhile, the noise budget was critical to determine if this scheme would be viable in the lock process. Ultimately, the advent of the arm length stabilization to the lock process has been successful, a decisive milestone for future prospect of collecting meaningful astrophysical data. The technique has been implemented at both detectors and proven reliable and robust. Given the complexity of the interferometers, the success of this scheme to bring the detectors operational was a large accomplishment for the collaboration. With the technique's repeatable performance, efforts can be focused on tuning the interferometers sensitivity and achieving a first direct detection.

This thesis begins with an introduction on the theory of general relativity and gravitational waves. Common astrophysical sources are described in Chapter 2. Chapter 3 begins with a description of the installed instrument. A discussion on the detector design sensitivity, limiting noise sources, and estimated detection rates is also given. At the end of Chapter 3, the complications of lock acquisition are highlighted. The arm length stabilization system was introduced to Advanced LIGO as a partial way to solve the difficulties of locking. Chapter 4 discusses the motivation for the use of this scheme and explains the methodology. A detailed discussion on the arm length stabilization model is given, along with the noise budget in Chapters 5 and 6 respectively. The full lock sequence is described in Chapter 7. The thesis concludes with the current status of the interferometers.

Table of Contents

List of Figures

List of Tables

Glossary

List of abbreviations

For more abbreviations please refer to Ref. [132].

ADC	analog-to-digital converter
ALS	arm length stabilization
AOM	acousto-optical modulator
AS	anti-symmetric [port]
ASC	alignment sensing and control [system]
aLIGO	Advanced LIGO (2^{nd} generation of LIGO)
BNS	binary nuetron star
BS	beam splitter
CARM	common arm motion
CDS	control and data system
CMB	cosmic microwave background
DAC	digital-to-analog converter
DARM	dommon arm motion
DAQ	data acquisition [network]
DOF	degree of freedom
DRMI	dual-recycled michelson interferometer

EOM	electro-optical modulator
ETM	end test mass
ETMX	end test mass in X-arm
ETMY	end test mass in Y-arm
EX	end-X [station]
EY	end-Y [station]
FFT	Fast-Fourier-Transform
FI	Faraday isolator
GPS	global positioning system
GR	[The Theory of] General Relativity
GW	gravitational wave(s)
HAM	horizontal access module
HD	homodyne detection (or detector)
HEPI	hydraulic external pre-isolator
HR	highly reflective [dielectric coating]
IMC	input-mode cleaner
ISC	interferometer sensing and control
ISCO	innermost stable circular orbit
ISI	internal seismic isolation [system]
ITM	input test mass
ITMX	input test mass in X-arm
ITMY	input test mass in Y-arm
iLIGO	Initial LIGO (1st generation of LIGO)
KAGRA	Kamioka Gravitational Wave Detector
LHO	LIGO-Hanford Observatory
LIGO	Laser Interferometer Gravitational Wave Observatory

LISA	Laser Interferometer Space Antenna
LLO	LIGO-Livingston Observatory
LO	local oscillator
LSC	length sensing and control
LVEA	Laser and Vacuum Equipment Area [of LHO or LLO]
M˙⊙	solar masses
MC	mode-cleaner
MEDM	Motif Editor and Display Manager
MICH	michelson interferometer
Nd:YAG	neodymium (Nd) doped YAG (see YAG)
NPRO	non-planar ring oscillator
OCXO	oven-controlled XO (see XO)
OMC	output mode-cleaner
PBS	polarizing beam splitter
PD	photo-diode OR photo-detector
PDH	Pound - Drever - Hall [technique]
PFD	phase-frequency discriminator
PLL	phase-locked loop
POP	pick off port
PRCL	power recycling cavity length
PRM	power-recycling mirror
PSL	pre-stabilized laser
PZT	$\mathrm{Pb[Zr}_x\mathrm{Ti}_{1-x}\mathrm{]O}_3$-based piezo-electric actuator
QPD	quadrant photodiodes
REFL	reflection port
RF	radio frequency

RMS	root mean square
SEI	seismic isolation [system]
SHG	second - harmonic generation (or generator)
SNR	signal-to-noise ratio
SR	[The Theory of] Special Relativity
SRCL	ssignal recycling cavity length
TEM	transverse electro-magnetic [spatial mode]
TT	transverse-traceless [gauge]
UTC	Universal Time Coordinate
VCO	voltage-controlled oscillator
VEA	Vacuum Equipment Area [of LHO or LLO]
WFS	wave-front sensors
YAG	yttrium aluminum garnet [$\mathrm{Y_3Al_5O_{12}}$]
zpk	zero, pole, and gain

Acknowledgments

There are an abundant number of people I owe thanks to that got me to where I am today. I will acknowledge some of these people here, but this list is by no means exclusive.

To Marianne Duldner and Arlene Fox: thanks for tutoring me all those years and never giving up on a young kid who could barely read or write.

To Dr. Prasad Akavoor: thanks for sparking my interest in physics.

To Professor Thomas Baumgarte: thanks for being such a wonderful undergraduate adviser, encouraging me to be a physics major, and introducing me to gravitational waves.

To Sheila Dwyer: thank you for being my best friend and mentor at LIGO. I am so happy we were on "the green team" together. I learned so much from you, and you never got annoyed with all the questions I asked. On top of that, you were a fantastic friend and I am so glad we got close.

To Daniel Sigg: thanks for being the best boss anyone could ever ask for (although you will deny being my boss). I have learned so much from you over the past two years, so thank you for having the patience to teach me. I had so much fun working for you; it made my experience at LHO unforgettable. Thanks for also being a friend—from hiking, to road trips, to thursday dinners—there are many moments and laughs I will cherish.

To Stefan Ballmer: thanks for being such a great mentor. I am so happy we overlapped while at LHO. It was a pleasure to work with you. And of course, I am thrilled that you were my flight instructor! I will never forget the beautiful flight to Seattle and all the times aboard GX.

To Christopher Wipf: thanks for all your help on the model and developing several of the tools used in the noise budget simulink model. You were also extremely patient with me, and your help was invaluable to the success of this code.

To Jeff Kissel: thanks for teaching me all about the LIGO suspensions. But more importantly thanks for being a great friend and taking care of me while at LHO. I would not have survived the tri-cities without my partner in crime—LHOSC!

To Dan Hoak, Kiwamu Izumi, Evan Hall, Eli King, Richard McCarthy, Keita Kawabe, Jax Sanders, Arnaud Pele, Maggie Tse, Thomas Vo, and many others at LHO: thanks for being such wonderful and helpful co-workers. My experience at LHO would not have been the same without you.

To Nicolas Smith, Jamie Rollins, Rana Adhikari, Peter Fritschel, David Shoemaker, Lisa Barsotti, and Matt Evans: thanks for the tremendous amount of advice given by each of you during visits to LHO. I learned so much for all of you and had a wonderful time working with you as well.

To Max Factourovich and Imre Bartos: thank you for being such great Columbia mentors. Your input and advice has been invaluable, and you have guided me along the way in this dissertation process.

To Zsuzsa and Szablocs Marka: thanks for giving me the opportunity to work at LHO for two years. None of this phenomenal experience would have been possible without your support.

To Sophia Staley: thanks for all your support throughout this process and for proofreading some of this thesis.

To Jes and Debora Staley: thanks for your unconditional love, support, and trust. You never gave up on me and never let me give up on myself. I would not be here without you.

Part I

Chapter 1

A General Overview of Gravitational Waves

In his theory of general relativity [63], Albert Einstein developed the notion that the gravitational field is measured by the curvature in space-time. The presence of mass-energy, or matter causes space-time to curve. Yet, vacuum space-times can also have non-zero curvature such as those around black holes. The warping of space-time causes the apparent attraction between nearby objects. Einstein derived a set of equations that relate how energy, momentum, and mass distort the geometry of space-time. These equations are given by

$$G^{\mu\nu} = 8\pi T^{\mu\nu} \tag{1.1}$$

where the Einstein tensor is defined by,

$$G^{\mu\nu} = R^{\mu\nu} - \frac{1}{2} g^{\mu\nu} R. \tag{1.2}$$

Note, hereafter I will be using abstract summation notation with gravitational constant $G = 1$ and the speed of light $c = 1$ as outlined in Ref. [43]. In the above equations, $T^{\mu\nu}$ is the symmetric stress-energy tensor that represents the energy and momentum of the matter in space-time. Meanwhile,

$R^{\mu\nu}$ and R are the Ricci tensor and scalar respectively; they both are formed from the Riemann tensor, which is computed from second partial derivatives of the space-time metric. The four-dimensional space-time metric is given by $g_{\mu\nu}$ such that the line element of two events is

$$ds^2 = g_{\mu\nu} dx^\mu dx^\nu. \tag{1.3}$$

Einstein's field equations describe how mass interacts with space-time curvature much likes Maxwell's field equations describes how charged particles interact with electric and magnetic fields.

As a consequence of his theory, Einstein predicted the existence of gravitational radiation or gravitational waves. These waves are ripples in space-time, much like ripples in a pond, that propagate outward traveling at the speed of light [64]. Gravitational waves are produced by a disturbance in space-time, such as a large masses accelerating in a strong gravitational field or a change in energy distribution. Gravitational waves arise from several cosmic sources (see Chapter 2) and range in frequency from $\sim 10^{-17}$ Hz to $\sim 10^{4}$ Hz. The low frequency band generally corresponds to gravitational waves emanating from the cosmological background. Meanwhile, the formation of neutron stars in supernova explosions create gravitational waves at higher frequencies, for example [120]. A prominent gravitational wave source are binary pulsars. In 1974, Hulse and Taylor [88] discovered a pulsar in a binary neutron star system which provided the first indirect proof of the existence of gravitational waves. The data demonstrated that the orbital period of the binary pulsar decreased over time, consistent with the energy loss due to the emission of gravitational waves [158]. As of today, several other binary pulsars have been observed further supporting the reality of gravitational waves. In 2014, results were published by BICEP2 indicating a spiral formation in the cosmic microwave background polarization was caused by gravitational radiation from the early universe [25]. However, follow-up measurements by Planck suggested these findings were not from primordial gravitational waves [121]. Regardless, gravitational waves have never been directly detected. Numerous ground-based detectors around the world, including Advanced LIGO in the United States, are seeking these elusive waves. The Advanced LIGO detectors are the most optimistic of the first detection. These detectors, which will be described in great detail in Chapter 3, exploit specific properties of gravitational waves that will be discussed in the coming sections.

If detected, gravitational waves would be extremely useful. For one, a direct detection would further verify Einstein's theory of general relativity. Additionally, since gravitational waves can penetrate regions of space where electromagnetic radiation cannot, detection would enable researchers to examine the universe with a different tool. Gravitational waves interact weakly with matter and are not scattered or absorbed as they traverse space-time, unlike their electromagnetic wave counterpart. This feature implies that gravitational waves carry astrophysical information from their source with little to no interruption. Lastly, since electromagnetic waves and gravitational waves are generated with different mechanisms, its likely they carry different information from the same source [164].

Unfortunately gravitational waves are very difficult to detect since these waves are very small. As will be shown, they arise from small perturbations in the space-time metric. Since the gravitational wave sources are generally at astronomical distance from observatories on Earth and the amplitude of these waves decrease inversely with distance, the waves are even smaller by the time they reach ground-based observatories. As a result, a direct detection of gravitational waves has been elusive for many years, and requires several advances in instrumentation that are described in Chapter 3.

In this chapter, I outline specific features of gravitational waves. In Section 1.1, I explain why gravitational waves are quadrupole in nature. In Section 1.2, I simplify Einstein's equations to the linearized regime. It follows that with certain coordinate system choices, gravitational waves travel at the speed of light, are transverse, and have two polarizations. In Section 1.2.1, I also derive the strain amplitude of the gravitational wave assuming a plane wave solution. In Section 1.2.2, this solution is generalized further, and the strain amplitude is derived in terms of the gravitational wave quadruple moment. I conclude, in Section 1.3, generalizing to higher order moments.

1.1 Quadrupole Radiation

Gravitational radiation is similar to electromagnetic radiation in that they both travel at the speed of light. In addition, both forms of radiation are transverse in that their oscillation is perpendicular to the direction of propagation. An important difference between the two is that gravitational radiation interacts weakly with matter and thus can penetrate regions of space unperturbed unlike electromagnetic radiation. Gravitational radiation also differs from electromagnetic radiation in that the latter is dipolar whereas the former is approximated to be quadrupolar [52]. A gravitational monopole is simply the total mass-energy. By the conservation of mass, this does not change in time and thus cannot be a radiative field. Meanwhile, the conservation of linear and angular momentum eliminate dipole radiation [20]. The latter can easily be seen by examining the radiation formula in electromagnetic theory and replacing $e^2 \rightarrow -m^2$. Dipole radiation is proportional to $\ddot{\mathbf{d}}$, where $\mathbf{d}$ is the electric dipole moment,

$$\mathbf{d} = \sum_{\text{particles a}} e_a \mathbf{x_a}. \tag{1.4}$$

Analogously, the mass dipole moment is given by

$$\mathbf{d} = \sum_{\text{particles a}} m_a \mathbf{x_a}. \tag{1.5}$$

Thus,

$$\ddot{\mathbf{d}} = \sum_{\text{particles a}} m_a \ddot{\mathbf{x}}_{\mathbf{a}} = \dot{\mathbf{p}}. \tag{1.6}$$

The mass dipole radiation is evidently zero since conservation of momentum requires $\ddot{\mathbf{d}} = \dot{\mathbf{p}} = 0$. Similarly, the conservation of angular momentum rules out magnetic-dipole radiation. As a result, there is no gravitational dipole radiation [108]. This leaves quadrupole and higher order radiation as the only form of gravitational radiation. Generally, this can be approximated by the leading order quadrupole radiation.

1.2 Linearized Gravity

In the region close to their astrophysical source, gravitational waves can be considered a strong or weak field. Regardless, as these gravitational waves traverse space-time, they approach an asymptotic form which can be modeled by a linear perturbation of Minkowski space-time. As a result, linearized gravitational waves can still provide information on their non-linear source [43]. A set of linearized equations can easily be derived, and will be outlined here. This regime is also known as the weak field limit. Consider a metric that consists of a small perturbation

$$g_{\mu\nu} = \overline{g_{\mu\nu}} + h_{\mu\nu} \tag{1.7}$$

where $\overline{g_{\mu\nu}}$ is a known solution of Einstein's equation (1.1), and assumed to be the Minkowski metric, $\overline{g_{\mu\nu}} = \eta_{\mu\nu}$. The Minkowski metric corresponds to a space-time of zero gravitation field. Then $h_{\mu\nu} << 1$ describes the weak gravitational field perturbation. Subsequently, we can compute the affine connection, Reimann tensor, Ricci tensor, and Ricci scalar up to first order in $h_{\mu\nu}$ in order to solve equation (1.1) as done in [52]. If we impose a coordinate gauge condition such as the Lorentz Gauge,

$$\partial_\mu \overline{h^{\mu\nu}} = 0, \tag{1.8}$$

Einstein's equations become linearized in the form of

$$\Box \overline{h_{\mu\nu}} = -16\pi T_{\mu\nu} \tag{1.9}$$

where $\Box$ is the D'Alembertian and one defines:

$$\overline{h_{\mu\nu}} \equiv h_{\mu\nu} - \frac{1}{2}\eta_{\mu\nu}h, \qquad h \equiv \eta^{\mu\nu}h_{\mu\nu}. \tag{1.10}$$

It is important to note that the lorentz gauge is not unique under coordinate transformations as long as the transformation, ζ^α, $x^\alpha \rightarrow x^\alpha + \zeta^\alpha$, satisfies

$$\Box \zeta^\alpha = 0. \tag{1.11}$$

1.2.1 Plane Wave Vacuum Solutions and TT Gauge

Using linearized gravity, one can apply the plane wave vacuum solution to show specific properties of gravitational waves. In particular, gravitational waves travel at the speed of light and are transverse to the propagation direction. Applying the standard transverse-traceless gauge, the polarization of the gravitational wave is deduced. The mathematics are outlined in this section.

Let's first consider the plane wave vacuum solutions to equation (1.9):

$$\overline{h_{\mu\nu}} = A_{\mu\nu} e^{i\vec{k}\cdot\vec{x}} \tag{1.12}$$

where $A_{\mu\nu}$ are constants. Inserting this solution into the vacuum form of equation (1.9), gives

$$k_\alpha k^\alpha = 0. \tag{1.13}$$

This implies that k^α is the null vector and that the gravitational wave must be traveling at the speed of light as expected. Using the lorentz gauge equation (1.8), one also finds that

$$A_{\mu\nu} k^\nu = 0 \tag{1.14}$$

which constrains $A_{\mu\nu}$ to be transverse to k^ν. Finally, one can use equation (1.11) to impose four more conditions on $A_{\mu\nu}$. Consider the transverse-traceless (TT) gauge, where $A^\mu_\mu = 0$. In this gauge, one finds that

$$h^{TT}_{\mu 0} = 0, \text{(only the spatial components of } h_{\mu\nu} \text{ are non-zero)} \tag{1.15}$$

$$\partial_\mu h^{TT}_{\mu\nu} = 0, \text{(the spatial components are divergence free)} \tag{1.16}$$

$$h_{\mu\mu} = 0, \text{(the spatial components are trace-free).} \tag{1.17}$$

These conditions imply that $\overline{h^{TT}_{\mu\nu}} = h^{TT}_{\mu\nu}$ and that the ten component symmetric rank-2 tensor $h_{\mu\nu}$ is subject to eight constraints. The two remaining dynamical degrees of freedom correspond to two polarizations of the gravitational wave. If we consider a wave propagating along the z-direction,

$$k^\alpha = (k, 0, 0, k) \tag{1.18}$$

it can be shown that

$$\overline{h^{TT}_{\mu\nu}} = \begin{pmatrix} 0 & 0 & 0 & 0 \\ 0 & h_+ & h_\times & 0 \\ 0 & h_\times & -h_+ & 0 \\ 0 & 0 & 0 & 0 \end{pmatrix} \tag{1.19}$$

This implies that gravitational waves have two different states of polarization that are oriented at forty-five degrees to one another. These polarizations can be seen as the gravitational waves pass through a ring of particles in Figures 1.1, 1.2, and 1.3. These figures, courtesy of [52], clearly demonstrate the quadrupole nature of gravitational waves discussed in Section 1.1.

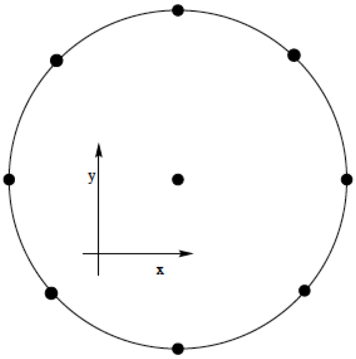

Figure 1.1: Initial configuration of a ring of particles orthogonal to wave vector prior to gravitational wave passing by.

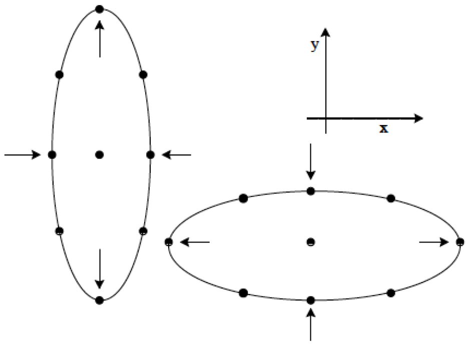

Figure 1.2: Displacement of particles for + polarization of gravitational waves.

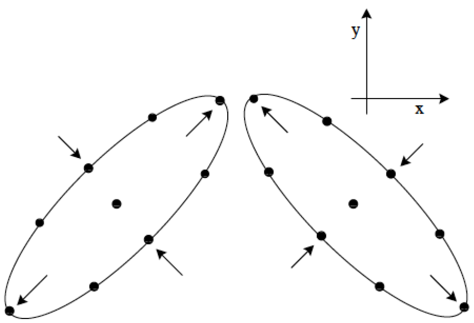

Figure 1.3: Displacement of particles for × polarization of gravitational waves.

An important entity we can compute is the coordinate change in distance between two points on the circle. Recall the distance between two events is given by

$$L = \int_0^{L_*} \sqrt{g_{\mu\nu} dx^\mu dx^\nu} \tag{1.20}$$

where L_* is the proper distance. One can find,

$$\frac{\delta L}{L_*} = \frac{1}{2} h_{ij} n^i n^j \tag{1.21}$$

where n^i is the unit vector pointing from one object to the other. As will be discussed later, this is the fundamental quantity measured by gravitational wave detectors, known as the strain amplitude.

1.2.2 Quadrupole Moment Tensor

With the use of Green's function, one can obtain the formal solution to equation (1.9):

$$\overline{h^{\mu\nu}}(\vec{x}, t) = 4 \int d^3\vec{x}' \frac{T^{\mu\nu}(t', \vec{x}')}{|\vec{x} - \vec{x}'|} \tag{1.22}$$

where $t' = t - |\vec{x} - \vec{x}'|$ is the retarded time (see [52] for complete derivation). If we assume the observer is in the radiation zone, i.e. the observer is very far away from the source, then the above can be approximated with

$$\overline{h^{\mu\nu}}(\vec{x},t) \approx \frac{4}{r}\int d^3\vec{x}' T^{\mu\nu}(t-r,\vec{x}') \tag{1.23}$$

where $r = |\vec{x}|$. In the TT gauge, where there are two polarizations of gravitational radiation and $h_{\mu\nu}^{TT}$ is purely spatial ($h_{\mu 0}^{TT} = 0$), it can be shown that

$$h_{TT}^{ij} \approx \frac{2}{r}\ddot{I}^{ij}(t-r) \tag{1.24}$$

where we define the quadrupole moment tensor:

$$I^{ij} = \int d^3\vec{x}\rho(\vec{x},t)x^i x^j \tag{1.25}$$

with $T^{00} = \rho(\vec{x},t)$ [51].

1.2.3 A simple example: Calculating the gravitational strain of a binary system

To get a sense for the order of magnitude of the strain amplitude h of a gravitational wave, let's consider a circular binary system consisting of black holes separated by an orbital distance of R. Following the example in Ref. [43], if we approximate the density of the system with delta functions,

$$T^{00} = \rho(\vec{x},t) \approx M_1\delta^3(\vec{x}-\vec{x}_1(t)) + M_2\delta^3(\vec{x}-\vec{x}_2(t)) \tag{1.26}$$

where M_1, M_2 are the masses of the two black holes at positions $\vec{x}_1$ and $\vec{x}_2$ respectively, then calculating the quadrupole moment is easily computed since the delta functions collapse the integral. The result is,

$$I^{ij}(t-r) = M_1(x_1^i(t-r)x_1^j(t-r)) + M_2(x_2^i(t-r)x_2^j(t-r)). \tag{1.27}$$

In the center-of-mass frame it can be shown via equation (1.24) that the gravitational wave polarizations at location (r, θ, ϕ) are [43]:

$$h_+ = -\frac{2}{r}\Omega^2 \mu R^2 (1 + \cos\theta^2)\cos(2\Omega(t - r)) \tag{1.28}$$

$$h_\times = -\frac{4}{r}\Omega^2 \mu R^2 \cos\theta \sin(2\Omega(t - r)). \tag{1.29}$$

In the above equations, $\mu = M_1 M_2/(M_1 + M_2)$ is the reduced mass, $\phi = 0$ without loss of generality, and Ω is the orbital frequency given by Kepler's law; i.e., $\Omega = \sqrt{(M_1 + M_2)/R^3}$. Then the magnitude of the strain produced by the gravitational wave is approximately,

$$h \approx \frac{4\mu\Omega^2 R^2}{r} = \frac{4}{r}\frac{M_1 M_2}{R}. \tag{1.30}$$

Let's consider the case where we have stellar mass black holes of equal mass with $M = 3M_\odot$. Further, consider the binary separation to be roughly $R = 7M$ and that the black holes are located in the Virgo cluster at a distance of about 20 Mpc from earth. Plugging in these numbers, one finds that the strain of the gravitational wave produced by the stellar mass black hole binary system measured on earth is approximately $h \sim 10^{-21}$.

1.3 Higher Order Approximation

In the previous section, we only considered the first order correction to newtonian gravity. However, higher orders have also been computed [122,123]. In this section, I will summarize the second order correction, also known as the first order post-newtonian limit [54].

In the lorentz gauge, the exact form of Einstein's equations is given by

$$\Box\overline{h_{\mu\nu}} = -16\pi\tau_{\mu\nu}. \tag{1.31}$$

In comparison to equation (1.9), $\tau_{\mu\nu}$ is the "effective" stress-energy tensor, which includes the original stress-energy tensor $T_{\mu\nu}$ plus the second-order correction terms of h. Now, the general solutions becomes,

$$\overline{h^{\mu\nu}}(\vec{x},t) = 4\int d^3\vec{x}'\,\frac{\tau^{\mu\nu}(t-|\vec{x}-\vec{x}'|,\vec{x}')}{|\vec{x}-\vec{x}'|}. \tag{1.32}$$

Once again we can consider the radiation zone, and approximate $|\vec{x}-\vec{x}'|^{-1} \approx r^{-1}$; however, as noted by Ref. [54], we must still consider the retardation effects of the source integration. Thus,

$$\overline{h^{\mu\nu}}(x,t) \approx \frac{4}{r}\int d^3\vec{x}'\tau^{\mu\nu}(t-r+\hat{r}\cdot\vec{x}',\vec{x}') \tag{1.33}$$

Following Ref. [54], by expanding in multipoles we find that in the TT gauge,

$$h^{ij}_{TT} = \frac{2}{r}\left[\frac{\partial^2}{\partial^2 t}\sum_{m=0}^{\infty}\hat{r}_{k_1}\hat{r}_{k_1}...\hat{r}_{k_m}I^{ijk_1k_2...k_m}(t-r)\right]_{TT} \tag{1.34}$$

where

$$I^{ij} = \int d^3\vec{x}\tau^{00}(\vec{x},t)x^ix^j \tag{1.35}$$

describes the quadruple moment as before, and

$$I^{ijk} = \int d^3\vec{x}\left[\tau^{0i}(\vec{x},t)x^jx^k + \tau^{0j}(\vec{x},t)x^ix^k - \tau^{0k}(\vec{x},t)x^ix^j\right] \tag{1.36}$$

$$I^{ijk_1k_2...k_m} = \frac{2}{m!}\frac{\partial^{m-2}}{\partial^{m-2}}\int d^3\vec{x}\tau^{ij}(\vec{x},t)x^k_1x^k_2...x^k_m \tag{1.37}$$

represent the higher moments.

Chapter 2

Astrophysical Sources

Gravitational waves arise from a variety of different astrophysical sources; these range from compact stars to processes in the early universe that might be observable today. In this chapter, I will discuss several possible sources, and indicate their detection likelihood given the sensitive frequency band of Advanced LIGO.

The sources are divided into different frequency bands: the high frequency band includes frequencies in the range of $1\,\mathrm{Hz} \lesssim f \lesssim 10^4\,\mathrm{Hz}$, the low frequency band covers $10^{-3}\,\mathrm{Hz} \lesssim f \lesssim 1\,\mathrm{Hz}$, the very low frequency band covers $10^{-9}\,\mathrm{Hz} \lesssim f \lesssim 10^{-3}\,\mathrm{Hz}$, and finally the ultra low frequency band spans $10^{-18}\,\mathrm{Hz} \lesssim f \lesssim 10^{-15}\,\mathrm{Hz}$. The high frequency band comprises of the most promising sources for a gravitational wave detection by ground based detectors such as Advanced LIGO. However, I will briefly discuss the common known sources in each of these bands. Figure 2.1 summarizes the relevant frequency bands and provides an overview of the typical sources and detectors.

Alternatively, astrophysical sources can be characterized by their signal time scale. Some sources produce continuous signals, in which the signals are periodic and hold a steady frequency over a period of time longer than the observational time [54]. The stochastic background, which will be described shortly, is a common example of a continuous signal. On the other hand, there are burst signals, in which the duration of the signal is shorter than the observation time. Burst signals can come from a violent event such as a supernova explosion, for example.

Frequency Band	**Typical Sources**	**Detectors**
Ultra low frequency $H_0 \sim 10^{-19} - 10^{-15}$ Hz	Primordial stochastic background	Gravitational-wave signature in the Cosmic Microwave Background
Very low frequency $1\,\mathrm{nHz} - 1\,\mathrm{mHz}$	Supermassive black hole binaries ($M \sim 10^9 M_\odot$); Cosmic string cusps; Stochastic background (supermassive black hole binaries, QCD-scale phase transitions)	Pulsar Timing Arrays
Low frequency $1\,\mathrm{mHz} - 1\,\mathrm{Hz}$	Supermassive black hole binaries ($M \sim 10^3 M_\odot - 10^9 M_\odot$); Extreme mass ratio inspirals; Dwarf/white dwarf binaries; Stochastic background (dwarf binaries, cosmic strings, electroweak phase transitions)	Space-based interferometers (LISA)
High frequency $1\,\mathrm{Hz} - 10\,\mathrm{kHz}$	Neutron star/black hole binaries ($M \sim 1 M_\odot - 10^3 M_\odot$); Supernovae; Pulsars, X-ray binaries; Stochastic background (cosmic strings, binary mergers, SUSY-scale phase transitions)	Ground-based interferometers

Table 2.1: This table highlights the frequency bands and corresponding sources and detectors. This table is taken from Ref. [54].

2.1 High Frequency Band

The high frequency band is the band most likely detectable by the ground-based interferometers such as Advanced LIGO.

2.1.1 Compact Binaries

Compact astrophysical objects, such as black holes or neutron stars, exhibit strong gravity, and are relatively abundant in space. A pair of compact objects will emit gravitational waves as they orbit. Due to this radiation, energy is lost causing the two objects to fall in-ward in an inspiral and eventually merge. During the inspiral phase, the orbital period decreases producing a characteristic chirp signal, in which the gravitational wave frequency increases. The inspiral is followed by a merger and then a ring-down as the combined object settles. The gravitational wave strain produced by these sources then depends on the orbital frequency and distance to the observatories, as well as other factors such as the chirp mass[1] and inclination angle. The gravitational wave signal produced by these events has been studied by the general relativity community. The inspiral phase is believed to be well modeled, and various efforts are in place to study the merger phase with the use of numerical relativity. Having a known signal waveform is a useful tool for the data analysts who are searching for a gravitational wave signal in the presence of background noise. In addition, if a gravitational wave signal is detected, one can extrapolate with known waveforms and try to discern the source. Due to the believed abundance of binary compact objects, the frequency band of their gravitational wave signal, and our knowledge of the signal waveform, binary compact objects are a very likely candidate for detection. For specific predicted detection rates refer to Table 3.10.

2.1.2 Stellar Core Collapse

Stellar core collapse, which occur during Type II, Type 1b and 1c supernovae explosions [119], also emit strong gravitational waves when the collapse deviates from being spherically symmetric. The core collapse process begins when the nuclear fusion in the core is exhausted. The dynamics of the core collapse then vary based on the properties of the progenitor. Generally, the progenitor star will collapse into a neutron star or black hole [43]. During the explosion a large amount of mass is accelerated in a short time scale. Thus, the gravitational waves produced from such a core collapse are generally of a short duration and considered a burst. These gravitational waves could provide insight into the dynamics within the star during the collapse process. Such information is usually obscured from electromagnetic observations since electromagnetic waves can scatter or be absorbed, unlike for gravitational waves. Supernovae core collapse only occur once every approximately twenty to fifty years in our galaxy, and generally these strain amplitudes are weak [54]. These sources are still in the frequency band for ground-based interferometers; however their detection likelihood is not very likely.

---

[1] The chirp mass is given by $\mathcal{M} = (m_1 m_2)^{3/5}/(m_1 + m_2)^{1/5}$ where m_1, m_2 are the masses of each star in the binary.

2.1.3 Rotating Neutron Stars

Rotating neutron stars are another promising source of gravitational waves in the high frequency regime. These objects will emit gravitational waves when the star's axial symmetry is broken, or when the rotation axis is not aligned with the axis of symmetry [54]. Since these compact objects are rapidly spinning, they produce continuous signals whose frequency is proportional to the frequency of rotation [93]. In addition, the gravitational waves emitted by these stars have a constant periodicity, which would improve the signal-to-noise ratio in the event of a detection.

Rotating neutron stars are commonly observed as pulsars [16,81]. These rotating neutron stars are highly magnetized and emit a beam of electromagnetic radiation. This radiation can only be detected when the beam points to the Earth. As a result, to observers, the star appears to pulsate as it rotates. The number of known pulsars is constantly growing. These pulsar can be targeted for a gravitational wave detection, and can be verified with the use of multi-messenger astronomy [53]. Search for unknown pulsars with gravitational waves requires more effort. More details about pulsars and rotation neutron stars can be found in Ref. [54].

2.1.4 Stochastic Backgrounds

Stochastic background radiation arises from events in the early universe (such as gravitational waves produced by the Big Bang or inflation), or other astrophysical origins. The latter constitutes random, independent, and weak sources that overlap to produce a stochastic background of gravitational waves distributed over the sky. Since this radiation comes from a mixture of various sources, the gravitational wave frequency emitted should span all frequency bands. Such a detection requires a long integration of the signal and a correlated event in multiple interferometers [164]. A detection of the stochastic background could provide information on the evolution of the universe.

2.2 Low Frequency Band

The low frequency band gravitational waves cannot be detected by the ground based interferometers in practice. Sources in this range can only be hoped to be detected via space-base detectors such as LISA [115]. As previously mentioned, the stochastic background may lie in this band. Meanwhile, stellar sources of such frequency include compact supermassive objects and compact stellar-mass objects.

Supermassive black holes with a mass of $M \sim 10^7 - 10^9 M_\odot$ constitute the former source. These tend to exist in the center of every galaxy and exhibit strong gravity. Supermassive binary black holes can inspiral and merge, emitting gravitational waves in the frequency band suitable for space-based interferometer. Supernovae collapse into a supermassive black hole can also produce detectable waves [43].

White dwarf binaries [118] are typically low compact stellar-mass objects that produce signals in the lower region of the low frequency band. These objects are generally well understood, but a gravitational wave detection could provide insight into orbit inclination which is difficult to deduce from observation, for example [43]. Again, these are more suitable for space-based interferometers.

2.3 Very Low and Ultra Low Frequency Band

The very low and ultra low frequency regime is too low for a detection from Advanced LIGO, or any space-based interferometer. Pulsars with short timescales produce low frequency band gravitational waves and could be detected by pulsar timing arrays. In addition, quantum fluctuations of the early universe which were then amplified by inflation could create gravitational waves of ultra low frequency. The gravitational waves would leave an imprint on the cosmic microwave background (CMB) [117], and thus could be indirectly detected though CMB observations [43]. Alternatively, just as the cosmic microwave background exists, there is a possibility for a cosmic gravitational wave background. Unlike electromagnetic waves, which are limited to times after recombination, gravitational waves could provide insight into the early universe and allow scientists to look further back in time. These gravitational waves are extremely weak since they have traversed significant space and time. So, although primordial gravitational waves are very exciting, near-future detection is not foreseeable.

Chapter 3

LIGO Instrumentation

A direct detection of gravitational waves has been elusive to scientists for many decades. Currently, there are several ground-based interferometers around the world attempting discovery. The large detector network is referenced in Table 3.1 and 3.2. This network includes Advanced LIGO [159], GEO600 [82], Advanced VIRGO [56], KAGRA [152], and in the future LIGO India. Having multiple detectors around the world assists in coincident detection, increases confidence of detection, and improves sky localization of events. [124].

Detector	**Location**	**Description**
Initial Laser Interferometric Gravitational-wave Observatory (LIGO)	Hanford, WA USA Livingston, LA USA	Power-recycled Fabry-Perot Michelson Interferometer (4 km and 2 km arms).
Virgo	Pisa, Italy	Power-recycled Fabry-Perot Michelson Interferometer (3 km arms).
GEO 600	Hannover, Germany	Dual-recycled Michelson Interferometer (600 m arms).
TAMA 300	Tokyo, Japan	Dual-recycled Michelson Interferometer (300 m arms).

Table 3.1: A list of first generation detectors. Tables from Ref. [54].

Detector	**Location**	**Description**
Advanced LIGO	Hanford, WA USA Livingston, LA USA	Dual-recycled Fabry-Perot Michelson Interferometer (4 km arms).
Advanced Virgo	Pisa, Italy	Dual-recycled Fabry-Perot Michelson Interferometer (3 km arms).
KAGRA	Kamioka, Japan	Cryogenic, Underground, Dual-recycled Fabry-Perot Michelson Interferometer (3 km arms).

Table 3.2: A list of current and anticipated second and third generation detectors. Table from Ref. [54].

Based on its unprecedented design level of sensitivity, Advanced LIGO is the most promising ground-based detector in the high frequency band. In addition, it is the first second generation detector to come online, and will be the first advanced detector to have observation runs. The Advanced LIGO detectors consist of two observatories; one of the detectors is located in Hanford, WA, while the second is located in Livingston, LA. A minimum of two detectors is required for confidence in a detection.[1] These detectors have already exceeded Initial LIGO's best sensitivity by a factor of three to four. The impressive status of the Advanced LIGO detectors discussed in Chapter 8 suggests very exciting observations runs to come over the next five years.

In this chapter, I will provide an overview of the instrumentation in the Advanced LIGO interferometer, starting with the basic concept of the interferometer that was pioneered by Rainer Weiss's laboratory [7], among others. Significant contribution was provided from laboratories at Caltech and MIT in the United States, as well as those in Germany, France, and Glasgow to name a few.

These ground-based interferometers are large Michelson interferometers (see Figure 3.1). The basic idea behind these interferometers involves splitting laser light power between two perpendicular vacuum tubes, or arms, and after traveling through the arms, recombining and returning to a photodiode. Nominally, the photodiode is a dark port, where the light from each arm destructively

---

[1] At least three detectors are need to triangulate and locate the source. Even larger detector networks are useful for parameter estimation such as discerning the mass, spin, inclination, etc of the source

interferes. As a gravitational wave passes through the plane perpendicular to the detector, the arms lengths are relatively distorted via equation (1.21). Much like the test particles in Figures 1.1, 1.2, and 1.3, the test masses at the end of each arm will be displaced by the passing gravitational wave. As a result, one arm length increases, while the other decreases. This modulation of the arm length alters the interference pattern at the photodiode, signaling the presence of a gravitational wave. The interferometer acts as a transducer, turning gravitational waves into photocurrent proportional to the strain amplitude $h = \Delta L/L$, where L is the nominal length of each arm and ΔL is the change in length between the two arms.

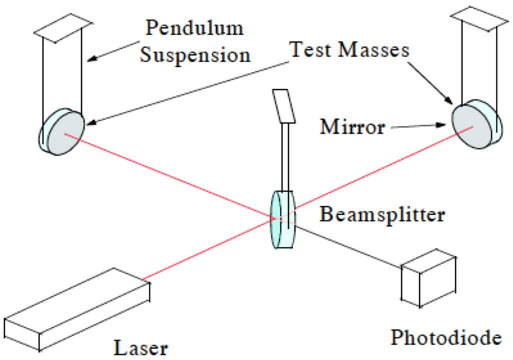

Figure 3.1: Michelson-Morley Interferometer demonstrating the proof of concept of Advanced LIGO. Image from [120].

The difficulty behind ground-based detection arises because gravitational waves are so small. In our example in Section 1.2.3, we saw that the gravitational wave strain produced by an equal-mass binary system is on the order of $h \sim 10^{-21}$. Thus, via equation (1.21), for a detector arm length on the order of a kilometer, we find that the length distortion is $\Delta L \sim 10^{-18}$ m. This displacement is approximately 1/10000 the size of a proton [43]. As a result, the operating detectors cannot be simple Michelson interferometers, but must consist of complicated multi-coupled cavities each designed to improve the sensitivity of the detector. These optical cavities will be described in this chapter.

3.1 Michelson Interferometer

A simple Michelson interferometer depicted in Figure 3.1 is commonly used as an optical phase detector, and thus is capable of detecting a gravitational wave strain in the correct polarization. The incident laser field with amplitude E_0 and laser frequency ω given by,

$$E_{in} = E_0 e^{i\omega t} \tag{3.1}$$

is split by a beam splitter and travels down two orthogonal arms. The field acquires a phase shift as it travels to the end mirror and back. For each arm $i = x, y$, this phase shift is:

$$\phi_i = 2kL_i, \qquad k = \omega/c \tag{3.2}$$

where the factor of two appears from the round trip. In the presence of a gravitational wave strain given by equation (1.19), this phase shift becomes,

$$\begin{aligned}\phi_x &= \frac{2\omega L_x}{c}\left(1 + \frac{h_+}{2}\right)\\ \phi_y &= \frac{2\omega L_y}{c}\left(1 - \frac{h_+}{2}\right).\end{aligned} \tag{3.3}$$

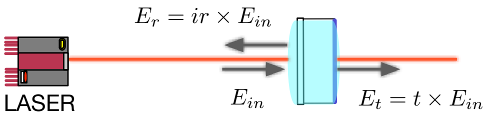

Figure 3.2: Simple laser and mirror set up with electric fields. The incident electric field is given by E_{in}. Meanwhile the reflected and transmitted field before and after the mirror are given by E_r and E_t respectively. The mirror's reflection and transmission amplitude is given by r, t respectively. Without any losses, $r^2 + t^2 = 1$.

The electric field can then be determined throughout the interferometer. For a plane mirror, the reflected field is given by $E_r = ir \cdot E_{in}$ where r is the mirror's reflection amplitude; notice the reflection gains a ninety degree phase change. Meanwhile, the transmitted field is given by $E_t = t \cdot E_{in}$ where t is the mirror's transmission amplitude. The electric fields that are first reflected (transmitted) at the beam splitter into the arm cavities, and then upon returning are transmitted (reflected) back at the beam splitter appear at the anti-symmetric port. Meanwhile, those that have been reflected (transmitted) successively arrive at the reflected port [37]. The LIGO Michelson interferometer is designed such that the anti-symmetric port is at the photodiode detector and the reflected port is at the laser source. Thus the field at the anti-symmetric port is:

$$\begin{aligned} E_{AS} &= -t_{BS} r_{BS} r E_0 e^{i(\omega t - \phi_x)} + t_{BS} r_{BS} r E_0 e^{i(\omega t - \phi_y)} && (3.4) \\ &= 2 i t_{BS} r_{BS} r E_0 e^{i(\omega t - (\phi_x + \phi_y)/2)} \sin\left(\frac{\phi_x - \phi_y}{2}\right) && (3.5) \end{aligned}$$

where t_{BS}, r_{BS} are the transmission and reflection amplitude of the beamsplitter respectively and r is the reflection amplitude of the end mirrors. A similar derivation can be done for the reflected port, as some of the field gets reflected back to the laser. The photodiodes that measure the power at the reflected and anti-symmetric ports find,

$$\begin{aligned} P_{REFL} &= 2(t_{BS} r_{BS} r E_0)^2 [1 + \cos(\phi_x - \phi_y)] && (3.6) \\ P_{AS} &= 2(t_{BS} r_{BS} r E_0)^2 [1 - \cos(\phi_x - \phi_y)] && (3.7) \end{aligned}$$

where the power is the square of the electric field. Evidently, the photodiodes measure the difference in the optical phase shift $\Delta\phi = \phi_x - \phi_y$. Given equation (3.2), this is equivalent to measuring the differential length of the arm cavities,

$$L_- = L_x - L_y. \tag{3.8}$$

In the advent of a gravitational wave, this phase difference manifests to:

$$\Delta\phi \propto L_- + \frac{h_+}{2} L_+ \tag{3.9}$$

where I have used equation (3.3) and $L_+ = L_x + L_y$ represents the common length of the arm.

At the interferometers operational point, the anti-symmetric port exists on a dark fringe where there is no light present and $L_- = 0$. In reality, we introduce a DC offset at the dark fringe so that the photodiode's photo-current is linearly dependent on the gravitational wave strain [61]. The differential length is then $L_- = (\pi/2 + \Delta_{DC})c/2\omega$, and using the small angle approximation yields,

$$P_{AS} \propto \Delta_{DC}^2 + \frac{2\Delta_{DC}\omega L_+}{2} h_+ \tag{3.10}$$

as desired. A more detailed discussion of the DC offset will be given in Chapter 7.

As stated earlier, the simple Michelson interferometer is not sensitive enough to measure the small strains h produced by gravitational waves. Several amendments to the interferometer will be discussed in the following sections.

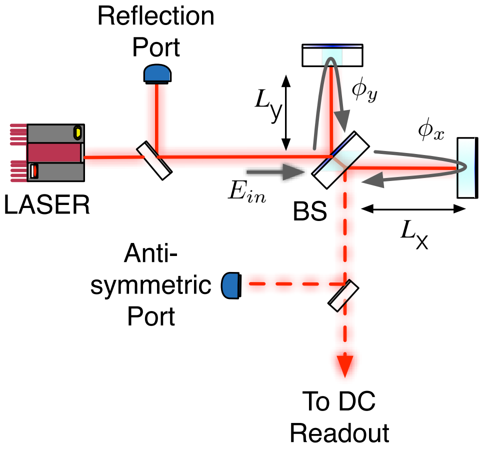

Figure 3.3: Simple Michelson interferometer with the beam splitter denoted as BS. Each arm acquires a phase shift $\phi = 2kL$. The reflected and antisymmetric ports are shown. The photodetector at the anti-symmetric port measures the phase shifts between the two arms.

3.2 Fabry-Perot Cavity

In order to amplify the signal at the photodiode of the Michelson interferometer, one would need to increase the phase shift $\Delta\phi$ acquired by the carrier light as the gravitational wave passes. This can be achieved by increasing the interaction time between the carrier light and the passing gravitational wave. Advanced LIGO uses Fabry-Perot cavities which artificially increase the size of the arm cavities, and thus the interaction time [26]. For Advanced LIGO, the Fabry-Perot cavity effectively increases the arm length by two orders of magnitude.

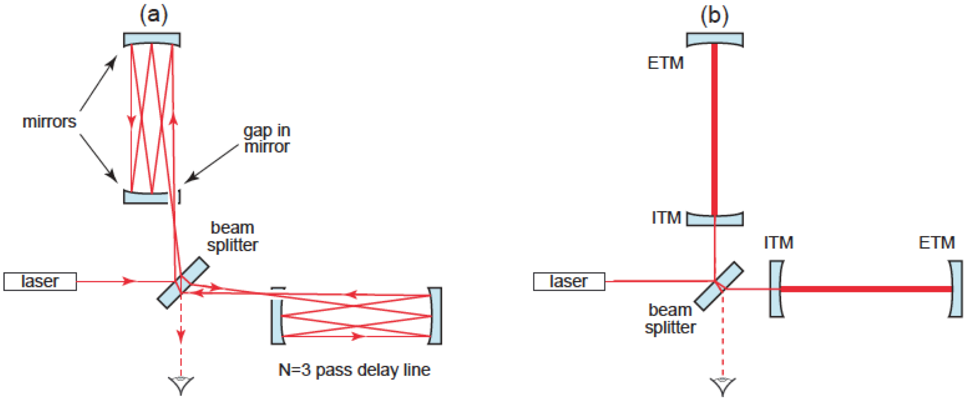

Figure 3.4: Image (a) illustrates a delay line where the laser light bounces back and forth without overlapping. Meanwhile, image (b) is of a Fabry-Perot cavity illustrating the overlapping of the intra-cavity beam. Image taken from [120]. An extensive comparison between delay lines and Fabry-Perot cavities can be found here [111].

In this configuration, the interferometer now has an intermediate test mass (ITM) and an end test mass (ETM) as shown in Figure 3.4. The intermediate mirrors are partly reflective so that the laser beam bounces back and fourth several times between the intermediate and end mirrors. Unique to the Fabry-Perot, is that the beams overlap as they traverse the cavity. Given an incident electric field E_{in}, one can compute the reflected, intra-cavity, and transmitted field as depicted in Figure 3.5. As can be seen, the reflected field, E_r, consists of a promptly reflected beam and a leakage beam. When on resonance, the leakage beam is 180 degrees out of phase from the promptly reflected beam. Applying the same principles discussed in Section 3.1, we find:

$$E = \frac{t_1}{1 - r_1 r_2 e^{-2ikL}} E_{in} \tag{3.11}$$

$$E_r = \left(-r_1 + \frac{r_2 t_1^2 e^{-2ikL}}{1 - r_1 r_2 e^{-2ikL}} \right) E_{in} \tag{3.12}$$

$$E_t = \frac{t_1 t_2}{1 - r_1 r_2 e^{-2ikL}} E_{in}. \tag{3.13}$$

where r_i, t_i are the reflection and transmission amplitudes respectively of each mirror, L is the length between the two mirrors, and k is the wave number. Evidently, the response of the optical cavity is dependent on the laser frequency, cavity length, and reflectivity of the input and output mirrors. If the reflectivity of the input and output mirrors are the same, the cavity is said to be critically coupled. In such a case, when on resonance, the leakage and promptly reflected field, exactly cancel and the incident light is fully transmitted. When $r_1 > r_2$ or $r_1 < r_2$ the cavity is said to be undercoupled or overcoupled, respectively. In the case of an undercoupled cavity, the promptly reflected beam is greater than the leakage beam; while the opposite is true for the overcoupled cavity. For Advanced LIGO, the arm cavities are overcoupled.[2]

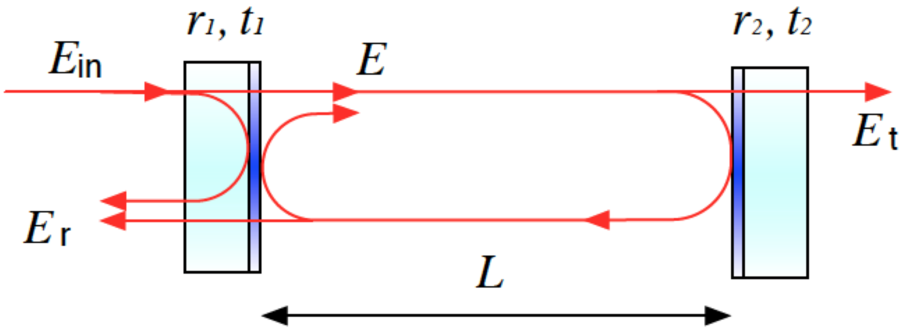

Figure 3.5: Fabry-Perot schematic from Ref. [93].

The cavity is resonate when the cavity length is an integer number of laser half-wavelengths,

---

[2] The input mode cleaner and output mode cleaner which will be discussed in the upcoming sections are both critically coupled cavities.

or equivalently when $\phi = 2\pi n$ where n is an integer. Recall the round trip phase is given by $\phi = 2kL = 4\pi L/\lambda$. When on resonance, light enters the cavity, the intra-cavity field power is maximal, and the reflected field's phase changes rapidly. This rapidly changing phase corresponds to increasing the phase shift $\Delta\phi$ as desired [93]. Meanwhile, when out of resonance, the electric field exhibits a ninety degree phase change as it reflects, and the intra-cavity field power is minimal, while the reflected field power reaches a maximum.

In the case of a Michelson interferometer we find $\Delta\phi \propto$ arm length, meanwhile, with Fabry-Perot cavities, $\Delta\phi \propto$ arm length $\times \mathcal{F}$ where $\mathcal{F}$ is the finesse. The rate of change of the reflected field's phase depends on the finesse, and thus so must the phase shift. The finesse of a cavity is defined by:

$$\mathcal{F} = \frac{FSR}{FWHM} \approx \frac{\pi\sqrt{r_1 r_2}}{1 - r_1 r_2}. \tag{3.14}$$

where the last approximation is true for $r_1 r_2 \sim 1$. The Free Spectral Range (FSR) frequency is the spacing in frequency, ν_{fsr}, between successive resonances; it is defined by $\nu_{fsr} = c/2L$. The round trip phase can be expressed in terms of the FSR: $\phi = 2\pi\frac{\nu}{\nu_{fsr}}$ where ν is the laser frequency. Meanwhile, the Full-Width-Half-Max (FWHM) is the spectral width of a waveform at half maximum. The FWHM is approximately twice the cavity pole f_{pole}. The cavity pole relates to the storage time, τ_s, of light in the cavity via the following expression[3]:

$$f_{pole} = \frac{1}{2\pi\tau_s}, \qquad \tau_s = \frac{2L}{c}\frac{1}{\ln r_1 r_2} \approx \frac{2L}{\pi c}\mathcal{F}. \tag{3.15}$$

Due to internal losses and mirror transmission, the energy in the cavity decays, and the photon lifetime in the cavity is given by the storage time. Since the storage time is finite, the cavity pole is the frequency at which the intra-cavity field is low passed and describes the bandwidth of the Fabry-Perot cavity. Intensity noise and frequency fluctuations that occur on a time scale faster than the storage time are filtered. In other words, these fluctuations are suppressed by the cavity response above the cavity pole.

---

[3] The last approximation is again valid only if $r_1 r_2 \sim 1$

The finesse of the cavity can also be used to describe the average number of round-trips in the cavity:

$$\langle N_{photons} \rangle = \frac{r_1 r_2}{1 - r_1 r_2} \approx \frac{\mathcal{F}}{\pi} \tag{3.16}$$

Thus, the finesse determines the power build-up, the average number of photon bounces in the cavity, and the rate of phase change [106]. The detector's sensitivity to arm length changes is dependent on the finesse of the Fabry-Perot cavity.

3.3 Laser System

The laser ejected into the interferometer is generated from a diode-pumped Nd:YAG laser made especially for LIGO, at 1064nm (infrared). This wavelength was chosen because lasers at this frequency are generally more stable and the optic coatings and mirrors are compatible with this light. The coatings must have low absorption, low scattering, and not burn with higher power build up. Blue and even sufficiently high power of green light could damage the optics; however, infrared does not. Prior to entering the interferometer, this pre-stabilized laser (PSL) beam is sent through a series of mode-cleaners and input optics (IOO) to improve the power stability and beam shape of the light. In addition, the light is frequency shifted and locked to a reference cavity [124]. At design sensitivity the laser power will be 180 W. As of June 2015, the Hanford detector operates at 23 W while the Livingston detector operates at 25 W.

3.4 Input Mode Cleaner

Before entering the interferometer, the main infrared beam is filtered through the input mode cleaner (IMC). The input mode cleaner is a triangular cavity that serves several purposes. One, it spatially filters the incoming laser beam. The beam's defects, which includes higher order transverse electromagnetic (TEM) modes, are reflected from the cavity and thus rejected. In theory, only the fundamental mode (TEM00) resonates in the input mode cleaner cavity and is completely transmitted to the interferometer [106]. Second, it provides frequency noise suppression. The frequency emitted from the laser source will naturally fluctuate, but by using a Pound-Drever-Hall locking technique [58] to lock the input mode cleaner, these fluctuations are reduced as the beam enters the interferometer. The Pound-Drever-Hall control loop ensures that the laser frequency stays on resonance and follows the length of the input mode cleaner, inherently suppressing frequency fluctuations. The frequency stability at the IMC output must be $< 1 \times 10^{-3}\mathrm{Hz}/\sqrt{\mathrm{Hz}}$ at 100 Hz [159]. And finally, the input mode cleaner can be used to attenuate laser beam jitter.

3.5 Power Recycling Cavity

Under nominal configurations, the interferometer operates in the dark fringe condition, where no carrier light reaches the photodiode at the anti-symmetric port. By the conservation of energy, almost all of the light returns to the main laser source. A partially transmissive mirror is inserted between the laser source and beam splitter, so that the returning light can be sent back into the interferometer. This recycled light constructively interferes with the outgoing laser beam, and resonates within the power recycling cavity. As a result, the power build up in the interferometer is increased, which consequently diminishes shot noise (see Section 3.9.2).

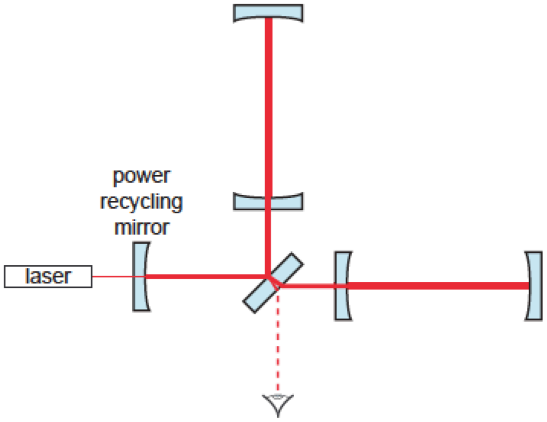

Figure 3.6: A power recycling mirror may be added to the interferometer in order to increase the power of the incoming laser beam. Image from Ref. [120].

3.6 Signal Extraction Cavity

A signal recycling mirror is placed after the interferometer and before the photodiode dark port. Despite its name, the purpose of this mirror is to extract the gravitational wave signal from the interferometer. This additional cavity is used to broaden the frequency response of the interferometer. For a gravitational wave detection, we desire that the detector be maximally sensitive. However, it is also important to have a broad bandwidth. The latter is determined by the signal storage time in the arms, while the former is determined by the carrier storage time. The signal extraction cavity allows for the sideband storage time to be consistent with the desired detector bandwidth, while allowing the carrier storage time to be increased. In other words, the finesse of the arm cavities is greater for the carrier than it is for the signal sidebands with the existence of the signal recycling mirror. The signal extraction cavity effectively reduces the finesse of the arm cavities for the gravitational wave signal. This allows for a broad detector bandwidth without sacrificing significant detector sensitivity, which is desirable. For further details on the signal extraction cavity refer to Ref. [111].

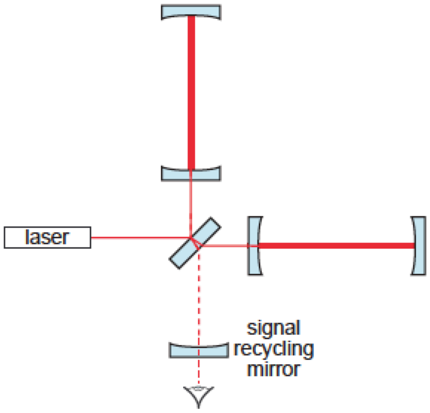

Figure 3.7: A signal recycling mirror may be added to the interferometer in order to increase the bandwidth of the interferometer. Image from Ref. [120].

3.7 Output Mode Cleaner

As the beam passes through the interferometer, the optical components and their deformations (mostly created by heating) cause non-fundamental modes (i. e. non-TEM00 modes) to reappear in the beam. Thus, before reaching the photodiode at the anti-symmetric port, the beam passes through the output mode cleaner (OMC), a four-mirror bow-tie configured cavity. The OMC rejects these non-fundamental modes and the RF sidebands of the carrier light. Details about the OMC can be found in Ref. [151].

3.8 Advanced LIGO

Advanced LIGO's optical layout consists of Michelson interferometers with 4 km Fabry-Perot cavities, an input and output mode cleaner, and signal and power recycling mirrors [159]. A brief description on the purpose of these cavities was given in the previous sections. The full optical layout can be seen in Figure 3.8.

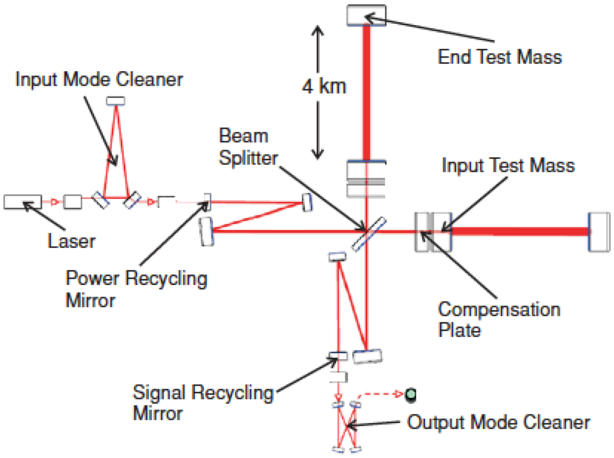

Figure 3.8: Advanced LIGO configuration consisting of two fabry-perot cavities, an input and output mode cleaner, and signal and power recycling mirrors. Image from Ref. [85].

Advanced LIGO's design goal is to measure a gravitational strain noise as small as $4\times10^{-24}/\sqrt{Hz}$, with best sensitivity in the 100 Hz region. Figure 3.9 shows the design sensitivity for Advanced LIGO, and compares the final design sensitivity for Advanced LIGO with Initial LIGO's sensitivity curve. Initial LIGO [22] was the first generation of the LIGO interferometer, whose main goal was to demonstrate the functionality of the detector. Unfortunately, no gravitational wave detection was made with Initial LIGO, but upper limits on event rates were set with the data collected. Advanced LIGO's design sensitivity goal is at least a factor of 10 greater than the sensitivity reached by Initial LIGO throughout the entire gravitational wave frequency band. This implies observing a factor of 1,000 times more volume. Besides the overall sensitivity gain, Advanced LIGO also had a much larger detection bandwidth; the lower limit of the gravitational wave frequency band is extended from ∼40 Hz down to ∼10 Hz. Ultimately, gravity gradients along the Earth's surface limits the detectors sensitivity such that the frequency band for detection must be above ∼ 10Hz [124]. The increase in sensitivity between 100 and 10 Hz is important for the study of supermassive compact binary coalescence since the inspiral and merger frequencies are generally in that band. In addition, Advanced LIGO should observe inspiraling binaries made up of two 1.4 solar mass neutron stars at distance of ∼ 200 Mpc, neutron star-black hole binaries at distance of 650 Mpc, and coalescing binary black holes at cosmological distance of $z = 0.4$ [1]. Due to the limited sensitivity, these sources were not visible to Initial LIGO.

To achieve such an improvement in sensitivity, three main contributing noises had to be mitigated. At low frequency, the seismic noise was reduced with the introduction of a seven stage pendulum with passive and active isolation systems. At intermediate frequencies, the brownian noise was reduced by using monolithic fused silica to suspend the last two stages of the mirrors [55]. For further improvement, the beam diameter was increased by a factor of 1.5 to improve coating brownian noise. Finally, at high frequency, the quantum noise was reduced by increasing the input power to 180 W, and adding the signal extraction cavity. Details about the limiting noise sources in Advanced LIGO can be found in the following section.

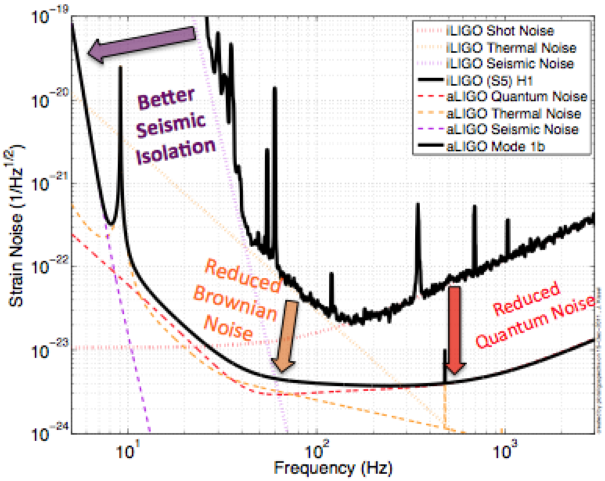

Figure 3.9: A comparison of Initial LIGO's 5th science run and Advanced LIGO's design sensitivity curves.

Here, are some designed specification for Advanced LIGO taken from Ref. [85]:

- Arm cavities have a finesse of 450 for 1064 nm which is determined primarily from thermal lensing.

- Input power of 180 W

- Stored optical power of ∼1 MW
- Goal is to have a sensitivity wide range band centered around 100 Hz
- Strain noise of $3 \times 10^{-24}/\sqrt{\mathrm{Hz}}$ in the most sensitive band.
- Bandwidth from 10 Hz to 10^4 Hz
- Beam tubes operate at 10^{-9} Torr.

A common figure of merit used to describe the sensitivity of the detectors is known as the binary inspiral range. This range is the distance to which the gravitational wave signal emitted by a binary neutron star (BNS) coalescence is detectable. The BNS range is defined in Ref. [159] as the volume-and orientation-averaged distance at which the coalescence of a pair of 1.4-solar mass neutron stars gives a matched filter signal-to-noise ratio of 8 in a single detector. Based on the improved sensitivity range, the detection rates for Advanced LIGO are more promising than for Initial LIGO. Figure 3.10 shows the expected detection rates for Advanced LIGO. The BNS range for Advanced LIGO will be around 60 Mpc for the first observation run and ultimately reach 200 Mpc. Notably, the first observation run will already exceed Initial LIGO's BNS range of ∼25 Mpc.[4]

3.9 Noise sources

Based on the design sensitivity goal for Advanced LIGO, differential arm displacements on the order of 10^{-19} m must be measured. It is therefore required that displacements up to this level are solely due to gravitational waves, and not masked by other factors. As a result, the design of these interferometers is driven by the need to mitigate noise. In Section 3.8, I allude to some of these mitigation techniques used for Advanced LIGO. The optical cavities of Advanced LIGO also all serve a particular purpose to reduce the noise of the interferometer. Regardless, the detection of

---

[4] this corresponds to a detection rate of approximately 1/50 per year assuming the average number of expected BNS inspirals.

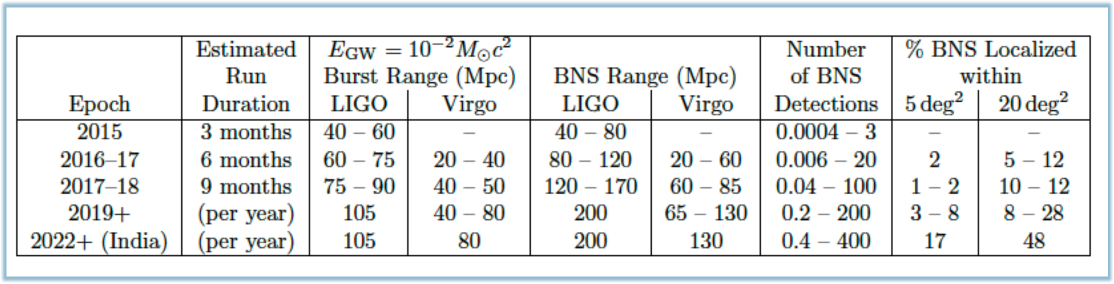

Epoch	Estimated Run Duration	$E_{\rm GW} = 10^{-2} M_{\odot} c^2$ Burst Range (Mpc)		BNS Range (Mpc)		Number of BNS Detections	% BNS Localized within	
		LIGO	Virgo	LIGO	Virgo		$5\,\mathrm{deg}^2$	$20\,\mathrm{deg}^2$
2015	3 months	40 – 60	–	40 – 80	–	0.0004 – 3	–	–
2016–17	6 months	60 – 75	20 – 40	80 – 120	20 – 60	0.006 – 20	2	5 – 12
2017–18	9 months	75 – 90	40 – 50	120 – 170	60 – 85	0.04 – 100	1 – 2	10 – 12
2019+	(per year)	105	40 – 80	200	65 – 130	0.2 – 200	3 – 8	8 – 28
2022+ (India)	(per year)	105	80	200	130	0.4 – 400	17	48

Figure 3.10: This is a table showing the expected detection rates from 2015 to 2022. The estimated run duration listed here are coincidence data taking times for two detectors of equal sensitivity. A binary neutron star detection becomes more promising starting in 2016 as the detector sensitivity is improved. Notably, these expected detections have a large uncertainty stemming from the uncertainty in the number of events present [65].

gravitational waves by ground-based detectors is still limited by several noise sources. Ideally, these interferometers should only be constrained by the Heisenberg Uncertainty Principle. However, in practice, there are many noise sources present, some of which cannot be diminished. Figure 3.11 shows the limiting noises sources expected for in the final design of Advanced LIGO; the main noise sources as discussed in Ref. [159] are:

- Below 10 Hz seismic noise, environmental disturbances, and technical noise will dominate.
- At frequencies between 10 and about 40 Hz radiation pressure noise, thermal noise from suspensions, and gravity gradient noise will dominate.
- At frequencies between 40 to 200 Hz thermal noise from mirror optical coatings and quantum effects from the light will dominate.
- Above 200 Hz the sensitivity will be shot noise limited.

In this section, I provide a brief overview of these main noise sources, which contaminate the gravitational wave readout signal. A full description of these noise sources and mitigation tactics can be found in Ref. [26]. As per common practice, the main noises are categorized as displacement or sensing noise. The former noise is one that couples directly to the displacement of the test masses, while the latter is noise that arises in the sensing of the gravitational wave readout.

Notably, prior to reaching the designed sensitivity level additional noise sources will be present. The commissioning effort will focus on determining and mitigating these other noise sources until the designed sensitivity is reached. The current status of the interferometer can be found in Chapter 8.

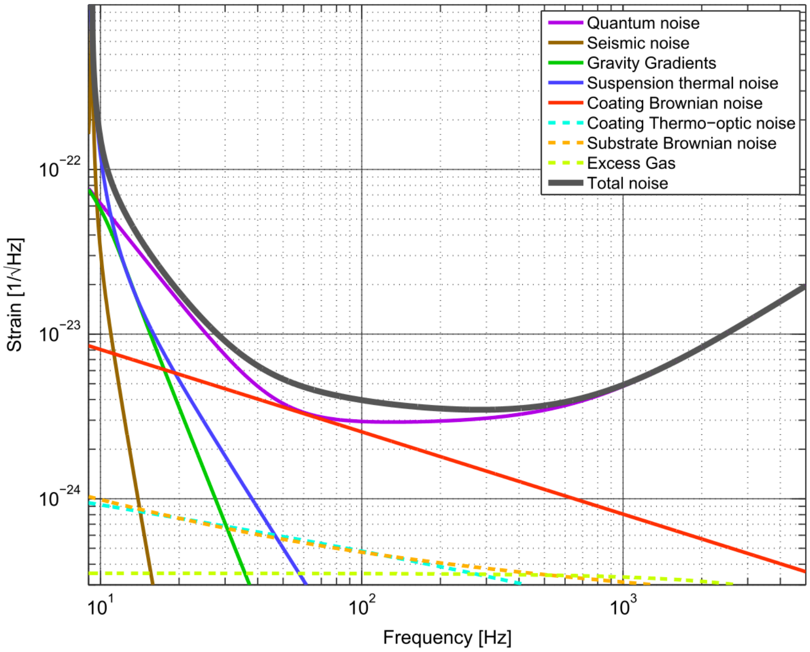

Figure 3.11: Advanced LIGO noise sources courtesy of [159]. The BNS of this total strain noise is 190 Mpc.

3.9.1 Displacement Noise

Displacement noise causes direct movement of the interferometer's suspended mirrors, and therefore, causes a differential arm length change which can interfere with gravitational wave detection. Seismic motion, thermal noise, radiation pressure, and residual gas noise are the main causes of displacement noise.

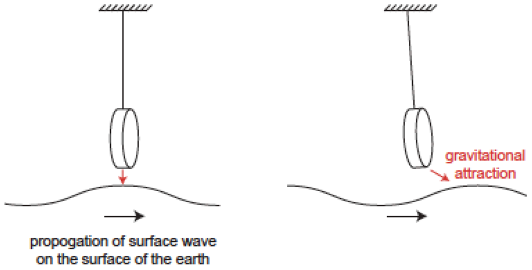

Figure 3.12: Suspended test mass can couple to earth's surface waves via gravitational attraction. Image from Ref. [120].

Seismic noise arises from density fluctuations along the earth's surface. These surface waves can gravitationally couple to the suspended test masses, causing them to swing. Several seismometers are located throughout the ground-based interferometers to monitor the seismic motion near the test masses. This information can be used to subtract out the noise from the detector waveform. LIGO is also located in remote areas where seismic motion is expected to be smaller. However, ground coupling to the test mass is inevitable. The test mass motion requirement is $< 10^{-19}$ m/rtHz at 10 Hz. Nominally, the ground motion at 10 Hz is $\sim 10^{-9}$ m/rtHz. Therefore, Advanced LIGO's isolation system must provide 10 orders of magnitude of isolation from ground motion [35, 105]. The test masses are suspended in either a triple or quadruple pendulum suspension. For a simple pendulum, the transfer function to the pendulum mass from the horizontal motion falls off as $1/(\text{frequency})^2$ above the pendulum resonance, and subsequently as $1/f^4$, $1/f^6$, etc for each suspending mass. As a results, at high frequencies, the mirrors are well isolated from ground motion, and can be considered as "free-falling" objects. At low frequency, further isolation is required. There are two active isolators: external pre-isolators and in-vacuum seismic isolators [35, 105]. To further mitigate the motion, we employ active and passive feedback control. Each mass in the pendulum is lined with magnetic coils that are used for actuation. The lowest stage of the end test masses have an electro-static driver, which has less drive strength, but also has less actuation noise.

Thermal noise is also a relevant noise source in the low frequency regime. The individual

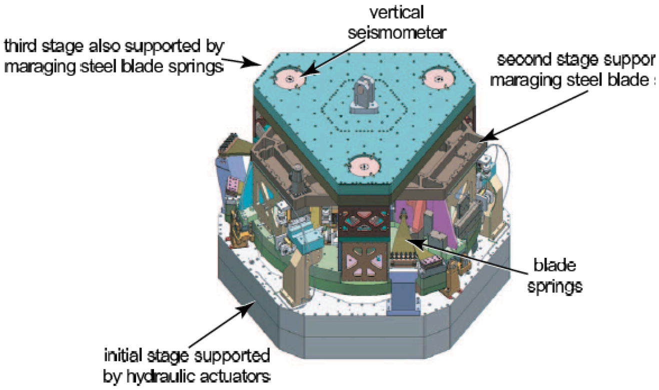

Figure 3.13: Internal stage of in-vacuum active isolation (from Ref. [120]).

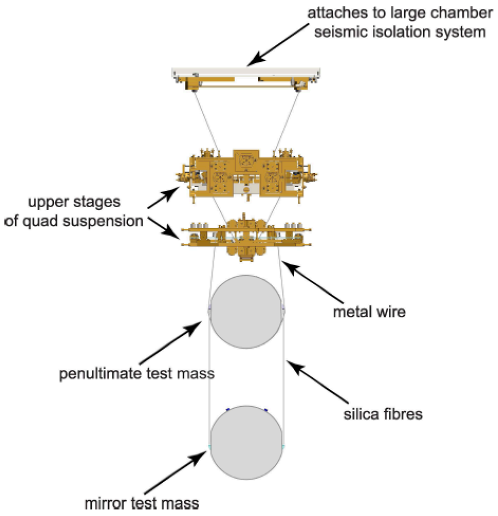

Figure 3.14: Test mass suspension (from Ref. [120]).

particles which make up the test mass (including both the glass and the coating) and the mirror suspensions are in a radiative thermal equilibrium with the vacuum. The thermal motion (also known as Brownian noise) of these particles can then cause a displacement in the mirror impacting the differential length of the arms. Low-loss coatings and high-Q materials are used to limit the thermal noise. In particular, fused silca suspends the last two stages, and a monolithic structure is used. Thermal noise can also appear in the form of thermal aberrations. With lossy coatings, laser power is partially absorbed by the test masses, resulting in thermal expansions and deformations. By acting as a lens, the deformations can create higher order TEM modes as the laser beam resonates in the arm cavity. Advanced LIGO employs a thermal compensation system [49, 102] which heats up the test mass, such that the thermal expansion is uniform throughout the test mass and there is minimal deformation in the region of the incident beam.

A third form of displacement noise is radiation pressure, which dominates from 10 to 50 Hz. There are two types of radiation pressure: quantum and technical radiation pressure. Technical radiation pressure arises from pressure applied to the test masses due to a variation in the laser intensity hitting the optic. Meanwhile, the quantum radiation pressure arises from the quantum nature of light. When photons scatter off surfaces in the vacuum, they each produce N numbers of photons creating a $\propto \sqrt{N}$ fluctuation force on each arm from radiation pressure. Since each arm is subject to a Poisson distribution of photons, a differential radiation pressure displacement between the two arms arises. Displacement noise due to radiation pressure is given by

$$\delta x^2(\omega) = \mathcal{N}^2 \times \left(\frac{4Ph}{m^2\omega^4 c\lambda}\right) \tag{3.17}$$

where $\mathcal{N}$ is the number of reflections in the Fabry-Perot cavity [120]. This noise can be mitigated by decreasing the laser power and increasing the mass of the test masses. However, shot noise, another type of quantum noise (which will be described in more detail in the following section), increases as the laser power decreases. Thus the overall sensitivity of the interferometer lies in the balance between radiation pressure and shot noise. The sensitivity limit is called the Standard Quantum Limit (SQL).

Recall that the gravitational wave strain is ultimately measured by the phase shift in the arms. Phase noise creates fluctuations in this phase shift, and is thus a limiting factor in gravitational wave detection. Phase noise arises from quantum vacuum fluctuations, scattering from residual gas, and backscatter. Quantum vacuum fluctuations cause variations in the arrival time of the photons at the photodetectors that are not from the presence of a gravitational wave. Since the vacuum tubes do not reach true vacuum, some residual gas and pressure remains. This residual gas will exhibit brownian motion and can displace the optics. In addition, photons can scatter off of these residual particles, producing noise in the detected phase shift. Similarly, backscattering can arise from imperfections on the mirror. Some backscattered light can recombine with the main laser beam, creating undesired phase noise.

3.9.2 Sensing noise

Sensing noise arises in the sensing or readout of the interferometric state. Typical sensing noise includes laser noise, electronics noise, and shot noise. Laser noise arises in the form of both amplitude and frequency fluctuations of the laser light. These laser noise sources couple to the gravitational wave readout through a variety of mechanisms described in Ref. [26]. Dark noise, which is electronics noise when no light is incident on photodetectors, can also pollute the sensing signal; however this is generally not a limiting noise. Other electronics noise in the sensing chain can also contribute to the overall noise.

At high frequencies the interferometer sensitivity will be limited by shot noise. Shot noise is a quantum noise and arises from the fluctuations in the number of photos on the laser light. These fluctuations are sensed in the gravitational wave readout, but have no impact on the displacement of the test masses. The photon shot noise follow poisson statistics: $\delta\phi_{shot} \propto \frac{1}{\sqrt{P_{laser}}}$ [106]. Therefore, increasing the input power of the laser to the interferometer will lower this noise contribution.

3.9.3 Miscellaneous noise

There are several other noise sources that do not fall in the category of sensing or displacement noise. These include control noise, cross-coupling noise, environmental noise (particularly acoustic noise). Details on these noises can be found in the literature [26, 59, 71, 164].

3.10 Lock Acquisition

The various optical cavities comprising of Advanced LIGO were briefly described at the beginning of this chapter. Since these cavities consist of suspended mirrors that are coupled to the ground motion, the general motion of these mirrors is on the μm level. In such a state where the optics are freely swinging, the interferometer is said be uncontrolled, and is useless to detect a gravitational wave. *Lock acquisition* is the process in which the interferometer is brought from an uncontrolled state to a controlled state. For Advanced LIGO there are five length degrees of freedom that must be controlled:

$$\begin{aligned}\text{Common Arm Length (CARM)} &= L_x + L_y\\ \text{Differential Arm Length (DARM)} &= L_x - L_y\\ \text{Power Recycling Cavity Length (PRCL)} &= l_p + (l_x + l_y)/2\\ \text{Michelson Interferometer Length (MICH)} &= l_x - l_y\\ \text{Signal Recycling Cavity Length (SRCL)} &= l_s + (l_x + l_y)/2\end{aligned}$$

where $L_{x,y}$ are the lengths of the two Fabry-Perot cavities, $l_{x,y}$ are the lengths between the beam splitter and the cavity arms, and $l_{p,s}$ are the lengths between the beam splitter and the power and signal recycling mirrors respectively. In the above, there are five equations and six variables. The final equation to determine the six lengths of the interferometer comes from the Schnupp asymmetry [130]. This asymmetry introduces a macroscopic arm length difference $l_{sch} = (L_x + l_x) - (L_y + l_y)$ and causes the sidebands to resonate at the anti-symmetric port. For Advanced LIGO, l_{sch} is approximately 8 cm. Of the above length degrees of freedom, DARM is the most important as it contains the gravitational wave signal. The displacements of all these DOFs, particularly DARM must be small enough to measure the gravitational wave strain amplitude. A servo system is used to reduce this displacement and control the interferometer. Generally, the cavity displacement is sensed and the servo sends a correction signal to an actuator that controls the motion of the optics. For optical cavities, displacement noise is interchangeable with frequency noise: $\Delta L = \frac{L\lambda}{c}\Delta\nu$. As a result, controlling these length degrees of freedom, also implies that specific resonance conditions must be achieved. The arm lengths, PRCL, and SRCL must be on resonance,

$$\frac{4\pi\nu}{c}L_{x,y} = 2\pi n, \qquad \frac{4\pi\nu}{c}L_{PRCL,SRCL} = 2\pi n, \qquad (n : \text{integer}) \tag{3.18}$$

while MICH must be held a dark fringe,

$$\frac{2\pi\nu}{c}L_{MICH} = 2\pi n, \qquad (n : \text{integer}). \tag{3.19}$$

The servo system can also keep the DOFs controlled by adjusting the frequency of the laser, as an alternative to adjusting the length of the cavity. In some cases, the servo feedbacks to both the laser and the optics. A cavity is said to be *locked* when the laser beam is resonating in the cavity and the displacements are less than the servo bandwidth. At this point the interferometer is said to be operational and can be used for gravitational wave observation.

When the cavities are unlocked, the DOFs are free to be any value up to physical limitations. Unfortunately, it is possible for the servo system to be unstable if the DOF that is to be controlled is not near its operating point (i. e. the point at which the servo system is designed to keep the DOF). This makes lock acquisition non-trivial. For high finesse cavities, the region where the servo system is utile can be quite small. As the cavities are freely swinging, the main laser will occasionally pass through resonance (without lock being acquired). These instances are known as cavity flashes. The flashes occur at the free-spectral range of the cavity. Given a cavity's velocity, the actuator has $t = v/L_{FWHM}$ to apply a sufficient force on the optic and acquire lock when it flashes. The cavity linewidth with respect to the laser frequency and baseline length is given by:

$$L_{FWHM} = \frac{\lambda}{2\mathcal{F}}, \qquad \nu_{FWHM} = \frac{\nu_{fsr}}{\mathcal{F}}$$

If we consider the 4 km arm cavities for Advanced LIGO, assuming a typical velocity of 1μm/s and a finesse of 450 with $\lambda = 1064\,$nm, this amounts to $t = 1\,$ms. As will be relevant later, for a finesse of 13 and $\lambda = 532\,$nm, this amounts to $t = 20\,$ms. Using a system with a wider linear range is significantly beneficial to lock acquisition since it's easier to catch lock.

The velocity of the cavity is important to consider in lock acquisition. If the velocity is above the threshold velocity,

$$v_{thresh} \le \sqrt{\frac{F_{max}\lambda}{2\mathcal{F}m}}$$

then the maximum force, F_{max}, from the servo actuator applied on the mass m will never be sufficient to lock the cavity. Thus it is desirable to reduce the velocity of the mirrors and increase the force of the actuators. However, F_{max} is limited by the electronics noise introduced to the interferometer. A seismic isolation system is applied in Advanced LIGO to mitigate the velocity of the cavities [105]. Further details on the reduction of the cavity velocity can be found in Refs. [93] and [164]. If this servo signal is fed back to the laser frequency instead of the cavity length, this threshold velocity obviously does not apply. Thus, laser feedback is ideal; however, for coupled DOFs that can only be applied to one DOF. As will be discussed in greater detail later, laser feedback is used to control CARM in Advanced LIGO, while the remaining DOFs use length actuation feedback subject to the threshold velocity.

Lock acquisition for coupled cavities is significantly more challenging than for single cavities. Since the five length DOFs of Advanced LIGO share optics, they are highly coupled. This implies that locking one cavity is likely to contaminate the error signal used to lock another cavity. Ref. [93] explains in detail that locking the arm length DOFs likely contaminates the signals used to the lock the dual-recycling Michelson interferometer. In addition, the sensing matrix used to convert the signals from the optical ports of the interferometer to the length DOFs is non-diagonal and difficult to invert with coupled cavities [164]. This makes choosing the correct sensors for lock acquisition more challenging. Solutions to all these challenges will be resolved in Chapter 4 and 7. Chapter 7 also briefly discusses controlling the angular DOFs of the interferometer not mentioned in this section.

3.10.1 Pound-Drever-Hall Locking Review

The standard servo used to lock optical cavities is known as the Pound-Drever-Hall locking technique [58]. This method locks the cavity by either forcing the laser frequency to track the length of the cavity by actuating on the laser frequency or by having the length follow the laser frequency by actuating on the optics; sometimes both are used. In either case, this technique provides a valuable measure of the mismatch between laser frequency and cavity length.

The author of [48] highlight the two benefits of the Pound-Drever-Hall locking technique: 1) it decouples the laser frequency measurement from the laser intensity, and 2) it can measure and suppress frequency noise faster than the cavity can respond. This is achieved by using the derivative of the reflected intensity as an error signal to adjust the locking point. Recall Equation 3.13, which describes the reflected electric field from a cavity, then the reflected intensity profile looks as follows:

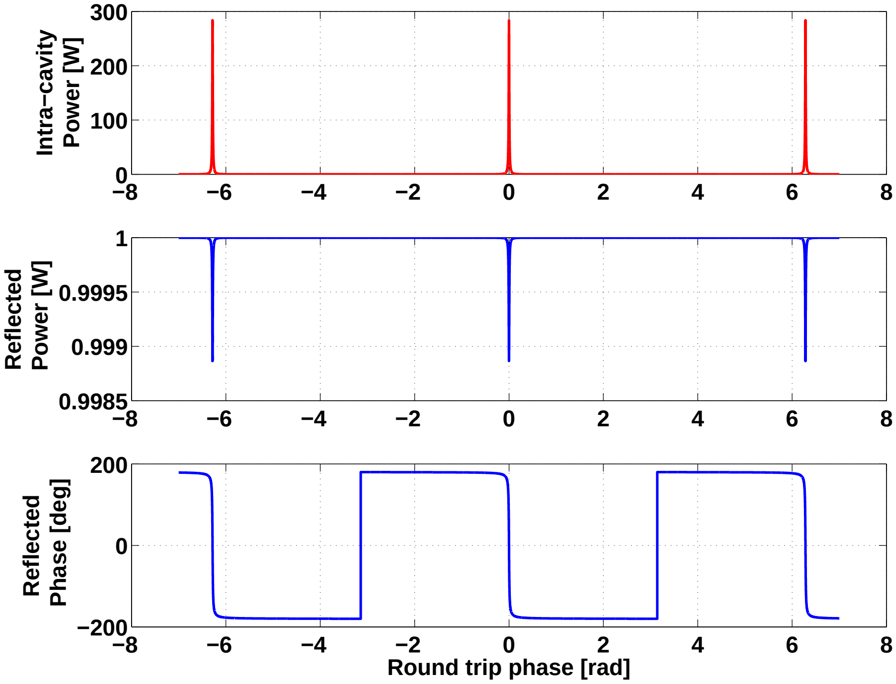

Figure 3.15: The intra-cavity power, reflected field power, and reflected field phase as a function of round trip phase. As an example, an incident laser power of 1W and a finesse of 450 is assumed.

The intensity profile indicates how for off resonance the cavity is. Meanwhile, the phase of the reflected field indicates which side of the resonance the cavity is on. This phase is measured by generating sidebands with a definite phase relationship to the incident and reflect field, and measuring the beat note between the sidebands and the reflected field. The phase modulation is typically at radio frequency (RF), satisfying that the phase modulation be at high frequencies above the cavity pole and at some significant fraction of the cavity FSR. When the carrier resonates in the cavity and the RF sidebands are anti-resonant, the PDH error signal is linear and the RF sidebands act as the local oscillator. Meanwhile, when the carrier is anti-resonant and the RF sidebands resonate in the cavity, the carrier is now the local oscillator and the PDH error signal is linear with opposite sign. Outside of these regions, the PDH error signal is non-linear. It is possible for both the RF sidebands and carrier to resonate in the cavity; however, in this configuration, the PDH error signal is zero and useless. Therefore, the frequency modulation is chosen so that the RF sideband resonance is set near the carrier off-resonance frequency. Thus, when locking the carrier, the RF sidebands are completely reflected and are used as the local oscillator. The Pound-Drever-Hall locking technique is known as a *heterodyne detection* scheme because the local oscillator, the RF sidebands, are at a different frequency from the carrier.

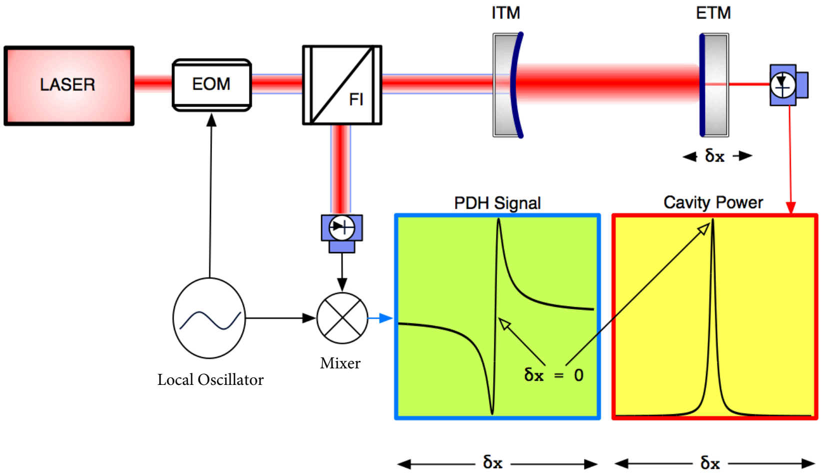

Figure 3.16: The configuration for the Pound-Drever-Hall reflection locking technique. The RF sidebands are produced with an electro-optic modulator (EOM); The EOM is driven by a local oscillator, which sets the modulation frequency. A faraday isolator (FI) is used to direct the reflected light onto the photodetector. The local oscillator provides the frequency modulation reference. A mixer is used to produce the PDH error signal in reflection. Also shown above is the transmitted signal, which is maximal on resonance. The cavity can be locked within the linear range of the PDH error signal by feeding back to the laser frequency or cavity length. Cartoon adapted from [164].

The RF sidebands are generated with a phase modulator located between the laser source and the cavity as shown in Figure 3.16. If the incident electric field out of the laser is $E_{inc} = E_0 e^{i\omega t}$, then the modulation produces, $E_{inc} = E_0 e^{(i\omega t + \Gamma \sin(\Omega t))}$, where Γ, Ω are the modulation depth and modulation frequencies respectively. This expression can be expanded in terms of Bessel functions:

$$E_{inc} = Ae^{i\omega_0 t}(J_0(\Gamma) + J_1(\Gamma)e^{i\Omega t} - J_1(\Gamma)e^{-i\Omega t}) \tag{3.20}$$

where the first term describes the carrier, and the second and third terms describe the upper and lower sidebands of the beam respectively. The electric field in reflection is then,

$$E_{refl} = Ae^{i\omega_0 t}(J_0 r(\omega) + J_1 r(\omega + \Omega)e^{i\Omega t} - J_1 r(\omega - \Omega)e^{-i\Omega t}) \tag{3.21}$$

where $r(\phi) = -r_1 + r_2 t_1^2 e^{-i\phi}/(1 - r_1 r_2 e^{-i\phi})$ is the reflection coefficient of the Fabry-Perot cavity as seen in Section 3.2. Then the incident power on the reflected photodetector is given by,

$$\begin{aligned} P_{refl} = |E_{refl}|^2 = {} & P_0 J_0^2 |r(\omega)|^2 + P_0 J_1^2 \left(|r(\omega + \Omega)|^2 + |r(\omega - \Omega)|^2\right) \\ & + 2P_0 J_0 J_1 \mathrm{Re}\left[r(\omega) r^*(\omega + \Omega) - r^*(\omega) r(\omega - \Omega)\right] \cos \Omega t \\ & + 2P_0 J_0 J_1 \mathrm{Im}\left[r(\omega) r^*(\omega + \Omega) - r^*(\omega) r(\omega - \Omega)\right] \sin \Omega t \\ & + (2\Omega \,\text{terms}) \end{aligned} \tag{3.22}$$

where the first three terms are the DC power of the beam and the second two terms are the modulated components. By convention, the cosine term is known as the Q-signal and the sine term is known as the I-signal. A synchronous demodulation of the photodetector I-signal produces the desired error signal to lock the cavity. The I-signal is zero at the carrier and sideband resonances, with a linear range of $\lambda/(4\mathcal{F})$ around these resonances. Only within the linear range of the carrier resonance, is the signal used to lock the cavity.

To demodulate the signal at the photodetector the mixer takes the product of two signals.

Demodulating at the same frequency as the modulation, one finds:

$$\cos\Omega t\cos\Omega t = \frac{1}{2}\left(1+\cos 2\Omega t\right) \tag{3.23}$$

$$\sin\Omega t\sin\Omega t = \frac{1}{2}\left(1-\cos 2\Omega t\right) \tag{3.24}$$

$$\cos\Omega t\sin\Omega t = \frac{1}{2}\sin 2\Omega t \tag{3.25}$$

Using a low pass filter, the 2Ω terms are removed, and the DC term is filtered through. The original signal scaled by a factor of a half is now available. From these product, its evident that the modulation and demolition frequencies must by synchronized. Typically a phase shifter is included in the signal chain to correct for any delays that might arise between the modulation and demodulation frequency. The full signal chain can be seen in Figure 3.17.

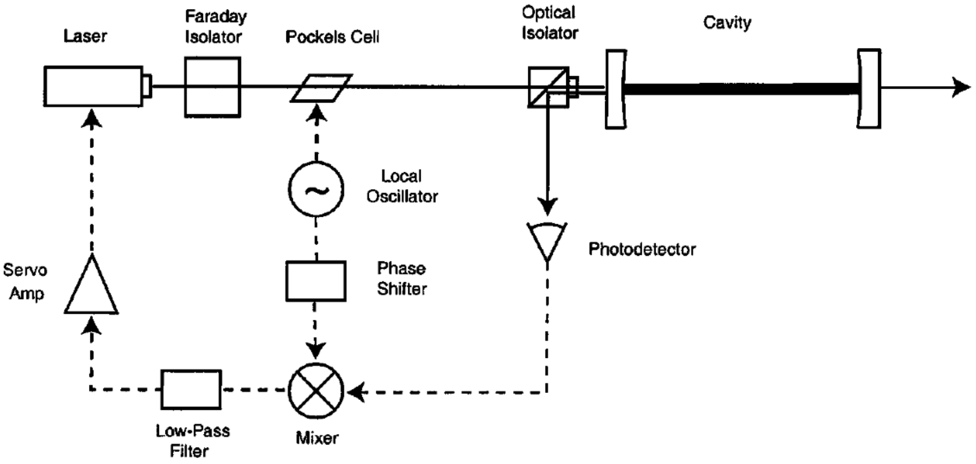

Figure 3.17: PDH set-up showing the complete signal chain. Image from Ref. [58].

As will become evident, the Pound-Drever-Hall locking technique is used throughout the interferometer control scheme.

3.10.2 Phase-Locked Loop Review

Another control scheme commonly used in Advanced LIGO is a phase-locked loop (PLL) [29]. As will be discussed and motivated in the next chapter, auxiliary lasers are introduced to the lock acquisition process in order to aid in the control of the five length degrees of freedom. Several phase-locked loops are used to ensure that these auxiliary lasers are in phase with the main infrared laser and each other, and thus, simultaneously resonant in the cavities. The beat note measured in the phase-locked loop is as follows:

$$E_{beat} = E_1 + E_2 = E_1^0 e^{i(\omega_1 t - \phi_1)} + E_2^0 e^{i(\omega_2 t - \phi_2)} \tag{3.26}$$

$$P_{beat} = 2E_1^0 E_2^0 \cos\left((\omega_1 - \omega_2)t - (\phi_1 - \phi_2)\right) \tag{3.27}$$

Where E_1 and E_2 are the two laser fields with frequencies ω_1, ω_2 respectively. The error signal derived from this beat note contains information on the frequency difference between these two laser fields and the cavity round trip phase [104].

Chapter 4

Arm Length Stabilization for Advanced LIGO

4.1 The ALS Scheme: Motivation and Components

Advanced LIGO's major goal is to establish the first direct detection of gravitational waves [11] and subsequently to start the regular observation of astrophysical sources [10,12,13,15,17,19]. The aim of the detector's design is to measure gravitational waves with a strain as small as $4 \times 10^{-24}/\sqrt{\text{Hz}}$. All advanced detectors have their best sensitivity in the 100 Hz region. The corresponding requirement for length resolution is then $\sim 10^{-19}$ m rms within a 100 Hz bandwidth [85]. This high sensitivity requires multiple optical cavities to enhance the response of the Michelson interferometer [113]. First, Fabry-Perot cavities are added to each Michelson arm to effectively increase the arm length by two orders of magnitude. Secondly, partially transparent mirrors are added to the symmetric and the anti-symmetric ports of the Michelson interferometer to recycle the laser power and extract the gravitational wave signal, respectively [57, 107]. These extra optical resonators are called power recycling cavity and signal recycling cavity. They further enhance the detected signal, but add the complication of keeping two additional cavities on resonance. The Michelson interferometer must also be held at the point of minimum output power (dark fringe condition). In doing so, most of the light returning from the arm cavities is directed back to the main laser and recycled to the interferometer, increasing the overall sensitivity.

Cavities can be locked to a resonance using the Pound-Drever-Hall (PDH) reflection locking technique [58]. This requires adding phase-modulated radio frequency (RF) sidebands to the input light and detecting the reflected light using a demodulation scheme [73]. A variant of this technique exploits the Schnupp asymmetry [130] to keep the Michelson operating on a dark fringe. For Advanced LIGO the three main detection ports are in reflection of the full interferometer, at the anti-symmetric port, and a small pick-off beam in the power recycling cavity as shown in Figure 4.1. With high finesse cavities the Pound-Drever-Hall technique has a very small linear operating point. Outside this region the error signal is either negligible or misleading (it can contain information other than the deviations of the system [164]). Furthermore, if the laser frequency sweeps over a resonance faster than the cavity storage time, the light inside the cavity does not have enough time to fully build up. The resulting Pound-Drever-Hall signal can display multiple Doppler peaks, further confusing any controls scheme [101, 109, 125].

The general goal of the initial controls of an advanced detector is to bring all five degrees of freedom to the linear operating point [21]. These five degrees of freedom consist of the common mode length, differential mode length, Michelson length, power recycling length, and the signal recycling length as described in Figure 4.1. Because of the two recycling cavities all degrees of freedom are strongly coupled. The state of the recycling cavities has a large effect on the signals from the arm cavities, whereas the state of the arm cavities can completely alter the signals used for locking the dual-recycled Michelson interferometer.

In the initial configuration of LIGO [22, 36] no signal recycling cavity was used [14, 18]. The locking scheme first locked the power-recycled Michelson interferometer before using a stochastic approach to catch each arm cavity [67]. This was neither predictable nor robust, and typically required multiple locking attempts. VIRGO used another approach whereby the arm cavities were locked first, followed by the power-recycled Michelson interferometer. This locking scheme transmitted most of the light into the anti-symmetric port to broaden the cavity linewidth of the power-recycled Michelson interferometer [23]. However, it is unclear how this technique can be extended to include a signal extraction cavity. For Advanced LIGO a new arm length stabilization system was devised to make locking reliable and repeatable, while being compatible with the new optical configuration.

The idea of the arm length stabilization system [90, 114] is to lock each arm cavity individually using lasers mounted behind each end test mass (see Figure 4.2), decoupling two of the five length degrees of freedom. The arm cavities are then kept away from resonance for the main laser light by offsetting the frequency of the end station lasers. In principle, keeping the main infrared light off-resonance in the arm cavities is similar to mis-aligning the end test masses and having no arm cavities. The dual-recycled Michelson interferometer can be locked in this configuration without signal contamination from the arm cavities. In practice, the arm cavities that are controlled with the individual lasers and held off resonance to the main infrared beam have some impact on the dual-recycled Michelson; however, this affect is minimal. With the main infrared beam off resonance in the arm cavities, the central dual-recycled Michelson interferometer is locked using the third harmonic technique (also called 3f technique) as previously demonstrated by the TAMA300 [32] and Virgo [24] interferometers. The 3f technique is based on the observation that the third harmonics of the phase-modulated RF sidebands produce error signals that are to first order independent of the arm cavity resonance [33], because a significant contribution to the 3f signal is due to the beat between the modulation RF sideband and its second harmonics on the other side of the carrier light. A phase modulator such as a Pockels cell will produce the second harmonics as a second order term. Neither the first nor the second harmonic RF sidebands are resonant in the arm cavities when the carrier is resonant. This allows the dual-recycled Michelson interferometer to stay locked while the arm cavities are slowly brought into resonance by zeroing the frequency offset. Once the arm cavities are fixed on resonance, they can no longer produce spurious signals that disturb the lock of the dual-recycled Michelson interferometer.

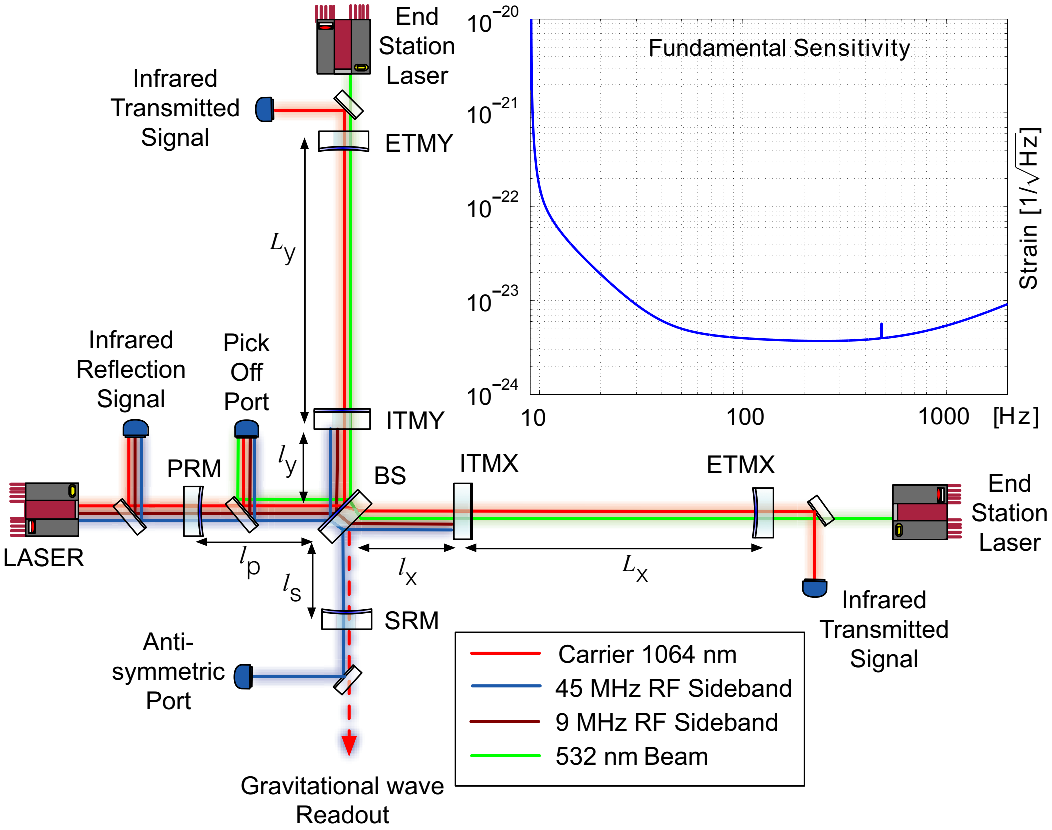

Figure 4.1: Simplified optical layout of the Advanced LIGO detector. A beamsplitter (BS) is used to separate the light into an X-arm and a Y-arm. Each arm is comprised of an input test mass (ITM) and an end test mass (ETM) forming the arm cavity. The Michelson interferometer is operated near a dark fringe which reflects most of the injected laser power back towards the laser. The partially transmitting power recycling mirror (PRM) is used to enhance the circulating power until most of the power is lost internally. The signal recycling mirror (SRM) is used to enhance the optical response to a gravitational-wave. The common mode is defined by $(L_x + L_y)/2$, the differential mode by $L_x - L_y$, the power recycling length by $l_p + (l_x + l_y)/2$, the signal recycling length by $l_s + (l_x + l_y)/2$, and the Michelson length by $l_x - l_y$. The macroscopic part of the Michelson length is called the Schnupp asymmetry. The interferometer detector ports are highlighted in the diagram. This includes the reflection port, pick-off port, and anti-symmetric port. The infrared transmitted signals are required for full locking (see Chapter 7). The various frequency components of the light used to control the five degrees of freedom of the interferometer are also depicted. The 9 MHz and 45 MHz RF sidebands are used to track the length of the power and signal recycling cavities, respectively. The 532 nm beam is used to independently control the two arm cavities. The 1064 nm carrier resonates in all cavities but the signal recycling one. The inset shows the fundamental noise limits of the Advanced LIGO design as an amplitude spectral density.

An implementation of the arm length stabilization system is shown in Figure 4.2. The main laser [100] is a 200 W injection locked Nd:YAG laser operating at 1064 nm (infrared). The arm length stabilization system uses a doubled Nd:YAG laser operating at 532 nm (green) deployed at each end station to distinguish them from the main laser. This requires that the main interferometer optics are dichroic (see Table 4.1). The requirements for the green wavelength optics are modest, only requiring a reasonable arm cavity build-up and a transmitted path to the vertex of the interferometer. This path includes the wedge of the beam splitter, which separates the transmitted green beams of each arm that nominally overlap with the main infrared beam in the arm cavities.

	ETM	**ITM**	**PRM**	**SRM**	**PR2**
1064 nm	3.6 ppm	1.4%	3.1%	37%	229 ppm
532 nm	35%	1%	—	—	100%

Table 4.1: Approximate transmission properties of the optics for 1064 nm and 532 nm wavelengths. The green ETM transmission was much higher than anticipated. This adversely affected the linewidth at 532 nm, but did not prevent the arm length stabilization system from working. The free spectral range of an arm cavity is 37.5 kHz. The arm cavity linewidth for 532 nm is 2.9 kHz which corresponds to a finesse of about 13. The linewidth for 1064 nm is 84 Hz corresponding to a finesse of about 450 [21].

In order to control the offset frequency of the end station lasers relative to the main laser, the green transmitted light interferes with a sample beam of the main laser which has been doubled using a second-harmonic-generator. In order to support an RF detection scheme, the X-arm laser runs at a frequency of 78.92 MHz below the doubled frequency of the main laser, whereas the Y-arm laser runs at a frequency 78.92 MHz above (see Table 4.2). In the corner station, the light of the Y-arm interferes with that of the X-arm to produce a differential mode signal. The X-arm interferes with the frequency-doubled sample beam from the main laser to deduce a common mode signal. Strictly speaking, this is just the difference between the X-arm and the laser. But, with the differential mode signal controlled to zero, it becomes a representation of the common mode mismatch.

Location	**Freq. (MHz)**	**Deviation**	**Comment**
Main Laser	0	$2\Delta f_{main}$	set by main laser VCO
Reference Cavity	316.8	fixed	frequency reference
Fiber	0	fixed	shifted back
X-arm laser	-78.92	Δf_x	down-shifted
Y-arm laser	78.92	Δf_y	up-shifted
Differential beat note	157.84	$\Delta f_y - \Delta f_x$	controlled to zero
Common beat note	-78.92	$2\Delta f_{main} - \Delta f_x$	offset from resonance

Table 4.2: Nominal RF frequencies referenced to the 532 nm light. The fiber beam is taken from the transmitted reference cavity beam, and then shifted back to DC. The main laser frequency can be actuated relative to the reference cavity using the main laser voltage controlled oscillator and the double-passed acousto-optic modulator [100].

Id	**Description**	**Wavelength**
I.	Infrared PDH reflection locking signal	1064 nm
II.	Infrared transmitted signal	1064 nm
III.	Fiber phase locked loop (PLL) signal	1064 nm
IV.	Green PDH reflection locking signal	532 nm
V.	Common mode signal	532 nm
VI.	Differential mode signal	532 nm
VII.	Input mode cleaner PDH reflection locking signal	1064 nm

Table 4.3: List of the photodetectors used for length sensing. Numerals are referenced in Figure 4.2.

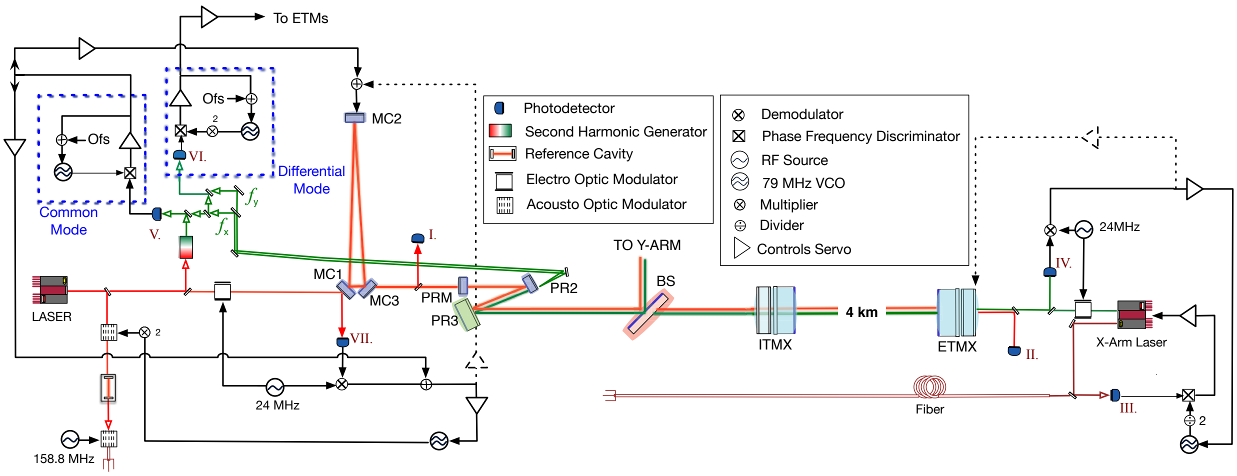

Figure 4.2: Layout of the arm length stabilization system. Only the X-arm is shown. See Table 4.3 for a list of detector ports. The system for the Y-arm is identical. In the end station a laser which is stabilized to a fiber coupled beam coming from the main laser is locked to the arm cavity using 532 nm light. Until the differential mode servo is engaged the feedback path to the ETM is used to keep the frequency of the local voltage controlled oscillator at nominal. In the corner station the main laser is first stabilized to a reference cavity and then to the suspended mode cleaner, which is formed by the three mirrors MC1, MC2 and MC3. Initially, for frequencies below ∼10 Hz the error signal of the mode cleaner is fed back to one of the mode cleaner mirrors, while at higher frequencies it is fed back to the main laser. After the green laser is locked to the arm cavities, the common mode signal provides the most quiet reference for stabilizing the main laser frequency. So, it is used to control the mode cleaner instead. The transmitted 532 nm light of the X-arm interferes with a frequency-doubled sample beam from the main laser to form the common mode feedback path. The transmitted 532 nm light from the X and Y-arms are interfered to form the differential feedback path.

Frequency offsets are adjusted using voltage controlled oscillators (VCO). The performance of these VCOs is critical for operations. The linewidth of the combined arm and power recycling cavities is only 1 Hz, requiring the vertex VCOs[1] to have a root-mean-square (rms) frequency noise of the same order. In order to cover at least one free spectral range of an arm cavity, the frequency tuning range needs to be at least 37.5 kHz, which is much larger than the range of a crystal oscillator. Microwave resonators on the other hand have sufficient range, but their frequency noise exceeds the requirement. A frequency difference divider is used to combine the low noise of a

---

[1] The vertex VCOs are those drawn within the Common and Differential Mode dashed boxes of Figure 4.2. The remaining VCOs include the two end station VCOs (only one is drawn) and one for the input mode cleaner.

fixed frequency crystal oscillator with the divided-down output of a microwave resonator. Dividing the output of a microwave oscillator reduces both its range and its phase noise by the divisor. We use a 1.05 GHz microwave oscillator with a range of ±140 MHz. Dividing it by 128 and adding it to a 71 MHz crystal oscillator gives us a 79.2 MHz VCO [8, 135] with a range of ±1 MHz. The root-mean-square frequency noise has been measured to be around 15 Hz. For the vertex VCOs we use a second stage frequency difference divider. Dividing the output of the first stage by 10 and again adding it to 71 MHz yields a 78.92 MHz VCO with a range of ±100 kHz and a frequency noise below 2 Hz. The frequency noise of the VCOs are below requirement [31].

4.1.1 End Station Phase-Locked Loop

At the end of each arm cavity, an auxiliary laser of both 1064 nm and 532 nm light is housed on an optical table. This free running non-planar ring-oscillator (NPRO) laser can drift in frequency by tens of MHz. However, the main laser eventually used to lock the arm cavities, passes first through a reference cavity, and only drifts by ±2 MHz. As a result, the initial frequency error of the end station auxiliary lasers must be less than this. To resolve this discrepancy, we phase-lock the end station laser to the main laser frequency. We take a sample of the main laser beam and send it to the end station using a fiber. The fiber absorption at 532 nm is large, so we use the 1064 nm light. The end station lasers are themselves doubled Nd:YAG lasers. Their 1064 nm output is locked to the fiber output using a phase-locked loop (PLL) [29].

The fiber and 1064 nm light from the auxiliary laser are combined on the end stations' optical table to form a beat note. This beat note is measured by an RF photodetector, whose signal is sent to a phase-frequency discriminator [80, 141]. A phase-frequency discriminator compares the phase of two input signals to produce an error signal. If the input signals are far away in frequency, the frequency discriminator overrides the phase detector and is used to compare the signals' frequency. As the signals are driven closer together toward the reference frequency, the circuit is switched back to the phase detector mode. A normal mixer does not have this capability. Thus, a phase-frequency discriminator is used in this phase-locked loop to produce an error signal instead of a mixer since it provides a larger range. The reference of the phase-locked loop is given by a 78.92 MHz VCO, after its frequency is divided down by two. This in turn guarantees that the green light at the end station lasers is set to a frequency offset near 78.92 MHz, either above or below that of the main laser depending on the sign of the PLL. Phase locking the end station lasers to the fiber output also brings the laser frequency close to the operation point by adjusting the laser's thermal controls, and ensures that the laser is not close to a mode-hopping region.

Since the main laser is first stabilized to a fixed-spacer reference cavity and then a suspended mode cleaner [77], its frequency fluctuations are suppressed by several orders of magnitude in the frequency band of interest. Locking the free-running end station laser to the fiber output has the added benefit of reducing its frequency noise far enough that it can be locked to the arm cavity directly. The additional noise added by the fiber is not significant, as will be seen in Chapter 6.

4.1.2 End Station Pound-Drever-Hall Loop

After stabilizing the end station laser, the 532 nm light is locked to the arm cavity using the Pound-Drever-Hall reflection locking technique. Before entering the cavity, the light is phase modulated by an electro-optic modulator, which is driven by a 24.9 MHz RF source. A photodetector is used to measure the power at reflection and the signal is demodulated at the corresponding frequency. A mixer produces an error signal between the demodulated signal and the RF source. This RF source is phase shifted to emulate the phase delay of the cavity. The output of the mixer goes through a servo amplifier, and to the "tune" input of the local VCO. At and below microseismic frequencies ($\sim$300 mHz), the signal is fed back to the suspension actuators of the end test mass. Above these frequencies, the signal is sent to the laser thermal controls. As a result, the frequency is locked to the cavity and follows the cavity length, except below 0.2 Hz where the cavity is locked to the laser. Now, the arm cavity serves as a much better frequency reference for the end station laser, suppressing any noise introduced by the fiber. Figure 4.3 is a block diagram of the end station PDH and PLL loops.

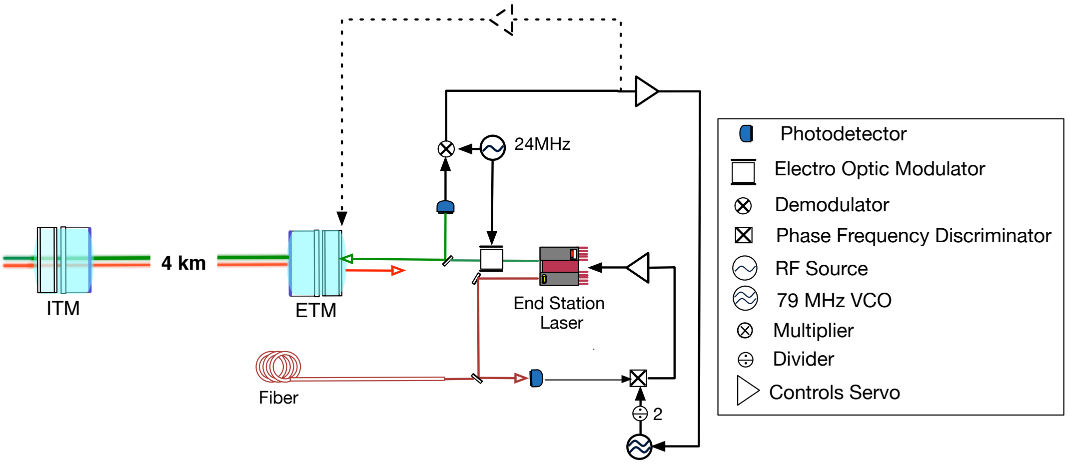

Figure 4.3: ALS schematic of end station Pound-Drever-Hall and phase-locked loop.

4.1.3 Input Mode Cleaner Loop

As will be explained in the following section, the input mode cleaner plays an important role in the arm length stabilization technique. Nominally, this cavity is locked using the standard Pound-Drever-Hall reflection locking technique, as shown in Figure 4.5. A 24 MHz RF source is used as a reference, and the error signal is sent to a servo amplifier. At frequencies above 70 Hz, the error signal is sent to the VCO of the main laser frequency. The frequency of the main laser is changed by using an acousto-optic modulator (AOM), which is driven by the main laser VCO. At frequencies below 70 Hz, we offset the length of the input mode cleaner by actuating on one of the suspensions, in particular MC2. MC2 is a triple suspension, with the mirror as the third pendulum (Figure 4.4). The MC2 feedback is an offloaded distribution, such that when actuating on the test mass, the signal gets propagated upward in the suspension chain (see Appendix C) [98].

Precise measurements of the input mode cleaner length and cavity linewidth were also conducted with a double-demodulation scheme as a separate study [154]. The technique and results are presented in Chapter 10.

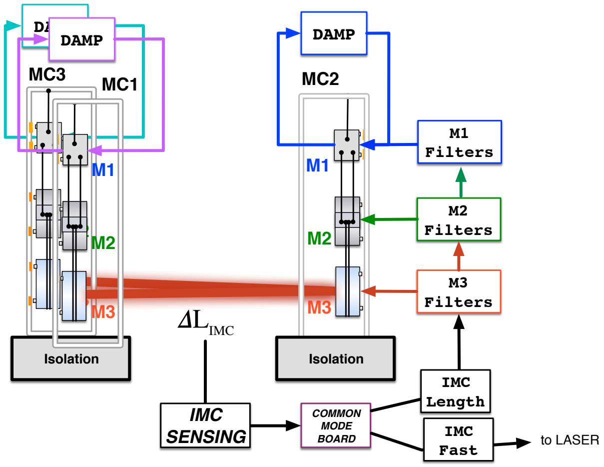

Figure 4.4: Diagram of the input mode cleaner loop highlighting the triple suspensions and the offloaded distribution actuation. Image adapted from Ref. [98].

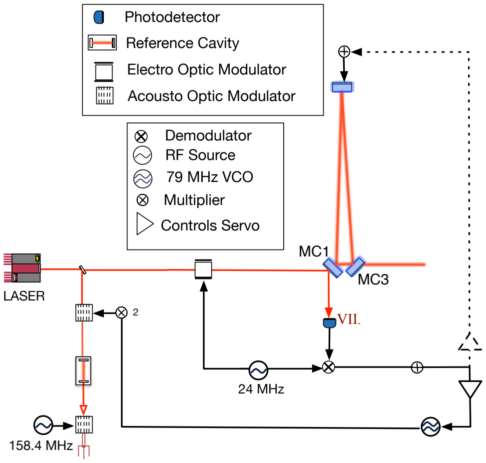

Figure 4.5: ALS Schematic of IMC Loop

4.1.4 Common Arm Locking

With the two arm cavities locked to the 532 nm beam, the transmitted light is then sampled in the corner station using a dichroic mirror. The light from the X-arm interferes with a frequency-doubled sample beam from the main laser. This beat note indicates how far off resonance the main laser is from the X-arm, and ultimately represents the common mode mismatch when the differential mode is nulled.

The common mode VCO, operating at 78.9 MHz, is locked to this beat note using a PLL. This PLL uses a broadband photodetector to detect the signal, a phase-frequency discriminator to produce an error signal, and a frequency difference divider to decrease the linear range of the common mode VCO and keep the PFD in the phase detection mode [75]. In principle the PLL is not needed and the phase-frequency discriminator can be used directly to provide the necessary error signals. However, in practice, the arm length fluctuations were large enough to force the phase-frequency discriminator to constantly switch between phase and frequency detector mode, introducing transients which the system was not prepared to handle. The PLLs are required to extended the linear range of the sensor and reduce the transients introduced into the control system.

In this configuration, the common mode VCO control signal is used as an error signal to offset the main laser frequency. We use the main laser frequency for the common mode control rather than feedback to the test masses, since it has higher range and bandwidth. At frequencies below 70 Hz, we offset the main laser frequency by applying a length offset to the input mode cleaner. As represented by the dashed line in Figure 4.2, the feedback from the input mode cleaner servo amplifier to MC2 is cut and substituted with the common mode VCO control signal. At frequencies above 70 Hz, we offset the main laser frequency through the main laser VCO by adding the common mode VCO control signal to the input mode cleaner locking point. During this transition, the input mode cleaner remains locked.

In the locking sequence, we introduce a frequency offset in the tune input of the common mode VCO. This in turn will shift the control signal feeding back to the VCO which is used to adjust the relative offset between the frequency of the main laser and the frequency of the green laser in the X-end station. For each free spectral range of the main 1064 nm light, there are two arm cavity resonances for the 532 nm light. As a first step we look for the infrared resonance in the X-arm by moving the main laser frequency to its nominal resonance frequency and to a point a full free spectral range away. We choose the frequency which gives us a resonance of the main laser light. This single arm locking sequence is shown in Figure 4.6. Finally, we move the frequency of the main laser to a fixed 500 Hz offset away from resonance. This offset is chosen such that the main infrared laser beam is sufficiently off resonance from the arm cavities, and won't interfere with the lock acquisition of the dual-recycled Michelson interferometer.

4.1.5 Differential Arm Locking

The same procedure is repeated for the Y-arm with the difference that the beat note is taken from the interference between the transmitted beams of the arm cavities. The differential mode VCO frequency has to be doubled first to 158.9 MHz, since the beat note is at twice the single arm offset. As before, the VCO is phase-locked to the beat note. Unlike the common mode controls, the signal

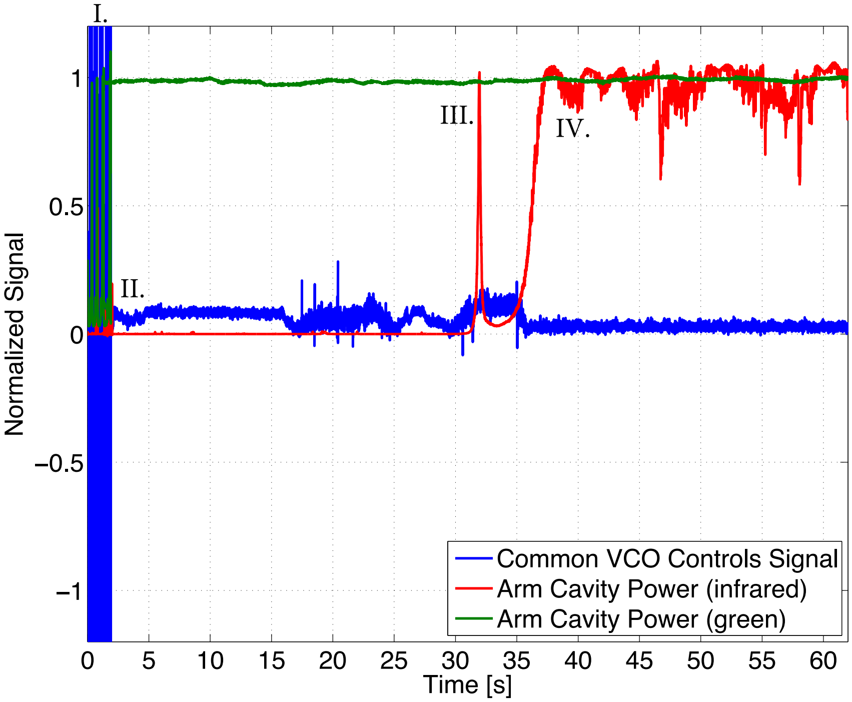

Figure 4.6: X-arm locking sequence and common mode arm length stabilization. In the first two seconds at point I, the end station laser tries to acquire a cavity lock. Both the VCO control signal and the arm cavity build-up are wildly fluctuating. At point II, the end station laser locks on the fundamental arm cavity mode indicated by the full build-up of the green cavity power. Once the cavity is locked, the corner station common VCO is locked to the transmitted beat note. Then, the common mode feedback path to the mode cleaner is engaged. At point III, the common mode is fully engaged and the offset is swept to find the infrared resonance, as seen by the arm cavity flashes of the 1064 nm light. Subsequently, at point IV, the common mode VCO is set to infrared resonance as seen by the full cavity build-up. Due to alignment fluctuations the infrared cavity power drifts around its set point, but the cavity build-up stays near 90% on average.

of the differential mode VCO is fed back to the differential position of the end test masses. In practice, only one test mass is used. Actuation is swapped to the other end test mass when the interferometer is fully locked in the low noise configuration. Again, we have to make sure that the green resonance in the Y-arm corresponds to a resonance of the main laser. Finally, the microscopic length difference between the two arm cavities is set to nominally zero.

A critical component to this stage of lock acquisition is the ability to control the test masses.

The end test masses are suspended in quadruple pendula in order to isolate them from seismic noise. To further mitigate the motion of the test mass, there are two active isolators: external pre-isolators and in-vacuum seismic isolators [35, 105]. The seismic isolation systems have sufficiently high performance that alignment control is not necessary during these initial steps [159]. Then, each of the upper three masses in the coupled pendula is actuated with magnetic coils [50]. Meanwhile, the lowest stage, the end test masses have electro-static drivers [87], which have less drive strength, but also have less actuation noise. Similar to the triple stage suspensions, the quadruple suspensions also use an offloaded distribution in the control scheme [99].

The quadruple suspension is formed by the top mass (TOP), the upper intermediate mass (UIM), the penultimate mass (PUM), and the test mass (TST). The dynamic response of these stages will be examined in Section 5.8; meanwhile, the longitudinal actuation strength of each of these stages can be found in Table 4.4. Based on the transfer function from force to position of the TST (see Section 5.8 Figure 5.28), the end test mass electrostatic actuator is optimal for high frequency control of the differential mode. Meanwhile, the penultimate mass has the same small longitudinal range as the test mass with an additional factor of $1/f^2$ actuation above resonance, making it useless to control the differential mode signal. As will be seen in Chapter 6, the arm length stabilization differential mode noise below 1 Hz has a $\sim$10 μm rms; this implies that the upper intermediate mass provides sufficient longitudinal range to control the differential signal. The top stage, although it has maximum actuation range, has an additional factor of $1/f^2$ actuation above resonance relative to the upper intermediate mass. As result, only the test mass and the upper intermediate mass are used and needed for actuation to control the differential mode. Figure 4.7 shows the actuation range used for the UIM and TST stages. The crossover between these two stages is limited by the saturation of the UIM.

Suspension Stage	**Longitudinal Range**
Top mass	$300\,\mu$m
Upper intermediate mass	$25\,\mu$m
Penultimate mass	$0.5\,\mu$m
Test mass	$0.5\,\mu$m

Table 4.4: Longitudinal range of each actuator stage of a quadruple suspension. As mentioned, the bottom stage uses electrostatic drivers; the listed longitudinal range corresponds to when the maximum bias of 400 V is engaged.

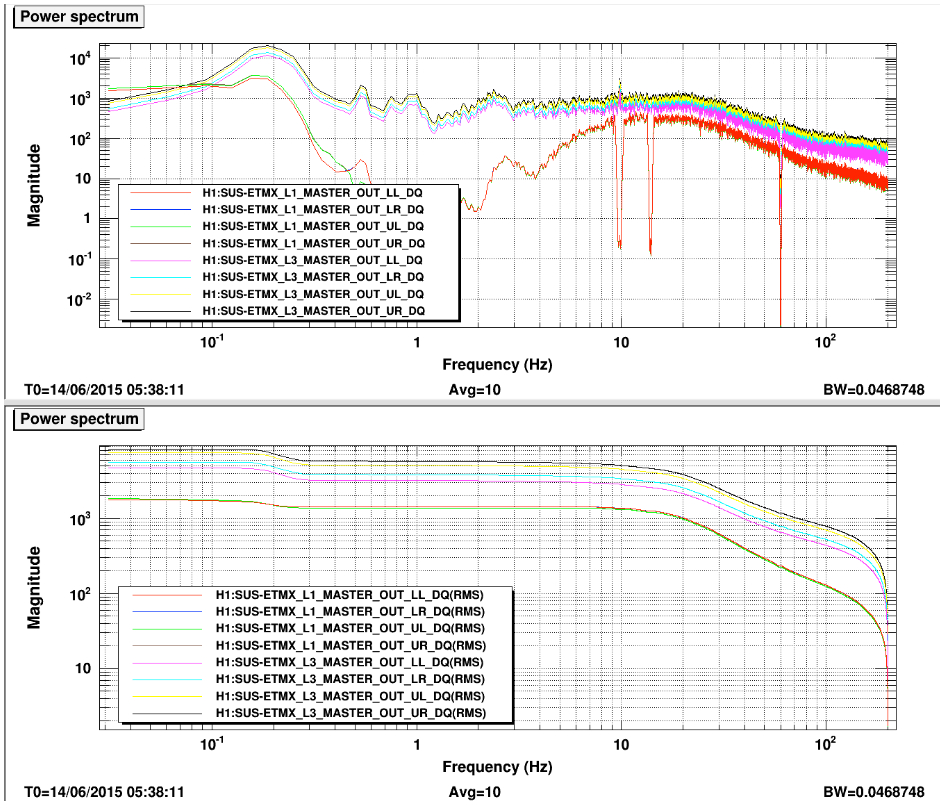

Figure 4.7: This plot shows the actuation range used for the arm length stabilization differential mode control for the X-arm end test mass upper intermediate and test mass stages. The top plot is of the power spectrum and the bottom plot is the rms. Here L1 represents the upper intermediate stage and L3 is the test mass stage. The are four channels for each stage, upper right (UR), upper left (UL), lower right (LR), and lower left (LL), corresponding to the location on the optic. These two stages will saturate at 32768 counts; the UIM stage is using more of it's range than the TST.

4.2 Chapter Summary

The arm length stabilization system was introduced to the lock acquisition process of Advanced LIGO to mitigate two challenges:

1. Narrow arm cavity locking range for infrared + weak actuators
2. Highly coupled length degrees of freedom

As the arm cavity mirrors swing freely, the main infrared beam will occasionally pass through resonance in the arms. However, they do not resonate for very long, making it difficult to apply feedback control and maintain resonance. The linear regime of the standard Pound-Drever-Hall locking signal is too small. This is compounded by the fact that Advanced LIGO has intentionally weak actuators on the end test masses, for noise reduction purposes. However, this is resolved with the arm length stabilization technique since the green light has a much larger linewidth than the infrared beam and is easier to lock.

In addition, the arm length stabilization technique decouples the two arm length degrees of freedom from the rest of the interferometer. This scheme introduces two lasers of green light at each end station that are used to independently lock the arm cavities. The beat note of the X-arm green transmitted light with a sample of the main infrared beam controls the common mode arm, while the beat note between the X- and Y-arm green transmitted light control the differential mode arm. These two beat notes compare the arm cavity resonance to the main infrared frequency. In the final step of the scheme, the differential mode offset is set to 0 Hz, while the common mode offset is set to 500 Hz. The main infrared beam is brought off resonance in the arm cavities, but the arm length degrees of freedom still remain controlled in preparation for the next locking steps. The arm length stabilization technique makes the overall lock acquisition faster and more deterministic than previous generation interferometers—this process takes about 3 minutes. This improvement is extremely important for the duty cycle of the interferometers and, therefore, inherently plays a crucial role for the study of gravitational waves. In the following chapters, it will be shown that this technique is well characterized, viable for locking, and proven successful at both detectors.

Chapter 5

Arm Length Stabilization Model

Since the arm length stabilization plays such a vital role in the full interferometer locking sequence, the technique had to be well understood. In addition, to ensure reliability, optimal performance, and robustness, a detailed study of the noise introduced by the arm length stabilization system was conducted. All of this was achieved by developing and utilizing a model of the scheme. The model contains the various loops described in the previous chapter, and emulates the controlled state of the arm cavities. This allows for commissioners to study and optimize each loop individually and the scheme as a whole. The model is also used to create a noise budget, which will be discussed in the following chapter. In order to use the model for such purposes, the model had to be validated. This was done by verifying the individual components of the model that constitute the arm length stabilization scheme. In this chapter, I discuss and validate the components of the model, as well as, briefly explain how the model functions.

5.1 The Code

A Matlab™ Simulink™ [160, 161] model was created in order to mimic all the servo loops used in the arm length stabilization scheme. The model is a state-space [79] representation of the scheme. In other words, the model represents a physical system with inputs and outputs related by linear differential equations. Using Laplace Transforms [167], these differential equations can be expressed in the frequency domain as polynomials. For example, if we consider an output $y(t)$ and an input $x(t)$, related linearly by:

$$a_n \frac{d^n y}{dt} + a_{n-1} \frac{d^{n-1} y}{dt} + \cdots + a_0 y = b_m \frac{d^n x}{dt} + b_{m-1} \frac{d^{n-1} x}{dt} + \cdots + b_0 x \tag{5.1}$$

where $a_1, \cdots, a_n$ and $b_1, \cdots, b_m$ are coefficients, taking the Laplace transform $\mathcal{L}$ of the output signal $Y(s) = \mathcal{L}[y(t)]$ and the input signal $X(s) = \mathcal{L}[x(t)]$, where $s = i2\pi f$ and f is the frequency gives,

$$(a_n s^n + a_{n-1} s^{n-1} + \cdots + a_0 s) Y(s) = (b_m s^m + b_{m-1} s^{m-1} + \cdots + b_0 s) X(s) \tag{5.2}$$

$$a(s) Y(s) = b(s) X(s) \tag{5.3}$$

The transfer function (TF) is the ratio $b(s)/a(s) = Y(s)/X(s)$. Factoring the polynomial in the numerator and denominator, allows one to express the transfer function by,

$$\mathrm{TF}(f) = k \frac{\Pi_n (1 + if/z_n)}{\Pi_m (1 + if/p_m)} \tag{5.4}$$

where p_m are the poles, z_n are the zeroes, and k is the gain [93]. The poles are the roots of the of $a(s)$ and the zeroes are the roots of $b(s)$. In a bode plot [4], which plots the magnitude and phase of the transfer function vs. logarithmic frequency, the poles have a negative slope and the zeroes have a positive slope with a ramp function of 20 dB per decade. At the pole/zero frequency the phase changes by -/+ 90 degrees respectively.

The arm length stabilization is sufficiently modeled by a linear time-invariant (LTI) system [129]. So, there is a linear map between the input $X(s)$ and the output $Y(s)$, and the relation between the input and output is identical regardless of the time. In such a case, the transfer functions provide a complete description of the systems dynamics. In cases where the system is non-linear, for example, with hysteresis, this is no longer true.

In the Matlab™ model, the transfer functions are prescribed in the form of functions blocks. These function blocks are assigned poles, zeroes (both in Hz), and a gain (specified in dB or magnitude) for each element in the control loop. Figure 5.3 shows all the function blocks describing the X-arm arm length stabilization scheme. The function blocks are then linked to mimic the feedback loops used in the arm length stabilization. For explanation on how to run the code see Appendix A. The code itself can be found in Appendix B.

5.2 Feedback Loops

An extensive overview of feedback loops can be found in Ref. [44]. The overall idea will be outlined here. In general, a feedback servo looks as follows:

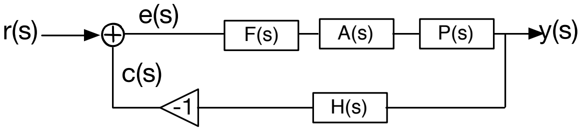

Figure 5.1: Generic feedback loop. The desired signal is $r(s)$, the output signal is $y(s)$, and the control signal is denoted as $c(s) = H(s)y(s)$. The error signal compares the desired signal and the output signal; it is given by $e(s) = r(s) - c(s)$. The loop is designed to minimize the error signal. Again, $s = i2\pi f$. Here, $H(s)$ is the loop sensor, $P(s)$ is the plant, $A(s)$ is the actuator, and $F(s)$ is the filter – for details see text.

The goal of the feedback system is to have the output $y(s)$ follow the desired signal $r(s)$ as close as possible. To do so, we measure the output and compare it with the desired signal. This difference is our error signal. A sensor, described by $H(s)$, is commonly used to measure the output. In such a case, the error signal is then defined by $e(s) = r(s) - c(s)$ where $c(s) = H(s)y(s)$. We adjust this error signal with the filter $F(s)$. This filter $F(s)$ is either a digital or analog servo designed to minimize the error signal. The filtered signal is then sent to the actuator $A(s)$, which operates on the plant $P(s)$ that is to be controlled. Under such a configuration, one can define the following transfer functions:

$$\text{Open Loop Gain } G(s) = F(s)A(s)P(s)H(s) \tag{5.5}$$

$$\text{System Sensitivity Function} = \frac{e}{r} = \frac{1}{1+G(s)} \tag{5.6}$$

$$\text{Closed Loop Transfer Function} = \frac{c}{r} = \frac{G(s)}{1+G(s)} \tag{5.7}$$

$$\text{Input Output Gain (IO)} = \frac{y}{r} = \frac{F(s)A(s)P(s)}{1+G(s)} \tag{5.8}$$

Studying these functions provides valuable information about the feedback system and how it handles noise introduced to the system. Typically noise, or a disturbance, causes the output signal $y(s)$ to differ from the reference signal $r(s)$. The feedback loop is required to correct for deviations of the output signal. There are many possible disturbances to the system; a common example is laser frequency noise in the Pound-Drever-Hall locking technique. In a closed feedback loop, the sensor used to measure the error signal will also add noise to the system. Figure 5.2 shows the previous feedback loop in the presence of noise.

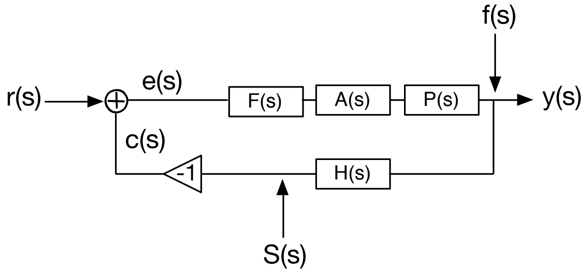

Figure 5.2: Diagram of a standard feedback loop identical to the one in Figure 5.1 with the presence of two noise sources. The sensor introduces sensor noise denoted by $S(s)$. All other non-sensor noise is considered as a disturbance to the system. Here, this disturbance is label as $f(s)$. In some loops this disturbance can be actuator noise, environmental noise, and/or laser frequency noise. Herein, I will refer to $f(s)$ as frequency noise.

We ultimately care about the noise at the output of the loop $y(s)$, this is commonly known as the out-of-loop noise. Contributions to the out-of-loop noise due to frequency noise and sensor noise are given by:

$$\text{Frequency noise:} \rightarrow \frac{f(s)}{1+G(s)} \tag{5.9}$$

$$\text{Sensor noise:} \rightarrow \frac{S(s)F(s)A(s)P(s)}{1+G(s)} \tag{5.10}$$

The purpose of the feedback loop is to suppress the noise of the loop. Not surprisingly then, the so called frequency noise at the output of the loop is suppressed by the loop gain as seen in Equation 5.9. However, there is a slight cost to the feedback. The sensor noise is imposed on the output at low frequency where $G(s) \gg 1$. The noise is also commonly examined at the error point $e(s)$; this is also known as the in-loop noise. The noise propagation at this point is given by:

$$\text{Frequency noise:} \rightarrow \frac{f(s)H(s)}{1+G(s)} \tag{5.11}$$

$$\text{Sensor noise:} \rightarrow \frac{S(s)}{1+G(s)} \tag{5.12}$$

At the error point, the sensor noise is now suppressed by the loop gain. Specific details on noise suppression and propagation for the arm length stabilization technique can be found in Chapter 6. In this chapter we study the transfer functions and loop design that ultimately dictate the noise suppression.

A common characteristic of a transfer function is known as the unity gain frequency (UGF). The UGF is the frequency at which the magnitude of the open loop transfer function is one, $||G||= 1$. This is also commonly known as the loop bandwidth. Due to the realities of the feedback loop, the servo used to correct for the deviations in the output will not have an infinitely fast response time. The response time of the servo is described by the detector bandwidth. Above this frequency, the servo is generally no longer doing useful work to mitigate any disturbance in the system. One can also define the phase margin of the open loop transfer function. The phase margin (in degrees) is the difference between the phase of the open loop transfer function to -180° at the UGF. In some conventions, the open loop absorbs the negative sign, and the phase margin is then the measured phase of the loop gain relative to 0°, as will be done herein. The phase of the open loop transfer function indicates the time delay of the system.[1] Meanwhile, the gain margin is the difference in gain from 0 dB at the frequency where the phase is -180 degrees. It is formally defined as $G_m = 1/|G(\omega_\pi)|$.

A feedback loop is viable only if it is stable. Consider injecting a signal into the junction point of Figure 5.1; this is an example of a disturbance to the system. A feedback loop is stable if a disturbance to the system does not grow with time as a result of the feedback mechanism. In fact, this disturbance will be suppressed by Equations 5.6-5.8. Therefore, the stability criteria implies that these equations must be finite, or equivalently, the loop is unstable when $G = -1$. A disturbance will also grow in time if the time delay in the system is in phase with the disturbance. As a result, the phase margin must be positive (typically above 20°) in order for the loop to be stable. The gain margin indicates how much one can increase the gain of the loop until the loop is unstable. For a stable a loop the amplitude of the transfer function falls off as f^{-1} at the UGF. It can also be shown that the feedback loop is stable if and only if the real part of the poles of the closed loop transfer function are negative [106].

Extensive work was required to verify the model before using it to produce a noise budget. The model is affirmed by comparing the transfer functions of the model to measurements. In the next sections, I examine the loops mentioned in Chapter 4 with context to the model and show each of their validations. Besides producing the noise budget, the model was useful to determine the optimal configuration of several of the loops.

5.3 End Station Phase-Locked Loop

The model contains two phase-locked loops which lock the end station lasers to the main infrared laser frequency as described in Section 4.1.1. As previously mentioned, this loop uses a phase-frequency discriminator (PFD) as a mixer. The PFD compares the phase of two input signals (in

---

[1] Time delays arise in both the analog and digital paths. Computational and signal processing can cause a delay. Meanwhile, analog boards the perform anti-aliasing and anti-imaging can introduce delays to the system. Albeit small, cable lengths must also be taken into account. A well designed loop has minimal delay.

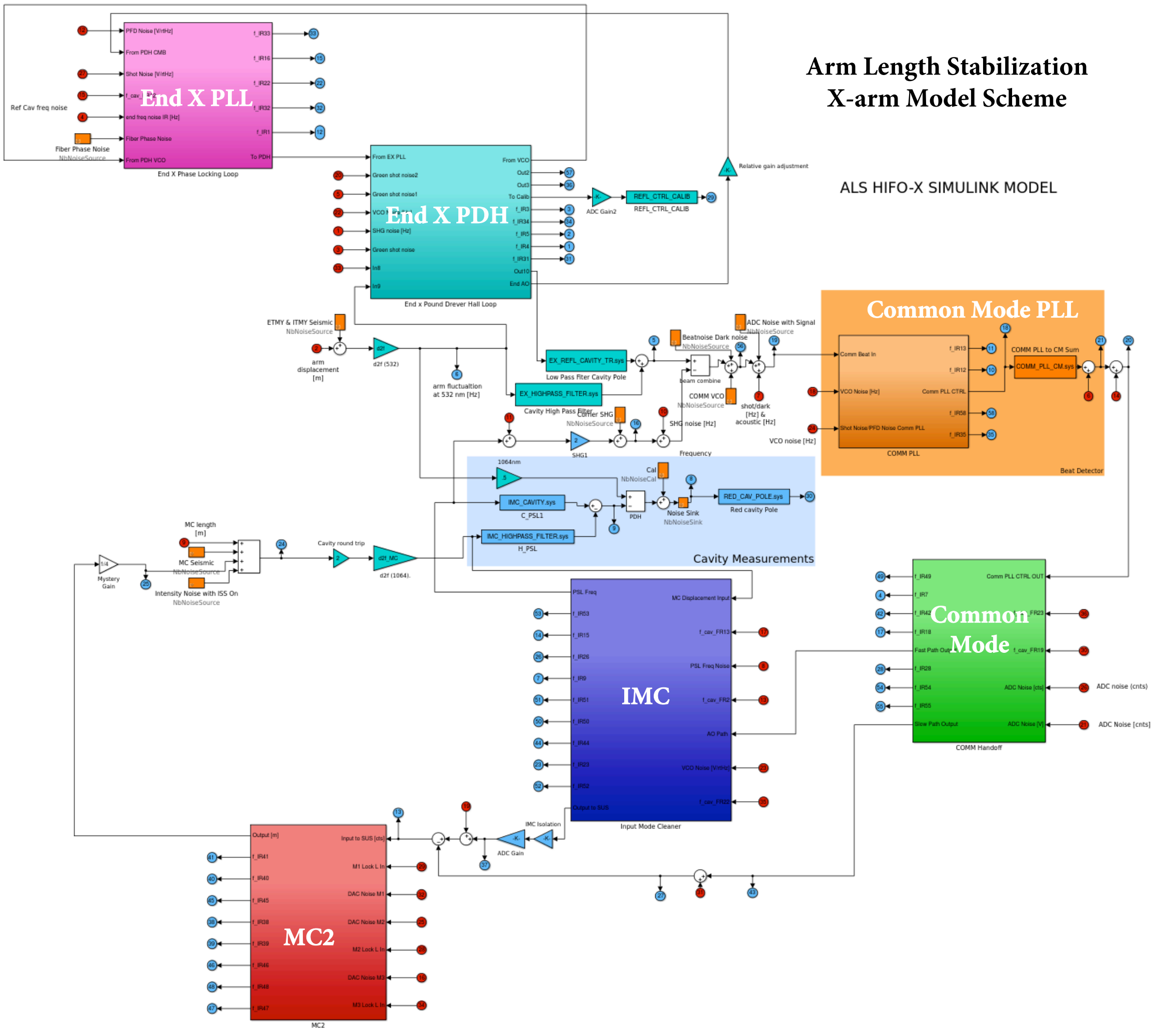

Figure 5.3: Image of the X-arm arm length stabilization simulink model. Each block is known as a function block and encapsulates the transfer functions of the scheme's components. The colored scheme goes as follows: magenta shows the end station phase-locked loop, turquoise shows the end station pound-drever-hall locking loop, orange shows the common mode beat note, green shows the beat note signal fed back to the MC2 suspension and the input mode cleaner locking point, dark blue shows the input mode cleaner locking loop, and red shows the MC2 offloaded suspension. The full Simulink model is similar, including identical end station loops for the Y-arm and the differential beat note control. For size and clarity, I have restricted this image to just the single arm. The light blue and red circles are input and output points respectively, used to measure transfer functions and inject noise.

this case the VCO frequency and beat note frequency) to produce an error voltage signal for the feedback loop to process [80]. Typically a PFD is linear in phase, so the PFD response in frequency is modeled as f^{-1} with a pole at 1 mHz. In reality, this pole is at 0 Hz, but was set to a small nonzero value for modeling. The phase detector gain for this PFD is 36 deg/volt. The reference oscillator is the voltage controlled oscillator (VCO), and is simulated with a 1.6 Hz/40 Hz pole/zero pair and a response of approximately 200 kHz/V. The designed response of the VCO is shaped like a low pass filter in order to reduce high frequency voltage noise, while preserving the DC gain [31]. In the control loop, the error signal from the PFD feeds back to the thermal controls of the end station lasers and to the piezoelectric transducer (PZT). The PZT response is flat with a resonance at 280 kHz. In the loop, there is a notch filter[2] to cancel this resonance, which is included in the model as well. The servo amplifier is an analog board, known as the PLL common mode board, that has several boost and input settings [139]. The configuration of this analog board can be found in the parameter and controls file of the code as highlighted in Appendix A and shown in Appendix B.

During the commissioning of these phase-locked loops, we examined whether the loop would be optimal with a boost (zero at 20 kHz, pole at 1 kHz) stage engaged in the PLL common mode board. Typically a boost is designed to increase the gain (or magnitude) of the open loop transfer function, with the cost of reducing the phase margin. A boost can be used to increase the unity gain frequency, which is sometimes desirable. However, one must ensure that the boost does not add a significant phase delay causing the loop to go unstable. Figure 5.4 is a graph of the measured transfer function of the PLL servo board with the boost stage on and off. Here the boost provided minimal gain, but caused a significant phase delay. This plot also compares the model and data in the case with the boost stage off. This plot is an affirmation that the PLL servo amplifier is modeled sufficiently accurate until high frequency.

The overall open and closed loop transfer functions for the phase-locked loop produced by the model are depicted in Figure 5.5. The PZT notch is clearly seen in the open loop transfer function.

---

[2] A notch filter is a band stop filter with a narrow stop band. The filter attenuates the signal in this narrow frequency region, while allowing the rest of the signal to pass unaltered [162].

The open loop transfer function is steep with a negative slope above the UGF due to the many poles in the analog servo filter and in the loop. As a result, the closed loop transfer function suppresses noise below the unity gain frequency (UGF), showing the design intent of the phase-locked loop.

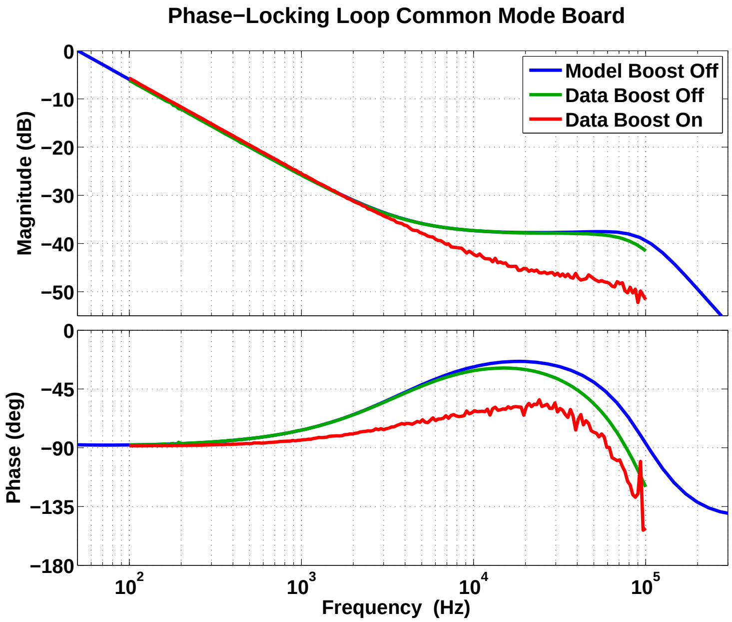

Figure 5.4: Open loop transfer function of X-arm phase-locked loop servo amplifier, known as the PLL common mode board. The blue line is the transfer function produced by the model, while the green line represents the data with the boost stage off. At high frequency, there is a slight roll off in the frequency, but the two transfer functions agree sufficiently. During the commissioning of the phase locking loops, a boost stage in the servo amplifier was considered. The measured open loop transfer function with the boost engaged is depicted in red.

It was determined that the phase-locked loop has a UGF of 26 kHz and a phase margin of 20 degrees with the boost on. Meanwhile, the loop has a UGF of 22 kHz and a phase margin of 50 degrees with the boost off. Due to the additional stability of the loop with the boost off, it was deemed more optimal. Figures 5.6, 5.7 are graphs of the open loop transfer function of the phase-locked loop from the model and the data for both end stations under the nominal configuration.

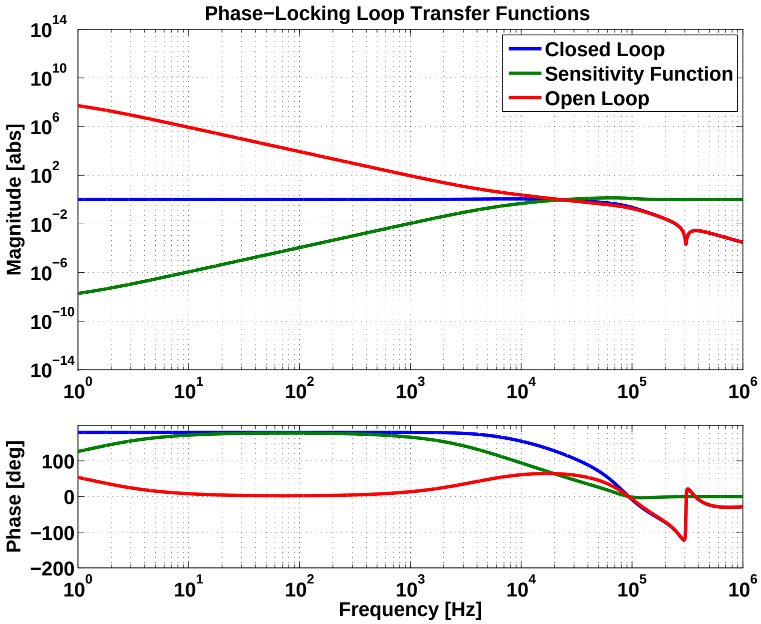

Figure 5.5: Phase-locked loop transfer functions produced by the model.

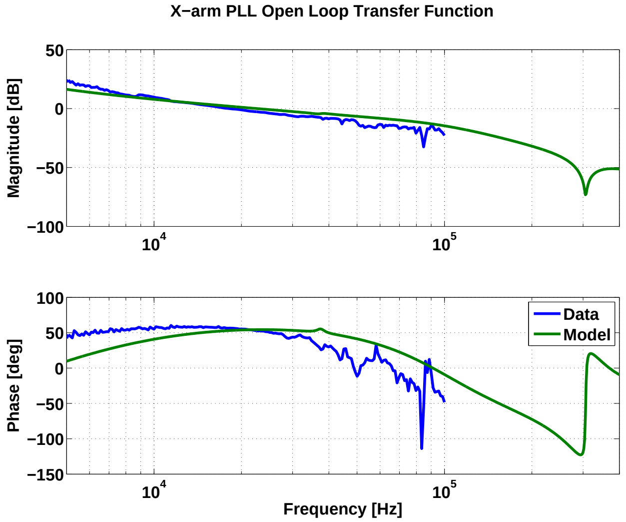

Figure 5.6: Open loop transfer function of X-arm phase-locked loop.

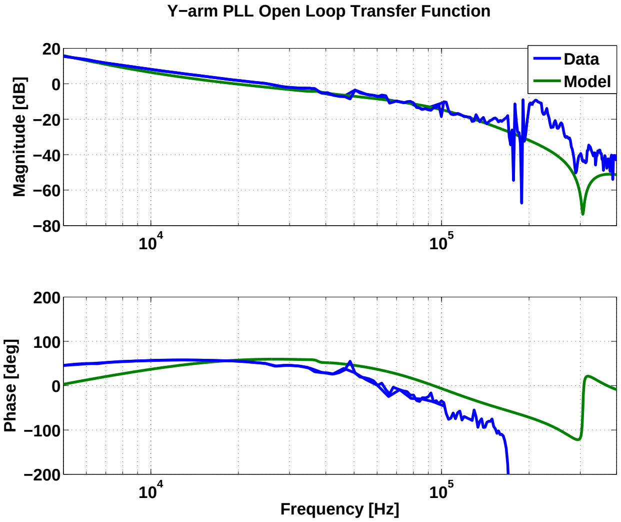

Figure 5.7: Open loop transfer function of Y-arm phase-locked loop.

5.4 End Station Pound-Drever-Hall Locking Loop

The green end station lasers are each locked to the arm cavities using a Pound-Drever-Hall reflection locking technique as described in Section 4.1.2. The model also accurately reproduces these two loops. The reflection error signal is fed back to the voltage controlled oscillator (VCO), which as before, is simulated with a 1.6 Hz/40 Hz pole/zero pair and a response of approximately 200 kHz/V. The model also replicates the servo amplifier, which is another common mode board with slightly different settings than the phase-locked loop. The dynamic response of the cavity is also reproduced in the model, and is described herein. In particular, the arm cavity light storage time is reproduced with a cavity pole in the model.

5.4.1 Dynamic Response

The Pound-Drever-Hall error signal in reflection arises from arm cavity length or frequency fluctuations. These two fluctuations dictate the cavity dynamic response and can be expressed as a transfer function in the frequency domain. Rakhmanov et al. [127] derive the normalized length-to-signal transfer function $H_L(s)$ and the normalized frequency-to-signal transfer function $H_\omega(s)$. These two transfer functions are plotted in Figures 5.8, 5.9. The length fluctuation response, $H_L(s)$, contains an infinite number of poles – the first order pole and those at multiple free-spectral ranges (FSR):

$$p_n = 1/\tau + i\omega_{\mathrm{FSR}} n \tag{5.13}$$

where n is an integer and τ is the storage time of the cavity. The 4 km Fabry-Perot arms are designed to increase the storage time of the photons in the cavity, in order to increase the interaction time with gravitational waves. Recall, the storage time is given by,

$$\tau = \frac{2L}{c}\frac{1}{\ln(r_1 r_2)} \approx \frac{2L}{\pi c}\mathcal{F}. \tag{5.14}$$

However, this storage time is finite. This is reflected by a pole in the dynamic response of the cavity. The cavity pole represents the frequency above which the intra-cavity field cancels. This frequency is expressed by,

$$f_c = \frac{1}{2\pi\tau}. \tag{5.15}$$

For the 4 km arms, the green cavity pole was measured to be at 1.46 kHz, and the FSR frequency is 37.5 kHz. Meanwhile, the cavity frequency fluctuation response, $H_\omega(s)$, consists of the zero-order pole, and zero-pole pairs at integer values of the FSR frequency. As expressed in Ref. [93], in some cases, the cavity frequency response can be approximated as a single-pole low pass filter with unity gain at DC, while the cavity length response can be expressed as a high pass filter:

$$H_\omega(f) \approx \frac{1}{1+i(f/f_c)}, \qquad H_L(f) \approx -\frac{if/f_c}{1+i(f/f_c)} \tag{5.16}$$

where f is the frequency of the signal and f_c is the cavity pole frequency.

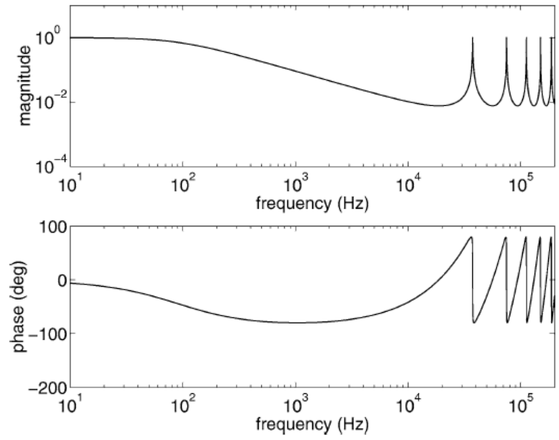

Figure 5.8: Normalized length-to-signal transfer function $H_L(s)$ for arm cavities. Image from Ref. [127].

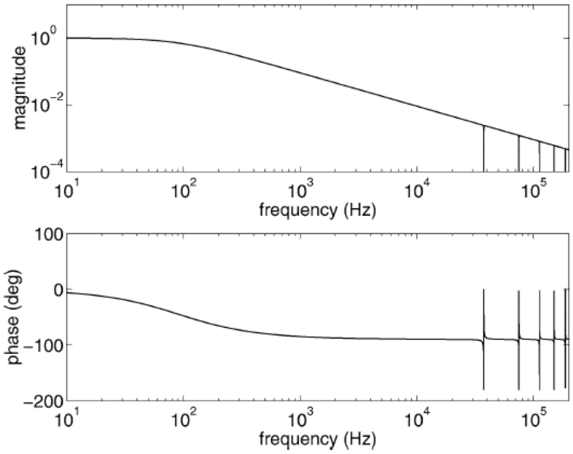

Figure 5.9: Normalized frequency-to-signal transfer function $H_\omega(s)$ for arm cavities. Image from Ref. [127].

In the arm length stabilization technique, we lock the green laser to the cavity above tidal frequency. As a result, in reflection we only model the cavity frequency fluctuation response and not the length fluctuations response. In particular, this response is approximated with the zero-order pole and the first zero-pole pair that constitutes $H_\omega(s)$. However, in transmission, we include both the length and frequency fluctuation response. In this case, the frequency response is different than in reflection and consists of only cavity poles. At integer FSRs, the light is maximally transmitted, which corresponds to poles in the transfer function. The model includes the zero-order cavity pole, and the pole at the first FSR. Since arm displacement also affects the frequency of the intra-cavity field, we introduce a cavity high pass filter to approximate the length fluctuations. Combining the effects of the frequency fluctuations and arm displacement return a linear model in the frequency of the intra-cavity field, as shown in Figure 5.10.

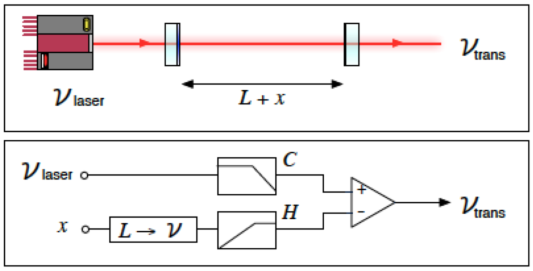

Figure 5.10: Schematic showing the effect of the frequency phase modulation and the arm displacement to the frequency of the intra-cavity field. Courtesy of [93].

Another important feature of the cavity dynamics to model is the optical gain. This gain describes the light amplification on resonance. The optical gain is deduced by measuring the error signal peak-to-peak as the cavity is freely swinging and scaling with the slope of the PDH error signal at the zero crossing. For the X-arm, the error signal peak-to-peak was measured to be 370mV, giving an optical gain[3] of 7.8972 kHz/V. Meanwhile, for the Y-arm, the error signal peak to peak was 816mV, corresponding to an optical gain of 1.43 kHz/V.

---

[3] Nominally the optical gain is measured in Hz/W; however this gain was measured at the mixer whose output signal is in volts. Since this optical gain was included following the mixer in the model the units are consistent and will be converted properly.

5.4.2 Transfer Functions

Figure 5.11 shows the various transfer functions produced by the model for the Pound-Drever-Hall locking loop. The unity gain frequency is between 3-4 kHz with a phase margin of 80 degrees. This loop is well validated by comparing the open loop transfer function produced by the model and data. The results for the two arms are depicted in Figures 5.12, 5.13. Notice the first zero-pole pair at the free-spectral range, $f_{\mathrm{FSR}} = 37.4\,\mathrm{kHz}$, is present in the model and data. In both of these plots, the data is not very clean. Due to the low finesse cavity for green light (13 Hz) and alignment fluctuations, the loop has high gain fluctuations.

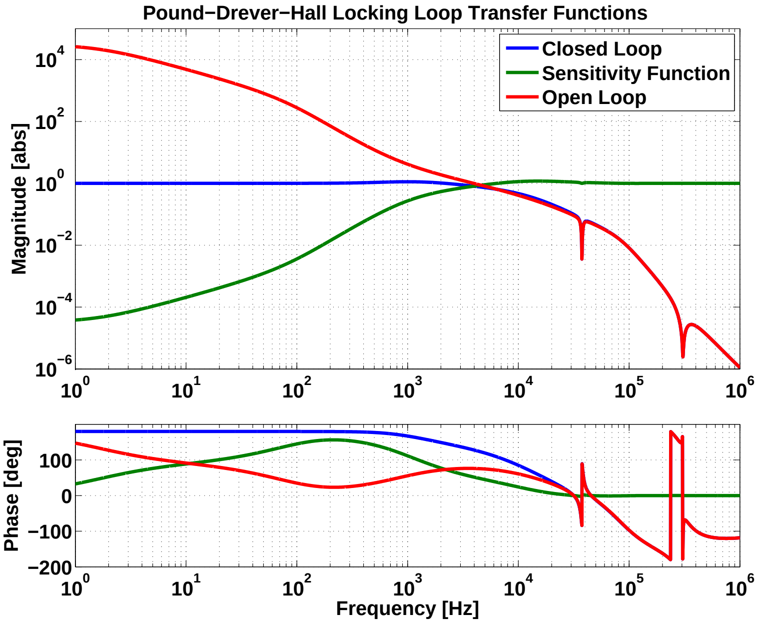

Figure 5.11: Pound-Drever-Hall locking loop transfer functions produced by the model.

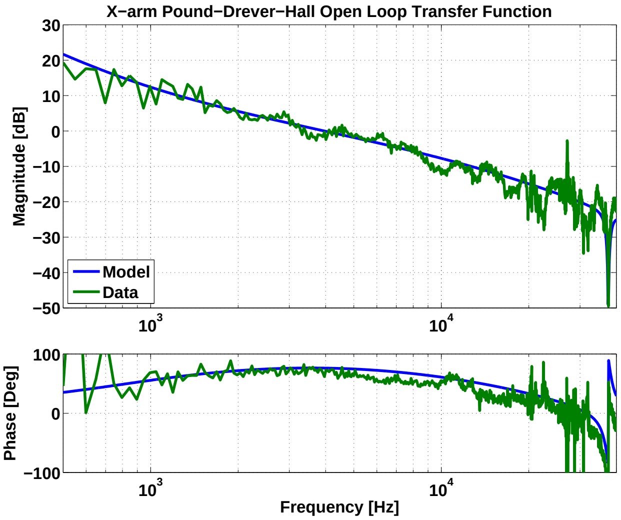

Figure 5.12: Open Loop Transfer Function of X-arm Pound-Drever-Hall locking loop.

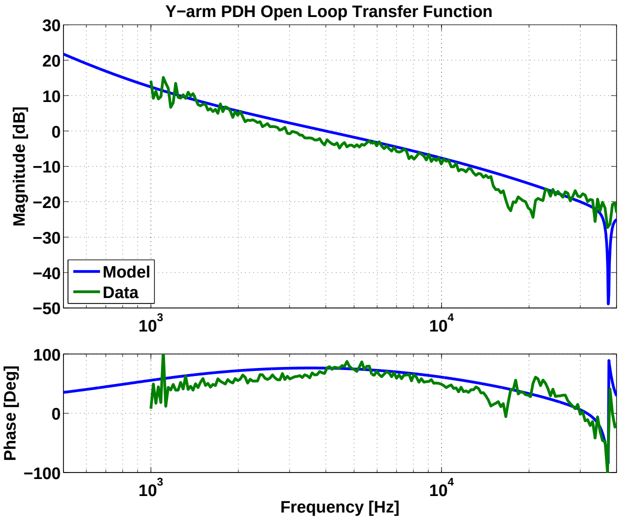

Figure 5.13: Open Loop Transfer Function of Y-arm Pound-Drever-Hall locking loop.

5.5 Common and Differential Mode Phase-Locking Loop

With each arm locked to the green end station lasers, we have two beat notes in transmission that are used to compare the arm resonance from the main infrared frequency. The beat note of the X-arm transmitted light and the frequency doubled sample of the main laser is phase-locked to a VCO; this is called the common mode phase-locked loop. Similarly, the beat note of the X- and Y-arm transmitted light is phase-locked to a second VCO; this is called the differential mode phase-locked loop. The configuration for these PLLs are identical with the exception that they each have a slightly different beat note signal to control the common and differential lengths of the arms as described in Section 4.1.4 and 4.1.5. This phase-locked loop is required to keep the beat note signals close enough in range to the VCO so that the phase-frequency discriminator stays in the phase detection mode.

The model contains both the common and differential mode phase-locked loops. These loops are characterized by a phase-frequency discriminator, a low-noise voltage controlled oscillator, and a servo amplifier. The PFD is the same as for the end station locking loops with a pole at 1 mHz and a gain coefficient of 360 deg/volt. The VCO has a 1.6 Hz/40 Hz pole/zero pair with a response of approximately 20 kHz/V. Note that this response is one tenth of that for the end station VCOs. This reduces the range of the VCO, yet simultaneously reduces the noise introduced to the system. The servo amplifier was a specially designed analog board known as the COMM and DIFF PLL boards [60]. These two boards have gains, filter, and boosts settings; for details see Appendix A.

The various transfer functions of the corner PLLs are depicted Figure 5.14. Figure 5.15 is a graph of the open loop transfer function of the common mode phase-locked loop. The magnitude of the transfer function as collected matches that of the model sufficiently. The measured phase is noisy at low frequency, but follows the shape of the model. The phase, however, deviates at higher frequency. This effect can be explained by a pole at high frequency of the VCO, which is difficult to measure directly from the VCO transfer function and not characterized in the model. A best fit pole could have been included in the model; however, this delay was deemed unnecessary to include since we are not noise dominated at these frequencies. The unity gain frequency of this loop is 30 kHz with a phase margin of 40 degrees. This is identical for the differential mode phase-locked loop.

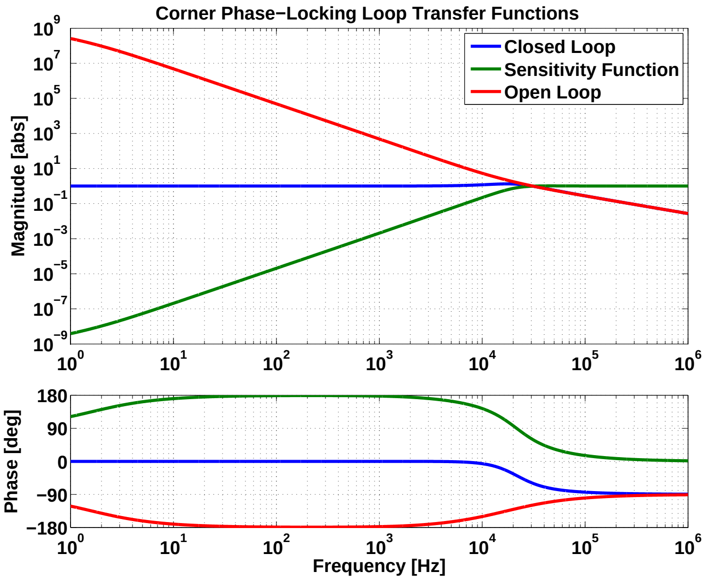

Figure 5.14: Corner phase-locked loop transfer functions produced by the model.

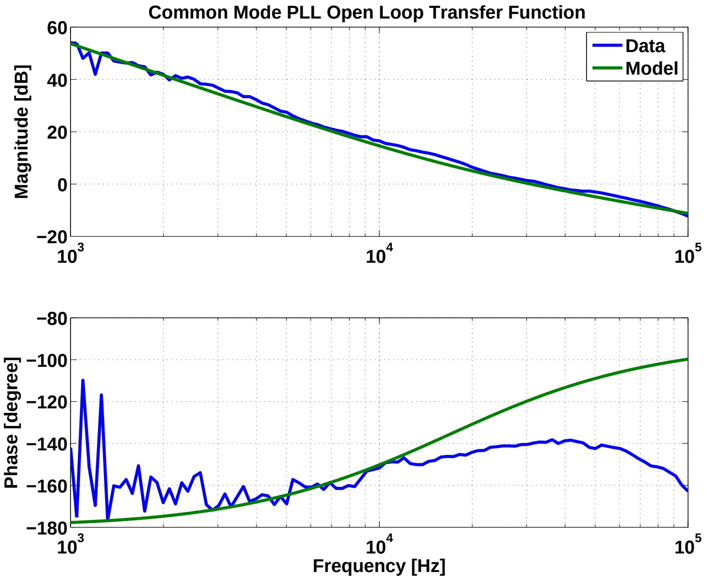

Figure 5.15: Open loop transfer function of the common mode phase-locked loop. The differential loop is identical.

5.6 Input Mode Cleaner Loop

The main laser is locked to the input mode cleaner cavity in order to filter unwanted spatial modes of the laser and to reduce laser frequency noise. This loop plays a role in the arm length stabilization, since it is used to adjust the main laser frequency as discussed in Section 4.1.3 and 4.1.4.

The model emulates the input mode cleaner loop under two configurations. The first is the input mode cleaner loop solely as described in Section 4.1.3. The second is the input mode cleaner loop with the addition of the common arm locking as described in Section 4.1.4. Here, I will validate the former version of the model.

The input mode cleaner loop is characterized by a cavity pole, a voltage controlled oscillator, and a servo amplifier. The servo amplifier is another analog common mode board, with once again, different settings from the end station PDH and PLL loops. The configuration for the input mode cleaner common mode board can be found in Appendix A. As before, the VCO is modeled with a 1.6 Hz/40 Hz pole/zero pair and a response of 200 kHz/V. The dynamic response of the cavity is modeled with the cavity pole at 8812.36 Hz. In this case, we do not model any of the higher order zero-pole pairs.

The various transfer functions of the input mode cleaner loop produced by the model are depicted in Figure 5.16. Meanwhile, Figure 5.17 is a plot of the open loop transfer function of the loop, comparing the data and the model. There is nice agreement between the two transfer functions. Again we see a roll-off in the phase at high frequency present in the data and not in the model due to the pole of the VCO not properly reflected in the model. The unity gain frequency is 53 kHz with phase margin of 45 deg.

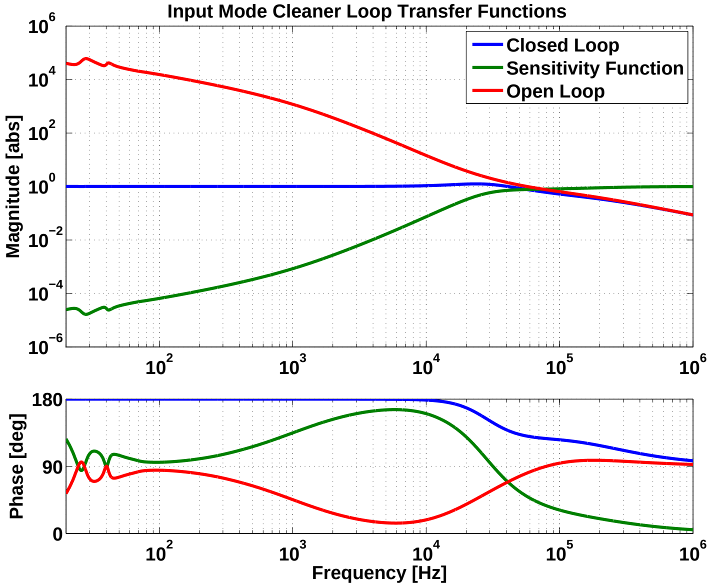

Figure 5.16: Transfer functions produced by the model for the input mode cleaner loop.

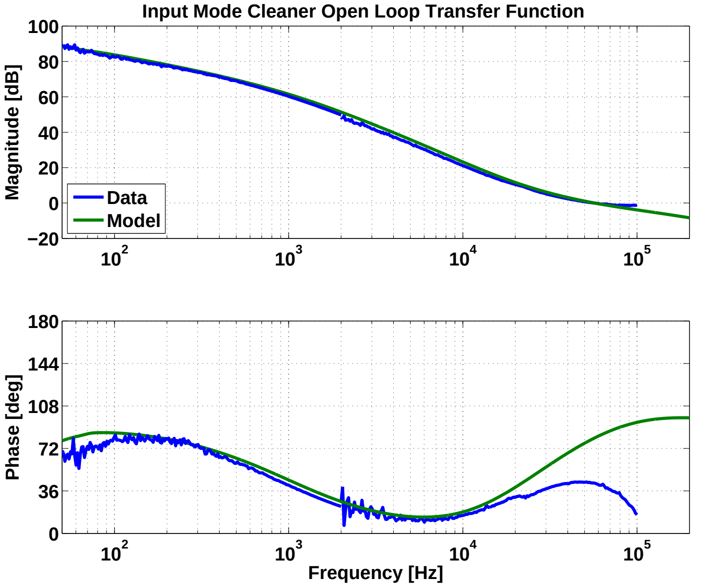

Figure 5.17: Input mode cleaner open loop transfer function.

5.6.1 MC2 Loop

For length control in the input mode clear loop, the MC2 suspension is used as an actuator. For frequencies below 70 Hz either the input mode cleaner reflection locking signal or the arm length stabilization common mode control signal is sent to this suspension. Regardless of the signal, the suspension configuration is this same. This configuration will be discussed here, and the model for this suspension will be validated.

As mentioned previously the MC2 suspension actuation follows an offloaded approach. The signal chain is depicted in Figure 5.18. In this diagram, K1, K2, K3 represent digital filters for each of the three suspension stages M1, M2, M3 respectively (recall Figure 4.4). The configuration for these filters can be found in Appendix A. These filters are designed to convert digital counts into force (N) onto the suspension. The conversion from counts to meters for each stage is listed in Table 5.1:

Table 5.1: MC2 Calibration

M1	11.9mA/V	0.963N/A	0.003405m/N
M2	2.8mA/V	0.0158N/A	0.006275m/N
M3	0.33mA/V	0.00281N/A	0.014057m/N

Additionally, there is an ADC conversion of $(2^{16}/40)$ counts/volts and a DAC conversion of $(2^{18}/20)$ counts/volts. Note: for some of the ADC conversions there is an additional factor of 2 if the output is differential. Meanwhile, P13, P23, P33 are known as the plants and characterize the mechanical response of the bottom stage in length to the motion of each of the stages. The suspensions are pendula—they each have resonance peaks around 1 Hz and the high frequency response of the bottom stage gains an additional factor of $1/f^2$ for each stage between the optic and actuator. These transfer functions were adapted from Jeffery Kissel, Mark Barton, et al [40,41,97] triple suspension model.

The crossovers between each stage can be measured. The crossover of M2/M3, for example, can be measured by exciting at the input of K2 and measuring (IN1/IN2) as shown in Figure 5.18. Figures 5.19 and 5.20, show the M1/M2 and M2/M3 crossovers of MC2 respectively. These figures show that the MC2 suspension in the model is well validated; the data and the model have consistent transfer functions. The unity gain frequencies and phase margins are as follows: M1/M2 crossover: 0.125 Hz, 36 deg and M2/M3 crossover: 7 Hz, 38 deg. Below the crossover frequency the M1 stage is the main actuator and after the crossover the M2 stage is the main actuator. Similarly, for M2/M3.

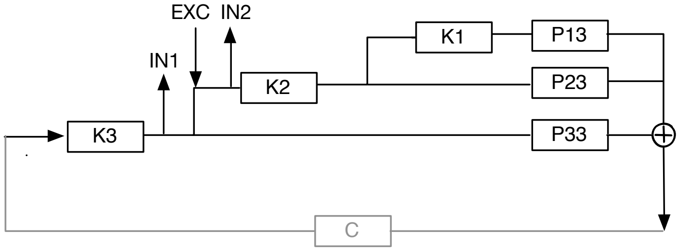

Figure 5.18: Triple Suspension Offloaded Configuration. M1, M2, M3 are the digital filters. P13, P23, P33 are the plants for the three suspension stages. C is the control loop.

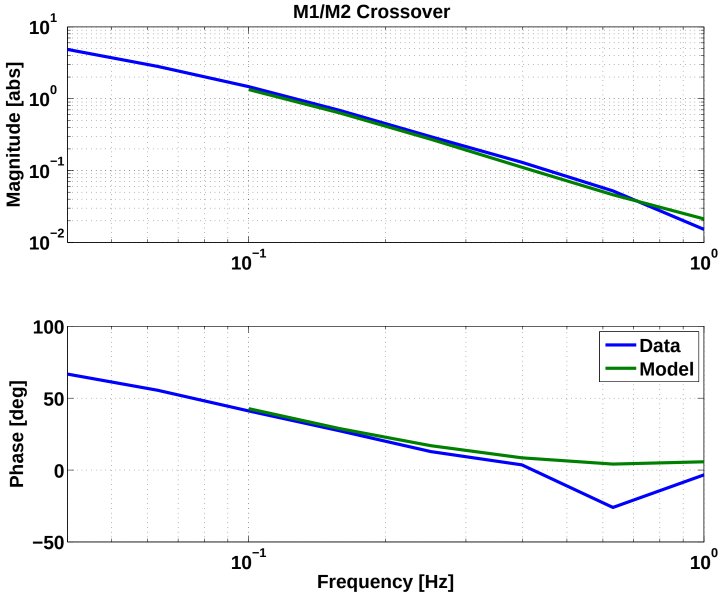

Figure 5.19: M1 M2 crossover for the MC2 suspension

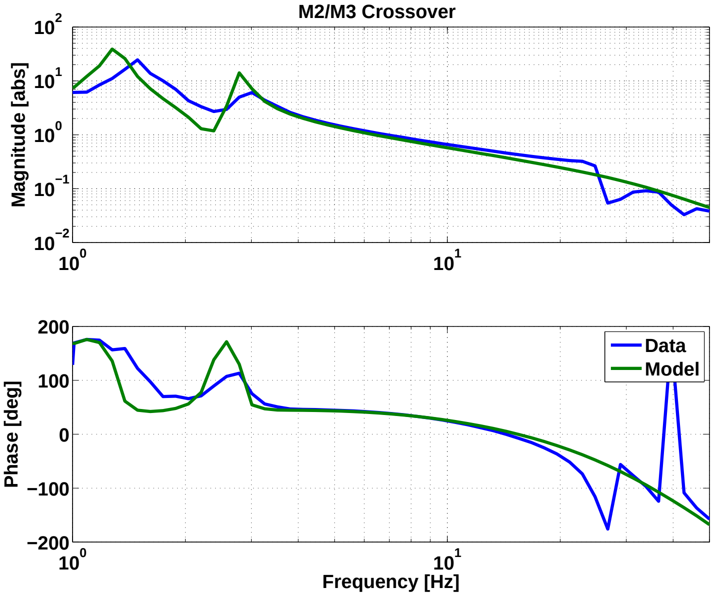

Figure 5.20: M2 M3 crossover for the MC2 suspension

In a similar manner, the crossover between the length and frequency actuation can be measured. As before, this crossover indicates the point at which we actuate on the length versus the frequency. Currently, below 70 Hz, we actuate on the MC2 suspension to respond to frequency fluctuations, whereas above 70 Hz we actuate on the VCO to change the main laser frequency in response to length fluctuations of the cavity. Figure 5.21 compares this crossover produced by the model and the data. This graph was taken when the crossover was at 14.5 Hz (39 deg phase margin) with solely the input mode cleaner locked. In addition, the data was taken with notches in the suspension that were eventually removed.

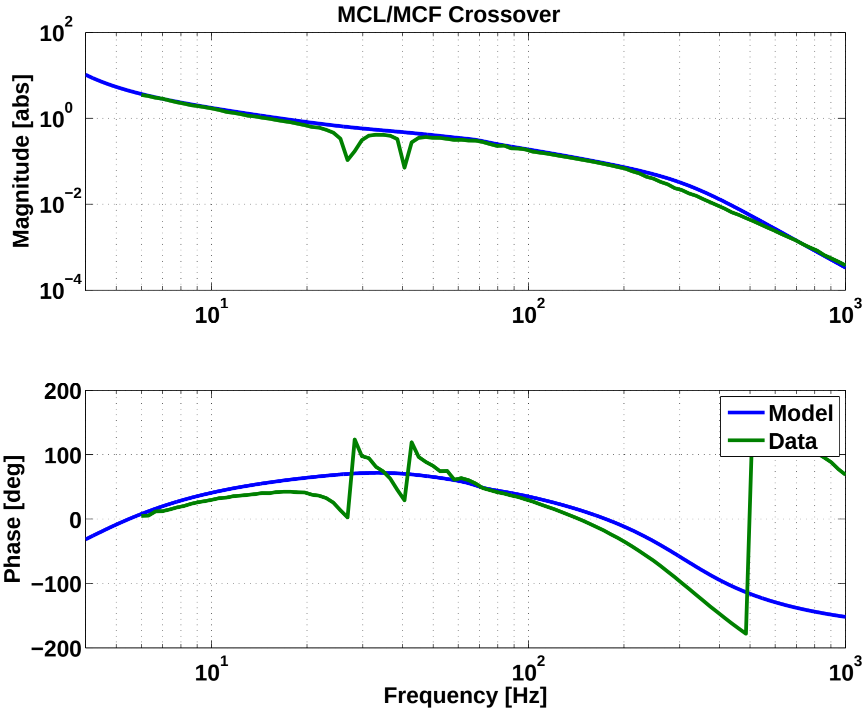

Figure 5.21: Crossover between the length and frequency feedback for the input mode cleaner.

5.7 Common Mode Loop

With the two arms locked to the green end station lasers, and the X-arm transmitted signal phase-locked to a double sample pick-off of the main laser, the control signal of this phase-locked loop indicates how far off the main laser frequency is from the arm cavity resonance and is ultimately used to control the common mode of the arm cavities as described in Section 4.1.4. As previously mentioned, this control signal passes through a servo amplifier. For high frequencies, above 70 Hz, the signal is sent to the frequency of the main laser beam via the error point of the input mode cleaner locking loop. Meanwhile, for slow frequencies, the signal is fed back to the MC2 suspension, and the length of the input mode cleaner cavity is adjusted which inherently adjusts the frequency of the main laser. The input mode cleaner loop adjusts the main laser frequency to keep the cavity locked, meaning that the input mode cleaner length can be used indirectly to actuate on the main laser frequency while preserving the lock of the cavity. Since the signal to the MC2 suspension is swapped from the input mode cleaner to the common mode control signal, the MC2 digital filters are slightly adjusted. The servo amplifier is again the analog common mode board. The settings of this board and the MC2 digital filters can be found in Appendix A. The block diagram in Figure 5.22 provides a sketch illustrating how the common mode beat note control signal is split between a fast and slow paths to the input mode cleaner loop and the MC2 suspension.

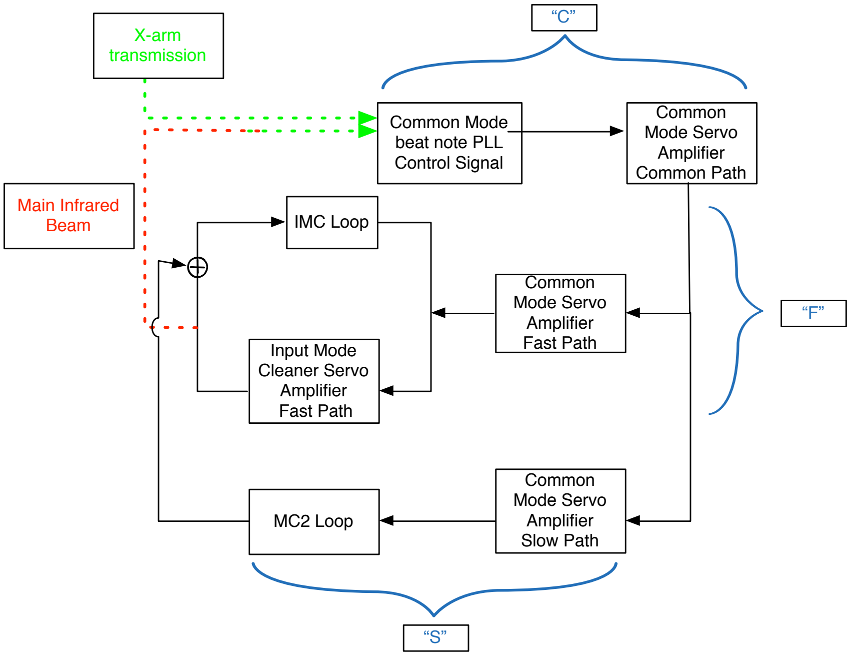

Figure 5.22: The common mode block diagram. This diagram does not picture the entire loop. In particular, the end station loops are missing. However, this diagram indicates how the control signal from the common mode phase-locked loop is split between fast and slow frequencies. The servo amplifier has a fast and a slow path. The fast path, at frequencies above 70 Hz is fed back to the error point of the input mode cleaner locking loop. At slow frequencies, the signal is fed back to the MC2 suspension. The slow path from the input mode cleaner loop has been cut and it not shown here. Here, I denote the common path as "C", the fast path as "F", and the slow path as "S."

Given the complexity of this loop, several different transfer functions were taken to validate the model. The first is the general open loop transfer function taken at the common path of the servo amplifier. In this scenario the open loop is $C(S+F)$, where S is the slow path, F is the fast path, and C is the common path including the common mode PLL loop as shown in Figure 5.22. Figure 5.23 depicts the open loop transfer function with the data and the model. At low frequency, the slow path dominates the open loop gain, until the crossover, at which point the fast path dominates. Notably in the plot, the data loses coherence at around 500 Hz because the injected noise is highly suppressed by the loop. Above 10 kHz, we again see a deviation between the model and data due to the VCO in the common mode PLL path not being modeled properly. This data was collected with a crossover at ∼14 Hz and a unity gain frequency of 27 kHz with a phase margin of 55 deg. The crossover was adjusted to 70 Hz and the UGF was changed to 400 Hz. This was done by slightly modifying the settings on the analog common mode board. The UGF was decreased in order to simplify the transition of the common mode signal in the next steps of the locking sequence; this will be clarified later.

Meanwhile, Figure 5.24 is a transfer function with the excitation point in the fast path of the servo amplifier common mode board. This transfer function is $CF/(1-CS)$. At high frequencies, $CS \ll 1$, so this transfer function approaches CF. Figure 5.25 is a transfer function with an injection in the slow path; i. e. measuring $CS/(1-CF)$. At low frequencies, $CF \gg 1$, so the transfer function becomes S/F and the unity crossing indicates the crossover between the fast and slow paths. For both of these transfer functions, the model matches the data.

We can also plot the open loop transfer function and the fast and slow paths individually as in Figure 5.26. This plot depicts the crossover between the fast and slow paths. Below the crossover, the open loop mirrors the slow path, and above the crossover, the open loop follows the fast path.

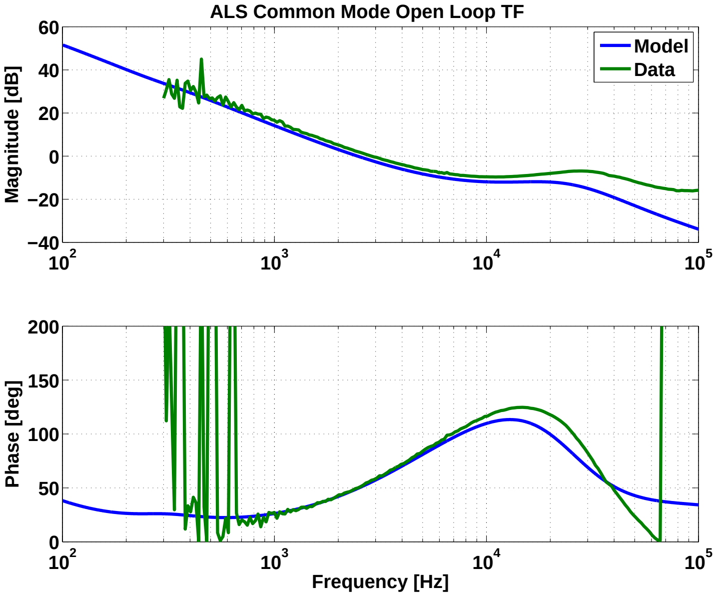

Figure 5.23: Common mode open loop transfer function

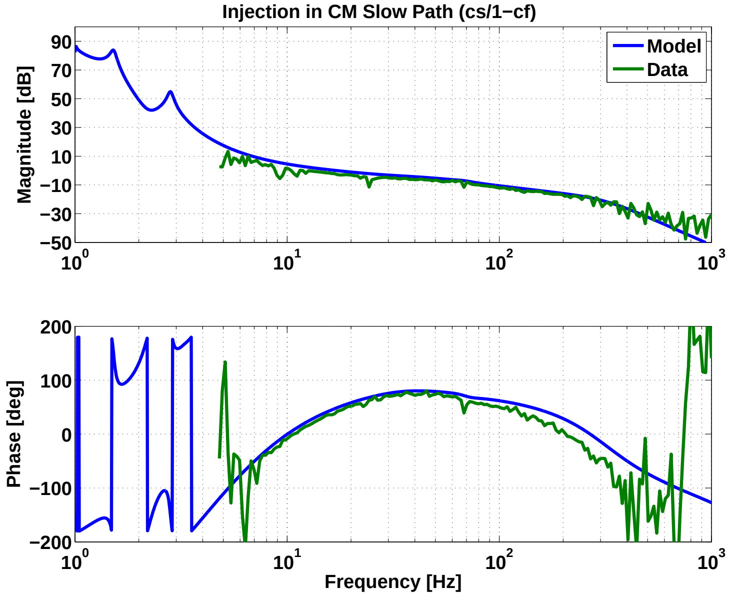

Figure 5.24: Common mode path transfer function showing CF/(1-CS)

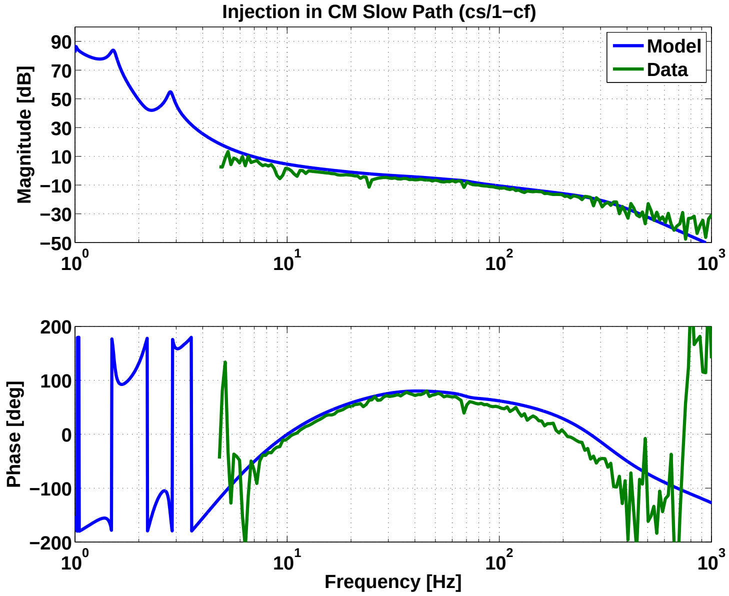

Figure 5.25: Common mode path transfer function showing CS/(1-CF)

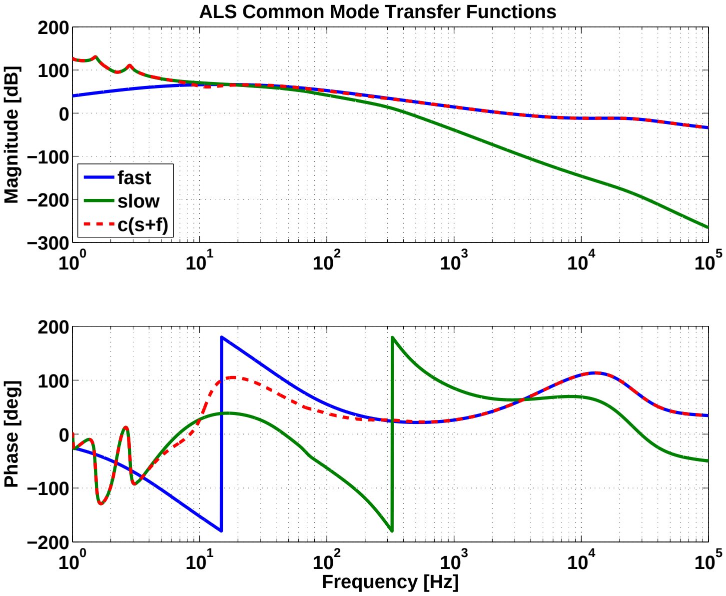

Figure 5.26: Common mode fast and slow crossover

5.8 Differential Mode Loop

The model also contains the servo loop required for locking the differential arm of the interferometer (see Section 4.1.5). Similar to the common mode control, the error signal comes from the differential mode phase-locked loop control signal. However, unlike for the common mode control, this signal is not sent to an analog servo board, but instead goes through several digital filters and ultimately to the end test masses. Therefore, an important part of modeling the differential mode control of the interferometer is properly modeling the dynamics of the end test mass suspension. The quadruple suspension used in the model was adapted from Jeffery Kissel, Mark Barton, et al model [40,41,97].

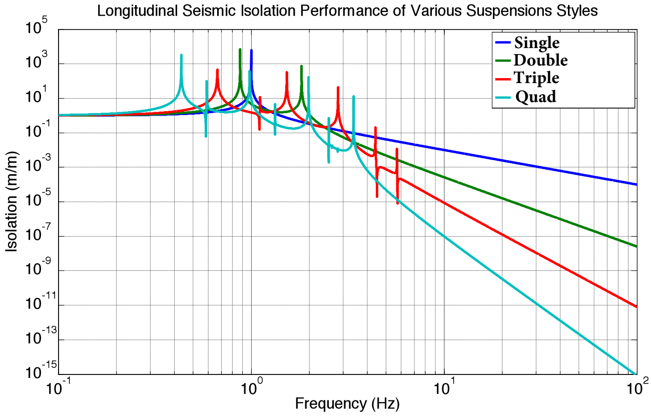

Figure 5.27: An example of longitudinal seismic isolation from various suspension types. Each isolation stages introduces a factor of $1/f^2$ in isolation above the resonances. The illustrated transfer function is from the ground motion (in meters) to the lowest stage of the pendulum (in meters) along the interferometer axis. Image adapted from Ref. [131].

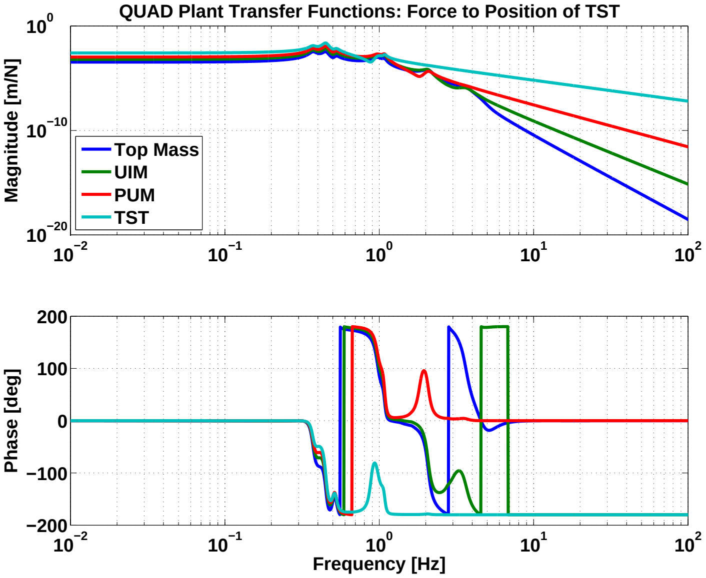

Figure 5.28: QUAD suspension transfer functions produced by the model. This plot depicts the transfer functions from each suspension stage in force (N) to displacement (m) at the end test mass. Here, the first suspension stage is the top mass, the second stage is the upper intermediate mass (UIM), the third suspension stage is the penultimate mass (PUM), and the final suspension stage is the end test mass (TST). In these transfer functions, damping of the resonances is included.

Each suspension stage will have suspension resonances around 1 Hz, and provide a factor of $1/f^2$ isolation from the ground as seen in Figure 5.27. The top mass (TOP) displacement goes as $1/f^2$, the upper intermediate mass (UIM) displacement goes as $1/f^4$, the penultimate mass (PUM) goes as $1/f^6$, and finally the test mass (TST) goes at $1/f^8$. This makes the test mass the most isolated suspension from the ground above 1 Hz, as desired. Figure 5.27 and 5.28 show only the degrees of freedom most relevant to the differential mode control, horizontal translation of each stage's center of mass along the beam direction (known as "longitudinal"). The other degrees of freedom include the other translations of each stage, "transverse" and "vertical", and the rotational degrees, "roll," "pitch," and "yaw." To verify the quad suspension model, all of these transfer functions had to be validated. Figures 5.29 and 5.30 show two of these transfer functions, as examples. The model (blue trace) matches well with the measured (green trace) transfer functions.

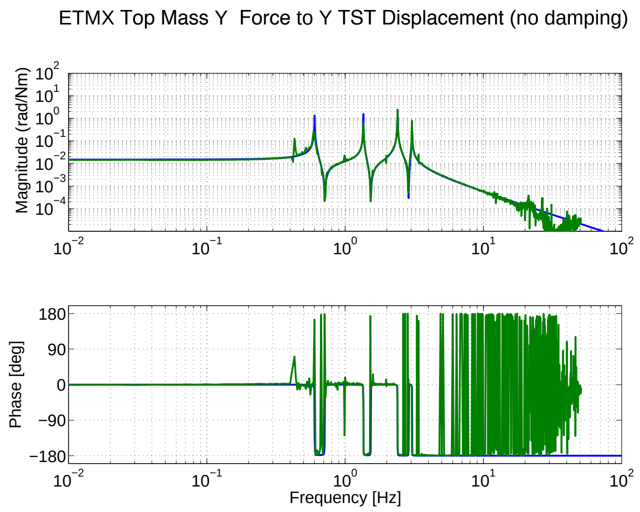

Figure 5.29: X-arm QUAD suspension transfer function from Yaw drive in Newtons from the top mass to Yaw displacement in meters at the end test mass. Here the damping of the resonance is turned off, so the resonance features are more pronounced. This measurement was taken by Arnaud Pele.

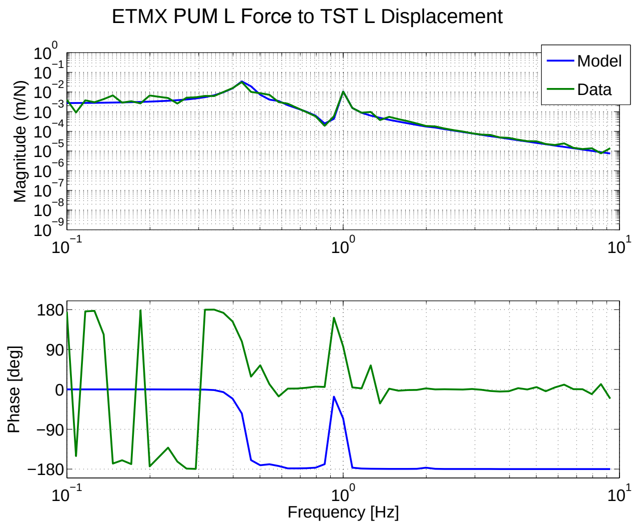

Figure 5.30: X-arm QUAD suspension transfer function from length drive in Newtons from the top mass to length displacement in meters at the end test mass. This measurement was taken by Arnaud Pele.

The remaining portion of the differential mode controls are all digital filters (see Appendix A).

The longitudinal digital filters are depicted in the diagram 5.31. The design of the filters are such that the end test mass transfer function goes as $1/f$ above the resonances, and that the upper intermediate mass goes is $1/f^2$. The frequency dependence of the digital filters is arranged such that the overall response of the sum of the suspension drive at each stage to the test mass as $1/f$ above the resonances. The top stage and penultimate mass are not used for actuation as discussed in Section 4.1.5.

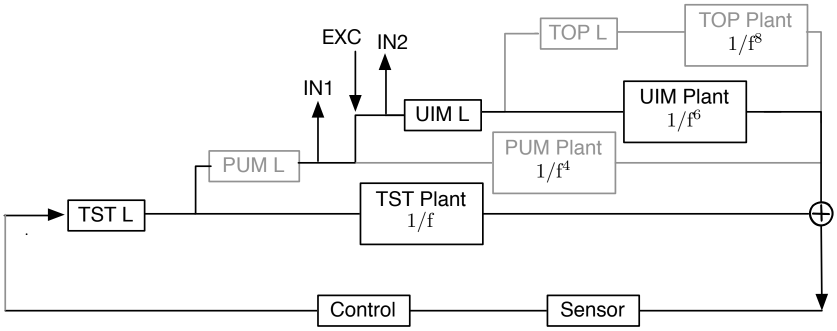

Figure 5.31: Differential mode servo loop. This diagram depicts the several length digital filters, including each suspension stage filter and the overall control filter. The sensor is the differential mode phase-locked loop control signal. Only the end test mass and UIM are used to lock the differential mode.

Figures 5.32 and 5.33 show a variety of transfer functions used to validate the model. In particular, Figure 5.32 shows the open loop of the servo, while Figure 5.33 indicates the crossovers of the suspension response. Both plots show a consistent agreement between the model and the collected data. The unity gain frequency of this loop is 8 Hz with a phase margin of 75 degrees and crossover at approximately 1 Hz.

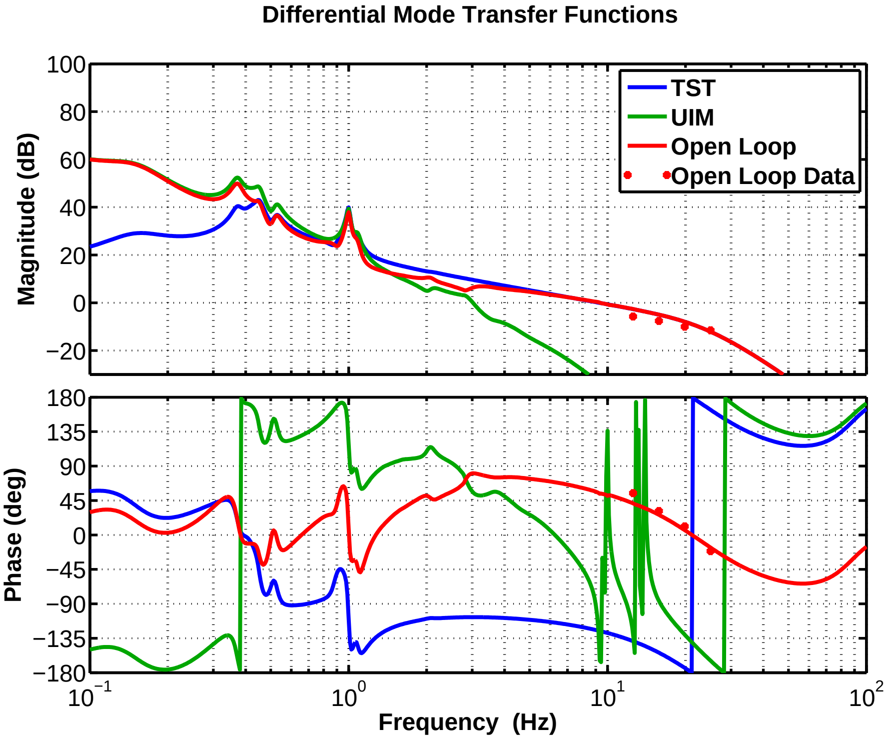

Figure 5.32: The two red traces show the arm length stabilization differential mode control open loop transfer function for the model and data. Below the suspension crossover, the open loop follows the upper intermediate open loop. While above the crossover, the open loops follows the end test mass open loop.

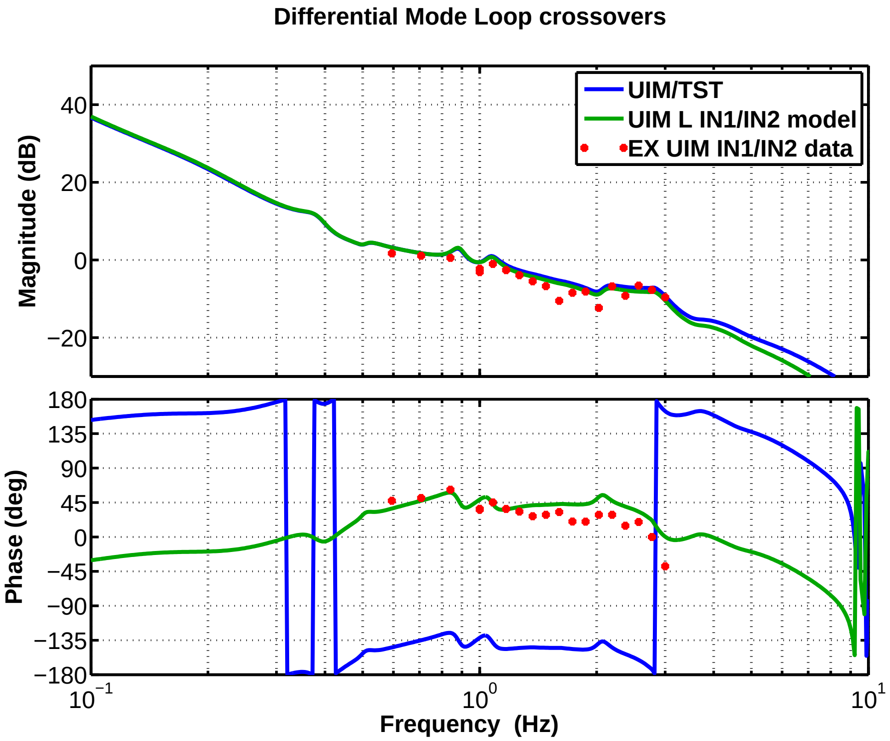

Figure 5.33: The blue trace shows the gain of the upper intermediate mass path over the gain of end test mass produced by the model. This transfer function gives the formal crossover between the two stages. Meanwhile, the green trace shows a slightly different transfer function with the injection at IN1/IN2 as depicted in Figure 5.31. Following loop algebra, this transfer function is almost UIM/TST, and is sufficient to measure the crossover frequency, but is primarily used as a metric for stability (See Appendix C). The equivalent measured transfer function is depicted in red.

5.9 Chapter Summary

In order to implement the arm length stabilization technique, stable and well-designed feedback loops were developed. This required the assistance of a validated, well-documented, and understood all encompassing model. This chapter described the composition of the model and verified its accuracy. Such a model can be used to produce a noise budget for the scheme.

Chapter 6

Arm Length Stabilization Noise Budget

The arm length stabilization technique is a critical component of the lock acquisition sequence. To ensure reliability and robustness, a detailed study of the noise introduced by the system was conducted. Using a separate stabilized laser source in the end station introduces fiber noise, laser frequency noise, and noise from the reflection locking servo onto the corner station laser. The heterodyne measurement determining the common mode degree of freedom contributes sensing noise to the overall arm length stabilization noise. Ultimately, these noise sources have no effect once the interferometer reaches its operational point and the end station lasers are turned off. However, these noise sources limit the reliability and repeatability of the lock acquisition.

To study the noise of the arm length stabilization technique, a noise budget was produced. Noise budgets explain the contributing sources to the overall noise of the system. Recall the simple feedback loop with disturbances in Figure 5.2 from Section 5. The transfer functions of Equations 5.9-5.12 indicate how the noises will propagate in the feedback loop. A noise budget is created by measuring the contributing noise sources and using a model to propagate these noises to the output and the error point. A basic model applies the aforementioned transfer functions to the noise sources. However, generally, the loop algebra is more complex. Using the model

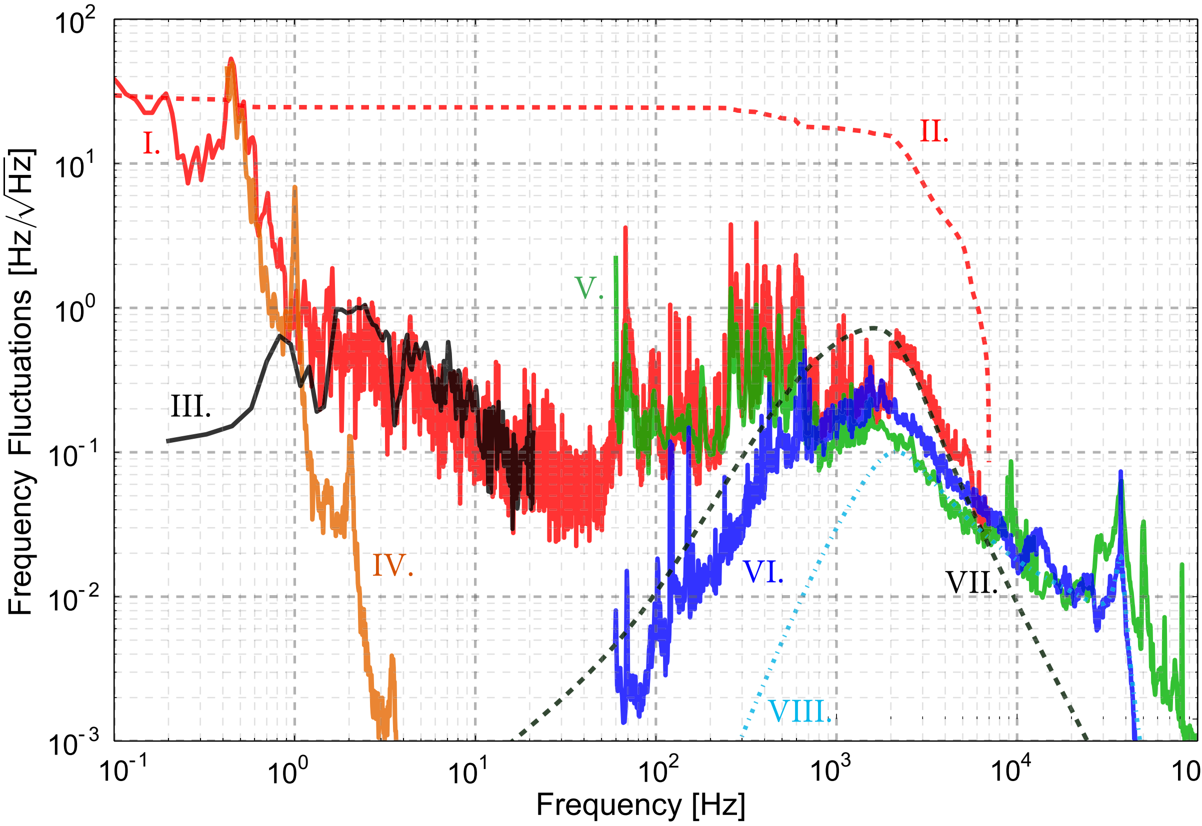

Figure 6.1: Noise budget of the arm length stabilization system with only the common mode degree-of-freedom controlled. The frequency fluctuations of the infrared light incident to the interferometer are shown. The solid red trace I is the out-of-loop noise measured with both the green and main infrared beams locked to the X-arm. The dashed red trace II is the corresponding rms in units of Hz. The remaining traces are the noise sources inherent to the arm length stabilization method imposed on the main laser beam, and used to explain the overall noise. The black trace III is phase noise produced from fringe wrapping of the common mode beat note. The dark orange trace IV comes from a measurement of the test mass longitudinal displacement noise. The green curve V and the blue curve VI are the sensing noise of the common mode and reflection servo error signal imposed on the out-of-loop measurement, respectively. Finally, the dashed black trace VII and the dashed light blue trace VIII are estimates of the fiber and laser noise, respectively.

to propagate all the noise sources to the output, one can compare this with the noise measured. Ideally, the measured noise should be well explained by the contributing noise sources, and at a tolerable level. As a result, a noise budget was crucial to establish confidence in the arm length stabilization technique.

This procedure was applied for the arm length stabilization technique. After implementing the arm length stabilization method to bring the main infrared beam on resonance in the X-arm, an out-of-loop noise measurement was taken by measuring the frequency difference between the infrared beam and the arm cavity resonance using the infrared PDH reflection signal. This measurement was taken without the dual-recycled Michelson interferometer locked. The rms frequency noise was between 10 Hz and 30 Hz for frequencies above 0.01 Hz. This is good enough to set the arm cavity off resonance and get enough build-up to switch the controls to the arm cavity infrared transmitted signals (see Chapter 7). The solid red trace in Figure 6.1 depicts the frequency noise of the infrared input light with the cavity pole at 42 Hz removed, meanwhile the dashed red trace represents its root-mean-square. This overall out-of-loop frequency noise is clearly well explained by known contributing sources inherent to the arm length stabilization method.

6.1 Contributing Noise Sources

The end station laser is a non-planar ring oscillator (NPRO) and its free-running frequency noise is approximately $1 \times 10^4\ \mathrm{Hz}/\sqrt{\mathrm{Hz}} \times \frac{1\ \mathrm{Hz}}{f}$ between 1 Hz and 10 kHz. This noise gets suppressed by locking it to the fiber-coupled sample beam from the corner up to the servo bandwidth of about 20 kHz. On the other hand, the noise introduced by the fiber gets added to the laser frequency. The fiber noise is roughly $3\ \mathrm{Hz}/\sqrt{\mathrm{Hz}}$ at 1 kHz, and then subsequently falls off as 1/f [83]. With the laser locked to the cavity the combined laser frequency noise is suppressed by the reflection locking servo up to its bandwidth of approximately 3 kHz. Finally, since we are looking at the transmitted beam in the corner station, the green cavity further suppresses this noise above the cavity pole of 1.5 kHz. This noise dominates at 500 Hz and above, as seen by the dashed black and light blue traces representing the fiber and laser frequency noise respectively. Figure 6.1 includes the sensing noise of the end station reflection servo error signal imposed in the out-of-loop measurement (blue trace).

Acoustic noise at the corner station accounts for the frequency noise from 60 Hz to about 1 kHz. Specifically, a large in-air periscope contributes to the peaks around 65 Hz – 75 Hz, and

95 Hz – 105 Hz. Similarly, an in-vacuum periscope produces the sharp peak at 68 Hz. The forest of peaks between 250 Hz and 700 Hz come from opto-mechanical structures along the beam paths. These periscopes and optics lie along the beam path of the green transmitted light and the frequency-doubled sample beam from the main laser. Since the beat note is locked with a phase locking loop, this sensing noise is imposed on the corner VCO up to the loop bandwidth at 30 kHz. Since the common mode signal is fed back to the input mode cleaner length and to the VCO of the main laser above $\sim$20 Hz (recall, this was later changed to 70 Hz), this acoustic noise is further imposed onto the laser frequency noise of the main infrared laser. The green trace in Figure 6.1 is the common mode sensing noise as measured by the control signal at the corner VCO and propagated to the main laser frequency noise, clearly demonstrating that the acoustic noise dominates this frequency region.

At frequencies well below 1 Hz the noise is due to angular fluctuations of the arm cavity mirrors. Angular misalignments of the cavity cause higher order modes to couple into the cavity [138]. This in turn introduces an offset to the reflection locking signal [128]. This offset is much larger for the green reflection locking signal, because the low finesse leads to insufficient suppression of higher order modes. The transverse mode spacing for 532 nm is 5.5 kHz, which is only 2 times larger than the cavity bandwidth. Our design called for a $\sim$ 10 times higher green cavity finesse, but unfortunately the dichroic coating for the current end test masses is far out of specification for green (see Table 4.1). The error in the green coatings of the end test mass could have been detrimental to the success of the arm length stabilization technique. The high frequency noise (specifically fiber and laser noise, as mentioned above), was higher than anticipated due to the low finesse cavities. However, the noise budget indicates that the high frequency noise does not limit the rms of the scheme, as can be seen in Figure 6.1. The increase in the high frequency noise due to the error in the coatings was not significant; however, the impact on the low frequency noise was almost costly. The low finesse cavity causes high sensitivity to angular misalignments. Upon first locking the X-arm cavity with the green light, the arm length stabilization noise was 100 Hz rms due to all the low frequency noise. This noise level was significantly above the target[1] 8 Hz rms and would have rendered the scheme useless for the lock acquisition scheme. The noise budget was extremely beneficial in targeting the source of the low frequency noise. With this information, the seismic isolation systems team greatly improved their feedback loop configuration to increase isolation of the end test masses at low frequency. Although the angular fluctuations were not completely eliminated, their work reduced the low frequency noise sufficiently to make the arm length stabilization scheme viable.

Meanwhile, between 0.4 Hz and 1 Hz, the noise is due to longitudinal displacement motion of the test masses. The displacement noise is $\sim 1 \times 10^{-8}$ m/$\sqrt{\text{Hz}}$ or 700 Hz/$\sqrt{\text{Hz}}$ at 1 Hz, and falls off steeply due to the seismic isolation system. This noise is suppressed by the common mode stabilization of the interferometer.

Slow path length variations between the X-arm transmission and the frequency-doubled sample beam from the main laser create up-converted phase noise from 1 Hz to 10 Hz. While the arm cavity is locked, the green transmission path to the photodetector can move freely. As this path varies by multiple wavelengths, the fringe pattern produced by the two beams changes. This fringe wrapping causes an effective motion at higher harmonics and thus up-converted noise with a spectrum that falls off as 1/f [150]. We measured this effect by looking at the difference between the main laser sample beam and the infrared pick-off beam used for locking the power recycling cavity (see Figure 6.2 for set-up). Since the latter beam travels the same path as the green transmitted beam, this allowed us to measure the path length variations of the input path relative to the green path. The resulting noise spectrum is depicted as the solid black trace in the figure. Notably, since this noise depends on the motion of freely moving suspended mirrors, it varies with the variation of the seismic noise.

---

[1] The arm length stabilization rms requirement for the common mode degree of freedom as was follows: the cavity fluctuations must be reduced by one tenth of the equivalent arm cavity linewidth for 1064 nm [68].

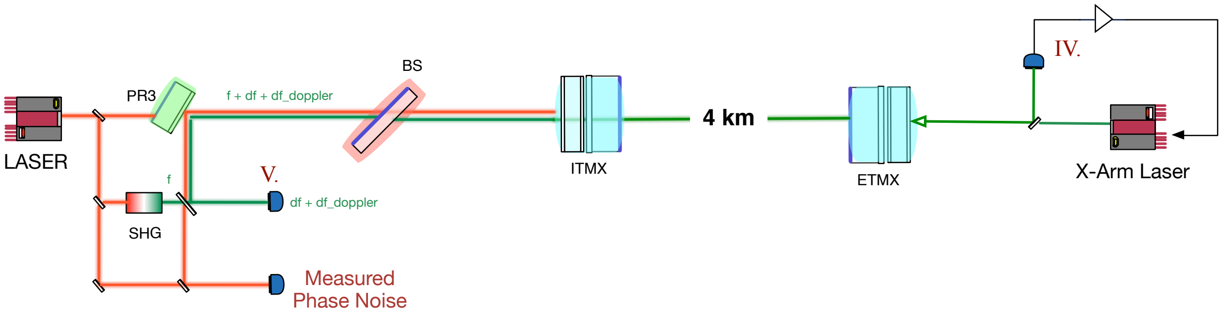

Figure 6.2: Recall that the common mode is controlled by a beat note between a frequency-doubled sample beam of the main laser and the green transmitted signal from the X-arm. However, these two beams do not traverse the same optical paths. Additionally, the green transmitted path to the photodetector can move freely, unlike the locked arm cavity. These path variations create phase noise. This was measured by installing an additional photodetector to compare the infrared beams that travel equivalent paths to the frequency-double sample beam of the main laser and the green transmitted beam. Here, I simplify the schematic and only show the Pound-Drever-Hall locking loop for the end station. I have labeled the corresponding photodetectors shown in Figure 4.2.

Other sensing noise, such as electronics noise and shot noise, are not significant. The noise for the differential mode of the arm length stabilization system looks almost identical. The only real difference is the absence of the fringe wrapping effect, since the two green transmitted beams used for the heterodyne measurement travel nearly the same path.

6.2 Noise Budget Breakdown

To determine the dominant noise sources listed in Figure 6.1, a variety of other noise sources were measured and ruled insignificant. In this section, I provide further detail into the measured noises. In addition, I break down the full noise budget into smaller noise budgets describing each servo loop of the arm length stabilization scheme. These smaller noise budgets are useful to explain and validate the overall noise propagation.

Figure 6.3 shows a noise budget solely for the end station phase-locked loop. In this graph, the blue solid trace is the measured in-loop noise, i. e., the loop suppressed noise at the error point of the phase-locked loop. The rms is 20 mrad/$\sqrt{\text{Hz}}$. The dominant noise source for this loop is the laser frequency noise. However, at frequencies above 100 kHz, the noise is limited by shot noise.

The standard sensor noises are electronic noise, dark noise, and shot noise. The electronic noise of the phase-frequency-discriminator was estimated as a flat response of 460 nVrms/$\sqrt{\text{Hz}}$ using the board's tests results [136]. The dark noise was measured by blocking the light at the photodetector used in the phase-locked loop; it was found to be -119 dBm at 100 Hz bandwidth. The shot noise can be both measured and calculated from first principles. The shot noise was measured to be -114 dBm with 100 Hz bandwidth. Using that the phase-locked loop beat note was -32 dBm, the shot noise was converted from dBm into rad/$\sqrt{\text{Hz}}$ via the following expression:

$$\sigma_{\text{shot noise}}[rad/\sqrt{\text{HZ}}] = \sqrt{2} \times 10^{(\text{shot noise}-\text{beat note})/20} \tag{6.1}$$

During this measurement, the power at the photodetector was 5.2 mW. The majority of this light comes from the end station laser and not the fiber. From this we can can compute the shot noise from first principles:

$$\sigma_{\text{shot noise}}[rad/\sqrt{\text{HZ}}] = \sqrt{2qI}/I_{carrier} \tag{6.2}$$

where q is the charge of an electron, and I is the current on the photodetector whose responsivity is .1 A/W. Meanwhile, $I_{carrier}$ is the current of the carrier computed from the beat note assuming a 2 kOhm transimpedance. Notably, the dark noise of the photodetector was subtracted from this shot noise. The discrepancy between the measured and calculated shot noise seen in the figure is within uncertainty of the measurement.

All of these sensor noises are depicted in Figure 6.3. Recall that the sensor noise is suppressed by the sensitivity function at the error point (Equation 5.12). However, since these noises only contribute above the unity gain frequency of the phase-locked loop, at which point the sensitivity function is unity, the noises in this plot are shown as pure sensor noise (with no suppression below the UGF).

The frequency noise present in the loop consists of the end station laser and the fiber noise as already described. In order to compare this to the measured noise at the error point, both of these noises are loop suppressed via Equation 5.11.

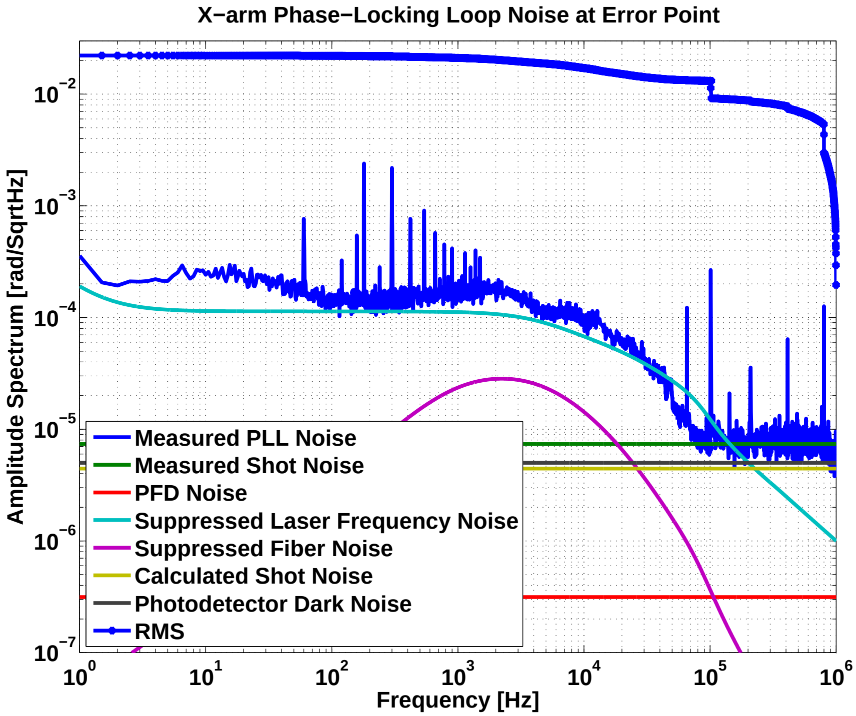

Figure 6.3: End station phase-locked loop noise budget. This graph specifically shows the measurement for the X-arm, but the Y-arm is similar.

These noises can also be propagated to the out-of-loop noise of the phase-locked loop as depicted in Figure 6.4. Here, the laser frequency noise is suppressed by the loop gain via Equation 5.9. The fiber noise is now treated a little differently. The fiber noise is only imposed on the Pound-Drever-Hall locking loop through the phase-locked loop, i. e., the fiber noise only appears in the PDH loop up until the PLL UGF, at which point it is not seen by the PDH. As a result, this noise is propagated with the closed loop transfer function. Meanwhile, the sensor noise follows Equation 5.10 — at low frequency the noise is imposed at the output, while suppressed by the loop gain above the unity gain frequency. The sum of these noises is the laser frequency noise imposed onto the PDH loop and into the arm cavity.

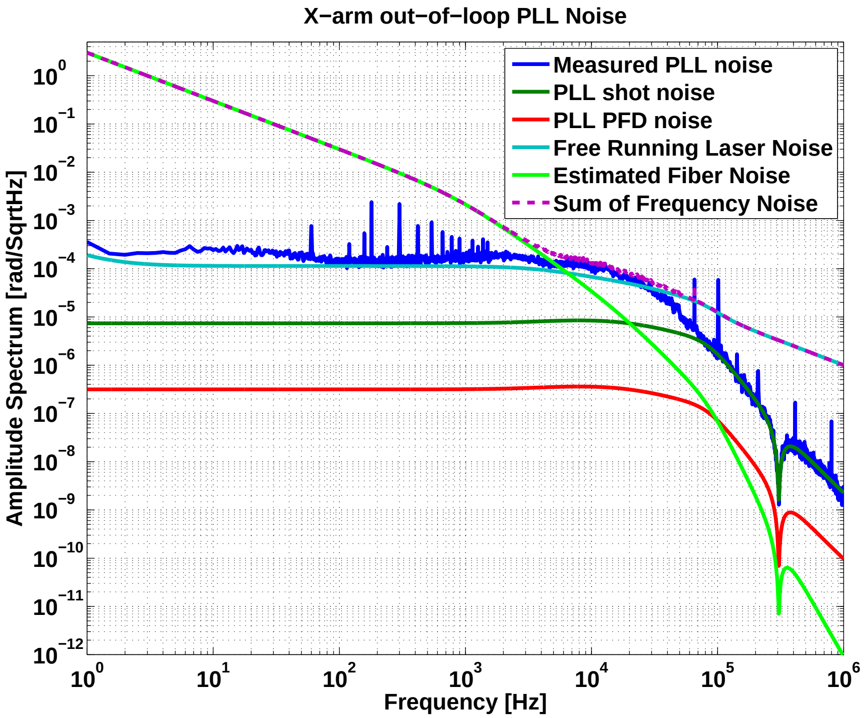

Figure 6.4: Out-of-loop noise budget of X-arm PLL.

The noises from the end station phase-locked loop can be propagated to the end station Pound-Drever-Hall locked loop, and a similar noise budget can be produced at the error point of the PDH loop. Figure 6.5 depicts the measured noise spectrum at the error point of the loop in blue. The dominating noise sources in the reflection locking servo are the fiber and laser noises.

The out-of-loop noises from the phase-locked loop behave as a disturbance to the PDH loop. Additional sensor noise arrises from the PDH electronics and shot noise. The PDH dark noise was measured by blocking the reflection lock servo photodiode. Meanwhile, the shot noise at the photodetector was measured by misaligning the input test mass and placing a HR 532 nm mirror between the end test mass and the photodetector. As a result, this measurement is not of pure shot noise, except at high frequencies. Some of this noise comes from scattering and acoustic noise on the optics table housing the photodetector. The voltage controlled oscillator noise was also measured [31] and propagated accordingly.

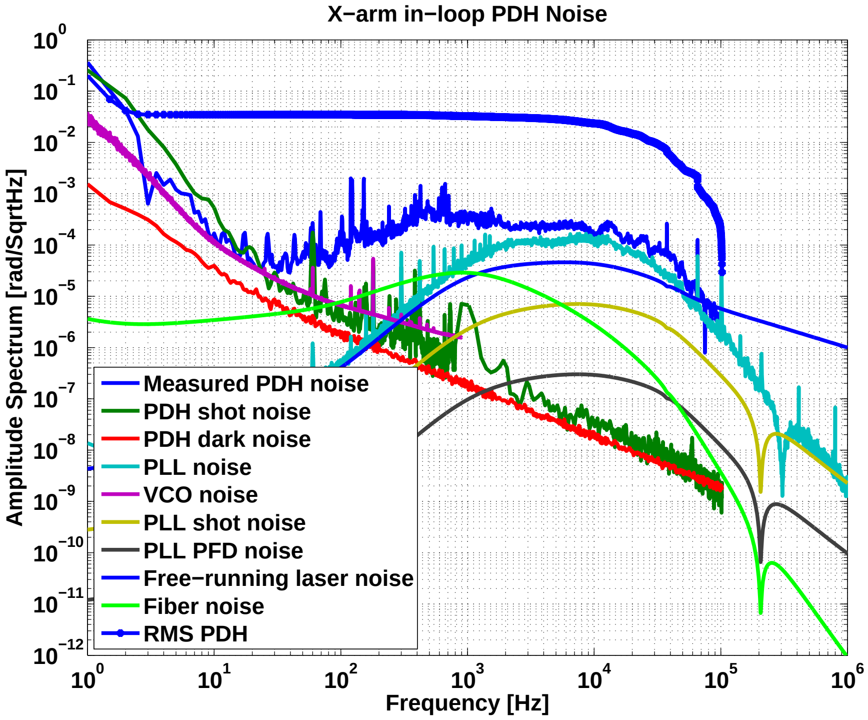

Figure 6.5: Noise Budget of X-arm Pound-Drever-Hall loop.

The end stations noises are then projected to the corner station. Figure 6.6 is a plot of the noise budget of the out-of-loop reflection locking servo noises with the cavity response. In the plot, the end station PLL noises exhibit the cavity pole. Meanwhile, the PDH signal sources are suppressed by Equation 5.10 and then exhibit the cavity pole. Due to this gain suppression at high frequency, we expect to see the PDH sources fall off faster than the PLL sources after the UGF (i.e. it is not just simply a cavity pole behavior at high frequency), which is seen in the graph.

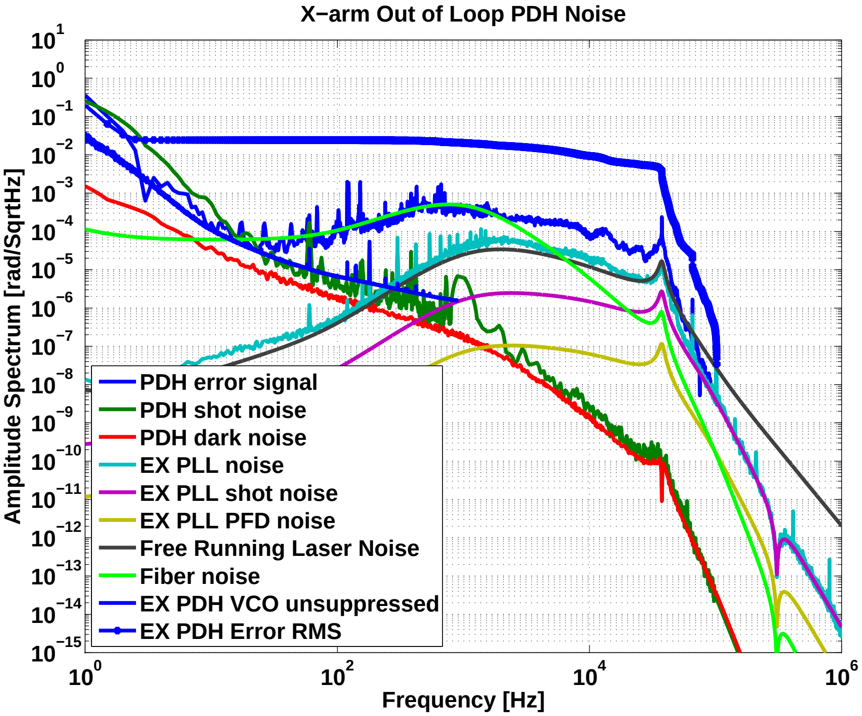

Figure 6.6: Noise Budget of X-arm end station to vertex loops.

The end station noises are imposed onto the common mode noise via the beat note of the green transmitted light and the frequency-doubled sample of the main infrared beam. Recall, there is an additional phase-locked loop of this signal as described in Section 4.1.4. Figure 6.7 shows the noise budget for the common mode phase-locked loop at the error point. Here, the red trace represents the measured noise at the error point. The end station noises are propagated following the usual prescription for sensor noises. The common mode phase-locked loop also introduces additional noise. Again, the electronics noise for this phase-frequency discriminator was assumed to be a flat 460 nVrms/$\sqrt{\text{Hz}}$ response. Meanwhile, the shot noise was calculated from the power incident on photodetector used for the common mode beat note. Meanwhile, the dark noise for the photodetector was estimated using the value measured from the end station photodetector. Length displacement noise was also included in the noise budget.

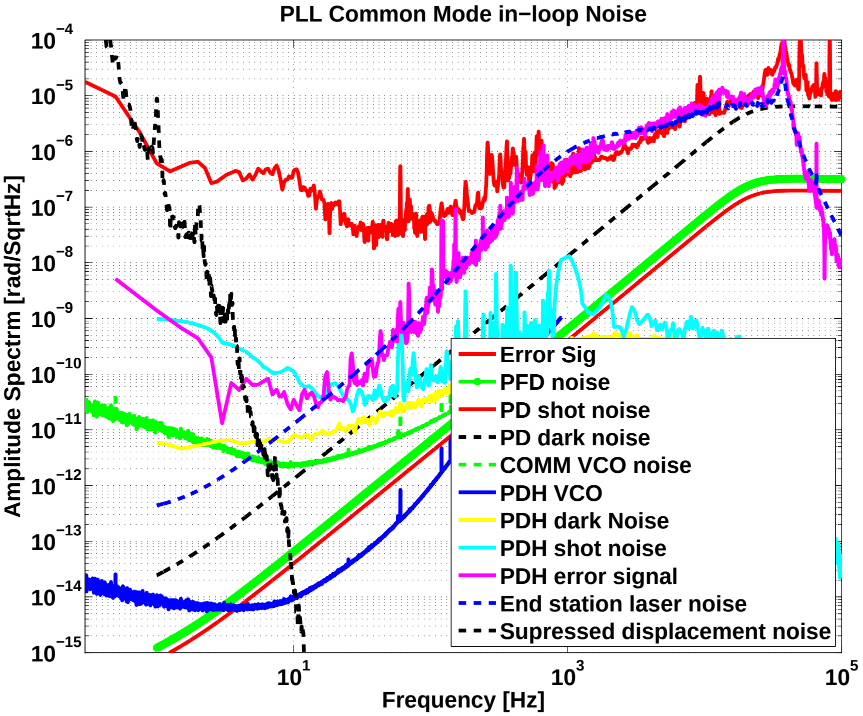

Figure 6.7: Noise budget of Common mode PLL.

In this plot, between ~5-100 Hz it appears that the noise is unexplained; however this measured noise is limited by the noise floor of the SR785 [157] that was used to take the amplitude spectrum. The aforementioned acoustic noise present in the common mode path is nicely seen in the red trace. Notably, the projected end station PDH noise does not contain these acoustic peaks, but matches the measured noise above these frequencies. The peak at 37 kHz in the plot comes from the repeated cavity pole in transmission at another FSR (recall Section 5.4.1). The repeated cavity pole results in no suppression of the free running laser noise.

Finally, this noise is then projected to the infrared beam once locked on resonance with the arm length stabilization. Only the dominant noise sources are depicted in Figure 6.1. The same noise budget propagation was done for the Y-arm and was used to measure the differential mode noise. As expected, the end station noises were nearly identical. Again, the fiber and laser noise limit the overall differential mode noise at high frequency. Meanwhile, the low frequency noise of the differential mode is dominated by the motion of the suspensions. In this case, there is no phase noise, since the green transmitted paths for the differential beat note travel nearly the same path.

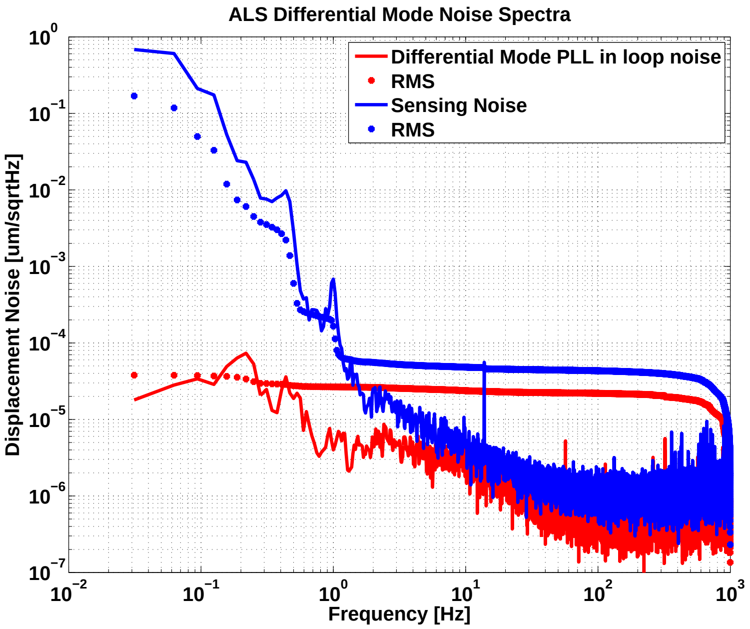

Figure 6.8: Differential mode spectra measured at the error point of the differential mode phase-locking loop. A comparison of the two traces shows the differential mode loop suppression.

The differential mode noise suppression for the arm length stabilization was also deemed sufficient, just as the case for the common mode noise. Figure 6.8 shows two traces for the differential mode spectrum measured at the error point of the differential mode phase-locked loop. The blue trace is essentially the free swinging spectra; the measurement was taken with a very low differential mode bandwidth such that this trace represents the free sensing noise and alignment noise at low frequency. Meanwhile, the red trace is the in-loop noise spectrum. Recall, that the sensor noise is loop suppressed at the error point via Equation 5.12. Comparing the two traces, depicts the overall loop suppression and indicates that the differential mode UGF is about 10 Hz. This loop suppresses the differential length motion to below $0.1\,\mathrm{nm}/\sqrt{\mathrm{Hz}}$. This displacement noise is sufficient for the arm length stabilization technique to maintain lock and eventually hand over to the nominal locking sensors as will be described in Chapter 7.

6.3 Chapter Summary

To ensure that the arm length stabilization technique would be viable for a lock acquisition process with a high duty cycle, the noise introduced by the system had to be well explained and at a tolerable level. The noise budget was essential for targeting the limiting noise sources throughout the frequency band of interest. Except at low frequencies, the noise was sufficiently low that action was not required after producing the noise budget. However, since the green coatings for the end test masses were far outside of specification, which made the low frequency noise of the arm length stabilization worse, a good model of the noise was even more critical. The isolations for the end test masses was improved, and the noise was brought to a tolerable level.

Using a well validated model, several noise sources were measured and propagated to the out-of-loop noise of the common mode and different mode degrees of freedom. It was deemed that the main contributing noise sources were fiber and laser frequency noise at high frequency, acoustic noise from periscopes or opto-mechanical structures and phase noise at intermediate frequency, and displacement noise and angular fluctuations at low frequency. The sum of all of these noise sources describe the overall noise of the system. The overall noise of the arm length stabilization system introduced to the common and differential modes are sufficiently low enough to include this scheme in the lock process and transition to the next locking step. With the noise budget, confidence in the technique was established.

Chapter 7

Full Interferometer Locking

The full locking sequence begins as follows: First each arm cavity is locked on the green laser using the arm length stabilization system. Secondly, the green corner station signals for common and differential modes are engaged. The differential mode is nominally set to 0 Hz, whereas the common mode is offset by about 500 Hz. With both arm cavities set off-resonance the dual-recycled Michelson interferometer is locked using the 3f technique [33].

Advanced LIGO uses two modulation frequencies to control the dual-recycled Michelson: One is used to sense the length of the power recycling cavity, and the other is used to sense the length of the signal recycling cavity and the Michelson length (recall Figure 4.1). Since all modulation frequencies have to pass through the input mode cleaner at a multiple of its free spectral range, the first modulation is set to the free spectral range frequency of 9.1 MHz. The second modulation frequency should be far enough away as not to interfere with the 3f signals of the first modulation. The fifth harmonic at 45.5 MHz is used. Both modulation frequencies are resonant in the power recycling cavity, but not in the arm cavities. While the carrier operates on a dark fringe at the anti-symmetric port, the RF sidebands do not. They transmit to the anti-symmetric port due to the macroscopic Schnupp asymmetry and their frequency offset from the carrier. The higher harmonics will have a higher transmission into the signal recycling cavity and can be used to sense its length. The traditional 1f signals, which are derived from a beat note between the carrier and the sidebands, are used in the final configuration to control all degrees of freedom except the differential arm length. In its final configuration the differential arm length uses a DC offset scheme [70]. The 3f technique is based on the observation that a phase modulator produces harmonics at all multiples of the modulation frequency. At small modulation depth the strength of the higher harmonics declines rapidly. Neither the first-order, second-order, nor any other higher-order modulation sidebands will be resonant in the arm cavities. Hence, their beat note at three times the modulation frequency can be used to deduce the lengths of the dual recycled Michelson interferometer, with little sensitivity to the resonance condition of the arm cavities. In reality, the arm cavity resonance condition does have a small effect on the 3f signals, but the effect is not large enough to cause significant problems during lock acquisition. Since the 3f signals are much weaker than the standard 1f signals controls have to be switched over to the 1f signal during the final steps of the lock acquisition sequence. In particular, the 3f signals are a factor of Γ^2 smaller than the 1f signals, where Γ is the modulation depth.

The complete locking sequence is shown in Figure 7.1. With the dual-recycled Michelson interferometer locked on 3f, and the arm cavities controlled by the arm length stabilization, the frequency offset in the common arm length must ultimately be brought to 0 Hz in order to bring the carrier beam into resonance in the arm cavity. To do so, the VCO used as a reference for the beat note between the green transmission and infrared reference beam is adjusted. Since the VCO is locked to the beat note and the VCO control signal is fed back to the input mode cleaner length and main laser frequency, adjusting the tune offset of the VCO inherently adjusts the main laser's frequency. In principle, all that is required is to reduce the common mode offset to 0 Hz and engage the Pound-Drever-Hall 1f signals for common and differential mode. However, the noise in the arm length stabilization system is larger than the linewidth of the double cavity resonance. This prohibits full power build-up, and does not yield a good common mode locking signals for the infrared light. The noise introduced by the arm length stabilization system can clearly be seen in the reflection locking signal at 180 sec in the full lock sequence of Figure 7.1.

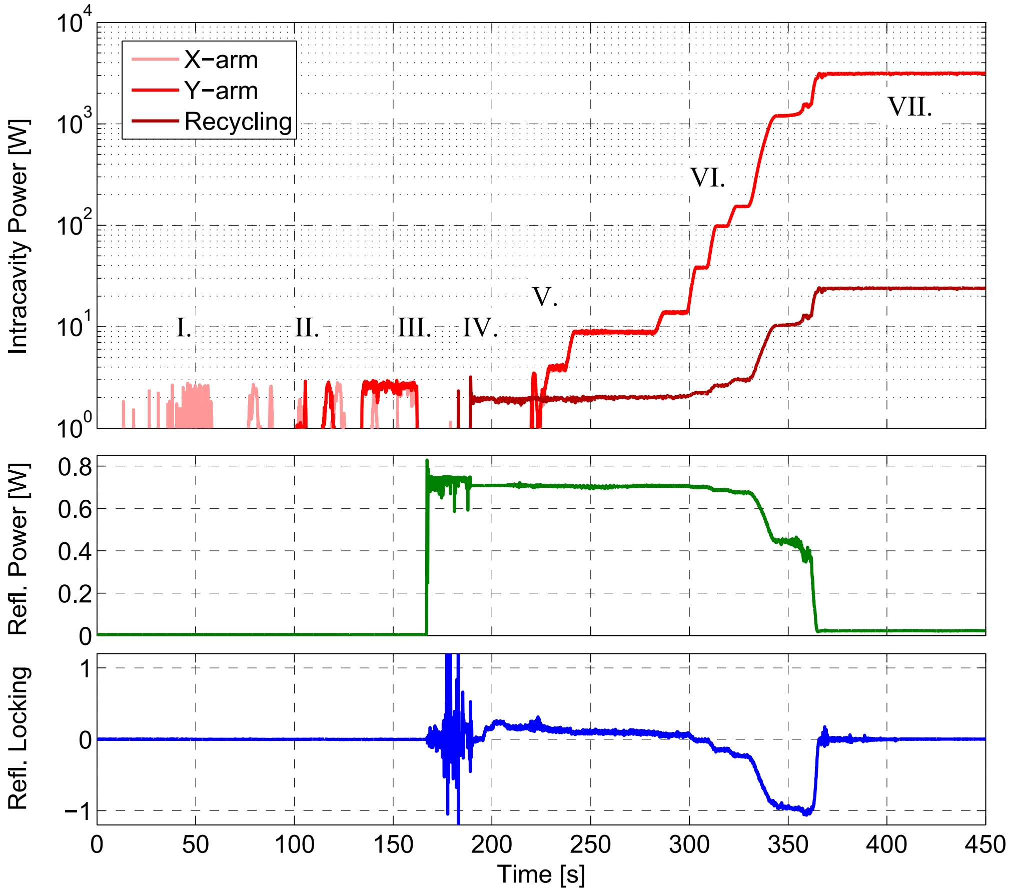

Figure 7.1: Lock sequence of the full interferometer. The top panel shows the intra-cavity power for each arm cavity as well as for the power recycling cavity. The input power is currently 0.75 W. The center panel shows the power in reflection, whereas the bottom panel shows the 1f signal in reflection of the interferometer. During period I each arm cavity is locked using the green laser in the end station and then switched over to the corner station signals for common and differential mode. During phase II the arm cavities are scanned to find the resonance for the infrared light. At point III both the arm cavities are moved off resonance by 500 Hz, and the recycling cavities are aligned from the initial misaligned state. At point IV the dual recycled Michelson interferometer is locked using 1f signals and immediately switched over to the 3f signals. A build-up of 2 W can be seen in the power recycling cavity. At point V the power in the arm cavities is approximately 4 W and the common and differential controls are switched from the green transmitted signals in the corner to the arm cavity transmitted infrared power and the anti-symmetric port Pound-Drever-Hall signal, respectively. The arm cavities are then brought closer to resonance and the power build-up increases. Once we reach VI, we have a significant reflection locking signal, which is now used to control the common mode. Finally, in phase VII, the dual recycled Michelson interferometer is switched to the 1f signals. The power in each arm cavity reaches approximately 3 kW, whereas the recycling gain reaches a value around 30. The reflected power decreases to about 3% indicating that most of the laser power is lost in the detector. During future commissioning work, the power into the interferometer will be increased significantly, aiming for the final intra-cavity power to be roughly 200 times higher.

Two methods to overcome this issue have been studied: self-locking and the use of the transmitted infrared power. Self-locking relies on the occasional build-up that occurs when the double cavity fringe is close to resonance. When this build-up occurs, the main reflection locking signal self-engages, as described in Ref. [92]. However, locking is generally achieved using the infrared transmitted signals instead. These signals do not suffer from most of the noise sources dominating the arm length stabilization system. In particular, the noise generated by the end station laser, the acoustic noise on the green transmitted light, the up-conversion noise and the noise due to angular drifts are not present. Angular fluctuations couple strongly in our case because the green arm cavity finesse is quite low and provides insufficient suppression of higher order optical modes. We first reduce the common mode offset to an intermediate point, where there is partial power build-up in the arm cavities. Then, the differential mode controls are switched from the arm length stabilization system to the Pound-Drever-Hall reflection locking signal at the anti-symmetric port, while the common mode controls are switched from the arm length stabilization system to a signal derived from the transmitted arm cavity power for the infrared light [82, 110, 164]. In particular, the square-root of the sum of the transmitted infrared light from each arm is used. When a cavity is off-resonance, the transmitted power can be used as a locking signal by subtracting a fixed offset, this is known as the CARM offset. Increasing the size of the subtracted offset will bring the cavity closer to resonance. As this is done, the optical gain of the arm cavities increases, so a normalized transmitted signal is used such that the loop gain can go unaltered. Since these signals are digital, the loop bandwidth is limited. At this stage the CARM bandwidth is approximately 400 Hz. The arm length stabilization common mode bandwidth was modified to match this bandwidth for ease in transitioning. However, using the transmitted power to control the common mode will not work when exactly on resonance. Once the power builds up to about the half of the maximum, the Pound-Drever-Hall reflection locking signal in reflection of the interferometer becomes available. Figure 7.2 shows the simulated common mode closed loop transfer function for the reflection and transmitted signals; this plot highlights that the reflection signal is only viable after a certain point in the offset reduction. Once locked on the signal in reflection, this control loop is completely analog and the loop bandwidth is increased to 35 kHz. At this point, the common mode controls are switched over to the final configuration, and full lock is achieved. Concurrently, the 3f dual-recycled Michelson signals are transitioned back to the nominal 1f locking signals.

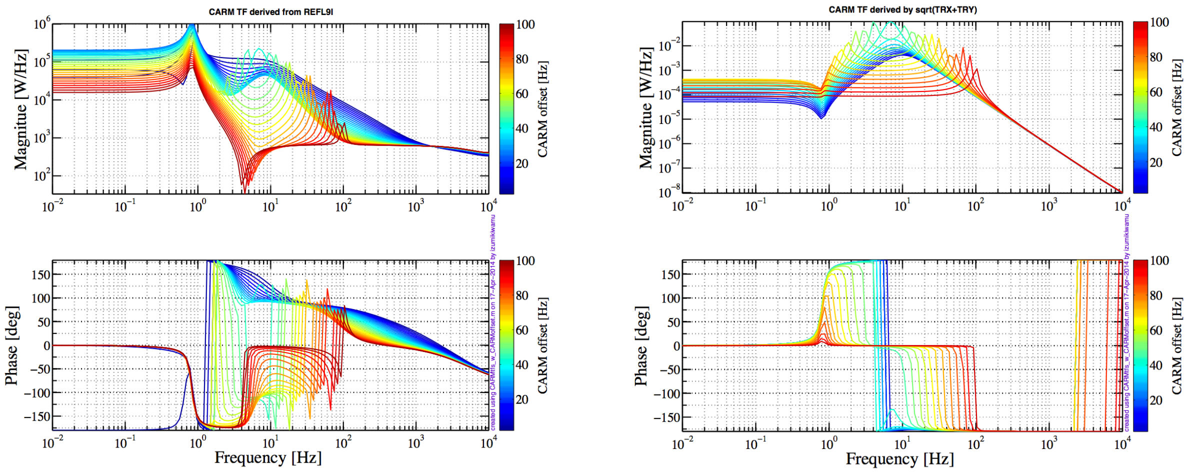

Figure 7.2: A simulation of the CARM closed loop transfer function at various offsets for the reflection locking signal (right) and the IR transmitted signal (left). The reflection signal only becomes available around 40 Hz CARM offset with the response shape goes as 1/f above the cavity pole. Images courtesy of Ref. [91].

The final step in the sequence involves transitioning the differential mode from the anti-symmetric port RF sideband to DC readout. These two signals differ in that the former is a heterodyne detection scheme, while the latter is a homodyne detection scheme; the main difference being that in a homodyne detection scheme the local oscillator is the same frequency as the carrier. DC readout is achieved by introducing a small differential mode offset of 25 pm, so that the interferometer is slightly off the dark fringe. The carrier light that leaks to the anti-symmetric port is now the local oscillator. The authors of [71, 151, 164] explain some of the drawbacks of this method—for example, the introduction of the DARM offset introduces more noise coupling into DARM. However, the use of DC readout is advantageous for bringing the detector to a low noise state. Recall that at this point the carrier light resonates in all of the interferometer's cavities, and that the common mode degree of freedom is controlled. Locking the common mode degree of freedom suppresses the laser frequency fluctuations. The coupled cavity pole at 0.6 Hz of the arm cavities and the power recycling cavity, acts as a low pass filter, making the carrier light the most quiet light in the frequency band of the interferometer. The carrier light is the best possible choice for a local oscillator. As a result, the transition to DC readout for the differential mode is beneficial. Notably, the use of a homodyne detection scheme is limited to one degree of freedom, since it requires a single frequency for the local oscillators. The differential length is chosen due to its required sensitivity. After this step, the detector is now at its operational point and is in a low-noise state where gravitational-wave detection is possible.

Degree of Freedom	**Initial Steps**	**Resonance Achieved**	**Final Configuration**
CARM	ALS: Common mode beat note → IR transmitted signal	Normalized signal, reflection port 9 MHz	Analog signal, reflection port 9 MHz
DARM	ALS: Differential mode beat note	PDH signal, anti-symmetric port 45 MHz	DC readout, 25 pm offset
PRCL		In-air reflection port 27 MHz	In-vacumm pick-off port 9 MHz
SRCL		In-air reflection port 135 MHz	In-vacuum pick-off port 45 MHz
MICH		In-air reflection port 135 MHz	In-vacuum pick-off port 45 MHz

Table 7.1: The table lists the locking signals used at various steps in the acquisition for each of the five length degrees of freedom that must be controlled. The photodetectors at the reflection port, pick-off port, and antisymmetric port are labeled in Figure 4.1. Notably, MICH and SRCL use the same RF sideband for locking; however MICH uses the Pound-Drever-Hall Q-signal, while SRCL uses the I-signal by convention. The actuators for each degree of freedom is listed in Table 7.2.

Degree of Freedom	**Actuator**
MICH	Beam Splitter (BS)
PRCL	Power Recycling Mirror (PRM)
SRCL	Signal Recycling Mirror (SRM)
DARM	End test mass (ETM), ETMX then ETMY
CARM	MC2, laser frequency (via the error point of the input mode cleaner loop)

Table 7.2: A list of the actuators used to control each respective length degree of freedom. During the arm length stabilization technique, the differential motion is first controlled with the X-arm end test mass (using one optic instead of two is sufficient to control this DOF). However, once on DC readout, the DARM signal is transitioned to the Y-arm end test mass which is fitted with a low noise voltage driver [72]. This driver has less force than that on the X-arm and thus cannot be used to acquire lock. However, once locked, the low noise driver is beneficial to reduce noise in DARM and at the gravitational wave readout signal.

Signal	**CARM offset**
ALS common mode	14 nm - 400 pm
$\sqrt{TR_X + TR_Y}$	400 pm - 3 pm
Normalized I-signal, reflection port 9 MHz	3 pm - 0 pm
Analog I-signal, reflection port 9 MHz	0 pm

Table 7.3: The table lists CARM locking signals as a function of the CARM offset. Here TR_X, TR_Y denote the transmitted infrared signal of each of the arm cavities.

Signal	**CARM offset**
ALS differerntial mode	14 nm - 50 pm
Anti-symmetric port 45 Mhz	50 pm - 0 pm
DC readout	0 pm

Table 7.4: The table lists DARM locking signals as a function of the CARM offset.

Tables 7.1, 7.3, and 7.4 review some of the lock acquisition steps; the signals used to lock each of the five length degrees of freedom at various steps are highlighted. Table 7.1 elucidates the importance of the interferometer's ports. The reflection port is near the laser and measures all the light reflected back to the laser. This port is sensitive to the common modes, L_+, l_+, and laser frequency changes. Meanwhile, the pick-off port, which is located between the beam splitter and the power-recycling mirror, is sensitive to various modes. Finally, the anti-symmetric port located at the output photodetector, is sensitive to the differential modes, L_-, l_- by design. Evidently, the signal at the reflection port is ideal to control CARM in the final configuration. The signal at the pick-off port could be used to control CARM; however the shot noise level at this detector is higher than at the reflection port. Since CARM is used to suppress frequency noise, the less noisy sensor is chosen. The only sensor to sense differential displacement is at the anti-symmetric port, so DARM is controlled by this sensor (up until DC readout). The only remaining sensor is at the pick-off port. The signals from this port are then used to control MICH, PRCL, and SRCL. Recall in Section 3.10, that the MICH resonance condition is to be on a dark fringe. This condition is critical to split the common and differential modes spatially. This is what ultimately makes the reflection port sensitive to the common mode and the anti-symmetric port sensitive to the differential modes [73].

The feedback loops to all these length degrees of freedom must be stable. Figures 7.3-7.8 show the open loop transfer functions for the length DOFs. The CARM UGF is 35 kHz with 25 degrees of phase, selected for a maximal stable bandwidth. The remaining UGFs are limited by gain hierarchy. SRCL, MICH, and PRCL couple into DARM, so feed forward loops are ultimately introduced [104, 156]. As is thoroughly discussed in Ref. [104], damping of the high Q suspensions modes (bounce: ~9 Hz, roll: ~14 Hz, violin: ~512 Hz + harmonics) is also required.

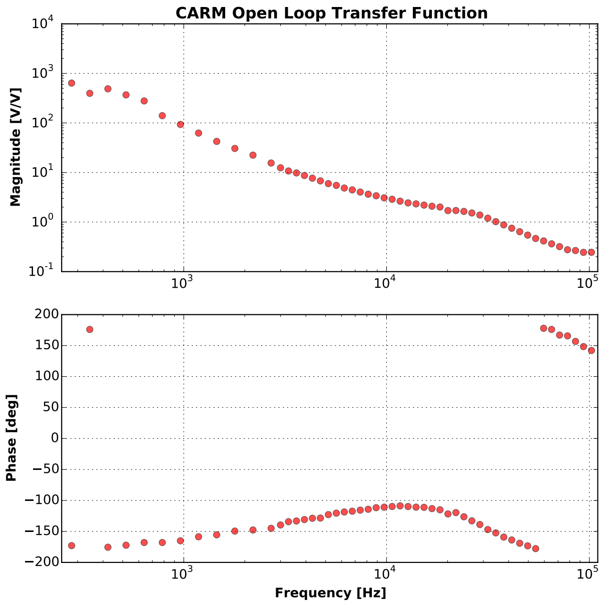

Figure 7.3: Open loop transfer function of the CARM degree of freedom in the analog configuration.

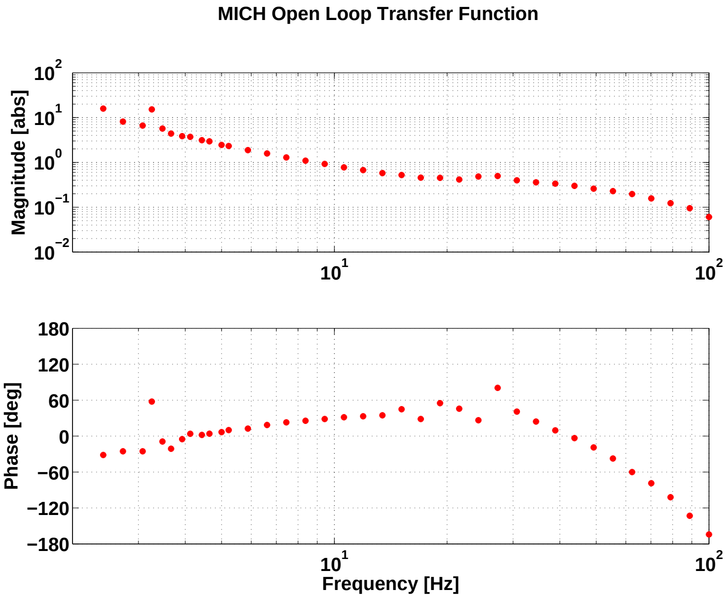

Figure 7.4: Open loop transfer function of the MICH degree of freedom. MICH UGF ~10 Hz.

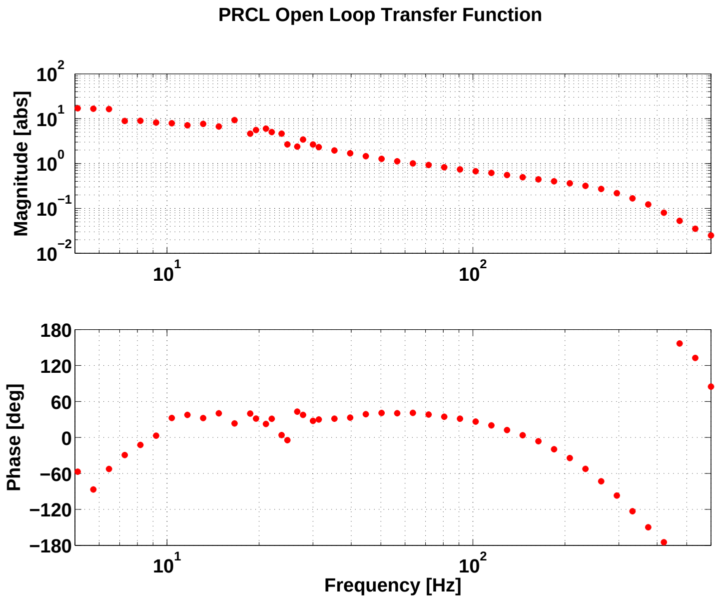

Figure 7.5: Open loop transfer function of the PRCL degree of freedom. PRCL UGF ∼45 Hz.

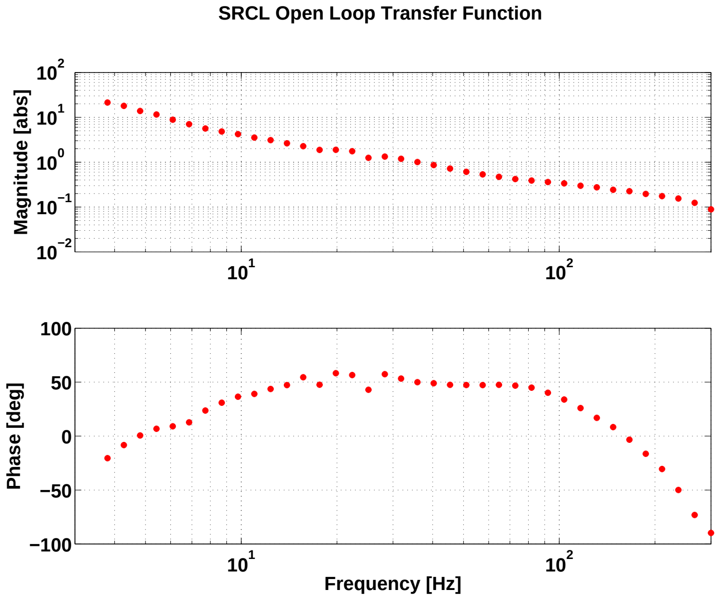

Figure 7.6: Open loop transfer function of the SRCL degree of freedom. SRCL UGF ∼25 Hz.

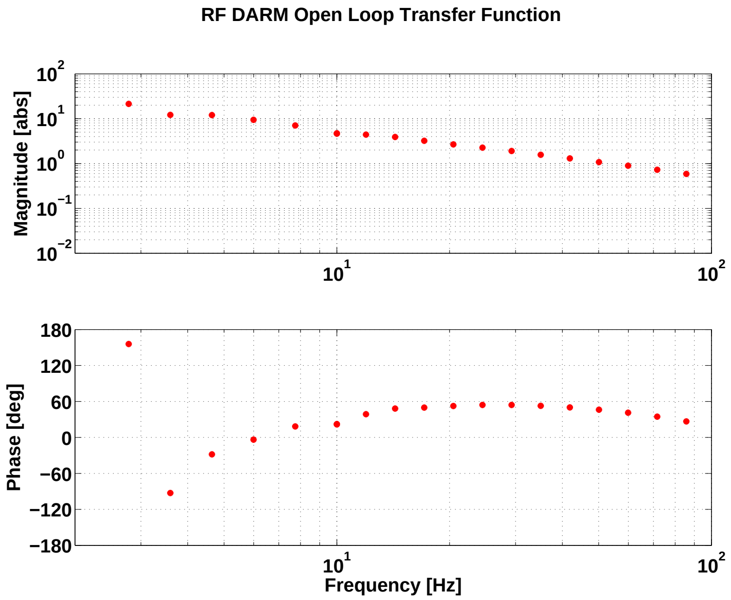

Figure 7.7: Open loop transfer function of RF DARM degree of freedom.

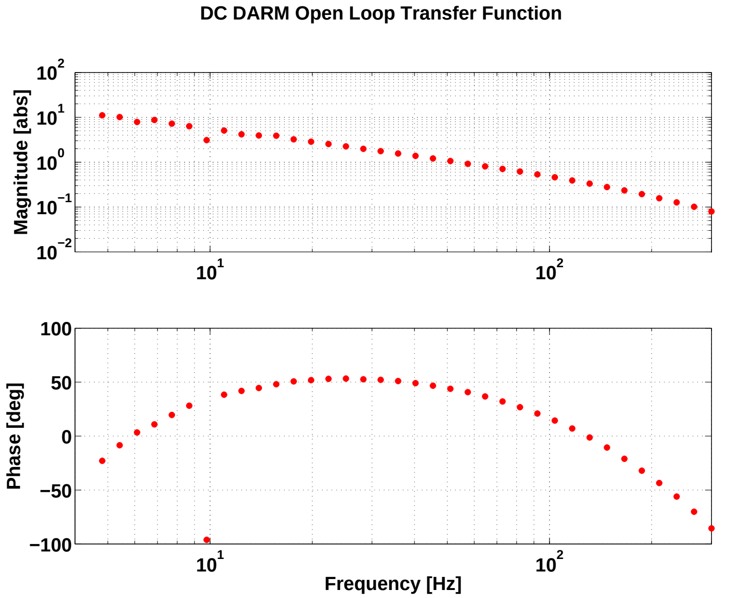

Figure 7.8: Open loop transfer function of the DC DARM degree of freedom.

7.1 Angular Alignment

An important step of lock acquisition is the alignment sensing and control [78, 112]. In addition to the five length degrees of freedom there are also fourteen angular degrees of freedom that must be controlled. Each of the seven interferometeric optics (four for the arm cavities, the beam splitter, the power recycling mirror, and the signal recycling mirror) introduce two angles of motion that must be controlled: "pitch" refers to the angle of motion about the horizontal axis and "yaw" to the angle of motion about the vertical axis [78]. The alignment of the beam on these optics is essential to keep the interferometer lock stable. A misalignment can cause a torque on the optics, and make the mirrors oscillate [133]. In addition, the power build-up in the interferometer is generally less with poor alignment. The requirement for Advanced LIGO as stated in Ref. [78] is:

> "angular orientations of the optics be within 10^{-8}rad rms of the optical axis, the beam must be kept centered on the mirrors within 1 mm, fluctuations in the input laser beam direction must be less than $1.5\times10^{-14}\,\mathrm{rad}/\sqrt{\mathrm{Hz}}$ in angle and less than $2.8\times10^{-10}\,\mathrm{m}/\sqrt{\mathrm{Hz}}$ in transverse displacement for frequencies $f > 150Hz$."

Alignment sensor and control loops use wavefront sensors and/or quadrant photodiodes to sense the position of the beam. Feedback loops are generated to adjust steering optics and ensure central alignment of the beams and full power build-up. Details of the current alignment sensing and control loops for Advanced LIGO will not be discussed in this thesis, but can be found in Ref. [104]. Extensive work was involved to design and implement these loops. Plant transfer functions of the optics were taken, digital filters were designed, and useful sensors had to be found. The interferometer would not be locking stably and returning to the same configuration without these loops.

7.2 Initial Alignment

Initial alignment of the interferometer is also a nominal procedure prior to lock acquisition. The general steps implemented at the Hanford observatory are as follows [3]:

- Using photodiodes located on the end test mass baffles, the transmission monitor table which is used to align the green beam into the arm (among other things), is centered.
- An alignment loop using wavefront sensors adjusts the input and end test mass alignment for maximal power build up in both the arm cavities.
- IM4 and PR2 are aligned by locking the main infrared beam to the X-arm to maximal build-up. PR2 is mirror used for the power recycling cavity and is drawn in Figure 4.2. IM4 is a small input mirror used to steer in the main infrared beam. With the combination of these two mirrors the input pointing of the main infrared beam is controlled.
- A third mirror in the power recycling cavity, known as PR3, is aligned to ensure a maximal beat note of the transmitted green light in the vertex.
- The power recycling mirror is adjusted for maximal build-up in the power recycling cavity.
- The beam splitter is adjusted for the dark fringe condition in the Michelson interferometer.
- SR3, a mirror in the signal extraction cavity, is aligned for proper centering of the output beam at the anti-symmetric port to the output mode cleaner.
- The signal recycling mirror is adjusted for maximal build-up in the signal extraction cavity.

In the above steps, the input mode cleaner is assumed to be aligned and locked. All of these steps have been fully automated. Typically this procedure is done once a day, unless there is a large disturbance to the alignment of the optics. Further details on these steps can be found in Ref. [104].

7.3 Signal Transitions

The signals used to control the five length degrees of freedom at various stages in the lock acquisition process were previously discussed. The transitions among signals are done differently depending on the degree of freedom.

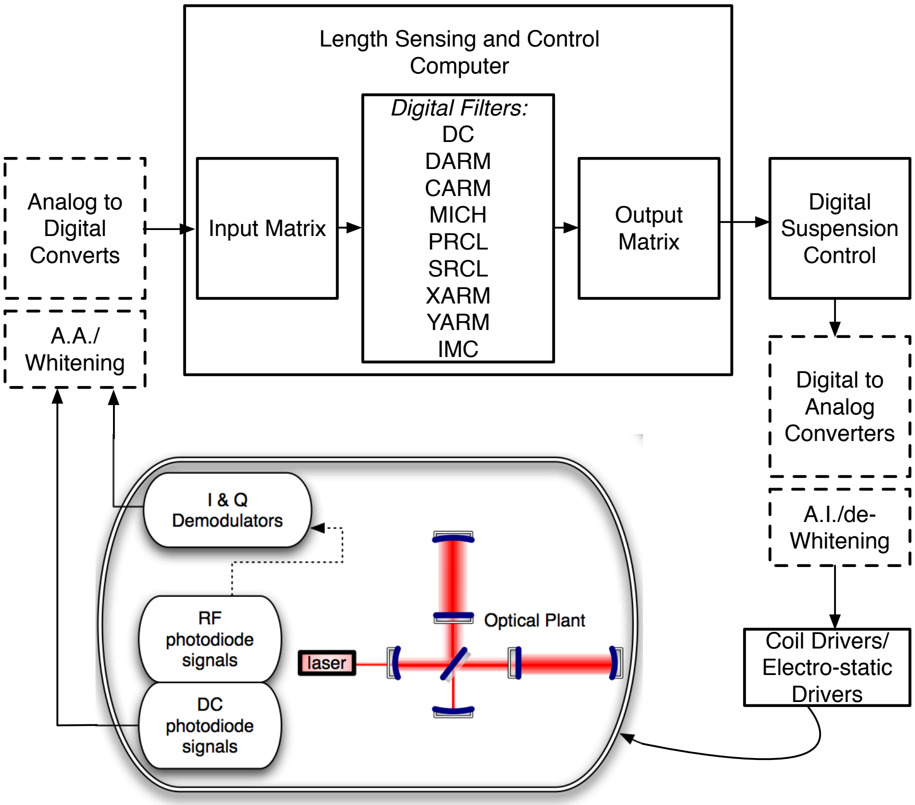

Figure 7.9: Length sensing and control schematic. Image adapted from Ref. [164].

Figure 7.9 shows a schematic for the length sensing and control (LSC) of the interferometer [164]. The signals from both DC and RF photodetectors are processed and converted digitally. The digital signals are then sent into an input matrix, which converts the signals into the length degree of freedom basis. Each degree of freedom has a digital filter. These filters are followed by an output matrix, which converts the signals into the optical basis. These signals are then processed and the optical plant is actuated on accordingly.

The dual-recycled Michelson degrees of freedom, MICH, PRCL, and SRCL, are easily transitioned between the 3f and 1f photodetectors by ramping and adjusting the gain of the LSC input matrix.

As seen in Table 7.4, DARM control undergoes two signal transitions. At 50 pm CARM offset, the 45 MHz Pound-Drever-Hall reflection signal at the anti-symmetric port is in linear range and can substitute for the arm length stabilization differential beat note signal as a less noisy signal. This step is done by ramping the LSC input matrix and adjusting the DARM digital filters. The digital filters are adjusted to increase the DARM UGF from ∼10 Hz to 55 Hz. These digital filters cannot be used for differential mode control during the arm length stabilization because of the broadband noise of the signal and the limited actuation range; the UGF in this configuration is limited. Figure 7.10 compares the digital filters used during the arm length stabilization versus with the 45 MHz anti-symmetric port signal. Meanwhile, when DARM is transitioned from the 45 MHz signal at the antisymmetric port to DC readout, the adjustment is straight forward and just requires a series of digital gain adjustments in the input matrix. The UGF of the loop remains the same, but the signal is much less noisy now and improves the detector sensitivity.

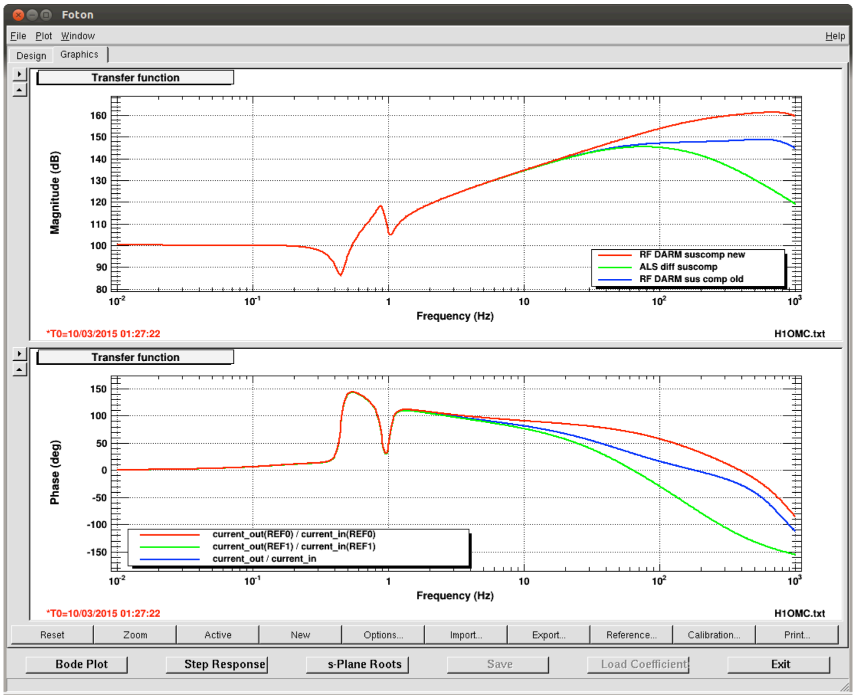

Figure 7.10: The green and red trace compare the digital filters used to control DARM with the arm length stabilization beat note and the 45 MHz RF sideband at the antisymmetric port as a signal, respectively. The filter shape for the latter signal shows a significant gain in phase margin at higher frequency, which allows for an increase in the DARM UGF. The blue trace was an intermediate step that got discarded.

Control of the CARM degree of freedom undergoes several steps as seen in Table 7.3 and is the most complicated transition. Recall that the arm length stabilization scheme controls the common mode by using the common mode phase-locked loop control signal and filtering it with the analog common mode board. The signal from the common mode board then adjust the position of MC2 and the main infrared beam frequency accordingly. At 400 pm CARM offset, the transmitted infrared signals[1] become viable for locking and are more stable than the common mode PLL control signal. The transition is done by blending the error signals [59]. Digital filters are applied to the $\sqrt{TR_X + TR_Y}$ signal to match the shape (i. e. slope and UGF) of the arm length stabilization common mode PLL control signal. This requires calibrating the signals to the same physical measurement of length. More importantly, however, the transmitted infrared signal has a different plant since the optical response includes a couple cavity pole at ~ 40 Hz. This gives the infrared transmitted signal a $1/f^2$ shape compared to the $1/f$ for the arm length stabilization common mode PLL control signal. Adding a zero at the cavity pole frequency removes this affect and provides matching slopes for the two signals (see Figure 7.12). A low frequency boost is added to the infrared transmitted signals so that the blended error signal is dominated by the lower noise signal at low frequency. A pure integrator (pole at 0 Hz) is introduced to ramp the infrared transmitted error signals into the blend. The digitalized output of the infrared transmitted signal is converted into analog and sent to the summing junction of the command mode board. The layout can be found in Figure 7.11. Once the gain of infrared transmitted signal is sufficient, the gain of the ALS error signal can be set to zero and removed from the blend.

At 3 pm CARM offset the normalized 9 MHz RF Pound-Drever-Hall reflection signal becomes available. Using a normalized signal increases the linear range of the signal. This signal is filtered digitally and then summed at the analog common mode board. The digital filters are used to blend the error signals similar to before. This blend is made easier since the 9 MHz reflection signal already has a $1/f$ shape once in the linear range. The last transition from the normalized 9 MHz

---

[1] This signal is first acquired with photodetector. As the CARM offset is reduced, the transmitted signal increases and the in-air PDs eventually saturate. At 150 pm CARM offset the transmitted signal is measured with quadrant photodiodes. The transition only requires a gain calibration.

signal at the reflection port to the analog 9 MHz signal is done by adjusting the analog gains at the summing junction of these two signals.

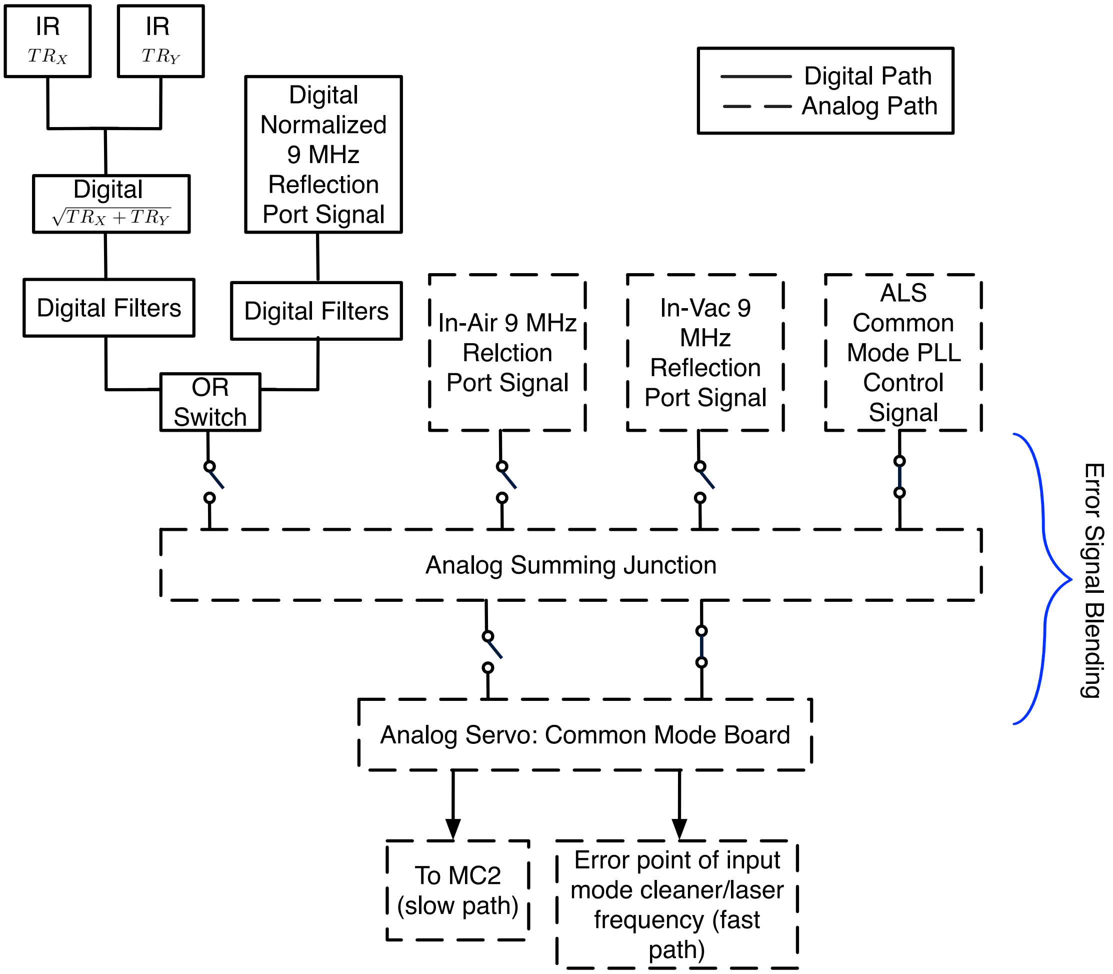

Figure 7.11: The schematic shows the layout of the CARM analog and digital signals. The configuration as drawn shows the arm length stabilization common mode PLL control signal controlling CARM. The switches and gains of the other signals can be adjusted accordingly for the error signal blending during a transition.

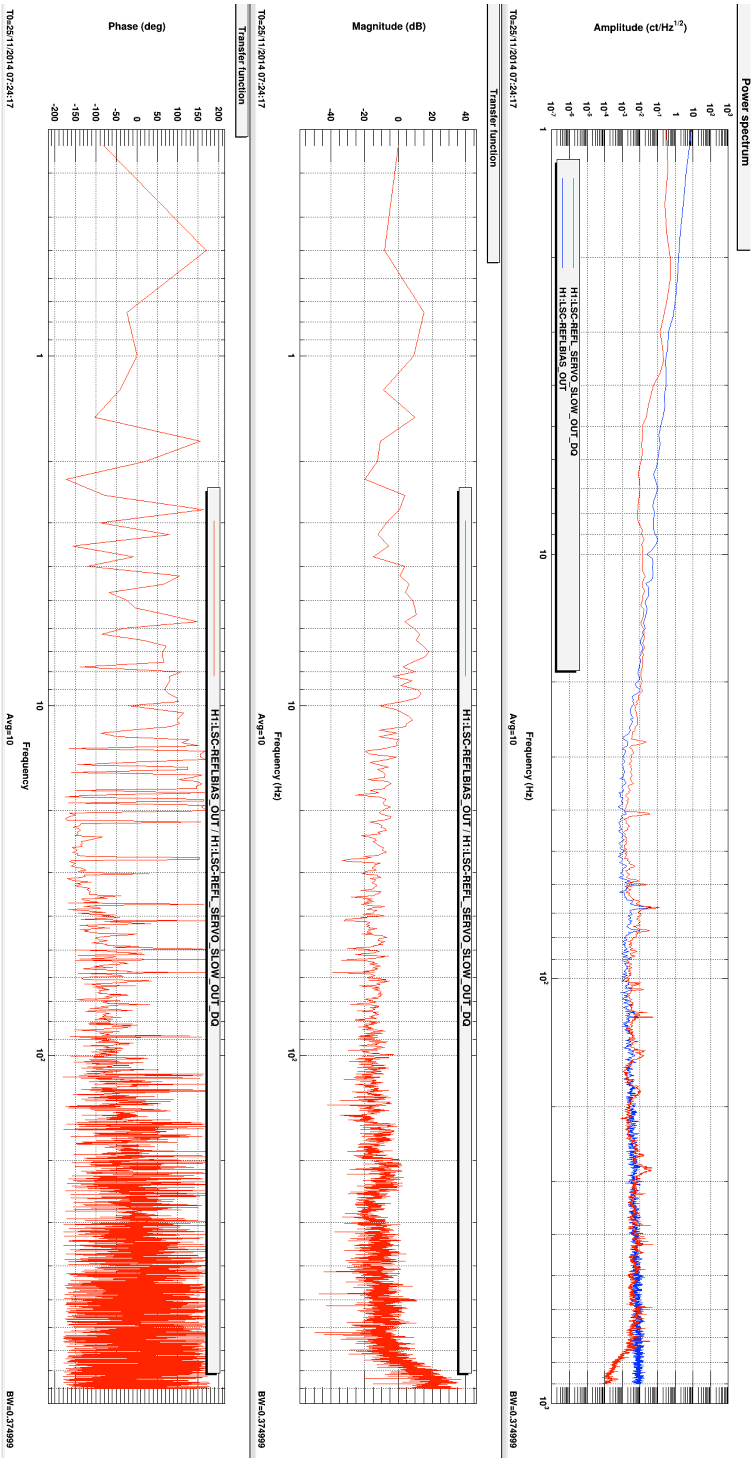

Figure 7.12: The blue and red trace in the top panel shows the power spectrum for the transmitted infrared signal and ALS common mode PLL control signal respectively. The middle and bottom panel are the ratio of the two signals. The magnitude of 0 dB throughout shows that the two signal are equivalent; meanwhile, 0 degree phase indicates the sign of the signals are the same [153]. In such a configuration, the two error signals can be blended together for a transition.

7.4 Duty Cycle

As will be evident in the following chapter, this lock acquisition sequence has proven successful at both observatories. More importantly though, this sequence is repeatable and reliable. The duty cycle of the interferometer will be as essential as the sensitivity of the detector for a gravitational wave detection. Several uncontrollable factors, such as earthquakes, can cause the interferometer to unlock. Therefore, re-locking the interferometer quickly and in a dependable fashion is crucial. The lock sequence prescribed above is fully automated and takes about 20 minutes, usually less, with the arm length stabilization scheme accounting for ≈3 minutes. Figure 7.13 shows several lock and unlocking events. Here, the interferometer was intentionally unlocked, and shows quick successful re-locks. During the June 2015 engineering run, the LIGO Hanford observatory had a 63% duty cycle [62]. Reducing the time of lock acquisition and determining the common causes of lockless will improve this percentage.

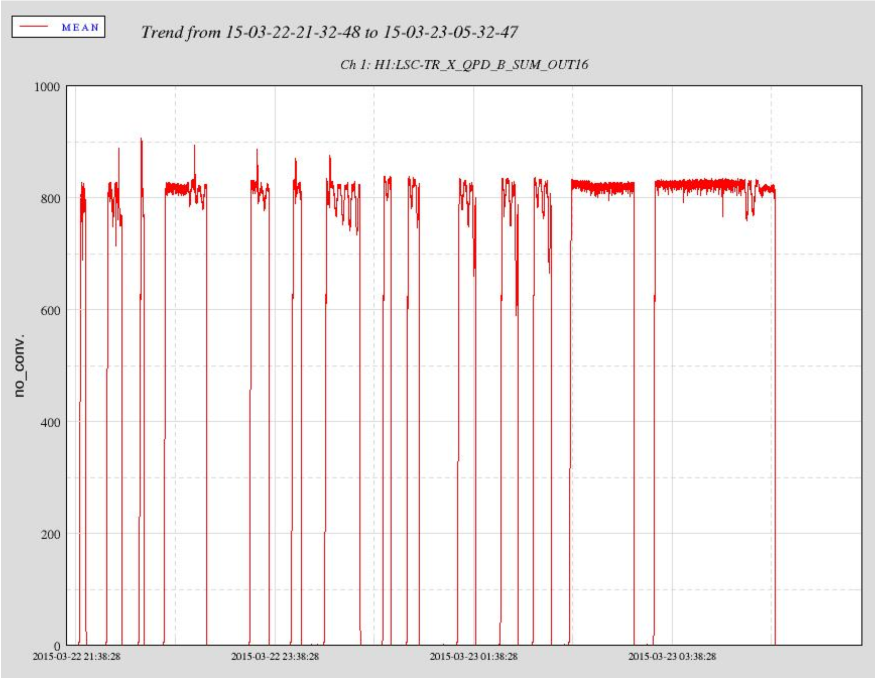

Figure 7.13: This plot shows the transmitted infrared signal of the X-arm as a function a time. The build up of 800 counts indicates that the interferometer is locked. This plot shows the the interferometer (intentionally) unlocked and re-locked several times consecutively.

Chapter 8

Current Status of Advanced LIGO

The installation timeline for the two Advanced LIGO detectors can be seen in Figure 8.1. The installation began at the beginning of 2011 for both detectors, and was finished by the end of 2014. The two observatories had staggered installation schedules, with Livingston completed 6 months before Hanford. This timeline also shows the commissioning progress at the two detectors. The Livingston Observatory started from the corner station and worked outward, while the Hanford Observatory followed the opposite trajectory. This was done to ensure that all of the interferometer's components were studied as soon as possible to catch any major issues.

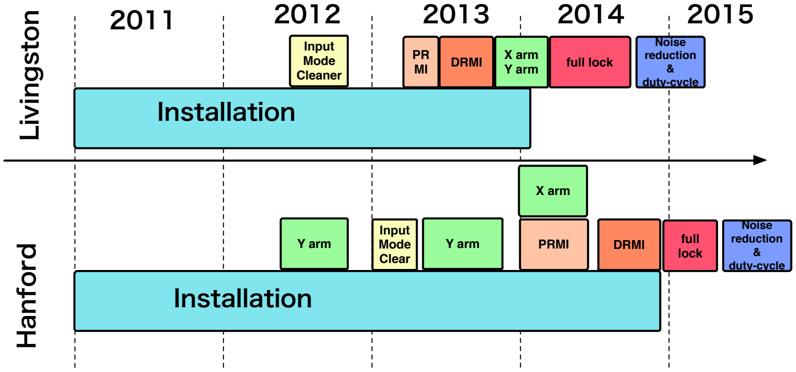

Figure 8.1: Advanced LIGO installation and commissioning timeline from Ref. [89]. Here, PRMI stands for power-recycled Michelson interferometer, while DRMI stands for dual-recycled Michelson interferometer.

The Livingston Observatory achieved first lock on May 26, 2014 and the Hanford Observatory achieved first lock on February 11, 2015. Both interferometers have been locked for several hours at a time, with the longest lock of 30 hours at Livingston. Figure 8.2 shows the BNS range of each detector since their first respective locks.

The Livingston detector has an input power of 25 W with a BNS range of ∼65 Mpc as of April 2015. Meanwhile, the Hanford detector has a input power of 23 W with a BNS range of ∼70 Mpc as of June 2015. These instruments are the most sensitive ground-based interferometer to-date. They span a volume of ∼50 times greater than Initial LIGO. If these detectors had a ∼80% duty cycle with their current sensitivity, we could carry out the 'Initial LIGO one year observing run' in terms of event likelihood in about a week. Under this configuration, the detectors have already reached the criteria for the first observation run, scheduled for the fall of 2015. Figures 8.3, 8.4, and 8.5 depict each of the detectors sensitivity level as of June 2015. Both detectors are making astounding progress.

The sensitivities have a 20%, 50% uncertainty in calibration for L1, H1 respectively. The value at each frequency point of the amplitude spectral density has an amplitude uncertainty. We are 68% confident that the amplitude spectral density lies within 20%, 50% of the quoted value for L1, H1 respectively. Since the inspiral range is calculated from the amplitude spectral density [69], these uncertainties are also true for the inspiral range as well. The uncertainty comes from characterizing the actuation and sensing function of the DARM loop. In order to measure the strain, ΔL must be measured. However, the readout channels are at the error point and control point of the DARM feedback loop. Using loop algebra, the change in length of the two arms can be calculated. However, this requires understanding the sensing and actuation functions, which have some uncertainties. The sensing function measures the interferometers response to differential arm displacement. The uncertainties for this function lies in the DARM couple cavity pole frequency, variation in the optical gain, and sensor electronics. Meanwhile, the actuation function measures the response of the suspension to the requested drive. The uncertainty here lies in the suspension response, actuation delay, and driver electronics. For details refer to Ref. [46].

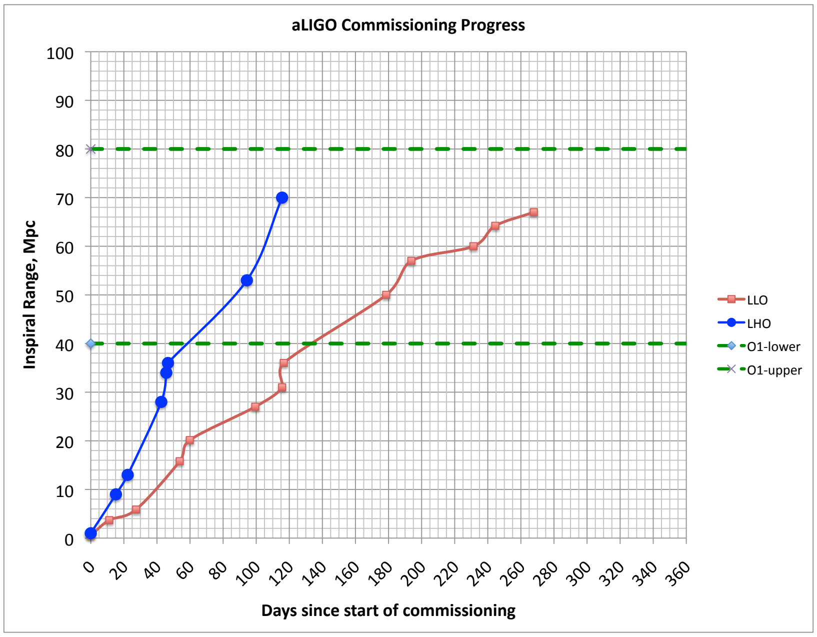

Figure 8.2: This plot depicts the sensitivity of each Advanced LIGO detector in terms of the binary neutron star inspiral range as a function of commissioning time. The commissioning time is marked by the first full lock of each interferometer. Additionally, this graph shows the sensitivity range targeted for the first observation run (O1). O1 is scheduled to take place at about day 200 of the Hanford commissioning. Here, LHO is denoted to represent the LIGO Hanford Observatory and LLO represent the LIGO Livingston Observatory.

The Advanced LIGO detectors have completed installation and have been fully locked. The lock acquisition scheme has proven to be deterministic and reliable at both observatories. Both detector are the most sensitive detectors to-date and already meet the criteria for the first observation run. During the month of June 2015, the Advanced LIGO detectors participated in their first engineering run (known as ER7). The purpose of this run was to have stable and reliable locking of both detectors in a configuration that could be plausible during observation runs, with similar sensitivities. Hardware injections and testing was also done in preparation for the data analysis. Since there was also maintenance during this run, it was not considered an observation run. However, the data collected is the best gravitational wave data measured to-date. Figure 8.5 shows 24 hours of coincidence data taking during ER7.

Over the coming years, the commissioning effort will continue to focus on tuning the sensitivity

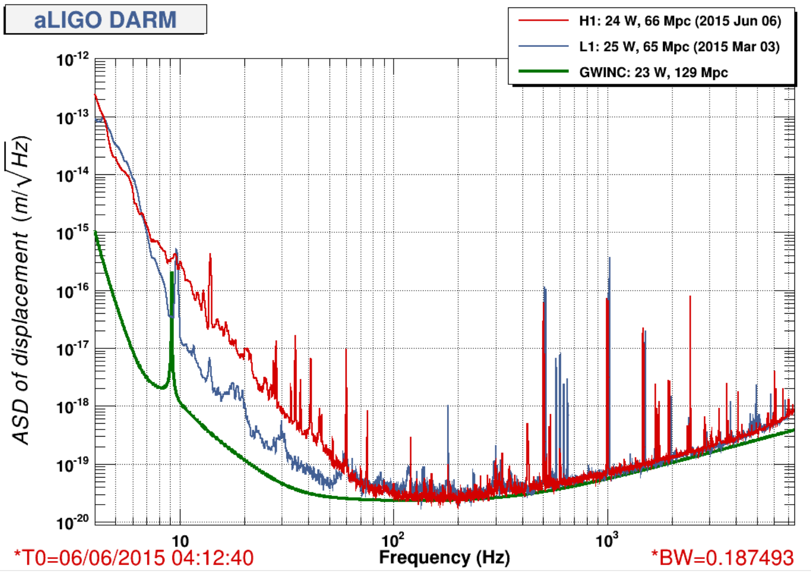

Figure 8.3: This plot shows sensitivity curves for the Hanford (H1) and Livingston (L1) detectors as of June 2015. The quoted inspiral ranges have a 20%, 50% uncertainty for L1, H1 respectively. The GWINC trace is the model sensitivity trace expected for an input power of 23 W.

of each detector. Notably, as the sensitivity improves, commissioning will become more challenging. Foreseen challenges, such as parametric instabilities, have already appeared at the both detectors [66]. Parametric instabilities aries when the higher order optical modes couple and transfer energy to the mechanical modes. The energy is transferred via radiation pressure and can turn into an unstable positive feedback. Currently, at 25 W input power, both detectors have seen a parametric instability at 15 kHz. This mode has been damped with ring heaters which change the radius of curvature of the optic and decouple the modes. As the input power increases, more parametric instabilities will arise, and more damping procedures of the modes will need to be established. Radiation pressure, which provides a torque on the optics, is also expected to play a large role as the input power increases [133]. Extensive research on squeezing light has been done as either an alternative to higher power or to further increase the sensitivity at high frequency [94, 116].

There is a lot of work to be done, but the current status of the detectors is promising. There are exciting observation runs to come!

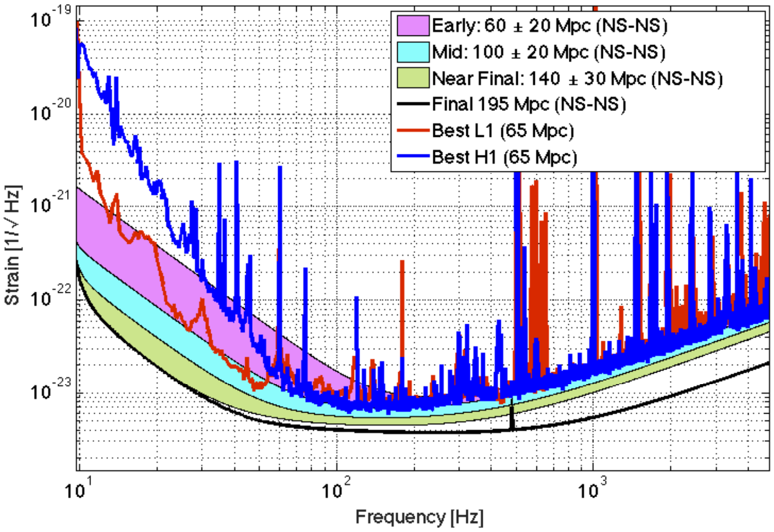

Figure 8.4: This plot shows sensitivity curves for the Hanford (H1) and Livingston (L1) detectors as of June 2015. These sensitivity curves are compared to the design sensitivity goals of the detector over the next few years. The quoted inspiral ranges have a 20% uncertainty for L1 and 50% uncertainty for H1. The data is taken from Refs. [45, 96], and the design traces are from Ref. [38]. The data is slightly different than shown in Figure 8.3; the integration time, calibration, and time stamp all slightly vary.

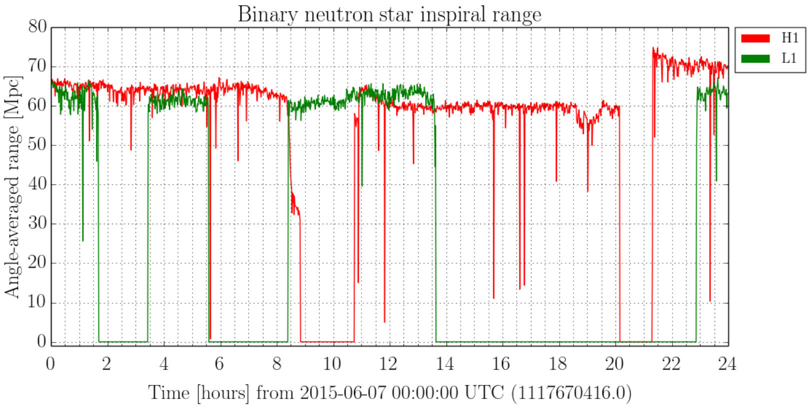

Figure 8.5: This plot shows the BNS inspiral range for the Hanford (H1) and Livingston (L1) detectors on June 7th, 2015 for a span of 24 hours during engineering run 7. The quoted inspiral ranges have a 20%, 50% uncertainty for L1, H1 respectively. The coincidence data taken during this run is the best gravitational wave data taken so far.

Chapter 9

Conclusion

Achieving resonance in the Advanced LIGO detectors is essential for a gravitational wave detection, but is a non-trivial task given the complexity of the instruments. Consequently, a robust and reliable locking sequence had to be developed. The arm length stabilization system is implemented as the first step in the locking sequence following interferometer alignment. The technique is introduced for easier arm locking and to decouple the arm length degrees of freedom from the remaining length degrees of freedom. Given it's importance in the locking sequence, the arm length stabilization method had to be well understood. Primarily, the noise introduced by the system had to be sufficiently low to proceed with locking. Thus, a model of the arm length stabilization scheme, including all of the intertwined feedback loops, was created. In order to utilize the model, the model had to be carefully verified. This was achieved by comparing transfer functions measured and those produced by the model. The model assisted in optimizing the feedback loops implemented. More importantly, the model was used to produce a noise budget. Several noise sources were measured and propagated to the two arm length degrees of freedom. The model showed that the noise of the system was made worse by the unintended low finesse of the arm cavity. With an improvement in the mirror seismic isolation system at low frequency, the noise was reduced sufficiently enough. The other dominant noise sources were also determined. The noise budget showed the the arm length stabilization system was viable and could be used for locking.

After successfully implement the arm length stabilization technique and being confident in its repeatability, the remaining locking steps were commissioned. The three degrees of freedom of the dual-recycled Michelson interferometer have to be controlled, and all the five length degrees of freedom must be transitioned to nominal locking sensors at the proper operating point. Fourteen angular degrees of freedom also have be controlled. These steps have all been automated and take an average of twenty minutes to run.

Currently, the detectors are being tuned for sensitivity. Upon first lock, the detector sensitivity was already comparable to history's best sensitivity, but is expected to improve towards the designed sensitivity goal of $\sim$ 200 Mpc binary inspiral range. As of June 2015, the detectors are at a sensitivity of $\sim 60 - 80$ Mpc. This sensitivity is already a factor of three to four times better than previous generation detectors, and was achieved at an astounding pace (between 120-200 days since first lock). The first observation run is scheduled for the fall of 2015. Following this run, the detectors will be continuously tuned for sensitivity. Albeit, this task will become more challenging as the input power of the interferometer is increased. With improved sensitivity, comes an increased likelihood for a gravitational wave detection. It is an exciting time for gravitational wave astronomy and Advanced LIGO!

Part II

Chapter 10

Double-Demodulation Technique

We use doubly phase modulated light to measure both the length and the linewidth of an optical resonator with high precision [154]. The first modulation is at RF frequencies and is set near a multiple of the free spectral range, whereas the second modulation is at audio frequencies to eliminate offset errors at DC. The light in transmission or in reflection of the optical resonator is demodulated while sweeping the RF frequency over the optical resonance. We derive expressions for the demodulated power in transmission, and show that the zero crossings of the demodulated signal in transmission serve as a precise measure of the cavity linewidth at half maximum intensity. We demonstrate the technique on two resonant cavities, with lengths 16 m and a 4 km, and achieve an absolute length accuracy as low as 70 ppb. The cavity width for the 16 m cavity was determined with an accuracy of approximately 6000 ppm. Through an analysis of the systematic errors we show that this result could be substantially improved with the reduction of technical sources of uncertainty.

10.1 Introduction

A Fabry-Perot cavity near resonance can be used to convert phase modulated laser light into amplitude modulation. If the laser is phase modulated at a single RF frequency using an electro-optic modulator, this effect is proportional to the offset of the carrier frequency from resonance for small deviations. The Pound-Drever-Hall (PDH) technique [58] takes advantage of this to lock the cavity on resonance. However, if the RF sidebands are simultaneously resonant the amplitude modulation vanishes for all frequency offsets. We exploit this property by dithering the laser frequency or cavity length around the resonant point and by sweeping the RF frequency over a resonance near a multiple of the free spectral range. The measured amplitude modulation then shows zero crossings at the multiple of the free spectral range as well as near each half maximum point of the resonance.

The technique was first documented in 1997. A Glasgow group realized that the transmitted RF modulation could be useful to tune the RF frequency such that the sidebands maximally transmit though a mode cleaner [142, 143]. In their method they did not apply a synchronous demodulation, but instead used the amount of the residual amplitude modulation to find the resonant RF frequency.

Further mathematical effort was performed by P. Manson in 1999 [103]. He demonstrated that a small offset in the carrier locking point was necessary to generate the amplitude modula-

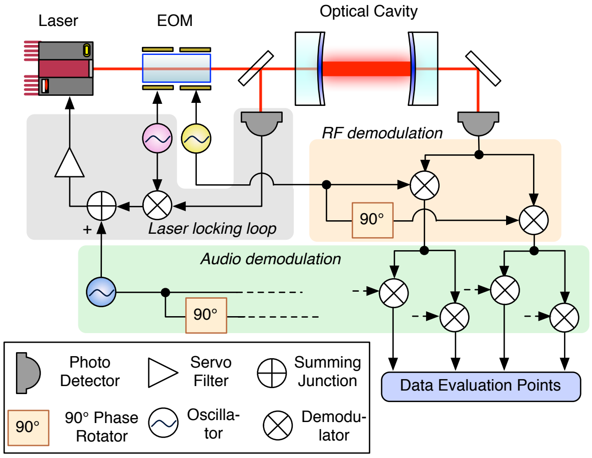

Figure 10.1: Measurement setup. A laser beam is doubly phase modulated using an electro-optic modulator (EOM) and then locked to an optical cavity. The first phase modulation is used for deriving a cavity length signal using the Pound-Drever-Hall reflection locking technique. The second phase modulation is used to generate RF sidebands near a multiple of the full spectral range.

tion in transmission. He also performed an experiment and reported that the residual amplitude modulation would strongly affect the precision of estimating the free-spectral range, but gave no quantitative arguments. In parallel, a novel double-demodulation technique was demonstrated by TAMA in 1999 [34] which introduced dithering of the carrier locking point rather than a static offset. The RF sidebands in reflection were locked on a resonance to track the change in the absolute length of a 300 m suspended cavity.

In recent years, the method has been investigated by a Japanese group [27, 28] and an initial analysis of the uncertainties was performed. Despite these efforts, there has been no application of the method for estimating the cavity linewidth. A related approach was used by an ANU group in 2000 [149], in which the phase information in reflection was used to measure the cavity linewidth by determining the turning points in the response. In 2003, another method using frequency modulated light and tuning of the PDH sideband frequency was used at the LIGO Hanford Observatory to measure the 4 km cavity lengths [126].

In this paper, we demonstrate that the amplitude modulation in transmission can be used as a precise measure of the cavity linewidth, and we exploit the double demodulation of an optical resonator to measure the cavity length and linewidth to high precision. We apply the same double-demodulation technique to measure the cavity length using the reflected signal. The technique uses one modulation frequency at RF and the other at audio frequency; the second modulation at audio frequency is important to increase the accuracy of the measurement by avoiding electronics noise at DC. The audio modulation also reduces the coupling of Residual Amplitude Modulation (RAM) to the measurement. We provide the analytic expression to both transmitted and reflected signals, and a detailed analysis of statistical and systematic uncertainties.

With measurements of the cavity length and linewidth, the round-trip reflectivity and finesse can be calculated. In particular, the cavity finesse can be used to deduce the intra-cavity power build up, the average number of photon round trips in the cavity, and the size of the linear range of the Pound-Drever-Hall reflection locking signal. All of this information is vital to locking and characterizing the Advanced LIGO interferometer. In multi-cavity configurations more than one set of RF modulation sidebands are generally needed for locking. Typically, at least one RF wavelength will be set to a multiple of one of the cavity lengths—requiring an accurate length measurement. Precise measurements of the cavity linewidth is a useful tool to characterize the transmission coefficients and losses of the cavity mirrors. Furthermore, long term monitoring gives insights into mirror degradation due to contamination.

The usefulness of these measurements can be extended outside of Advanced LIGO. As highlighted in Ref. [28], length measurements with small uncertainty are required in the field of nanotechnology and ultra precision engineering. Fabry-Perot interferometers are also used for spectroscopy [30] and laser calibration [134]. Characterization of Fabry-Perot interferometers to high precision has important applications in optical metrology such as mirror characterization and contamination studies.

This paper is organized as follows. The experimental setup is described in Section 10.2 and the equations for the transmitted signal are presented in Section 10.3. Section 10.4 assess the accuracy of the technique for various sources of statistical and systematic error. In Section 10.5 we present the results obtained from applying this measurement on two different-length suspended cavities of the Laser Interferometer Gravitational-wave Observatory (LIGO) [22, 159], where this technique was first used in 2004 by R. Savage, D. Sigg, and M. Rakhmanov. We conclude with a summary of the limiting sources of uncertainty for the technique.

10.2 Setup

The measurement setup is shown in Fig. 10.1. The light of a laser source is modulated by an electro-optic modulator (EOM) at two RF frequencies. The first frequency, at a large offset from the cavity resonance, is used with a photodetector in reflection for locking the cavity with the Pound-Drever-Hall technique. This servo feeds back to the laser to keep its frequency locked on the cavity resonance. The second RF frequency, f_{RF}, is used for generating RF sidebands near a multiple of the free spectral range. This frequency is then swept over the cavity linewidth during the measurement. A third frequency in the audio band, f_a, is used to slightly detune the laser from the cavity resonance by adding a small electronic offset to the laser locking loop. A photodetector in transmission (or reflection) of the cavity is used to complete the measurement. Its output is first demodulated at f_{RF} to form an in-phase and a quadrature-phase down-converted output. The two outputs are acquired by analog-to-digital converters, and digitally demodulated a second time at the audio frequency f_a.

10.3 Theory

The RF modulation is applied at frequency f_{RF} with a phase modulation index Γ. The phase of the laser light can then be written as $\varphi(t) = \Gamma \cos 2\pi f_{\mathrm{RF}}\, t$. A second modulation at audio frequency f_a is applied to the laser frequency with strength δf, i.e., $f(t) = f_0 + \delta f \cos 2\pi f_a t$, where f_0 is the laser carrier frequency. For our measurements we operate in the phase modulation regime and require that $\delta f \ll f_a$. The double demodulated signal in transmission of the cavity can then be written as:

$$\begin{aligned} S_{tr}(\phi_f, \phi_a) = S_{tr}(\phi_f) & \frac{(1-R)\left(e^{i\phi_f} - R\right)}{\left(e^{i\phi_f + i\phi_a} - R\right)\left(e^{i\phi_f} - e^{i\phi_a} R\right)\left(1 - 2R\cos\phi_a + R^2\right)} \\ & \times \begin{cases} \dfrac{e^{2i\phi_a} - 1}{2i\phi_a}\left(e^{i\phi_f}(1-R) - R\,(1 - 2R\cos\phi_a + R)\right) & \text{audio in-phase} \\ \dfrac{\left(e^{i\phi_a} - 1\right)^2}{2\phi_a}\left(e^{i\phi_f}(1+R) + R\,(1 - 2R\cos\phi_a - R)\right) & \text{audio quad-phase} \end{cases} \end{aligned} \tag{10.1}$$

$$\begin{aligned} S_{tr}(\phi_f) = p_0\, g_{tr}^2\, R\, e^{i\phi_f} \frac{1 - e^{i\phi_f}}{(e^{i\phi_f} - R)^2} &= p_0\, g_{tr}^2 \, \frac{-2R}{(1 - 2R\cos\phi_f + R^2)^2} \sin\frac{\phi_f}{2} \\ & \times \left[\sin\frac{\phi_f}{2}\left(1 + 2R - (1 + 2\cos\phi_f)R^2\right) + i\cos\frac{\phi_f}{2}\left(1 - 2R - (1 - 2\cos\phi_f)R^2\right)\right] \end{aligned} \tag{10.2}$$

$$\text{with } p_0 = 2\pi\frac{\delta f}{f_{\mathrm{FSR}}}\Gamma P_{\mathrm{in}},\; g_{tr}^2 = \frac{(1 - r_1^2)(1 - r_2^2)}{(1 - R)^2},\; R = r_1 r_2,\; f_{\mathrm{FSR}} = \frac{c}{2L},$$

$$\phi_a = 2\pi\frac{f_{\mathrm{a}}}{f_{\mathrm{FSR}}} \text{ and } \phi_f = 2\pi\frac{f_{\mathrm{RF}}}{f_{\mathrm{FSR}}}.$$

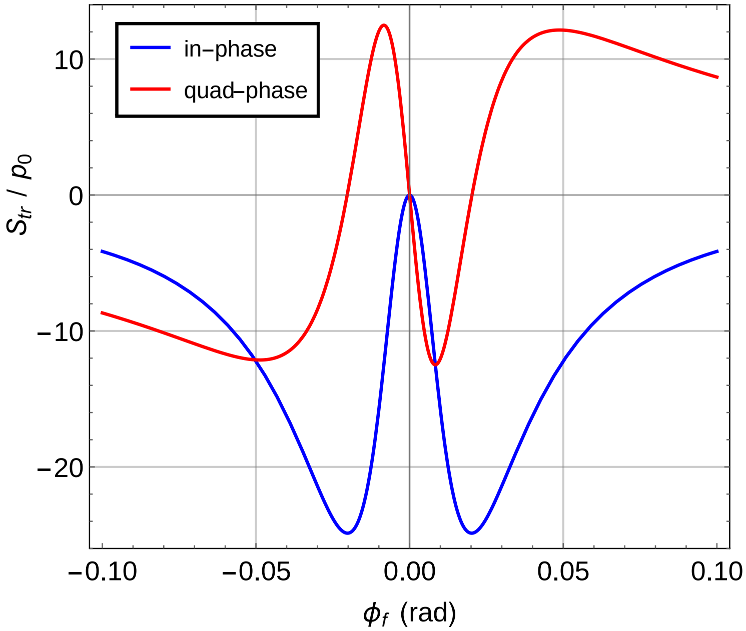

Figure 10.2: Double demodulation signal in transmission of a cavity. Shown are the RF in-phase and quadrature-phase signals assuming the audio modulation frequency is small compared to the cavity linewidth. The finesse of the cavity is $\mathcal{F} = 156$.

The real part describes the RF in-phase signal and the imaginary part the RF quadrature-phase signal. The cavity length is L, P_{in} is the input laser power, and r_1 and r_2 are the amplitude reflectivity coefficients of the input and output mirrors, respectively. If the frequency of the audio modulation is small compared to the cavity linewidth, we can show that

$$\lim_{\phi_a \to 0} S_{tr}^{\text{I}}(\phi_f, \phi_a) = S_{tr}(\phi_f) \text{ and } \lim_{\phi_a \to 0} S_{tr}^{\text{Q}}(\phi_f, \phi_a) = 0$$

for the in-phase and quadrature-phase terms, respectively. The theoretical signal for a cavity with $R = 0.98$ and $\phi_a \to 0$ is shown in Figure 10.2.

Realistic mirrors have $0 < R < 1$ which leads to $1 + 2R - (1 + 2\cos\phi_f)R^2 > 0$ for all ϕ_f. Hence, the in-phase signal is strictly negative with the exception of zeros at $f_0 = nf_{\text{FSR}}$ due to the sine term. This is the only true zero of the doubly demodulated signal S_{tr}. The quadrature-phase signal has additional zeroes: one is located at $f_1 = (n + \frac{1}{2})f_{\text{FSR}}$ and is not interesting. Setting

$1 - 2R - (1 - 2\cos\phi_f)R^2 = 0$, we find two additional zeros at

$$\begin{aligned} f_\pm = \pm\frac{f_{\mathrm{FSR}}}{\pi}\sin^{-1}(\frac{\pi}{2\mathcal{F}\sqrt{R}}) + nf_{\mathrm{FSR}} = \pm\frac{f_{\mathrm{pole}}}{\sqrt{R}} + nf_{\mathrm{FSR}} \\ \text{with } f_{\mathrm{pole}} \approx \frac{f_{\mathrm{FSR}}}{2\mathcal{F}} \text{ and } \mathcal{F} = \frac{\pi\sqrt{R}}{1-R}. \end{aligned} \tag{10.3}$$

where we use $\mathcal{F}$ to denote the finesse of the optical cavity, and where f_{FSR} denotes the free-spectral-range of the cavity. We can see that the difference between the two secondary zero crossing is equal to the cavity linewidth divided by $\sqrt{R}$.

10.4 Analysis and Uncertainties

The FSR can be measured to high precision from the main zero crossing; the measured frequency is simply divided by the order n. The cavity length can then be calculated accordingly.

The two secondary zero crossings of the quadrature-phase signal provide important additional information about the optical cavity. In particular, the expression for $f_\pm$ depends only on the FSR of the cavity and on the round-trip reflectivity R. Thus the measurement of the secondary zero crossings can be inverted using Eqn. 10.3 to obtain a precise measure of the round-trip reflectivity R. This is then used to calculate the cavity finesse and the cavity pole frequency (halfwidth), f_{pole}, which characterizes the dynamical response of the laser field on resonance.

The remainder of this section provides a comprehensive discussion of the measurement uncertainties.

10.4.1 Timing Accuracy

Any systematic offset in the measurement of the RF frequency will directly translate into length errors. The measurement of the cavity linewidth will be immune to static offsets, but a changing relative frequency error will shift the secondary zero crossings. GPS synchronization can be used to stabilize an RF frequency source to the ppb level. For the experimental demonstration, we used a GPS synchronized RF source and verified its accuracy with a frequency counter which was also synchronized to GPS. An accuracy of $< 10^{-7}$ and $< 10^{-8}$ was achieved over $T = 1\,\mathrm{s}$ and $T = 10\,\mathrm{s}$ measurement periods, respectively.

10.4.2 Sensing Noise

Sensing noise will typically be composed of shot noise and electronics noise. Any fixed electronics offsets will be rejected by the use of the audio modulation. For simplicity, we assume that the transmission and reflection photodetectors are shot noise limited. At each free spectral range the transmitted power will be $g_{tr}^2 P_{\mathrm{in}}$. The shot noise is then given by $\sqrt{2 g_{tr}^2 P_{\mathrm{in}} hc/\lambda}$, with λ the laser wavelength.

To calculate the effect of uncertainty from shot noise on the zero crossings, we evaluate the derivatives of Eqn. 10.2 at the zero crossings:

$$\left.\frac{d\,S_{tr}}{d\phi_f}\right|_{\phi_f=0} = -p_0\, g_{tr}^2 \,\frac{R}{(1-R)^2} \approx -\frac{2}{R}\,\left.\frac{d\,S_{tr}}{d\phi_f}\right|_{\phi_f=\phi_\pm}$$

The frequency error due to shot noise can then be written as

$$\Delta f_{\mathrm{RF}}^{\mathrm{shot}} = \frac{(1-R)^2}{R}\sqrt{\frac{2\,hc}{\lambda\, g_{tr}^2 P_{\mathrm{in}}\, T}}\left(\frac{1}{\delta f\,\Gamma}\right)\left(\frac{f_{\mathrm{FSR}}}{2\pi}\right)^2 \tag{10.4}$$

with T the measurement period. At the half maximum points a similar equation can be derived. Since the power at the secondary zero crossings is only half and the slope is roughly half, the frequency error becomes approximately $\sqrt{2}$ smaller.

10.4.3 Audio Modulation Frequency Response

When deriving Eqn. 10.2, we assumed that the audio modulation frequency is small compared to the cavity linewidth. Relaxing this condition will generate a phase shift in the corresponding demodulated signal. This will not affect the cavity length measurement, but it will increase the separation of the zeroes near the half maximum points. The zero crossing of the in-phase audio modulation component can be approximated by

$$f_\pm(\phi_a) = f_\pm\left(1 + \frac{\phi_a^2}{R f_\pm^2}\right).$$

For $R > 0.8$ and $\phi_a < 0.1 f_\pm$ the approximation is better than 150 ppm; and 1 ppm or less for $\phi_a < 0.01 f_\pm$. The exact equation can be used for higher audio frequencies, or when higher accuracy is required.

10.4.4 RF Modulation Phase Variations

RF phase shifts do not affect the zero crossing at the free spectral range, because both in-phase and quadrature-phase terms are simultaneously zero. However, at the half maximum points, the in-phase signal is near maximum and will admix into the quadrature-phase with a demodulation phase error. We distinguish between common and differential RF phase shifts. To first order a common RF phase error will shift the secondary zero crossings in the same direction. Hence, if we calculate the linewidth by taking the difference between the two secondary zero crossings, we are first order insensitive to small common RF phase errors. Differential RF phase errors will directly change the linewidth measurement.

A time delay will produce a common RF phase shift at a fixed frequency. But due to its linear frequency dependency, it will also produce a differential RF phase shift. The latter needs to be taken into account, if the delay is significant relative to the RF signal period. This is certainly true in our case, since the cavity geometry is of the same scale as the RF wavelength. The electro-optic modulator and the RF demodulation electronics can also generate a differential phase shift—especially if they include tuned resonant circuits. Again, this is not a problem for the length determination, but it can easily be the dominant uncertainty in the linewidth measurement. We write the frequency error due to a differential RF phase variation $\Delta\phi_{\mathrm{RF}}$ between the half maximum points as

$$\Delta f_{\mathrm{RF}}^{\mathrm{phase}} \approx (1 - R)\,\Delta\phi_{\mathrm{RF}} \frac{f_{\mathrm{FSR}}}{2\pi} \approx \Delta\phi_{\mathrm{RF}} f_{\mathrm{pole}}. \tag{10.5}$$

10.4.5 Cavity Length Fluctuations

Due to the double demodulation scheme this technique is first order insensitive to any electronics offset, such as offsets in the locking servo amplifier, as well as locking point offsets in the cavity. Length measurements utilizing only a single modulation frequency are not immune to DC offsets in the signal chain, which introduce an error. The addition of the audio frequency modulation behaves as a second lock-in amplifier and nulls this uncertainty. However, both cavity length and laser frequency variations at the audio frequency will appear as statistical uncertainties in the measurement. They can always be minimized by increasing the measurement time.

10.4.6 Higher Order RF Modulation Terms

Aketagawa et al [27] derive an expression for the reflected and transmitted signal with a single RF demodulation including higher-order RF modes. Including higher-order RF terms in Eqn. 10.2 increases the slope of the quadrature-phase signal at the main zero crossing, and shifts the location of the secondary zero crossings inward. Thus the effect of the higher-order RF terms is to improve the accuracy of the length measurement, but to bias the measurement of the linewidth. The bias is proportional to Γ^2, the square of the RF modulation index.

10.4.7 Residual Amplitude Modulation Noise (RAM)

RAM is a significant problem for high precision cavity locking using the Pound-Drever-Hall technique. RAM generated in the electro-optic modulator has been characterized [165, 168] and active suppression schemes have been developed [170]. The technique presented here is intrinsically less sensitive to RAM because of the double demodulation.

We can model the effect of RAM at both RF and audio frequencies as a modulation of the input field to the cavity. If we multiply the input field by the following term,

$$\left(1 + \epsilon\Gamma\cos(2\pi f_{\mathrm{RF}}t - \psi)\right)\left(1 + \eta\frac{\delta f}{2\pi f_a}\sin 2\pi f_a t\right),$$

we get a signal in transmission with terms bilinear in the coefficients ϵ and η:

$$S_{tr}^{\mathrm{AM}}(\phi_f) = -p_0\, g_{tr}^2\, R\, e^{i\phi_f} \frac{1 + e^{i\phi_f} - 2R}{(e^{i\phi_f} - R)^2} e^{i\psi} \epsilon\eta. \tag{10.6}$$

The coefficients ϵ and η describe the fraction of amplitude modulation relative to the RF and audio phase modulation, respectively. Neither a RAM generated by the electro-optic modulator nor the laser has an effect on its own. Furthermore, the RAM generated by the audio modulation of the laser frequency and therefore η can always be suppressed with an intensity stabilization servo system. For the length measurement the signal due to the RAM becomes:

$$S_{tr}^{\mathrm{AM}}(0) = p_0\, g_{tr}^2\, \frac{2R}{1-R} e^{i\psi} \epsilon\eta. \tag{10.7}$$

One can see that the quadrature phase signal is only sensitive to the RF RAM generated in the quadrature-phase. The above equations do not include a RAM generated in the quadrature phase of the frequency modulation. This term will always appear in the quadrature phase of the audio demodulation, but is not important for small audio frequencies.

10.5 Results

We applied the double-demodulation technique to two of the optical cavities in the advanced LIGO Hanford detector. The cavities are the 16 m input mode cleaner, a triangular cavity that suppresses higher order mode content on the input beam and stabilizes the laser frequency, and one of the 4 km Fabry-Perot arm cavities [57, 159].

10.5.1 16 m Cavity

For the input mode cleaner, we used two RF modulation frequencies, one around the free spectral range of 9.1 MHz and a second at five times the free spectral range near 45.5 MHz. We applied three different audio frequency modulations, at 103 Hz, 303 Hz, and 1 kHz. The variety of RF and audio modulation frequencies was used to check our sensitivity to particular elements of the readout chain and to estimate some of our systematic uncertainties.

The setup is as described in Section 10.2, where the light source is the main 1064 nm laser of the interferometer, and the photodetector for the double-demodulation is in transmission. The RF frequency was scanned across a range slightly larger than the cavity linewidth. In our setup the audio frequency was not negligible compared to the cavity linewidth. It also included an unknown optical delay. Since both of these parameters have a small effect on the position of the secondary zero crossings, we account for this by fitting Eq. (10.1) to the data using a seven-parameter non-linear least-squares fit. The seven parameters included an overall amplitude coefficient, A, the free spectral range of the cavity, f_{FSR}, and the round-trip reflectivity of the mirrors, R. Two other parameters, f_{EOM} and Q, were used to characterize the response of the resonant circuit in the EOM used to generate the RF sidebands. The effect of this circuit was to change the phase and amplitude response of the system as a function of frequency; the fit treated the circuit response as a Lorentzian function with central frequency, f_{EOM}, and width, f_{EOM}/Q. The fit results for these parameters were in good agreement with independent measurements of the EOM response. Finally, two additional parameters, θ_0 and ϕ_0, were used to account for static phase delays between the modulation and demodulation of the RF and audio sidebands, respectively. Overall, the seven fit parameters were found to be consistent across the six data sets consisting of two RF frequencies with three audio frequencies each.

Parameter	Fit result	Stat. Uncertainty
f_{FSR} (Hz)	9100235.6	±2.8
R	0.9939317	±0.0000026

Table 10.1: Results from the fit of Eqn. 10.1 to the data of the 16 m input mode cleaner cavity.

Data for the 1 kHz modulation for the input mode cleaner is presented in Fig. 10.3, along with fit lines and residuals. We estimate our 67% confidence level uncertainties using the statistical errors

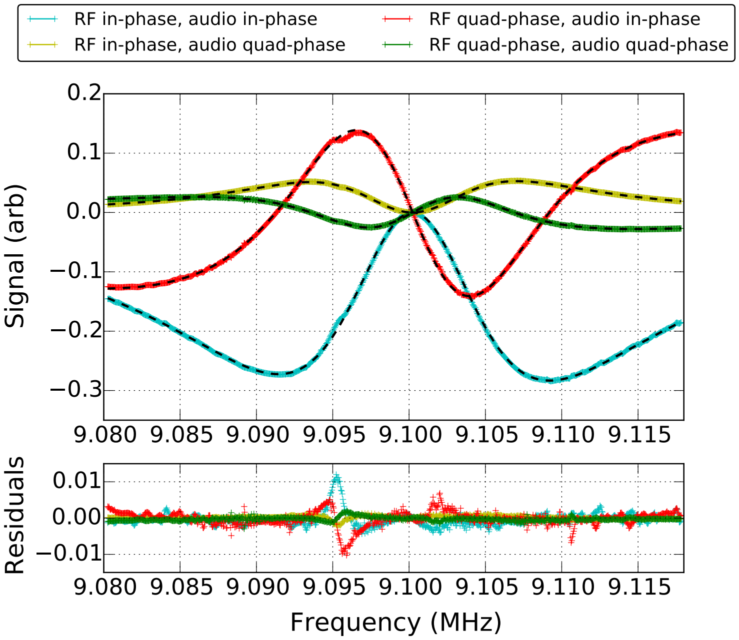

Figure 10.3: The black dashed traces represent the fit of Eqn. 10.1 to the double-demodulated data for a 16 m cavity. For this data, the audio modulation frequency was 1 kHz, and the RF modulation frequency was scanned from 9.08 to 9.12 MHz. The deviation from the model around 9.095 MHz is due to an unknown feature in the signal path. Masking out the data in a 5 kHz band around this feature does not change the results of the parameter estimation.

derived from the nonlinear fit to the data, as well as the variation in the fit parameters across data sets and across permutations of data selection and downsampling. The results of the fit for the important physical parameters along with their 67% statistical uncertainties are presented in Table 10.1. Following Eqn. 10.3, the cavity length and linewidth are calculated using the measured FSR and round-trip reflectivity. For each of these parameters, results from the six data sets are combined using a straight-forward χ^2 estimation. These final results are given in Table 10.2 along with their statistical uncertainty.

10.5.2 4 km Cavity

The length of a single 4 km arm cavity was also measured with the double-demodulation technique, albeit with some slight modifications in the setup. Instead of using the interferometer's main infrared beam as the light source, as used for the input mode cleaner measurement, we used an auxiliary green laser that is nominally used to lock the arm cavities separately [155]. Additionally, the double-demodulation signal was measured in reflection, instead of in transmission. The expression for the signal in reflection can be found in Section 10.8.

As before, we applied the three audio modulation frequencies at 103 Hz, 303 Hz, and 1 kHz. Applying a linear fit to the quadrature-phase signal near the main zero crossing, the length of the cavity was measured to sub-millimeter precision. The cavity pole was not measured, since the linewidth is around 2.9 kHz and of little relevance. The results are listed in Table 10.2.

For the 4 km cavity, our accuracy was limited by reduced finesse due to a manufacturing error in the reflectivity of the input mirror. However, we used an RF modulation frequency of 24.9 MHz, or approximately 666 times the free spectral range of the arm cavity; this in turn greatly enhanced our accuracy. Overall, the relative accuracy of the 4 km cavity length measurement was approximately a factor of four better than the measurement of the 16 m cavity.

Cavity	Parameter	Result	Stat. Uncertainty
16 m	f_{pole} (Hz)	8806	±10
	L (m)	16.471701	±0.000003
4 km	$N \times f_{\text{FSR}}$ (Hz)	24992279	±1
	L (m)	3994.4692	±0.0002

Table 10.2: The top rows show the derived length and cavity pole from the fit for the 16 m cavity. The bottom rows show the free spectral range and exact length for the 4 km cavity, here $N = 666$. The statistical uncertainties from fitting the data are presented. The systematic errors are discussed is Section 10.5.3.

10.5.3 Uncertainties

In this section we provide details of the estimation of our systematic uncertainties which were discussed in Section 10.4. Sensor noise such as shot noise is already included in the uncertainties derived from the fit, since it has a statistical behavior. It is also rather small and contributing only at the level of ±0.01 Hz or less to each measurement point. Since we fit the complete expression given by Eqn. 10.1, we do not account for the approximation of the audio modulation frequency response. The laser locking loop which controlled the laser frequency had high gain, and the residual cavity length fluctuations were too small to be of importance. We are left with the systematic uncertainties due to the accuracy of the frequency determination, variations of the RF modulation phase, the residual amplitude modulation, and the influence of higher order harmonics in the RF modulation. For each of these uncertainties, we calculate quantitative values using the expressions derived in Section 10.4. The results are summarized in Table 10.3, expressed as frequency shifts to the relevant zero crossings of the doubly-demodulated signal.

Sys. Uncertainty (Hz)	16 m Cavity		4 km Cavity
	Length	f_{pole}	Length
Absolute Timing	1	0	1
RAM	$\ll$0.001	$\ll$0.001	$\ll$0.001
RF Modulation Phase	0	48	0
RF Harmonics	0	4	0
Total	±1	±52	±1

Table 10.3: Estimated systematic errors in Hertz to the measured frequencies of the main zero crossing (length) and difference between the secondary zero crossings divided by two (used for the cavity pole). The frequency errors are split among the length and linewidth measurements for the 16 m cavity; the linewidth was not measured for the 4 km cavity. These systematic uncertainties are estimated with a 67% confidence level.

At the time of the measurement the frequency counter was calibrated to ±1 Hz absolute. This directly translates into a systematic uncertainty in determining the frequency of the main zero crossing. With our RF frequencies of 9.1 MHz, 45.5 MHz and 24.9 MHz this corresponds to a relative error of 100 ppb, 20 ppb and 40 ppb, respectively. The timing error for the width measurement is negligible, since we are computing the difference between the two secondary zero crossings.

The frequency error from the RAM, $S_{tr}^{RAM}(0)$, can be approximated by $\Delta f^{\text{RAM}} \approx \eta\epsilon f_{\text{pole}} \sin\psi$.

Assuming the worst case scenario, with all the RAM in the quadrature phase, we set $\psi = \pi/2$. We measured $\epsilon \lesssim 10^{-3}$ for the RF modulation and $\eta \lesssim 10^{-5}$ for the audio frequency modulation. The frequency error due to RAM for the width measurement is significantly smaller still. The audio modulation and the small value of η is crucial to make the effect of the RAM insignificant in our measurement.

With these systematic uncertainties, the results for the lengths of the two cavities are:

$$L = 16.471701\,\mathrm{m} \pm 3\mu\mathrm{m}\,(\mathrm{stat}) \pm 1\mu\mathrm{m}\,(\mathrm{sys})$$

and

$$L = 3994.4692\,\mathrm{m} \pm 0.2\mathrm{mm}\,(\mathrm{stat}) \pm 0.2\mathrm{mm}\,(\mathrm{sys}).$$

The model for our fit to the 16 m cavity includes a resonance to account for the tuned circuit of the EOM used to generated the RF sidebands. To investigate our systematics we also used models with linear RF phase and different amplitude terms. The amplitude terms were linear, quadratic, and linear with quadratic. The resulting measurements of f_{pole} varied over a total range of about 100 Hz. For our final result of the cavity pole measurement we take the average and include the standard deviation as a systematic error; in this way we account for the uncertainty of the RF modulation phase.

The higher order RF modulation terms will improve the length measurement, but worsen the linewidth [27]. The modulation depth for the 9.1 MHz and 45.5 MHz modulation frequencies was $\Gamma = 0.20$ and $\Gamma = 0.28$, respectively. Following Section 10.7 and 10.8, and comparing to equations 9 and 10 of [27], one can extrapolate to the higher-order mode equation for the double-demodulation. Terms of the form $S_{tr}(\phi_f) + \frac{\Gamma^2}{8} S_{tr}(2\phi_f)$ appear in the expression. The secondary zero-crossings used to determine the cavity pole are shifted with the presence of higher order RF modulation terms. Using numerical methods we find a reduction by 42 Hz and 82 Hz of the linewidth for the two modulation frequencies, respectively. Assuming a 10% uncertainty in the modulation depth the uncertainty of this correction to the cavity pole frequency is no larger than 4 Hz.

Including the uncertainty arising from the RF modulation phase and the correction from the RF harmonics, the final result for the cavity pole becomes:

$$f_{\mathrm{pole}} = 8804\,\mathrm{Hz} \pm 10\,\mathrm{Hz}\ (\mathrm{stat}) \pm 52\,\mathrm{Hz}\ (\mathrm{sys}).$$

10.6 Conclusions

We have presented a precision measurement technique for the characterization of resonant optical cavities. We have demonstrated this technique on two cavities of the LIGO Hanford gravitational-wave detector, and measured the cavity length to a precision as low as 70 ppb and the width to approximately 6000 ppm.

Our length measurement for the 16 m cavity can probably only be improved by using a substantially higher modulation frequency. At 500 MHz one should be able to achieve sub micron precision. Our measurement of the 4 km cavity length was substantially limited by the poor signal-to-noise due to low finesse. Fixing the coating error will improve the signal in reflection by at least two orders of magnitude (see Section 10.8). There is no fundamental limit which would prevent us from improving our timing accuracy by the same amount. This could potentially lead to a cavity length determination below the 1 ppb level. This is well below the length changes introduced by tidal forces which are of order 200 μm and even below the $\sim$5 μm motion of the free swinging test masses.

For our width measurement the largest error is due to the use of a tuned EOM. By using an EOM with flat frequency response and by reducing the modulation depth one could reduce the systematic error below the statistical one, and achieve an accuracy better than 1000 ppm.

10.7 Audio Frequency Expansion

In this Section we provide details of the derivation of Eqn. 10.1. We begin with a simplified scenario without the audio modulation. Instead, we shift the laser frequency away from resonance by a small fixed offset, δf. We write the laser frequency as $f_0 = N f_{\mathrm{FSR}} + \delta f$. Recall, the transmitted electric field is given by,

$$E_t = t(\phi) E_{inc}$$

where the transmission coefficient is defined below and can be expressed in our notation:

$$t(\phi) = \frac{t_1 t_2}{1 - r_1 r_2 e^{i\phi}} = \frac{g_t(1-R)}{1 - Re^{i\phi}}. \tag{10.8}$$

If we then apply a phase modulation at an RF frequency, f_{RF}, the incident electric field is expressed as

$$E_{inc} = E_0 e^{iN\omega_{\mathrm{FSR}}t} e^{i\delta\omega t} e^{i\Gamma\cos\omega_{\mathrm{RF}}t}.$$

where we switched to a more concise notation using $\omega = 2\pi f$.

Using the Jacobi-Anger expression, the transmitted electric field, expressed in terms of Bessel functions of the first kind, is then

$$E_t = E_0 e^{i\omega_0 t}\left\{ J_0(\Gamma) t(\phi_c) + iJ_1(\Gamma) t(\phi^{sb}_{up}) e^{i\omega_{\mathrm{RF}}t} + iJ_1(\Gamma) t(\phi^{sb}_{low}) e^{-i\omega_{\mathrm{RF}}t} \right\}$$

where

$$\begin{aligned} \phi_c &= \frac{\delta\omega}{f_{\mathrm{FSR}}} \\ \phi^{\mathrm{sb}}_{\mathrm{up,low}} &= \frac{\pm\omega_{\mathrm{RF}} + \delta\omega}{f_{\mathrm{FSR}}} = \pm\phi_f + \phi_c. \end{aligned} \tag{10.9}$$

The transmitted signal is mixed with a local oscillator of the same RF frequency, and low passed, so that we can extract the terms in the power that oscillate with f_{RF}. The demodulated

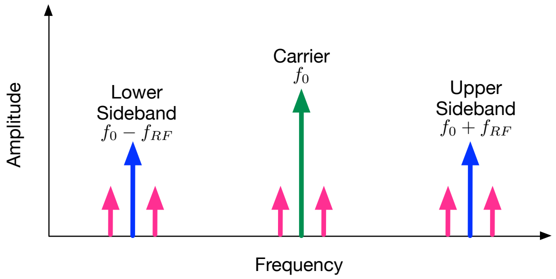

Figure 10.4: The green arrow represents the laser frequency, which has an offset δf from the locking point. The RF sidebands produced by the first phase modulation are depicted by the blue arrows. An additional modulation at audio frequencies f_a produces four audio sidebands as seen by the pink arrows. In this case $\delta f \ll f_a$. The plotted amplitudes are arbitrary and depend on the modulation depths.

signal at the photodetector is then given by,

$$\begin{aligned} P_t^{\mathrm{RF}} = & 2J_0(\Gamma)J_1(\Gamma)P_{\mathrm{in}}\times \\ & \Big\{\mathrm{Im}\left[t(\phi_c)t^*(\phi_{\mathrm{low}}^{\mathrm{sb}}) - t^*(\phi_c)t(\phi_{\mathrm{up}}^{\mathrm{sb}})\right]\cos(\omega_{\mathrm{RF}}t) \\ & +\mathrm{Re}\left[t(\phi_c)t^*(\phi_{\mathrm{low}}^{\mathrm{sb}}) - t^*(\phi_c)t(\phi_{\mathrm{up}}^{\mathrm{sb}})\right]\sin(\omega_{\mathrm{RF}}t)\Big\} \end{aligned} \tag{10.10}$$

where the cosine term corresponds to the in-phase signal and the sine term is the quadrature phase signal. Notice, that without the frequency offset δf, Eqn 10.10 is zero. When the carrier is resonant, $f_0 = N * f_{\mathrm{FSR}}$, then $t^*(\phi_c) = t(\phi_c)$ and $t(\phi_{\mathrm{sb}}) = t(-\phi_{\mathrm{sb}})$. In this configuration the I, Q signals are zero. When the RF sidebands are on resonance $\phi_{\mathrm{RF}} = N * \phi_{\mathrm{FSR}}$, then $t(\pm\phi_{\mathrm{RF}}) = t(\phi_c)$ and again the signals are null. However, with a frequency offset, when the carrier and RF sidebands are both slightly off resonance, the signals are non-zero. These conditions produce the I, Q signals seen in Figure 10.2.

Using Eqns 10.8 and 10.9, along with the following approximations,

$$J_0(\Gamma) \approx 1, \qquad J_1(\Gamma) \approx \Gamma/2, \qquad e^{i\phi_c} \approx 1 + i\phi_c$$

one arrives at Eqn 10.2.

To get the full expression in Eqn 10.1, a similar derivation is done including the second modulation at the audio frequency, f_a. The incident electric field becomes,

$$E_{inc} = E_0 e^{iN\omega_\mathrm{FSR}t} e^{i\delta\omega/\omega_\mathrm{a}\sin\omega_\mathrm{a}t} e^{i\Gamma\cos\omega_\mathrm{RF}t}.$$

The transmitted electric field is now,

$$E_t = E_0 e^{i\omega_0 t} \times \left[J_0(\Gamma)F(\phi_c) + iJ_1(\Gamma)F(\phi^\mathrm{sb}_\mathrm{low})e^{-i\omega_\mathrm{RF}t} + iJ_1(\Gamma)F(\phi^\mathrm{sb}_\mathrm{up})e^{i\omega_\mathrm{RF}t}\right],$$
$$F(\phi) = J_0(\delta\omega/\omega_\mathrm{a})t(\phi) + J_1(\delta\omega/\omega_\mathrm{a})t(\phi+\phi_\mathrm{a})e^{i\omega_\mathrm{a}t} - J_1(\delta\omega/\omega_\mathrm{a})t(\phi-\phi_\mathrm{a})e^{-i\omega_\mathrm{a}t}$$

such that it describes the carrier field and all the modulated sidebands as depicted in Fig 10.4. The derivation to Eqn 10.1 follows as before.

10.8 Signals in Reflection

The equation in reflection follows a similar derivation, with the transmission coefficient $t(\theta)$ replaced everywhere with the reflection coefficient:

$$r(\theta) = -r_1 + \frac{t_1^2 r_2 e^{-i\phi}}{1 - r_1 r_2 e^{-i\phi}} \tag{10.11}$$

The signal in reflection of the cavity can be written as

$$
\begin{aligned}
S_{\text{refl}}(\phi_f,\phi_a) = S_{\text{refl}}(\phi_f)\,&\frac{e^{i\phi_a}\,(1-R)\left(e^{i\phi_f}-R\right)}{\left(e^{i\phi_f+i\phi_a}-R\right)\left(e^{i\phi_f}-Re^{i\phi_a}\right)(1-2R\cos\phi_a+R^2)\left(e^{i\phi_f}-r_2^2\right)} \qquad (10.12)\\
\times &\left\{\begin{array}{l}
\dfrac{\sin\phi_a}{\phi_a}\left[\left(e^{2i\phi_f}+Rr_2^2\right)(1-R)-e^{i\phi_f}\left((1+R)\left(R-r_2^2\right)-2\cos\phi_a\left(R^2-r_2^2\right)\right)\right]\\
\dfrac{(\cos\phi_a-1)}{\phi_a}\left[\left(e^{2i\phi_f}+Rr_2^2\right)(1+R)+e^{i\phi_f}\left((1-R)\left(R-r_2^2\right)-2\cos\phi_a\left(R^2+r_2^2\right)\right)\right]
\end{array}\right.\\
S_{\text{refl}}(\phi_f) = p_0\,g_{\text{refl}}^2\,R\,&\frac{\left(1-e^{i\phi_f}\right)\left(r_2^2-e^{i\phi_f}\right)}{(e^{i\phi_f}-R)^2} = p_0\,g_{\text{refl}}^2\,\frac{-2R}{\left(1-2R\cos\phi_f+R^2\right)^2}\sin\frac{\phi_f}{2}\\
&\times\left[\sin\frac{\phi_f}{2}\left(1+2R-(1+2\cos\phi_f)\left(R^2+r_2^2\right)+Rr_2^2\,(2+R)\right)\right.\\
&\left.\quad+\,i\cos\frac{\phi_f}{2}\left(1-2R-(1-2\cos\phi_f)\left(R^2-r_2^2\right)+Rr_2^2\,(2-R)\right)\right] \qquad (10.13)
\end{aligned}
$$

with $g_{\text{refl}}^2 = -\frac{1-r_1^2}{(1-R)^2}$, the first case of Eqn. (10.12) is the audio in-phase, and the second case is the audio quad-phase. If the frequency of the audio modulation is small compared to the cavity linewidth, we can show that

$$
\lim_{\phi_a\to 0} S_{\text{refl}}^{\text{I}}(\phi_f,\phi_a) = S_{\text{refl}}(\phi_f) \quad \text{and} \quad \lim_{\phi_a\to 0} S_{\text{refl}}^{\text{Q}}(\phi_f,\phi_a) = 0.
$$

for the in-phase and quadrature-phase terms, respectively. The theoretical signals for two cavities with $R = 0.98$ and $\phi_a \to 0$ are shown in Figure 10.5. One of the cavities has equal transmission mirrors, whereas the other has a high reflector as the rear mirror. In the first case, the only interesting zeroes are at the origin, and there are no secondary zero crossing near the cavity pole. Hence, the signals in reflection are less suitable to determine the finesse of the resonator. In the second case, an additional pair of zeroes appears in the in-phase signal. We can show that these secondary zeroes require $r_2^2 \geq (1+3R)/(3+R)$. The solutions then become:

$$
\begin{aligned}
f_\pm &= \pm\frac{f_{\mathrm{FSR}}}{\pi}\sin^{-1}\left(\frac{\pi}{2\mathcal{F}}\sqrt{\frac{R(Rr_2^2+3r_2^2-3R-1)}{(1-R)(R^2+r_2^2)}}\right) \\
&\to \pm\frac{f_{\mathrm{FSR}}}{\pi}\sin^{-1}\left(\frac{\pi}{2\mathcal{F}}\sqrt{\frac{2r_1}{1+r_1^2}}\right) \qquad \text{for } r_2 \to 1
\end{aligned}
$$

The derivative at the zero crossing of the quadrature phase signal is:

$$
\left.\frac{d\,S_{\mathrm{refl}}}{d\phi_f}\right|_{\phi_f=0} = -p_0\, g_{\mathrm{refl}}^2\, \frac{R\left(1-r_2^2\right)}{\left(1-R\right)^2} = -\left.\frac{d\,S_{tr}}{d\phi_f}\right|_{\phi_f=0}
$$

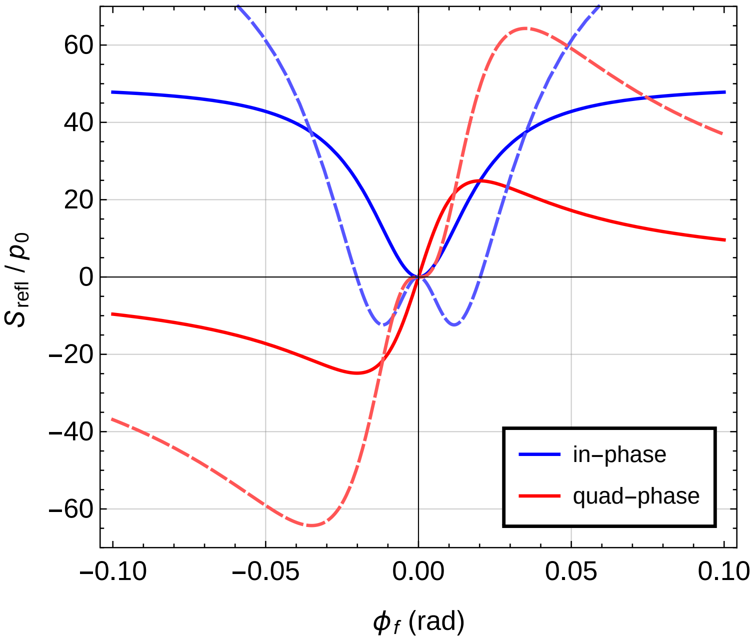

Figure 10.5: Double demodulation signal in reflection of a cavity. Shown are the RF in-phase and quadrature-phase signals assuming the audio modulation frequency is small compared to the cavity linewidth. The solid curve represent a cavity with equal transmission front and rear mirrors, whereas the dashed lines represent a cavity with a high reflector as the rear mirror. In both cases the finesse is $\mathcal{F} = 156$.

Part III

Bibliography

Bibliography

[1] A comprehensive overview of Advanced LIGO. `https://www.advancedligo.mit.edu/summary.html`.

[2] Current schedule LHO. Technical Report LIGO-G1000061, LIGO DCC.

[3] Initial alignment of H1. `https://lhocds.ligo-_wa.caltech.edu/wiki/InitialAlignment`.

[4] Introduction to Bode plot. `http://www.ece.utah.edu/~ee3110/bodeplot.pdf`.

[5] LSC RFPD enclosure—in air—top assembly drawing. Technical Report LIGO-D1101174-v5, LIGO DCC.

[6] Suspension foton files SusSvn. `https://daqsvn.ligo-_la.caltech.edu/websvn/`.

[7] *Interferometric Gravitational Wave Detectors*, Proceedings of the Twelth Internation Conference on General Relativity and Gravitation, 1990. Cambridge University Press.

[8] Voltage controlled oscillator surface mount model: MFC91119-10. Technical report, Synergy Microwave Corporation, 201 McLean Boulevard, Paterson, New Jersey 07504, 2008.

[9] `http://cqgplus.com/2014/12/03/achieving-_resonance-_in-_the-_advanced-_ligo-_gravitational-_wave-_interferometer/`, December 2014.

[10] J. Aasi et al. Search for long-lived gravitational-wave transients coincident with long gamma-ray burts. *Physical Review D*, 88(12):122004, December 2013.

[11] J. Abadie et al. Predictions for the rates of compact binary coalescences observable by ground-based gravitational-wave detectors. *Classical and Quantum Gravity*, 27(17):173001, April 2010.

[12] J. Abadie et al. Search for gravitational waves from binary black hole inspiral, merger, and ringdown. *Physical Review D*, 83(12):122005, June 2011.

[13] J. Abadie et al. Search for gravitational waves from low mass compact binary coalescence in LIGO's sixth science run and Virgo's science runs 2 and 3. *Physical Review D*, 85(8):082002, April 2012.

[14] B. Abbott et al. Detector description and performance for the first coincidence observations between LIGO and GEO. *Nuclear Instruments and Methods A*, 517(1-3):154–179, January 2004.

[15] B. Abbott et al. Search for gravitational waves from galactic and extra-galactic binary neutron stars. *Physical Review D*, 72(8):082001, October 2005.

[16] B. Abbott et al. Beating the spin-down limit on gravitational wave emission from the crab pulsar. *The Astrophysical Journal Letters*, 683(1):L45, 2008.

[17] B. Abbott et al. Beating the spin-down limit on gravitational wave emission from the Crab pulsar. *Astrophysical Journal Letters*, 683(1):L45–L49, August 2008.

[18] B. Abbott et al. LIGO: the Laser Interferometer Gravitational-wave Observatory. *Reports on Progress in Physics*, 72(7):076901, July 2009.

[19] B. Abbott et al. An upper limit on the stochastic gravitational-wave background of cosmological origin. *Nature*, 460(7258):990–994, August 2009.

[20] B. P. Abbott et al. *LIGO: the laser interferometer gravitational-wave observatory*, volume 72. IOP Publishing, 2009.

[21] R. Abbott, R. Adhikari, S. Ballmer, L. Barsotti, M. Evans, P. Fritschel, V. Frolov, G. Mueller, B. Slagmolen, and S. Waldman. Advanced LIGO length sensing and control final design. Technical Report LIGO-T1000298, LIGO DCC, June 2010.

[22] A. Abramovici et al. LIGO: the Laser Interferometer Gravitational-wave Observatory. *Science*, 256(5055):325–333, April 1992.

[23] F. Acernese et al. The variable finesse locking technique. *Classical and Quantum Gravity*, 23(8):S85–S89, March 2006.

[24] F. Acernese et al. Lock acquisition of the Virgo gravitational wave detector. *Astroparticle Physics*, 30(1):29–38, August 2008.

[25] P. A. R. Ade, R. W. Aikin, D. Barkats, S. J. Benton, C. A. Bischoff, J. J. Bock, J. A. Brevik, I. Buder, E. Bullock, C. D. Dowell, L. Duband, J. P. Filippini, S. Fliescher, S. R. Golwala, M. Halpern, M. Hasselfield, S. R. Hildebrandt, G. C. Hilton, V. V. Hristov, K. D. Irwin, K. S. Karkare, J. P. Kaufman, B. G. Keating, S. A. Kernasovskiy, J. M. Kovac, C. L. Kuo, E. M. Leitch, M. Lueker, P. Mason, C. B. Netterfield, H. T. Nguyen, R. O'Brient, R. W. Ogburn, A. Orlando, C. Pryke, C. D. Reintsema, S. Richter, R. Schwarz, C. D. Sheehy, Z. K. Staniszewski, R. V. Sudiwala, G. P. Teply, J. E. Tolan, A. D. Turner, A. G. Vieregg, C. L. Wong, and K. W. Yoon. Detection of b-mode polarization at degree angular scales by bicep2. *Phys. Rev. Lett.*, 112:241101, Jun 2014.

[26] Rana Adhikari. Gravitational radiation detection with laser interferometry. Technical Report LIGO-P1200121-v1, LIGO DCC, 2012.

[27] Masato Aketagawa, Shohei Kimura, Takuya Yashiki, Hiroshi Iwata, Tuan Quoc Banh, and Kenji Hirata. Measurement of a free spectral range of a fabry–perot cavity using frequency modulation and null method under off-resonance conditions. *Meas. Sci. and Tech.*, 22(2):025302, 2011.

[28] Masato Aketagawa, Takuya Yashiki, Shohei Kimura, and TuanQuoc Banh. Free spectral range measurement of fabry-perot cavity using frequency modulation. *Int. Jour. of Precision Engineering and Manufacturing*, 11(6):851–856, 2010.

[29] Analog Devices. Fundamentals of Phase Locked Loops (PLLs). MT-086 Tutorial, October 2008.

[30] T. Andreae, W. Konig, R. Wynands, D. Leibfried, F. Schmidt-Kaler, C. Zimmermann, D. Meschede, and T. W. Hansch. Absolute frequency measurement of the hydrogen 1 S -2 S transition and a new value of the rydberg constant. *Phys. Rev. Lett.*, 69:1923–1926, Sep 1992.

[31] Isaac Angert. Characterization of a voltage controlled oscillator. Technical Report LIGO-T0900451-v1, LIGO DCC, October 2009.

[32] K. Arai. Sensing and controls for the power-recycling of TAMA300. *Classical and Quantum Gravity*, 19(7):1843, March 2002.

[33] K. Arai, M. Ando, S. Moriwaki, K. Kawabe, and K. Tsubono. New signal extraction scheme with harmonic demodulation for power recycled Fabry-Perot-Michelson interferometers. *Physics Letters A*, 273(1-2):15–24, August 2000.

[34] Akito Araya, Souichi Telada, Kuniharu Tochikubo, Shinsuke Taniguchi, Ryutaro Takahashi, Keita Kawabe, Daisuke Tatsumi, Toshitaka Yamazaki, Seiji Kawamura, Shinji Miyoki, Shigenori Moriwaki, Mitsuru Musha, Shigeo Nagano, Masa-Katsu Fujimoto, Kazuo Horikoshi, Norikatsu Mio, Yutaka Naito, Akiteru Takamori, and Kazuhiro Yamamoto. Absolute-length determination of a long-baseline fabry–perot cavity by means ofresonating modulation sidebands. *Appl. Opt.*, 38(13):2848–2856, May 1999.

[35] S.M. Aston et al. Update on quadruple suspension design for Advanced LIGO. *Classical and Quantum Gravity*, 29(23):235004, October 2012.

[36] B. C. Barish and R. Weiss. LIGO and the detection of gravitational waves. *Physics Today*, 52:44–50, October 1999.

[37] Barry C. Barish. *Gravitational Waves the New Generation of Laser Interferometric Detectors*, chapter 10, pages 125–144.

[38] L Barsotti. Early aLIGO configurations: example scenarios toward design sensitivity. Technical Report LIGO-T1200307, LIGO DCC, January 2014.

[39] L. Barsotti and M. Evans. Lock acquisition study for Advanced LIGO. Technical Report LIGO-T1000294-v1, LIGO DCC, 2010.

[40] M Barton et al. Model of the Advanced LIGO suspensions in Mathematica. Technical Report LIGO-T020205, LIGO DCC.

[41] M Barton et al. Model of the Advanced LIGO suspensions in MATLAB. Technical Report LIGO-T080188, LIGO DCC.

[42] Thomas W. Baumgarte. Lecture notes on General Relativity, 2008.

[43] Thomas W. Baumgarte and Stuart L. Shapiro. *Numerical Relativity: Solving Einstein's Equations on the Computer*. Cambridge University Press, 2010.

[44] John Bechhoefer. Feedback for physicists: A tutorial essay on control. *Rev. Mod. Phys.*, 77:783–836, August 2005.

[45] J Betzwieser. L1 calibrated sensitivity specta jun 6 2015 (best for ER7). Technical Report LIGO-G1500904, LIGO DCC, June 2015.

[46] J Betzwieser et al. Uncertainty estimation in Advanced LIGO calibration. Technical Report LIGO-G1500837, LIGO DCC, June 2015.

[47] Lars Bildsten. Gravitational radiation and rotation of accreting neutron stars. *The Astrophysical Journal Letters*, 501(1):L89, 1998.

[48] Eric D. Black. An introduction to Pound-Drever-Hall laser frequnecy stabilization. *American Association of Physics Teachers*, April 2004.

[49] Aidan Brooks et al. Direct measurement of absorption-induced wavefront distortion in high optical power systems. *Applied Optics*, 48(2):355–364, 2009.

[50] L Carbone, S M Aston, R M Cutler, A Freise, J Greenhalgh, J Heefner, D Hoyland, N A Lockerbie, D Lodhia, N A Robertson, C C Speake, K A Strain, and A Vecchio. Sensors and actuators for the Advanced LIGO mirror suspensions. *Classical and Quantum Gravity*, 29(11):115005, 2012.

[51] Sean M. Carroll. Lecture notes on General Relativity, December 1997.

[52] Indrajit Chakrabarty. Gravitational Waves: an introduction. *arXiv:physics/9908041*, August 1999.

[53] N. L. Christensen. Mutlimessenger astronomy. In *46th Rencontres de Moriond and GPhyS Colloquium on Gravitational Waves and Experimental Gravity*, 2011.

[54] Jolien D.E. Creighton and Warren G. Anderson. *Gravitational-Wave Phyiscs and Astronomy: An Intrudction to Theory, Experiment and Data Analysis*. WILEY-VCH, 2011.

[55] A V Cumming, A S Bell, L Barsotti, M A Barton, G Cagnoli, D Cook, L Cunningham, M Evans, G D Hammond, G M Harry, A Heptonstall, J Hough, R Jones, R Kumar, R Mittleman, N A Robertson, S Rowan, B Shapiro, K A Strain, K Tokmakov, C Torrie, and A A van Veggel. Design and development of the Advanced LIGO monolithic fused silica suspension. *Classical and Quantum Gravity*, 29(3):035003, 2012.

[56] J. Degallaix et al. Advanced Virgo status. In *9th LISA Symposium*, volume 467 of *Astronomical Society of the Pacific Conference Series*, page 151, 2012.

[57] R. W. P. Drever. *Fabry-Perot cavity gravity wave detectors.* Cambridge University Press, July 1991.

[58] R.W.P. Drever, J.L. Hall, F.V. Kowalski, J. Hough, G.M. Ford, A.J. Munley, and H. Ward. Laser phase and frequency stabilization using an optical resonator. *Applied Physics B*, 31(2):97–105, 1983.

[59] Jenne Driggers. *Noise Cancellation for Gravtiational Wave Detectors.* PhD thesis, Califronia Institute of Technology, May 2015.

[60] S Dwyer. aLIGO, ISC, RF system, low noise VCO, PLL. Technical Report LIGO-E1300728, LIGO DCC, 2013.

[61] Sheila Dwyer. *Quantume noise reduction using squeezed states in LIGO.* PhD thesis, Massachusetts Institue of Technology, February 2013.

[62] Sheila Dwyer. A note about H1 duty cycle during ER7. Technical Report LIGO-T1500368, LIGO DCC, July 2015.

[63] Albert Einstein. The foundation of the General Relativity. *Annalen der Physik*, 1916.

[64] Albert Einstein. On gravitational waves. *Preussische Akademie der Wissenschaften*, 1918.

[65] J Abadie et al. Predictions for the rates of compact binary coalescences observable by ground-based gravitational-wave detectors. *Classical and Quantum Gravity*, 27(17):173001, 2010.

[66] M Evans et al. Observation of parametric instability in Advanced LIGO. *Phys. Rev. Lett.*, 114(16):161102, April 2015.

[67] M. Evans, N. Mavalvala, P. Fritschel, R. Bork, B. Bhawal, R. Gustafson, W. Kells, M. Landry, D. Sigg, R. Weiss, S. Whitcomb, and H. Yamamoto. Lock acquisition of a gravitational-wave interferometer. *Optics Letters*, 27(8):598–600, April 2002.

[68] Matt Evans et al. Advanced LIGO arm length stabilisation system design. Technical Report LIGO-T0900144-v4, LIGO DCC, October 2010.

[69] L. S. Finn and D. F. Chernoff. Observing binary inspiral in gravitational radiation: one interferometer. *Phys. Rev. D*, 47(6):2198–2219, March 1993.

[70] T. Fricke et al. DC readout experiment in Enhanced LIGO. *Classical and Quantum Gravity*, 29(6):065005, February 2012.

[71] Tobin Fricke. *Homodyne Detection for Laser-Interferometric Gravitational Wave Detectors.* PhD thesis, Louisiana State University, 2011.

[72] P. Fritschel and R Abbott. Design overview for the new test mass electro-static driver. Technical Report LIGO-T1500016-v2, LIGO DCC, January 22 2015.

[73] P. Fritschel, R. Bork, G. Gonzalez, N. Mavalvala, D. Ouimetter, H.S. Rong, D. Sigg, and M. Zucker. Readout and control of power-recycled interferometric gravitational-wave antenna. *Applied Optics*, 40(28):4988–4998, October 2001.

[74] P. Fritschel and V. Frolov. LIGO DRMI measurements: a checklist. Technical Report LIGO-T1300558-v1, LIGO DCC, June 2013.

[75] Peter Fritschel. Arm length stabilization (ALS) vertex detection system. Technical Report LIGO-T1400317, LIGO DCC, May 2014.

[76] Peter Fritschel et al. Advanced LIGO arm length stabilisation requirements. Technical Report LIGO-T0900095-v2-D, LIGO DCC, April 2009.

[77] Peter Fritschel, Valera Frolov, and David Reitze. Commissioning the Advanced LIGO L1 input mode cleaner. Technical Report LIGO-T1100201-v2, LIGO DCC, March 2012.

[78] Peter Fritschel, Nergis Mavalvala, David Shoemaker, Daniel Sigg, Michael Zucker, and Gabriela González. Alignment of an interferometric gravitational wave detector. *Appl. Opt.*, 37(28):6734–6747, Oct 1998.

[79] Z Gajic. State space models. `http://www.ece.rutgers.edu/~gajic/psfiles/canonicalforms.pdf`.

[80] Stanley Goldman. *Phase-locked loop engineering handbook for integrated circuit*, chapter Components, Part 2 – Detectors and Other circuits. Artech House, 2007.

[81] Peter Goldreich and William H. Julian. Pulsar Electrodynamics. *The Astrophysical Journal*, 157, 1969.

[82] H. Grote et al. The status of GEO 600. *Classical and Quantum Gravity*, 22(10):S193–W198, April 2005.

[83] Dick Gustafson, Ewan Douglas, Peter Fritschel, and Sam Waldman. Fiber phase noise measurements at LHO. Technical Report LIGO-T0900376-v1, LIGO DCC, 2009.

[84] G. M. Harry. Advanced LIGO: the next generation of gravitational waves detectors. *Class. Quantum Grav.*, 27(084006):12, April 2010.

[85] G. M. Harry. Advanced LIGO: the next generation of gravitational waves detectors. *Classical and Quantum Gravity*, 27(084006):12, April 2010.

[86] Gregory M Harry. Advanced ligo: the next generation of gravitational waves detectors. *Class. Quantum Grav.*, 27(08006):12, 2010.

[87] M Hewitson, K Danzmann, H Grote, S Hild, J Hough, H Lück, S Rowan, J R Smith, K A Strain, and B Willke. Charge measurement and mitigation for the main test masses of the geo 600 gravitational wave observatory. *Classical and Quantum Gravity*, 24(24):6379, 2007.

[88] Russell A Hulse and Joseph H Taylor. Discovery of a pulsar in a binary system. *Astrophyiscal Journal*, 195, January 1975.

[89] K Izumi. Current status of advanced LIGO. Technical Report LIGO-G1500170, LIGO DCC, 2015.

[90] K. Izumi, K. Arai, B. Barr, J. Betzwieser, A. Brooks, K. Dahl, S. Doravari, J. Driggers, W. Z. Korth, H. Miao, J. Rollins, S. Vass, D. Yeaton-Massey, and R. Adhikari. Multicolor cavity metrology. *Journal of the Optical Society of America A*, 29(10):2092–2103, October 2012.

[91] K Izumi, S Dwyer, and L Barsotti. Simulation study for aLIGO lock acquiistion. Technical Report LIGO-T1400298, LIGO DCC, 2014.

[92] K. Izumi, D. Sigg, and L. Barsotti. Self amplified lock-in of an ultra-narrow linewidth optical cavity. *Optics Letters*, 39(18):5285—5288, September 2014.

[93] Kiwamy Izumi. *Mutli-Color Interferometry for Lock Acquisition of Laser Interfeometric Gravitation-wave Detectors*. PhD thesis, The University of Tokyo, JULY 2012.

[94] Aasi J. et al. Enhanced sensitivity of the LIGO gravitational wave detector by using squeezed states of light. *Nat Photon*, 7(8):613–619, 08 2013.

[95] Hyjunjoo Kim et al. PSL final design. Technical Report LIGO-T0900649-v4, LIGO DCC, February 2010.

[96] J Kissel. H1 calibrated sensitivity specta jun 8 2015 (best for ER7). Technical Report LIGO-G1500823, LIGO DCC, June 2015.

[97] Jeffery Kissel. Summary of aLIGO SUS model transfer functions. Technical Report LIGO-T1200404-v1, LIGO DCC, August 2012.

[98] Jeffery Kissel. aLIGO commissioning with suspension goggles. Technical Report LIGO-G1300979, LIGO DCC, September 2013.

[99] Jeffery Kissel and Sheila Dwyer. HIFO-XY, ALS DIFF global control with QUAD: Distributed hierarchy loop design. Technical Report LIGO-G1400146-v2, LIGO DCC, 2014.

[100] P. Kwee, C. Bogan, K. Danzmann, M. Frede, H. Kim, P. King, J. Pöld, O. Puncken, R. L. Savage, F. Seifert, P. Wessels, L. Winkelmann, and B. Willke. Stabilized high-power laser system for the gravitational wave detector Advanced LIGO. *Optics Express*, 20(10):10617–10634, May 2012.

[101] M. J. Lawrence, B. Willke, M. E. Husman, E. K. Gustafson, and R. L. Byer. Dynamic response of a fabry–perot interferometer. *J. Opt. Soc. Am. B*, 16(4):523–532, Apr 1999.

[102] Ryan Lawrence et al. Adaptive thermal compensation of test masses in Advanced LIGO. *Class. Quantum Grav.*, 19:1803–1812, 2002.

[103] P. J. Manson. High precision free spectral range measurement using a phase modulated laser beam. *Rev. of Sci. Inst.*, 70(10):3834–3839, 1999.

[104] Denis Martynov. *Lock acquistion and sensitivity analysis of Advanced LIGO Interferometers*. PhD thesis, Califronia Institute of Technology, May 2015.

[105] F. Matichard et al. Seismic isolation of Advanced LIGO gravitational waves detectors: Review of strategy, instrumentation, and performance. *arXiv:1502.06300*, 2015.

[106] Luca Matone. An overview of Advanced LIGO interferometry. Technical Report LIGO-G1200743, LIGO DCC, 2012.

[107] B. J. Meers. Recycling in laser-interferometric gravitational-wave detectors. *Physical Review D*, 38(8):2317–2326, October 1988.

[108] Charles W. Misner, Kip S. Thorne, and John Archiblad Wheeler. *Gravitation*. W. H. Freeman and Company, 1973.

[109] O. Miyakawa and H. Yamamoto. Lock acquisition study for advanced interferometers. *Journal of Physics: Conference Series*, 122:012024, 2008.

[110] Osamu Miyakawa, Robert Ward, Rana Adhikari, Benjamin Abbott, Rolf Bork, Daniel Busby, Matthew Evans, Hartmut Grote, Jay Heefner, Alexander Ivanov, Seiji Kawamura, Fumiko Kawazoe, Shihori Sakata, Michael Smith, Robert Taylor, Monica Varvella, Stephen Vass, and Alan Weinstein. Lock acquisition study for Advanced LIGO optical configuration. *Journal of Physics: Conference Series*, 32:265–269, 2006.

[111] Jun Mizuno. *Comparison of optical configurations for laser-interferometric gravitational-wave detectors*. PhD thesis, Hannover University, 1995.

[112] Euan Morrison, Brian J. Meers, David I. Robertson, and Henry Ward. Automatic alignment of optical interferometers. *Appl. Opt.*, 33(22):5041–5049, Aug 1994.

[113] G. E. Moss, L. R. Miller, and R. L. Forward. Photon-noise-limited laser transducer for gravitational antenna. *Appl. Opt.*, 10(11):2495–2498, Nov 1971.

[114] Adam J. Mullavey, Bram J. J. Slagmolen, John Miller, Matthew Evans, Peter Fritschel, Daniel Sigg, Sam J. Waldman, Daniel A. Shaddock, and David E. McClelland. Arm-length stabilisation for interferometric gravitational-wave detectors using frequency-doubled auxiliary lasers. *Optics Express*, 20(1):81–89, Jan 2012.

[115] NASA. LISA: Laser Interferometer Space Antenna. `lisa.nasa.gov`.

[116] E. Oelker, L. Barsotti, S. Dwyer, D. Sigg, and N. Mavalvala. Squeezed light for advanced gravitational wave detectors and beyond. *Opt. Express*, 22(17):21106–21121, Aug 2014.

[117] K.A. Olive and others (Particle Data Group). Cosmic microwave background. *Chin. Physics C*, 38, 2014.

[118] A. C. Phillips. *The Physics of Stars*, chapter Cooling of White Dwarfs. John Wiley and Sons Ltd, 1999.

[119] A.C. Phillips. *The Physics of Stars*, chapter Collapse of a stellar core. John Wiley and Sons Ltd, 1999.

[120] Matthew Pitkin et al. Gravitational wave detection by interferometry (ground and space). Technical Report LIGO-P110004-v3, LIGO DCC, 2011.

[121] Planck Collaboration. Planck intermediate results. XXX. the angular power spectrum of polairzed dust emission at intermediate and high Galatic latitude. *Astronomy and Astrophysics*, December 2014.

[122] E. Poisson and C. M. Will. *Gravity: Newtonian, Post-Newtonian, Relativistic.* Cambridge University Press, 2014.

[123] I. Quandt and H. J. Schmidt. The newtonian limit of the fourth and higher order gravity. *Astronomische Nachrichten*, 312:97, February 1991.

[124] Frederick J. Raab. Overview of LIGO instrumentation, 2004.

[125] M. Rakhmanov. Doppler-induced dynamics of fields in Fabry-Perot cavities with suspended mirrors. *Appl. Opt.*, 40(12):1942–1949, April 2001.

[126] M. Rakhmanov, F Bondu, O Debieu, and R. L. Savage. Characterization of the LIGO 4 km Fabry-Perot cavities via their high-frequency dynamic responses to length and frequency variations. *Class. Quantum Grav.*, 21(5):S487–S492, 2004.

[127] M. Rakhmanov, R.L. Savage Jr., D.H. Reitze, and D.B. Tanner. Dynamic resonance of light in Fabry-Perot cavities.

[128] R. D. Reasenberg. Cavity length measurements: bias from misalignment and mismatching. *Applied Optics*, 52(33):8154–8160, November 2013.

[129] Wilson Rugh. Linear Time-Invariant Systems and Convolution. `http://pages.jh.edu/~signals/lecture1/frames.html`.

[130] L. Schnupp. Talk at European collaboration meeting on interferometric detection of gravitational waves, 1988.

[131] B. Shapiro. Overview of Advanced LIGO suspensions. Technical Report LIGO-G1100866, LIGO DCC, 2011.

[132] D. Shoemaker. LIGO abbreviations and acronyms lists. Technical Report LIGO-M080375, LIGO DCC, 2015.

[133] J. A. Sidles and D. Sigg. Optical torques in suspened Fabry-Perot interferometers. *Physics Letters A*, 354(3):162–172, January 2006.

[134] A. E. Siegman. *Lasers.* University Science Books, 1986.

[135] D. Sigg. Low noise voltage controlled oscillator. Technical Report LIGO-D0900605, LIGO DCC, 2009.

[136] D. Sigg. Phase frequency discriminator test report. Technical Report LIGO-E1100977, LIGO DCC, October 2011.

[137] D. Sigg, K. Kawabe, and P. Fritschel. Commissioning Advanced LIGO's HIFO-Y. Technical Report LIGO-T1300174-v1, LIGO DCC, March 2013.

[138] D. Sigg and N. Mavalvala. Principles of calculating the dynamical response of misaligned complex resonant optical interferometers. *Journal of the Optical Society of America A*, 17(9):1642–1649, September 2000.

[139] Daniel Sigg. Common mode servo board. Technical Report LIGO-T040148, LIGO DCC, July 15 2004.

[140] Daniel Sigg. Frequency difference divider. Technical Report LIGO-T0900138-v1, LIGO DCC, March 2009.

[141] Daniel Sigg. Phase frequency discriminator specification. Technical Report LIGO-E1000450-v1, LIGO DCC, 2010.

[142] Kenneth D. Skeldon and Kenneth A. Strain. Response of a Fabry–Perot optical cavity to phase modulation sidebands for use in electro-optic control systems. *Appl. Opt.*, 36(27):6802–6808, Sep 1997.

[143] Kenneth D. Skeldon and Kenneth A. Strain. Response of a Fabry–Perot optical cavity to phase modulation sidebands for use in electro-optic control systems: errata. *Appl. Opt.*, 37(21):4936–4936, Jul 1998.

[144] Bram Slagmolen. ALS lock acquisition. Technical Report LIGO-G1300226, LIGO DCC, March 2013.

[145] Bram Slagmolen, Aidan Brooks, and Daniel Hoak. ALS Y-END station optical tabel layout (ISCTEY). Technical Report LIGO-D1100607-v13, LIGO DCC, 2015.

[146] Bram Slagmolen et al. ISCT1 optical layout. D1201103-v13.

[147] Bram Slagmolen et al. Advanced LIGO arm length stabilisation - vertex layout overview. Technical Report LIGO-T1000555-v3-D, LIGO DCC, December 2011.

[148] Bram Slagmolen and Daniel Sigg. Arm length stabilisation - fibre phase-locked-loop. Technical Report LIGO-T1200429-v1, LIGO DCC, September 2012.

[149] Bram J. J. Slagmolen, Malcolm B. Gray, Karl G. Baigent, and David E. McClelland. Phase-sensitive reflection technique for characterization of a fabry–perot interferometer. *Appl. Opt.*, 39(21):3638–3643, Jul 2000.

[150] Michael R. Smith. Up-conversion of scattered light phase noise from large amplitude motions. Technical Report LIGO-T980101, LIGO DCC, October 1998.

[151] Nicolas Smith. *Techniques for Improving the Readout Sensitivity of Gravitational Wave Antennae.* PhD thesis, Massachusetts Institue of Technology, June 2012.

[152] K. Somiya. Detector configuration of KAGRA - the Japanese cryogenic gravitational-wave detector. *Classical and Quantum Gravity*, 29(12):124007, June 2011.

[153] A Staley et al. ALS COMM handoff to TRX+TRY. Technical Report alog 15272, aLIGO LHO Logbook, November 2014.

[154] A. Staley et al. High precision optical cavity length and width measurements using double modulation. *Opt. Express*, 23(15):19417–19431, July 2015.

[155] A Staley, D Martynov, R Abbott, R X Adhikari, K Arai, S Ballmer, L Barsotti, A F Brooks, R T DeRosa, S Dwyer, A Effler, M Evans, P Fritschel, V V Frolov, C Gray, C J Guido, R Gustafson, M Heintze, D Hoak, K Izumi, K Kawabe, E J King, J S Kissel, K Kokeyama, M Landry, D E McClelland, J Miller, A Mullavey, B OReilly, J G Rollins, J R Sanders, R M S Schofield, D Sigg, B J J Slagmolen, N D Smith-Lefebvre, G Vajente, R L Ward, and C Wipf. Achieving resonance in the advanced ligo gravitational-wave interferometer. *Classical and Quantum Gravity*, 31(24):245010, 2014.

[156] B Swinkels, E Campagna, G Vajente, L Barsotti, and M Evans. Longitudinal noise subtraction: the alpha-, beta-, and gamma-technique. Virgo note VIR-0050A-08, 2008.

[157] Stanford Research Systems. FFT spectrum analyzers. `http://www.thinksrs.com/downloads/PDFs/Catalog/SR785c.pdf`.

[158] Joseph H Taylor, L. A. Fowler, and P. M. McCulloch. Measurements of gnereal relativisitic effects in the binary pulsar psr1913+16. *Nature*, 277, February 1979.

[159] The LIGO Scientific Collaboration. Advanced LIGO. *Classical and Quantum Gravity*, 32(7):074001, 2015.

[160] The MathWorks, Inc. Matlab. `http://www.mathworks.com/products/matlab/`.

[161] The MathWorks, Inc. Simulink. `http://www.mathworks.com/products/simulink/`.

[162] Thor Labs. Notch filters. `https://www.thorlabs.com/NewGroupPage9.cfm?ObjectGroup_ID=3880`.

[163] K Thorne. Subversion repositores: h1_filter_files. `https://daqsvn.ligo-_la.caltech.edu/websvn/`.

[164] R.L. Ward. *Length Sensing and Control of a Prototype Advanced Interferometric Gravitational Wave Detector*. PhD thesis, Califronia Institute of Technology, 2010.

[165] Edward A. Whittaker, Manfred Gehrtz, and Gary C. Bjorklund. Residual amplitude modulation in laser electro-optic phase modulation. *J. Opt. Soc. Am. B*, 2(8):1320–1326, Aug 1985.

[166] C Wipf. Simulink NB - NoiseBudget toolbox for Simulink. `https://github.com/cwipf/SimulinkNb`.

[167] WolframMathWorld. Laplace Transform. `http://mathworld.wolfram.com/LaplaceTransform.html`.

[168] N. C. Wong and J. L. Hall. Servo control of amplitude modulation in frequency-modulation spectroscopy: demonstration of shot-noise-limited detection. *J. Opt. Soc. Am. B*, 2(9):1527–1533, Sep 1985.

[169] D. Yeaton-Massey and R. X. Adhikari. A new bound on excess frequency noise in second harmonic generation in ppktp at the 10^{-19} level. *Opt. Express*, 2012.

[170] W. Zhang, M. J. Martin, C. Benko, J. L. Hall, J. Ye, C. Hagemann, T. Legero, U. Sterr, F. Riehle, G. D. Cole, and M. Aspelmeyer. Reduction of residual amplitude modulation to 1×10^{-6} for frequency modulation and laser stabilization. *Opt. Lett.*, 39(7):1980–1983, Apr 2014.

Appendix

Appendix A

Details on Arm Length Stabilization MatLab Code

The arm length stabilization model was described and validated in Chapter 5. Details on how to run the code, and some specifics on the current configuration of the code are highlighted in this Appendix.

The code can be located in the LIGO subversion directory:

/ligo/svncommon/NbSvn/aligonoisebudget/trunk/HIFO/H1/ .

The README provides extensive details on files in this directory. All of the specialized functions required to run the model are located in /utils. Several of the zero, poles, and gains settings for the analog electronics are listed in /Params. The Simulink model is located in /simulink. Collected data and produced plots are saved in /data and /Plots respectively.

The relevant files are split as follows: the Simulink model, a control files that assigns the relevant information to the function blocks present in the Simulink model, a validation file, and a noise budget file. The validation file compares all the measured transfer functions with those produced by the model and returns several plots. In addition, this file shows the noise budget propagation by looking at the noise budget of each individual loop. Meanwhile, the noise budget file returns the overall noise budget of the arm length stabilization scheme. The latter two files call the controls file, which finds the Simulink model. Table A.1 list the relevant file names with descriptions.

A critical component to running the model is the use of LiveParts, which was developed by Christopher Wipf [166]. This utility collects the zero, poles, and gains at a specified GPS time for any filter file that is archived. Since many of the arm length stabilization filters are represented in digital form; this proved invaluable. Instead of developing a parameter file with all the zpk's, only the filter file name saved in the archive needs to be specified. Updating the GPS time will automatically update the LiveParts parameters when the code is run again.

File	**Type**	**Description**
ALS_SIMULINK_X.mdl	Simulink model	Specific for the half interferometer X-arm study. This reproduces the common mode arm locking.
ALS_SIMULINK_FULL.mdl	Simulink model	Emulates the full interferometer locking in the final configuration of the arm length stabilization system (with no tidal feedback).
ALScontrol_X.m	Controls file	Linearizes the simulink model for the common mode locking.
ALScontrol_FULL.m	Controls file	Linearizes the simulink model for the full interferometer locking.
ALS_TFtest_NB_X.m	Validation file	Model vs. Measured transfer functions for common mode arm locking. As well as some noise propagation plots.
ALS_TFtest_NB_FULL.m	Validation file	Model vs. Measured transfer functions for full interferometer. As well as some noise propagation plots.
noisebudget_X.m	Noise budget file	Common mode arm length stabilization noise budget
noisebudget_DIFF.m	Noise budget file	Differential mode arm length stabilization noise budget

Table A.1: A list of the relevant files to run the arm length stabilization model and their description. Details on the other files listed in the subversion directory can be found in the README.

A.1 Digital and Analog Configuration

The GPS time of 1084215436 (May 15th, 2014 18:57:00 UTC) and 1084230856 (May 15th, 2014 23:15:00 UTC) are the respective times used for the common and differential mode locking with the arm length stabilization when the model was fully validated and the noise budget was produced. Below, I will provide relevant digital filters and analog board configurations. Some of these have been slightly updated since the noise budget was created and the technique was validated.

First, I will list the settings of the analog servo boards used in all the loops. The end station phase-locked loop servo board settings are designated in Table A.2:

Table A.2: End Station Phase-Locking Loop Servo Board Settings

Switch	**Setting**	**Details**
Input 1 Enable	ON	
Input 1 Polarity	NEG	
Input 1 Gain	0dB	
DC Nominal Gain	-30dB	
Common Compensation	ON	z/p = 4 kHz /1.35 Hz
Boost 1	ON/OFF as indicated	z/p = 20 kHz / 1 kHz
Generic Filter	ON	z/p = 0 Hz, 1 MHz / 100 kHz, 0.85 Hz
Fast Option	ON	
Fast Gain	-8dB	
Rest	Off/Zero	

Meanwhile, the end station Pound-Drever-Hall servo settings are described in Table A.3:

Table A.3: End Station Pound-Drever-Hall Servo Board Settings

Switch	**Setting**	**Details**
Input 1 Enable	ON	
Input 1 Polarity	NEG	
Input 1 Gain	-7dB	
Common Compensation	ON	z/p = 200 Hz / 40 Hz
Boost 1	ON	z/p = 1 kHz / 100 Hz
Boost 2	ON	z/p = 1 kHz / 100 Hz
Rest	Off/Zero	

The servo board settings for the input mode cleaner loop on it's own are listed in Table A.4:

Table A.4: IMC Servo Board Settings

Switch	**Setting**	**Details**
Input 1 Enable	ON	
Input 1 Polarity	POS	
Input 1 Gain	9dB	
Input 2 Enable	OFF	
Input 2 Gain	16dB	
Common Compensation	ON	z/p = 4 kHz / 40 Hz
Boost 1	ON	z/p = 20 kHz / 1 kHz
Generic Filter	ON	z/p = 17 kHz / 4 khz
Fast Gain	-6dB	
Fast Enable	ON	z/p = 70 kHz / 140 kHz
Fast Polarity	POS	
Slow Bypass	ON	p = 2 kHz

The configuration for the common mode phase-locked loop servo board is listed in Table A.5 (note: only the first five settings are relevant in the common mode PLL loop; the control signal of this loop is then sent through the remaining filters of the board and then sent to the common mode analog servo board used to control the common mode degree of freedom).

Table A.5: Common Mode PLL Board Settings

Switch	**Setting**	**Details**
Input 1 Enable	ON	
Input 1 Polarity	POS	
Input 1 Gain	27dB	
Common Filter 1	ON	z/p = 2 kHz / 40 Hz
Common Filter 2	ON	z/p = 17 kHz / 2 kHz
Boost	OFF	z/p = 40 Hz / 1.6 Hz
Generic Filter	OFF	z/p = 0 Hz, 1 MHz / 100 kHz, 0.85 Hz
VCO Compensation	ON	z/p = 40 Hz / 1.6 Hz
Low Pass Filter	ON	p = 48 Hz
Daughter Board	OFF	
Internal VCO path	OFF	

Similarly, the settings of the differential phase-locked loop servo board are listed in Table A.6:

Table A.6: Differential Mode PLL Board Settings

Switch	**Setting**	**Details**
Input 1 Enable	ON	
Input 1 Polarity	POS	
Input 1 Gain	26dB	
Common Filter 1	ON	z/p = 2 kHz / 40 Hz
Common Filter 2	ON	z/p = 2 kHz / 40 Hz
Boost	OFF	z/p = 40 Hz / 1.6 Hz
Generic Filter	OFF	z/p = 0 Hz, 1 MHz / 100 kHz, 0.85 Hz
VCO Compensation	OFF	40 Hz / 1.6 Hz
Low Pass Filter	OFF	p = 48 Hz
Daughter Board	OFF	
Internal VCO path	OFF	

The analog servo used for the command mode control is configured as follows in Table A.7:

Table A.7: Common Mode Servo Board Settings

Switch	**Setting**	**Details**
Input 1 Enable	ON	
Input 1 Polarity	POS	
Input 1 Gain	11dB	
Common Compensation	ON	z/p = 4 kHz / 40 Hz
Boost 1	OFF	z/p = 20 kHz / 1 kHz
Fast Gain	6dB	
Fast Highpass	ON	z/p = 0.001 Hz / 5 Hz
Fast Polarity	POS	
Slow Bypass	OFF	p = 2 kHz

The relevant digital filters used in the arm length stabilization are listed below. The values for these filters are assigned using LiveParts. Excluded from the list are the end test mass damping filters. The configuration for the filters can be found on the filter files archive in Ref. [163].

Table A.8: MC2 Suspension Loop Settings for IMC locking alone

Filter Bank	**Filters ON**	**Gain (abs)**
IMC-L	FM1	1
LSC-MC	–	1
MC2_M3_ISCINF	FM6, FM7	1
MC2_M3_LOCK	FM3, FM9	-300
MC2_M2_LOCK	FM3, FM4, FM10	0.1
MC2_M1_LOCK	FM1, FM2	-1

Table A.9: Summary of Digital Filter Settings for Common and Differential Mode Control

Filter Bank	**Filters ON**	**Gain (abs)**
IMC-L	FM1	1
LSC-MC	–	0
MC2_M3_ISCINF	OFF	1
MC2_M3_LOCK	FM9	-300
MC2_M2_LOCK	FM3, FM4, FM10	0.1
MC2_M1_LOCK	FM1, FM2	-1
LSC-CARM	FM4, FM5, FM8	80
LSC-REFL_SERVO_SLOW	FM1	1
LSC-DARM	FM1, FM2, FM3, FM7, FM8, FM10	400
SUS-ETMX_L1_LOCK_L	FM1, FM2, FM3, FM5	0.18
SUS-ETMX_L3_LOCK_L	–	1

The suspension digital filters can be found in the archived foton files for the suspensions [6].

Table A.10: Details on Digital Filter Settings for Common and Differential Mode Control

Filter Bank	**Filter**	**Details**
IMC-L	FM1	zpk([100;100],[10;10],1,"n")
MC2_M3_LOCK	FM9	cheby1("LowPass",2,1,300)
MC2_M2_LOCK	FM3	zpk([1],[0.1],10,"n")
MC2_M2_LOCK	FM4	zpk([1],[100],1,"n")
MC2_M2_LOCK	FM10	ellip("LowPass",4,1,60,70)gain(1.12202)
MC2_M1_LOCK	FM1	zpk([0.01],[0],1,"n")gain(0.01)
MC2_M1_LOCK	FM2	zpk([],[0.01;0.1],-1,"n")gain(0.142127)
LSC-CARM	FM4	zpk([1],[0.003],1,"n")gain(333.333)
LSC-CARM	FM5	zpk([0.1],[0.003],1,"n")gain(33.3333)
LSC-CARM	FM8	notch(279.25,20,20) notch(360,80,20) notch(178.75,50,10) notch(150.25,50,6)
LSC-REFL_SERVO_SLOW	FM1	zpk([100;100],[10;10],1,"n")
LSC-DARM	FM1	zpk([0.025+0.442i; 0.025-0.442i; 0.06+1.01i; 0.06-1.01i], [0.3-0.5i; 0.3+0.5i; 0.06-0.887i; 0.06+0.887i], 1, "n")gain(-8.55, "dB")* zpk([-0.7], [-1.4], 1, "f")*zpk([0.5], [200; 500-800i; 500+800i], 1, "n") * gain(54.8, "dB")* gain(60,"dB")
LSC-DARM	FM2	zpk([2],[0],1,"n")*gain(2)
LSC-DARM	FM3	resgain(0.43,1.4,20)resgain(0.15,1.4,10)resgain(1,7,20)
LSC-DARM	FM7	ellip("BandStop",4,2,80,59,61)gain(1.25893)
LSC-DARM	FM8	zpk([80;500-800i;500+800i],[50;70;200],1,"n")
LSC-DARM	FM10	zpk([47.5663+i*56.6873;47.5663-i*56.6873],[14.5+i*25.1147;14.5-i*25.1147],1,"n")
SUS-ETMX_L1_LOCK_L	FM1	zpk([-0.3], [0], 1, "f")
SUS-ETMX_L1_LOCK_L	FM2	zpk([-0.1], [0], 1, "f")
SUS-ETMX_L1_LOCK_L	FM3	zpk([-0.8], [-1.2], 1, "f")
SUS-ETMX_L1_LOCK_L	FM5	ellip("BandStop", 4, 1, 20, 9.4, 10)ellip("BandStop", 4, 1, 20, 13, 14)gain(2, "dB")

Appendix B

The Arm Length Stabilization Code

In this Appendix I provide the Matlab code used for the Simulink Model and to produce the noise budget. ©2014, Alexa Staley

B.1 The Control File

```
% a script to setup the parameters associated with
% the simulink diagram, ALS_SIMULINK_X.mdl


% some fundamental parameters
c = 299792458;                   % speed of light
L = 4000;                        % arm length [m]
lambda = 1064e 9  ;              % wavelenght of the fundamental laser mode [m]
FSR_MC = 9099471;                % FSR for MC
L_MC = c/(2*FSR_MC);             % MC length [m]

% some coversion factors
m2Hz = c /lambda / L;            % conversion from meter to Hz at 1064 nm wavelength
d2f = c / (lambda/2) / L;        % conversion from meter to Hz at 532 nm wavelength
d2f_MC = c / lambda / L_MC;      % conversion from meter to Hz at 1064 nm wavelength
    for MC
f2d_IR = L * lambda / c;         % conversion to get the atctual displacement



% get live parts parameters
svnDir = '/ligo/svncommon/NbSVN/aligonoisebudget/trunk/';
%addpath(genpath([svnDir 'Dev/Utils/']))
addpath(genpath([svnDir 'Externals/SimulinkNb']))
IFO = 'H1';
site = 'lho';
clear svnDir
setenv('LIGONDSIP','h1nds0:8088');
%mdv_config;
f_all = logspace( 1, 5, 3000);
```

```
if strcmp(handoffstate,'commstate')
    liveParts('ALS_SIMULINK_FULL', 1084215436, 1, f_all); % GPS time May 15, 2014 18:57:00 UTC COMM handoff run
else strcmp(handoffstate,'diffstate')
  liveParts('ALS_SIMULINK_FULL',  1084230856, 1, f_all); % GPS time May 15, 2014 23:15 UTC DIFF run with IR in both arms
end



addpath('util');

% load paramaters;
addpath('Params');
params_PLL_X;
params_PDH_X;
params_COMMPLL;
params_DIFFPLL;
params_IMC;
params_CM;


%%%%%%%%%%%%%%%%%%%%%%%%%%%%%%%%%%%%%%%%
% End X FIBR Servo using PLL to lock the laser to the transmitted fiber
% light with a frequency offset
%%%%%%%%%%%%%%%%%%%%%%%%%%%%%%%%%%%%%%%%

% Common Mode Board A (FIBR) (from common mode servo awiki)
% Common Comp On, 0dB Gain,  30dB DC gain at nominal settings
EX_PLL_SERVO_COMMPATH = makeZPK([pll.common.comp.z], [pll.common.comp.p], db2mag(ex.pll.servo.g), Inf);

% Double pole at 100Khz/Q=.85     takes care of generic filter on CMB_FIBR
EX_FIBR_SERVO_GEN = makeZPKQ([pll.genfilter.z],[pll.genfilter.p],1,0);
FAST_GAIN = pll.fast.g;

% PZT coefficient 1.1 MHz/V (measured 06/20/13)
% Did not include pzt or temp response
% Fast option notch filter w/ resonance at 287.55kHz, depth
%  30dB and Q of 191 (From the transfer function TF942 this has a
% negligible effect below 100kHz)
EX_PZT_NOTCH = tf([L Rcoil 1/Cap], [L Res 1/Cap]);
EX_PZT = makeZPK([pll.pzt.z], [pll.pzt.p], pll.pzt.g , 0);


% Detector response (from phase frequency discriminator awiki)
% PFD coeffecient 36 Deg/V
EX_PFD = makeZPK([],[pll.pfd.p],pll.pfd.g,Inf);


%%%%%%%%%%%%%%%%%%%%%%%%%%%%%%%%%%%%%%%%
% End X REFL Servo: using PDH to lock the green laser light to the arm
% cavity
%%%%%%%%%%%%%%%%%%%%%%%%%%%%%%%%%%%%%%%%
```

```
% Configure cavity pole
FSR_freq = 3.7529e4;
T = 1/(2*FSR_freq);
EX_REFL_CAVITY.sys = zpk([],  wCav, wCav); % Cavity pole with gain to one;
    EX_PD_OpGain contains gain info of cavity pole, need to adjust optical gain
    relative to previous cavity pole gain setting
EX_REFL_CAVITY_REFL.sys = zpk([  1i*pi/T; + 1i*pi/T], [ wCav ;  wCav   1i*pi/T; wCav
     + 1i*pi/T], wCav); % zero order cavity pole, plus first FSR zero pole pair at
    reflection
EX_REFL_CAVITY_TR.sys = zpk([], [ wCav ;  wCav   1i*pi/T; wCav + 1i*pi/T], wCav
    ^3.75*.7); % zero order cavity pole, plus first FSR pole in transmission; gain
    value to make DC gain 1...
EX_HIGHPASS_FILTER.sys = zpk(0,  wCav, 1);

% PDH sensor (V/Hz)
% EX_PDH_OpGain

% Common Mode Board B (REFL)
EX_REFL_SERVO = makeZPK([pdh.common.comp.z pdh.boost.one.z pdh.boost.two.z],[pdh.
    common.comp.p pdh.boost.one.p pdh.boost.two.p], db2mag(ex.pdh.servo.g), Inf);

% EX VCO
EX_REFL_VCO = makeZPK(pdh.vco.z,pdh.vco.p,pdh.vco.g,0);

%%%%%%%%%%%%%%%%%%%%%%%%%%%%%%%%%%%%%%%%
% ALS Corner COMM
%%%%%%%%%%%%%%%%%%%%%%%%%%%%%%%%%%%%%%%%

% PFD Detector (from phase frequency discriminator awiki; 1/f response)
CORNER_PFD = makeZPK([],[comm.pll.pfd.p], comm.pll.pfd.g,Inf);

% VCO
% VCO Coeffecient ~200 (KHz/V)
CORNER_VCO = makeZPK([comm.pll.vco.z], [comm.pll.vco.p], comm.pll.vco.g, 0);

% COMM PLL to VCO
COMM_PLL_VCO = makeZPK([comm.pll.filter.one.z comm.pll.filter.two.z],[comm.pll.
    filter.one.p comm.pll.filter.two.p],db2mag(comm.pll.filter.one.g + comm.pll.
    filter.two.g),0);
COMM_PLL_VCO_DCgain = makeZPK([],[],db2mag(comm.pll.inputgain),0);

% COMM PLL to Common Mode Sum
% check configuration
COMM_PLL_CM = makeZPK([comm.pll.branch.vcocomp.z], [comm.pll.branch.vcocomp.p comm.
    pll.branch.p], db2mag(comm.pll.branch.vcocomp.g + comm.pll.branch.g), 0);


%%%%%%%%%%%%%%%%%%%%%%%%%%%%%%%%%%%%%%%%
% REFL Servo controlling the interferometer common mode consisting of the
% AO and the LSC mode cleaner length with input from REFLAIR_A, ALS_COMM,
% or REFL_B_DC
%%%%%%%%%%%%%%%%%%%%%%%%%%%%%%%%%%%%%%%%

```

```
% Interferometer common mode
CM_REFL_SERVO = makeZPK([cm.common.comp.z],[cm.common.comp.p],db2mag(cm.common.g),Inf);
%CM_REFL_SERVO = makeZPK([],[],db2mag(11),Inf);

CM_REFL_SERVO_FAST = makeZPK([cm.fast.highpass.z cm.fast.highpass.z],[cm.fast.highpass.p cm.fast.highpass.p],db2mag(cm.fast.g),Inf);

WHITENING = makeZPK([10 10], [100 100],1,0);

%%%%%%%%%%%%%%%%%%%%%%%%%%%%%%%%%%%%%%%%
% IMC REFL Servo locking the PSL to the IMC using the refercne cavity AOM
% and the mode cleaner leangth (MCL)
%%%%%%%%%%%%%%%%%%%%%%%%%%%%%%%%%%%%%%%%

% Cavity pole of MC (8812.36Hz)
wCav_MC = 2*pi* 8812.36;
IMC_CAVITY = makeZPK ([], 8812.36, 1, 0);
IMC_HIGHPASS_FILTER.sys = zpk(0,  wCav_MC, 1);
RED_CAV_POLE = makeZPK( [], [42], 1, 0);

% PDH sensor (V/Hz)
IMC_OpGain = 3.2673e 4;                              % measured from Vpp = 1.33V of PDH error signal

% IMC Board Common Path
IMC_REFL_SERVO_COMMPATH = makeZPK([imc.common.comp.z imc.boost.one.z imc.common.filter.z],[imc.common.comp.p imc.boost.one.p imc.common.filter.p],db2mag(0),Inf);

% Input 1 gain
IMC_In1_Gain  = db2mag(9);

% Input 2 gain
GainAO = db2mag(16);

% IMC Board Fast Path Filter
IMC_REFL_SERVO_FAST = makeZPK([imc.fast.comp.z],[imc.fast.comp.p],db2mag(imc.fast.g),Inf);

% IMC Board Slow Path Filter
IMC_REFL_SERVO_SLOW = makeZPK([],[imc.slow.comp.p],imc.slow.comp.g,0);

% PSL VCO
% VCO Coeffecient 268302 (Hz/V) measured (alog: 5556)
IMC_VCO = makeZPK(imc.vco.z,  imc.vco.p , imc.vco.g, 0);


%%%%%%%%%%%%%%%%%%%%%%%%%%%%%%%%%%%%%%%%
% MC2 SUS
%%%%%%%%%%%%%%%%%%%%%%%%%%%%%%%%%%%%%%%%
% All live filters and HSTS undamped model
% load hsts space for MC2_M3 actuators
load hstsmodelproduction rev4067_ssmake3MBf rev1891_hstsopt_metal rev2039_released 2013 01 31
```

```
% M3 Stage:
% MC2 Suspension filter uses live filters (H1:SUS_MC2_M3_LOCK_L   FM3, FM9 ON)
% Plant is in HSTS
CAL_DC_M3 =  7.0747e 11; % cnts to N

% M2 Stage:
% MC2 Suspension filter uses live filers (H1:SUS_MC2_M2_LOCK_L   FM 3, FM 4, FM10
    ON)
% Plant is in HSTS
CAL_DC_M2 =  3.3752e 09; % cnts to N


% M1 Stage:
% MC2 Suspension filter uses Live Filters (H1:SUS_MC2_M1_LOCK_L   FM 1, FM 2 ON)
% Plant is in HSTS
CAL_DC_M1 =  8.7431e 07; % cnts to N

%%%%%%%%%%%%%%%%%%%%%%%%%%%%%%%%%%%%%%%%
% End Y FIBR Servo using PLL to lock the laser to the transmitted fiber
% light with a frequency offset
%%%%%%%%%%%%%%%%%%%%%%%%%%%%%%%%%%%%%%%%

% Common Mode Board A (FIBR) (from common mode servo awiki)
% Common Comp On, 0dB Gain,  30dB DC gain at nominal settings
EY_PLL_SERVO_COMMPATH = makeZPK([pll.common.comp.z], [pll.common.comp.p], db2mag(ex.
     pll.servo.g), Inf);

% Double pole at 100Khz/Q=.85   takes care of generic filter on CMB_FIBR
EY_FIBR_SERVO_GEN = makeZPKQ([pll.genfilter.z],[pll.genfilter.p],1,0);
FAST_GAIN = pll.fast.g;

% PZT coefficient 1.1 MHz/V (measured 06/20/13)
% Did not include pzt or temp response
% Fast option notch filter w/ resonance at 287.55kHz, depth
%  30dB and Q of 191 (From the transfer function TF942 this has a
% negligible effect below 100kHz)
EY_PZT_NOTCH = tf([L Rcoil 1/Cap], [L Res 1/Cap]);
EY_PZT = makeZPK([pll.pzt.z], [pll.pzt.p], pll.pzt.g , 0);



% Detector response (from phase frequency discriminator awiki)
% PFD coeffecient 36 Deg/V
EY_PFD = makeZPK([],[pll.pfd.p],pll.pfd.g,Inf);


%%%%%%%%%%%%%%%%%%%%%%%%%%%%%%%%%%%%%%%%
% End Y REFL Servo: using PDH to lock the green laser light to the arm
% cavity
%%%%%%%%%%%%%%%%%%%%%%%%%%%%%%%%%%%%%%%%

% Configure cavity pole
EY_REFL_CAVITY_REFL.sys = zpk([  1i*pi/T; + 1i*pi/T], [ wCav ;  wCav   1i*pi/T; wCav
     + 1i*pi/T], wCav); % zero order cavity pole, plus first FSR zero pole pair at
```

```
    reflection
EY_REFL_CAVITY_TR.sys = zpk([], [ wCav ;  wCav   1i*pi/T; wCav + 1i*pi/T], wCav
    ^3.75*.7); % zero order cavity pole, plus first FSR pole in transmission; gain
    value to make DC gain 1...
EY_HIGHPASS_FILTER.sys = zpk(0,  wCav, 1);

% PDH sensor (V/Hz)
% EY_PDH_OpGain

% Common Mode Board B (REFL)
EY_REFL_SERVO = makeZPK([pdh.common.comp.z pdh.boost.one.z pdh.boost.two.z],[pdh.
    common.comp.p pdh.boost.one.p pdh.boost.two.p], db2mag(ex.pdh.servo.g), Inf);

% EY VCO
EY_REFL_VCO = makeZPK(pdh.vco.z,pdh.vco.p,pdh.vco.g,0);


%%%%%%%%%%%%%%%%%%%%%%%%%%%%%%%%%%%%%%%%
% ALS Corner DIFF
%%%%%%%%%%%%%%%%%%%%%%%%%%%%%%%%%%%%%%%%

% PFD Detector (from phase frequency discriminator awiki; 1/f response)
CORNER_DIFF_PFD = makeZPK([],[diff.pll.pfd.p], diff.pll.pfd.g,Inf);

% VCO
% VCO Coeffecient ~200 (KHz/V)
CORNER_DIFF_VCO = makeZPK([diff.pll.vco.z], [diff.pll.vco.p], diff.pll.vco.g, 0);

% DIFF PLL to VCO
DIFF_PLL_VCO = makeZPK([diff.pll.filter.one.z diff.pll.filter.two.z],[diff.pll.
    filter.one.p diff.pll.filter.two.p],db2mag(diff.pll.filter.one.g + diff.pll.
    filter.two.g),0);
DIFF_PLL_VCO_DCgain = makeZPK([],[],db2mag(diff.pll.inputgain),0);

% COMM PLL to Common Mode Sum
% check configuration
DIFF_PLL_CM = makeZPK([], [], db2mag(0), 0);



%%%%%%%%%%%%%%%%%%%%%%%%%%%%%%%%%%%%%%%%
% ETM QUAD SUS
%%%%%%%%%%%%%%%%%%%%%%%%%%%%%%%%%%%%%%%%
quad.f=logspace(2,6,3000);

load('quadmodelproduction rev3767_ssmake4pv2eMB5f_fiber rev3601_fiber
    rev3602_released 2013 01 31.mat');
% LSC Output Matrix
ifoParams.act.darm2etmx = 1;
ifoParams.act.darm2etmy = 1;
ifoParams.act.xarm2etmx = 0;
ifoParams.act.yarm2etmy = 0;

% ESD Bias [counts]
```

```
%ifoParams.act.esdBais_ct = 1.5e5; % [ct] = 11.4 [V] out of the DAC
ifoParams.act.esdBias_ct = 125000;

% DAC
ifoParams.act.dacGain = 20 / 2^18; % [V/ct] 18 Bit DAC

svnDir.cal = '/ligo/svncommon/CalSVN/aligocalibration/trunk/Runs/S7/';
calToolsDir = [svnDir.cal 'Common/MatlabTools/'];
% CDS IOP 16k Up/Down sampling filter
addpath(calToolsDir);
ifoParams.act.cdsUpsamplingFilter_16kto64k = iopdownsamplingfilters(quad.f,'16k','biquad');

%
% Makes the State Space object from the .mdl

[A,B,C,D] = linmod('ALS_SIMULINK_FULL');
sys = ss(A,B,C,D);
clear A B C D;
```

/ligo/svncommon/NbSvn/aligonoisebudget/trunk/HIFO/H1/simulink/ALScontrol˙Full.m

B.1.1 Parameter Files

```
% Parameters for PLL loop for EX

%% Servo Board
pll.comm.gain = 0;              % gain of input 1 (0dB nom,  4dB for PDH TF collected)
pll.nominal.gain =  30;          % DC nominal gain of  30dB at input of board
pll.common.comp.z = 4000;        % z/p for common comp
pll.common.comp.p = 1.35;
pll.boost.one.z  = 20e3;         % z/p for boost stag one
pll.boost.one.p  = 1e3;
pll.fast.g = db2mag( 8);         % gain of fast path in dB
ex.pll.servo.g = pll.comm.gain + pll.nominal.gain;
pll.genfilter.z = [1e6 0];
pll.genfilter.p = [100e3 0.85];


%% PZT resonance
% D1201404 schematic for notch
Res = 1e3;
L = 1e 3;
Cap = 270e 12;
Rcoil = 25;

pll.pzt.z = 1e6;
pll.pzt.p = 1e6;                % pole for pzt resonance changed from 1e5 ** why??? to match data
pll.pzt.g = 1.1e6;
```

```
%% PFD
% calibration 36 Deg/V
pll.pfd.p = 1e 3;              % from frequency to phase conversion
pll.pfd.g = 360/36;
```

/ligo/svncommon/NbSvn/aligonoisebudget/trunk/HIFO/H1/Params/params˙PLL˙X.m

```
% Parameters for PDH loop

%% Cavity
Finesse = 9.7;                    % finesse of the cavity for 532 nm
CavityPole = 1.46e3;                     % Arm Cavity Pole (fCav=2kHz)    alog 10423 LLO
wCav = 2*pi*1460;                  % wCav = 2*pi* c/4/L/Finesse;

%% Servo Board
pdh.comm.gain =  7;               % gain of input 1
pdh.common.comp.z = 200;        % z/p for common comp
pdh.common.comp.p = 40;
pdh.boost.one.z  = 1e3;         % z/p for boost stage one
pdh.boost.one.p  = 100;
pdh.boost.two.z = 1e3;            % z/p for boost stage two alog 9357
pdh.boost.two.p = 100;
ex.pdh.servo.g = pdh.comm.gain;

%% VCO
% VCO Coeffecient 200(KHz/V) !! check me!! or is 50kHz/V
pdh.vco.p = 1.6;
pdh.vco.z = 40;
pdh.vco.g = 2e5;
```

/ligo/svncommon/NbSvn/aligonoisebudget/trunk/HIFO/H1/Params/params˙PDH˙X.m

```
% Parameters for IMC loop

%% Servo Board
% Schematic D040180
imc.in1.gain = 9;
imc.in2.gain = 16;

imc.common.comp.p = 40;         % z/p for common comp
imc.common.comp.z = 4e3;

imc.boost.one.z  = 20e3;          % z/p for boost stage one
imc.boost.one.p  = 1e3;

imc.boost.two.z  = 20e3;          % z/p for boost stage two
imc.boost.two.p  = 1e3;

imc.common.filter.z = 17e3;
imc.common.filter.p = 4e3;

imc.fast.comp.z = 70e3;
imc.fast.comp.p = 140e3;
```

```
imc.fast.g =  6;

imc.slow.comp.p = 2e3;
imc.slow.comp.g = 5;


%% VCO
imc.vco.p = 1.6;
imc.vco.z = 40;
imc.vco.g = 268302;
```

/ligo/svncommon/NbSvn/aligonoisebudget/trunk/HIFO/H1/Params/params˙IMC.m

```
%% ALS CORNER COMM PLL Loop

% Parameters for COMM PLL board to VCO and Common Mode Sum
% D1300944
% p/z are in Hz, gains are in mag at DC
% see alog 9559

%% Servo Board
% to VCO
 diff.pll.inputgain = 27;

 diff.pll.filter.one.p = 40;
 diff.pll.filter.one.z = 2e3;
 diff.pll.filter.one.g = mag2db(50);

 diff.pll.filter.two.p = 1.9e3;
 diff.pll.filter.two.z = 17.1e3;
 diff.pll.filter.two.g = mag2db(9);

% to Common mode sum
 diff.pll.branch.boost.p = 1.6;
 diff.pll.branch.boost.z = 40;
 diff.pll.branch.boost.g = mag2db(25);

 diff.pll.branch.vcocomp.p = 1.6;
 diff.pll.branch.vcocomp.z = 40;
 diff.pll.branch.vcocomp.g = mag2db(5);

 diff.pll.branch.p = 48;   % note this is incorrect in the block diagram ; see schematic
 diff.pll.branch.g = mag2db(1); % note this is incorrect in the block diagram ; see schematic


%% Corner VCO
% VCO Coeffecient ~20 (KHz/V)
 diff.pll.vco.p = 1.6;
 diff.pll.vco.z = 40;
 diff.pll.vco.g = 285220/10 /1.5; %factor of 10 for corner vco; fudge factor of 1.5...
```

```
% From Adam's code: 20deg phase shift at 50Hz    then adjusted to fit data
 diff.pll.vcoHF.p = 70e3 ;%275e3;
 diff.pll.vcoHF.z = 3000e3;  %2750e3;

%% Corner PFD
% PFD coeffecient: 36 Degree/Volts
% returns cycles; not radians
 diff.pll.pfd.p = 1e 3;
 diff.pll.pfd.g = 360/36;
```

/ligo/svncommon/NbSvn/aligonoisebudget/trunk/HIFO/H1/Params/params˙DIFFPLL.m

```
%% ALS CORNER COMM PLL Loop

% Parameters for COMM PLL board to VCO and Common Mode Sum
% D1300944
% p/z are in Hz, gains are in mag at DC
% see alog 9559


%% Servo Board
% to VCO
comm.pll.inputgain = 27;

comm.pll.filter.one.p = 40;
comm.pll.filter.one.z = 2e3;
comm.pll.filter.one.g = mag2db(50);

comm.pll.filter.two.p = 1.9e3;
comm.pll.filter.two.z = 17.1e3;
comm.pll.filter.two.g = mag2db(9);

% to Common mode sum
comm.pll.branch.boost.p = 1.6;
comm.pll.branch.boost.z = 40;
comm.pll.branch.boost.g = mag2db(25);

comm.pll.branch.vcocomp.p = 1.6;
comm.pll.branch.vcocomp.z = 40;
comm.pll.branch.vcocomp.g = mag2db(5);

comm.pll.branch.p = 48;   % note this is incorrect in the block diagram ; see
    schematic
comm.pll.branch.g = mag2db(1); % note this is incorrect in the block diagram ; see
    schematic


%% Corner VCO
% VCO Coeffecient ~20 (KHz/V)
comm.pll.vco.p = 1.6;
comm.pll.vco.z = 40;
comm.pll.vco.g = 285220/10 /1.5; %factor of 10 for corner vco; fudge factor of
    1.5...

% From Adam's code: 20deg phase shift at 50Hz    then adjusted to fit data
```

```
comm.pll.vcoHF.p = 70e3 ;%275e3;
comm.pll.vcoHF.z = 3000e3;  %2750e3;

%% Corner PFD
% PFD coeffecient: 36 Degree/Volts
% returns cycles; not radians
comm.pll.pfd.p = 1e 3;
comm.pll.pfd.g = 360/36;
```

/ligo/svncommon/NbSvn/aligonoisebudget/trunk/HIFO/H1/Params/params˙COMMPLL.m

```
%% Paramters for the CM Board: LSC_REFL_SERVO Board


cm.fast.highpass.p = 5;
cm.fast.highpass.z  = 0.001; % place low enough
cm.fast.g = 6;

cm.common.g = 11;
cm.common.comp.z = 4e3;
cm.common.comp.p = 40;

cm.common.boost.one.z = 20e3;
cm.common.boost.one.p = 1e3;
```

/ligo/svncommon/NbSvn/aligonoisebudget/trunk/HIFO/H1/Params/params˙CM.m

B.2 Model Transfer Functions

```
% close all
% clear all
% clc

% Various Transfer Functions

 f_all = logspace( 1, 3.7, 3000);
 f=logspace(0,6,3000);

 addpath('simulink');
 addpath('util');
 addpath('data')




%% End X PLL Measurements taken Jan 13, 2014
% alog 9251
% PLL Servo Board Settings
%   Input 1 Pol: NEG
%   Input 1 Gain: 0dB
%   Common Compensation: ON
```

```
%   Generic Filter: ON
%   Fast Option: ON
%   Fast Gain:  8dB
%   Boost 1: On/Off (as specified)
%   Rest: Off/Zero


%% Noise of In Loop PLL
% load model
EX_PDH_OpGain = 0;
D_REL = db2mag( 22);
GainFast =0;
GainSlow =1;
IMCTEST = 1;
ALScontrol_X;

% PLL Noise Spectrum via PFD
EX_PLL_Noise_BoostOff = load('EX_PLL_Noise_PFD_BoostOff_Jan132014');
EX_PLL_Noise_BoostOn = load('EX_PLL_Noise_PFD_BoostOn_Jan132014');
EX_PLL_Noise_High = load('EX_PLL_Noise_PFD_High_Jan132014'); % in dBm, at 100Hz BW
BW = 100; %Hz
EX_PLL_Noise_High.dataname(:,2) = sqrt(50e3)* 10.^((EX_PLL_Noise_High.dataname(:,2)
    )/20)./sqrt(BW); % conversion to Vrms/SqrtHz
EX_PLLNoise_BoostOff(:,2) = vertcat(EX_PLL_Noise_BoostOff.EX_PLL_Noise_PFD_Jan132014
    (:,2), EX_PLL_Noise_High.dataname(81:801,2));
EX_PLLNoise_BoostOn(:,2) = vertcat(EX_PLL_Noise_BoostOn.name2(:,2),
    EX_PLL_Noise_High.dataname(81:801,2));
EX_PLLNoise_BoostOff(:,1) = vertcat(EX_PLL_Noise_BoostOff.EX_PLL_Noise_PFD_Jan132014
    (:,1), EX_PLL_Noise_High.dataname(81:801,1));
EX_PLLNoise_BoostOn(:,1) = vertcat(EX_PLL_Noise_BoostOn.name2(:,1),
    EX_PLL_Noise_High.dataname(81:801,1));

% Convert data from V to rad
EX_PLLNoise_BoostOff(:,2) = 36 * pi/180 .*  EX_PLLNoise_BoostOff(:,2);
EX_PLLNoise_BoostOn(:,2) = 36 * pi/180 .* EX_PLLNoise_BoostOn(:,2);


% data from alog 10286
% with MPC polarization controller off
% units in rad/sqrtHz
load('EX_PLL_NoiseSpecRad_BoostOn.txt');
load('EX_PLL_NoiseSpecRad_BoostOff.txt');

EX_PLL_NoiseRad_BoostOff(:,2) = vertcat(EX_PLL_NoiseSpecRad_BoostOff(:,2),
    EX_PLL_Noise_High.dataname(81:801,2));
EX_PLL_NoiseRad_BoostOff(:,1) = vertcat(EX_PLL_NoiseSpecRad_BoostOff(:,1),
    EX_PLL_Noise_High.dataname(81:801,1));
EX_PLL_NoiseRad_BoostOn(:,2) = vertcat(EX_PLL_NoiseSpecRad_BoostOn(:,2),
    EX_PLL_Noise_High.dataname(81:801,2));
EX_PLL_NoiseRad_BoostOn(:,1) = vertcat(EX_PLL_NoiseSpecRad_BoostOn(:,1),
    EX_PLL_Noise_High.dataname(81:801,1));

% BBPD noise    measured out of preamplifier direct (1dB), with BBPD
% blocked
```

```
BBPD_noise =  118*ones(size(f)); %  119 dBm, at 100Hz Bw
beatnote =   32*ones(size(f)); %  33 dBm, at 100Hz BW
dBc_BBPD = BBPD_noise   beatnote;
dBc_BBPD_Hz = dBc_BBPD   20; % dividing by 100Hz BW is the same as  20dB
BBPD_noise =  10.^(dBc_BBPD_Hz./20); % dBc to rad/sqrtHz

% shot noise    measured out of preamplifier direct ( 1dB)
shot_noise =  113*ones(size(f)); %  114 dBm, at 100Hz Bw
beatnote =   32*ones(size(f)); %  33 dBm, at 100Hz BW
dBc = shot_noise   beatnote;
dBc_Hz = dBc   20; % dividing by 100Hz BW is the same as  20dB
shot_noise =  sqrt((10.^(dBc_Hz./20)).^2   10.^(dBc_BBPD_Hz/20).^2); % dBc to rad/sqrtHz, subtracting out the dark noise of the BBPD


%alternate method to calculate shot noise (confirmed to match)
% Power onto BBPD is almost all laser; no fiber (FIBR_A_DC)
elec = 1.6e 19; % charge of electron
BBPD_power = 5.2e 3; % watts: 2kOhm trans, .09A/W responsivity
BBPD_curr = .52e 3;
Carrier_curr = 5.8e 3/2e3; % carrier  33dbm to current
shot_noise_temp = sqrt(2*elec*BBPD_curr)/Carrier_curr; % shot noise in 1/SqrtHz
shot_noise_2 = shot_noise_temp * ones(size(f));


% PFD Noise
% ~460nV/SqrtHz at 140Hz, assume flat for freq we care
PFD_noise_V = 500e 9*ones(size(f));
PFD_noise = 36 * pi/180 .* PFD_noise_V; % convert to rad


% Free Running Laser Noise
% NPRO_freqfluc_Hz = ones(size(f));
% for i = 1:length(f)
%    % if f(i) < 1
%     %  NPRO_freqfluc(i) = 1e4;
%     if f(i) <= 1e4
%         NPRO_freqfluc_Hz(i) = 1e4./f(i); % T0900649 pg 11 in Hz/sqrtHz from 1 to 10 kHz
%     else
%         NPRO_freqfluc_Hz(i) = 1;
%     end
% end
NPRO_freqfluc_zpk = makeZPK([1e4],[1e 5],1,Inf);
tf_temp = mybodesys(NPRO_freqfluc_zpk.sys, f);
NPRO_freqfluc_Hz = abs(tf_temp)';
NPRO_freqfluc = NPRO_freqfluc_Hz./f; % rad/sqrtHz
TF_endlaserfreq = mybodesys(sys(12,4),f);
EX_LaserFreqNoise_rad = abs(NPRO_freqfluc .* TF_endlaserfreq'); % rad/sqrtHz, supressed laser noise due to locking

% Fiber noise (see LIGO T0900376 v1)
% Fiber_noise_Hz = ones(size(f));
% for i = 1:length(f)
```

```
%     if f(i) <= 1e3
%        Fiber_noise_Hz(i) = 3;
%     else
%         Fiber_noise_Hz(i) = 3e3/f(i);
%     end
% end
Fiber_noise_zpk = makeZPK([],[1e3],3,0);
tf_temp = mybodesys(Fiber_noise_zpk.sys, f);
Fiber_noise_Hz = abs(tf_temp)';
Fiber_noise_rad = Fiber_noise_Hz./f;
EX_FiberNoise_rad = abs(Fiber_noise_rad .* TF_endlaserfreq'); % supressed fiber noise

data_1(:,:,1) = EX_PLL_NoiseRad_BoostOff;
data_1(:,:,2) = EX_PLL_NoiseRad_BoostOn;
for i=1:2
    rms_PLL(:,i) = [( 1.*cumtrapz(flipud(data_1(:,1, i)), flipud(data_1(:, 2,i)).^2)).^(0.5)]';
end
rms_PLL = flipud(rms_PLL);
freq = data_1(:,1,1);


% measurements with boost off and nominal gain
figure(1)
clf;
set(gcf, 'color', 'w');
ll=loglog(EX_PLL_NoiseRad_BoostOff(:,1), EX_PLL_NoiseRad_BoostOff(:,2), ...
    f,shot_noise,...
    f,PFD_noise, ...
    f, EX_LaserFreqNoise_rad, ...
    f, EX_FiberNoise_rad,...
    f, shot_noise_2,...
    f, BBPD_noise,...
    freq, rms_PLL(:,1),'b*');
%    EX_PLL_NoiseRad_BoostOn(:,1), EX_PLL_NoiseRad_BoostOn(:,2),'r',     freq, rms_PLL(:,2),'r*'...

legend('Measured PLL Noise','Measured Shot Noise', ...
    'PFD Noise', ...
    'Suppressed Laser Frequency Noise','Suppressed Fiber Noise', 'Calculated Shot Noise', 'Photodetector Dark Noise',...
    'RMS','Location', 'SouthWest');
xlabel('Frequency [Hz]');
ylabel('Amplitude Spectrum [rad/SqrtHz]');
set(ll,'LineWidth',3);
ylim([10^ 7 3e 2]);
set(gca, 'Ytick', 10.^( 7:2));
xlim([1 10^6]);
title('X arm Phase Locking Loop Noise at Error Point');
grid on;
set(findall(gcf, 'Type', 'text'), 'FontSize', 18, 'FontWeight','bold');
set(findall(gcf, 'Type', 'axes'), 'FontSize', 18,'FontWeight','bold');
```

```

%% Out of Loop PLL Noise
% load model
EX_PDH_OpGain = 0;
D_REL = db2mag(22);
GainFast =0;
GainSlow =0;
IMCTEST = 1;
ALScontrol_X;

% Data supressed by PLL loop     sent INTO PDH
% Convert data from rad to V
EX_PLLNoise_BoostOn(:,2) =  EX_PLLNoise_BoostOn(:,2).* 180/pi/36;
EX_PLL_NoiseSpecV_BoostOn(:,2) = EX_PLL_NoiseRad_BoostOn(:,2) .* 180/pi/36;
EX_PLL_NoiseSpecV_BoostOff(:,2) = EX_PLL_NoiseRad_BoostOff(:,2) .* 180/pi/36;
shot_noise_V = shot_noise .* 180/pi/36;

f_temp = EX_PLL_NoiseRad_BoostOn(:,1);
EX_PLL_TF_noise = mybodesys(sys(12,27),f_temp); %G/1+G
EX_PLL_NoiseSpecHz_BoostOn = abs( EX_PLL_NoiseSpecV_BoostOn(:,2).* EX_PLL_TF_noise);
     % units: Hz/SqrtHz
EX_PLL_NoiseSpecRad_BoostOn = EX_PLL_NoiseSpecHz_BoostOn ./f_temp;

f_temp = EX_PLL_NoiseRad_BoostOff(:,1);
EX_PLL_TF_noise = mybodesys(sys(12,27),f_temp); %G/1+G
EX_PLL_NoiseSpecHz_BoostOff = abs( EX_PLL_NoiseSpecV_BoostOff(:,2).* EX_PLL_TF_noise
    ); % units: Hz/SqrtHz
EX_PLL_NoiseSpecRad_BoostOff = EX_PLL_NoiseSpecHz_BoostOff ./f_temp; % units: rad/
    SqrtHz

EX_PLL_TF_noise = mybodesys(sys(12,27),f); %G/1+G
EX_PLL_TF_ShotNoise = abs(shot_noise_V .* EX_PLL_TF_noise'); % units: Hz/SqrtHz
EX_PLL_TF_PFDNoise = abs(PFD_noise_V .* EX_PLL_TF_noise');   % units: Hz/SqrtHz
EX_PLL_TF_ShotNoise_Rad = EX_PLL_TF_ShotNoise./f; % units: rad/SqrtHz
EX_PLL_TF_PFDNoise_Rad = EX_PLL_TF_PFDNoise./f;   % units: rad/SqrtHz

TF_endlaserfreq = mybodesys(sys(12,4),f); %1/1+G
EX_LaserFreqNoise_rad = abs(NPRO_freqfluc .* TF_endlaserfreq'); % rad/sqrtHz,
    supressed laser noise due to locking
EX_LaserFreqNoise_Hz = f .* EX_LaserFreqNoise_rad; % convert to Hz/sqrtHz

TF_fiber = mybodesys(sys(22,4),f); %G/1+G
EX_fiber = abs(Fiber_noise_rad .* TF_fiber'); % rad/sqrtHz


% interpolation to same frequency:
f_temp = EX_PLL_NoiseRad_BoostOff(:,1);
[b, i, j] = unique(f_temp);
EX_PLL_NoiseSpecRad_BoostOff_Int = interp1(b, EX_PLL_NoiseSpecRad_BoostOff(i), f, '
    linear', 'extrap');

Sum_EX_Laser = sqrt(EX_PLL_NoiseSpecRad_BoostOff_Int.^2 + EX_PLL_TF_ShotNoise_Rad.^2
     + EX_PLL_TF_PFDNoise_Rad.^2 + EX_LaserFreqNoise_rad.^2 + EX_fiber.^2);

```

```
figure(111)
clf;
set(gcf, 'color', 'w');
ll=loglog(EX_PLL_NoiseRad_BoostOff(:,1), EX_PLL_NoiseSpecRad_BoostOff, ...
    f,EX_PLL_TF_ShotNoise_Rad,...
    f,EX_PLL_TF_PFDNoise_Rad, ...
    f, EX_LaserFreqNoise_rad, ...
    f, EX_fiber, 'g',...
    f, Sum_EX_Laser,' ');
legend('Measured PLL noise ', 'PLL shot noise', 'PLL PFD noise','Free Running Laser Noise', ...
    'Estimated Fiber Noise','Sum of Frequency Noise');
xlabel('Frequency [Hz]')
ylabel('Amplitude Spectrum [rad/SqrtHz]')
set(ll, 'LineWidth',3);
title('X arm out of loop PLL Noise');
xlim([1 10^6]);
ylim([10^ 12 5]);
set(gca,'Ytick',10.^( 12:5));
grid on;
set(findall(gcf, 'Type', 'text'), 'FontSize', 18, 'FontWeight','bold');
set(findall(gcf, 'Type', 'axes'), 'FontSize', 18,'FontWeight','bold');
%% Open Loop Transfer Function of PLL
% ** check off/on   these are flipped from alog
EX_PLL_OpenLoopTF_mag_BoostOff = load('EX_PLL_OpenLoopTFmag_BoostOff_Jan132014');
EX_PLL_OpenLoopTF_mag_BoostOn = load('EX_PLL_OpenLoopTFmag_BoostOn_Jan132014');
EX_PLL_OpenLoopTF_phase_BoostOff = load('EX_PLL_OpenLoopTFphase_BoostOff_Jan132014');
EX_PLL_OpenLoopTF_phase_BoostOn = load('EX_PLL_OpenLoopTFphase_BoostOn_Jan132014');
EX_PLL_OpenLoopTF_high_BoostOn = load('EX_PLL_OpenLoopTF_High_BoostOn_Jan132014');
EX_PLL_OpenLoopTF_high_BoostOff = load('EX_PLL_OpenLoopTF_High_BoostOff_Jan132014');
% note: phase of data is of by 180 deg because test2/test1 have different signs

% make data into .sys file
EX_PLL_OpenLoopTF_BoostOff_sys = MakeSYS(EX_PLL_OpenLoopTF_mag_BoostOff.test2(:,2), EX_PLL_OpenLoopTF_phase_BoostOff.test2(:,2),EX_PLL_OpenLoopTF_mag_BoostOff.test2(:,1));
EX_PLL_OpenLoopTF_BoostOn_sys = MakeSYS(EX_PLL_OpenLoopTF_mag_BoostOn.test(:,2), EX_PLL_OpenLoopTF_phase_BoostOn.test3(:,2),EX_PLL_OpenLoopTF_mag_BoostOn.test(:,1));
EX_PLL_OpenLoopTF_High_BoostOff_sys = MakeSYS(EX_PLL_OpenLoopTF_high_BoostOff.test(:,2),EX_PLL_OpenLoopTF_high_BoostOff.test(:,4),EX_PLL_OpenLoopTF_high_BoostOff.test(:,1));
EX_PLL_OpenLoopTF_High_BoostOn_sys = MakeSYS(EX_PLL_OpenLoopTF_high_BoostOn.test2(:,2),EX_PLL_OpenLoopTF_high_BoostOn.test2(:,4),EX_PLL_OpenLoopTF_high_BoostOn.test2(:,1));
% model
ModelTF_OpenLoop = EX_PZT.sys * EX_PFD.sys * EX_PLL_SERVO_COMMPATH.sys * EX_FIBR_SERVO_GEN.sys * EX_PZT_NOTCH *FAST_GAIN;
EX_PLL_OLTF = mybodesys(sys(32,27),f)./mybodesys(sys(33,27),f);

figure(110);
clf;
subplot(2,1,1)
```

```
% sl=semilogx(EX_PLL_OpenLoopTF_mag_BoostOff.test2(:,1), EX_PLL_OpenLoopTF_mag_BoostOff.test2(:,2) ,...
%      EX_PLL_OpenLoopTF_high_BoostOn.test2(:,1), EX_PLL_OpenLoopTF_high_BoostOn.test2(:,2) ,...
%      f, mag2db(abs(EX_PLL_OLTF)));
sl=semilogx(EX_PLL_OpenLoopTF_mag_BoostOff.test2(:,1), EX_PLL_OpenLoopTF_mag_BoostOff.test2(:,2) ,...
     f, mag2db(abs(EX_PLL_OLTF)));
%    EX_PLL_OpenLoopTF_mag_BoostOn.test(:,1), EX_PLL_OpenLoopTF_mag_BoostOn.test(:,2) ,...

grid on;
xlim([5e3 4e5]);
ylabel('Magnitude [dB]');
set(sl, 'LineWidth', 3);
subplot(2,1,2)
% sl = semilogx(EX_PLL_OpenLoopTF_mag_BoostOff.test2(:,1),unwrap(EX_PLL_OpenLoopTF_phase_BoostOff.test2(:,2).*pi/180).*180/pi + 180, ...
%      EX_PLL_OpenLoopTF_high_BoostOn.test2(:,1),unwrap(EX_PLL_OpenLoopTF_high_BoostOn.test2(:,4).*pi/180).*180/pi + 180,...
%      f, angle(EX_PLL_OLTF)*180/pi);
sl = semilogx(EX_PLL_OpenLoopTF_mag_BoostOff.test2(:,1),unwrap(EX_PLL_OpenLoopTF_phase_BoostOff.test2(:,2).*pi/180).*180/pi + 180, ...
     f, angle(EX_PLL_OLTF)*180/pi);
%    EX_PLL_OpenLoopTF_mag_BoostOn.test(:,1), EX_PLL_OpenLoopTF_phase_BoostOn.test3(:,2) + 180, ...

xlim([5e3 4e5]);
set(sl, 'LineWidth', 3);
hold on;
grid on;
xlabel('Frequency [Hz]');
ylabel('Phase [deg]');
suptitle('X arm PLL Open Loop Transfer Function');
%legend('Data Boost Off' ,'High Data Boost On', 'Model Boost Off');
legend('Data' , 'Model');
set(gcf, 'color', 'w');
set(findall(gcf, 'Type', 'text'), 'FontSize', 18, 'FontWeight','bold');
set(findall(gcf, 'Type', 'axes'), 'FontSize', 18,'FontWeight','bold');


tf_closed = mybodesys(sys(33,27),f);
tf_blah = mybodesys(sys(32,27),f);
tf_open = tf_blah./tf_closed;
figure(20);
clf;
suptitle('Phase Locking Loop Transfer Functions')
subplot(3,1,[1 2]);
ll=loglog(f,abs(tf_blah),f,abs(tf_closed),f,abs(tf_open));
set(ll,'LineWidth',3);
ylabel('Magnitude [abs]');
xlim([1 10^6]);
ylim([10^ 14 10^14]);
set(gca,'Ytick',10.^( 14:4:14))
```

```
grid on
%legend('G/1 G', 'Closed Loop','Open Loop');
legend('Closed Loop', 'Sensitivity Function','Open Loop');
subplot(3,1,3)
sl = semilogx(f,angle(tf_blah)*180/pi,f,angle(tf_closed)*180/pi,f,angle(tf_open)*180/pi);
set(sl,'LineWidth',3);
ylabel('Phase [deg]');
xlabel('Frequency [Hz]');
set(gcf,'Color','w');
grid on;
xlim([1 10^6]);
set(gca,'Ytick',100*( 6:1))
set(findall(gcf, 'Type', 'text'), 'FontSize', 18, 'FontWeight','bold');
set(findall(gcf, 'Type', 'axes'), 'FontSize', 18,'FontWeight','bold');

%% PLL Servo Board
% data
EX_PLL_ServoBoardTF_mag_BoostOff = load('EX_PLL_ServoBoard_TFmag_BoostOff_Jan132014');
EX_PLL_ServoBoardTF_mag_BoostOn = load('EX_PLL_ServoBoard_TFmag_BoostOn_Jan132014');
EX_PLL_ServoBoardTF_phase_BoostOff = load('EX_PLL_ServoBoard_TFphase_BoostOff_Jan132014');
EX_PLL_ServoBoardTF_phase_BoostOn = load('EX_PLL_ServoBoard_TFphase_BoostOn_Jan132014');
% Unwrp phase of data
EX_PLL_ServoBoardTF_phase_BoostOff.test8(:,2) = unwrap(EX_PLL_ServoBoardTF_phase_BoostOff.test8(:,2)*pi/180)*180/pi;
EX_PLL_ServoBoardTF_phase_BoostOn.test10(:,2) = unwrap(EX_PLL_ServoBoardTF_phase_BoostOn.test10(:,2)*pi/180)*180/pi;
% make data into .sys file
EX_PLL_ServoBoardTF_BoostOff_sys = MakeSYS(EX_PLL_ServoBoardTF_mag_BoostOff.test7(:,2),EX_PLL_ServoBoardTF_phase_BoostOff.test8(:,2),EX_PLL_ServoBoardTF_mag_BoostOff.test7(:,1));
EX_PLL_ServoBoardTF_BoostOn_sys = MakeSYS(EX_PLL_ServoBoardTF_mag_BoostOn.test9(:,2),EX_PLL_ServoBoardTF_phase_BoostOn.test10(:,2),EX_PLL_ServoBoardTF_mag_BoostOn.test9(:,1));

% model
ModelTF_PLL_ServoBoard = EX_PLL_SERVO_COMMPATH.sys * EX_FIBR_SERVO_GEN.sys * FAST_GAIN;

plotOpt = bodeoptions('cstprefs');
plotOpt.FreqUnits = 'Hz';
plotOpt.PhaseWrapping = 'on';
plotOpt.XLim = [50 3e5];
plotOpt.YLim{1} = [ 55, 0];
plotOpt.YLim{2} = [ 180, 0];
plotOpt.Title.FontSize = 20;
plotOpt.Title.FontWeight = 'Bold';
plotOpt.XLabel.FontSize = 18;
plotOpt.XLabel.FontWeight = 'Bold';
plotOpt.YLabel.FontSize = 18;
plotOpt.YLabel.FontWeight = 'Bold';
```

```
plotOpt.TickLabel.FontSize = 18;
plotOpt.TickLabel.FontWeight = 'Bold';
plotOpt.TickLabel.Color = [0 0 0];

figure(1005)
clf;
bodeplot(ModelTF_PLL_ServoBoard, EX_PLL_ServoBoardTF_BoostOff_sys,
    EX_PLL_ServoBoardTF_BoostOn_sys,plotOpt);
hold on;
title('Phase Locking Loop Common Mode Board');
axes_handles = findall(gcf, 'type', 'axes');
legend(axes_handles(3),'Model Boost Off', 'Data Boost Off', 'Data Boost On','
    Location','NorthEast');
set(gcf, 'color', 'w');
grid on;
h = findobj(gcf,'type','line');
set(h,'linewidth',3);
%set(findall(gcf, 'type', 'axes'), 'FontSize', 14,'FontWeight','bold');


















%% EX PDH Open Loop TF
% alog 9401
% PLL Servo Board Settings
%   Input 1 Pol: NEG
%   Input 1 Gain: 0dB
%   Common Compensation: ON
%   Generic Filter: ON
%   Fast Option: ON
%   Fast Gain:  8dB
%   Boost 1: Off
%   Rest: Off/Zero
% PDH Servo Board Settings
%   Input 1 Pol; POS
%   Input 1 Gain:  11dB
%   Common Compensation: ON
%   Boost 1: On
%   Rest: off/zero
```

```

load('EX_PDH_OpenLoopTF_mag1.txt');
load('EX_PDH_OpenLoopTF_mag2.txt');
load('EX_PDH_OpenLoopTF_mag3.txt');
load('EX_PDH_OpenLoopTF_mag4.txt');
load('EX_PDH_OpenLoopTF_mag5.txt');
load('EX_PDH_OpenLoopTF_mag6.txt');
load('EX_PDH_OpenLoopTF_mag7.txt');
load('EX_PDH_OpenLoopTF_phase1.txt');
load('EX_PDH_OpenLoopTF_phase2.txt');
load('EX_PDH_OpenLoopTF_phase3.txt');
load('EX_PDH_OpenLoopTF_phase4.txt');
load('EX_PDH_OpenLoopTF_phase5.txt');
load('EX_PDH_OpenLoopTF_phase6.txt');
load('EX_PDH_OpenLoopTF_phase7.txt');

%% EX PDH Open Loop TF
% alog 9574
% PLL Servo Board Settings
%   Input 1 Pol: NEG
%   Input 1 Gain: 0dB
%   Common Compensation: ON
%   Generic Filter: ON
%   Fast Option: ON
%   Fast Gain:  8dB
%   Boost 1: Off
%   Rest: Off/Zero
% PDH Servo Board Settings
%   Input 1 Pol; POS
%   Input 1 Gain:  1dB
%   Common Compensation: ON
%   Boost 1: On
%   Rest: off/zero
load('EX_PDH_OpenLoopTF_mag.TXT');
load('EX_PDH_OpenLoopTF_phase.TXT');
load('EX_PDH_OpenLoopTF_phase_zoom.TXT');
load('EX_PDH_OpenLoopTF_mag_zoom.TXT'); % gives FSR resonance at 37.752kHz and arm
    cavity length of 3970.6m
EX_PDH_OpenLoopTF_phase(:,2) =unwrap(EX_PDH_OpenLoopTF_phase(:,2)*pi/180)*180/pi;


%% EX PDH Open Loop TF
% alog 9708    adjusted RF Freq (would change optical gain)
% PLL Servo Board Settings
%   Input 1 Pol: NEG
%   Input 1 Gain: 0dB
%   Common Compensation: ON
%   Generic Filter: ON
%   Fast Option: ON
%   Fast Gain:  8dB
%   Boost 1: ON
%   Rest: Off/Zero
% PDH Servo Board Settings
%   Input 1 Pol: NEG
```

```
%   Input 1 Gain:  1dB
%   Common Compensation: ON
%   Boost 1: On
%   Rest: off/zero (unless specified)
load('EX_PDH_OpenLoopTF_mag_Nom.txt');
load('EX_PDH_OpenLoopTF_phase_Nom.txt');
load('EX_PDH_OpenLoopTF_phase_6dbFast.txt');
load('EX_PDH_OpenLoopTF_mag_6dbFast.txt'); % 6dB of gain in fast path added
load('EX_PDH_OpenLoopTF_mag_Boost2On.txt');
load('EX_PDH_OpenLoopTF_phase_Boost2On.txt');
EX_PDH_OpenLoopTF_phase_Nom(:,2) =unwrap(EX_PDH_OpenLoopTF_phase_Nom(:,2)*pi/180)
    *180/pi;

% alog 9946
load('EX_PDH_TFOpenLoop_phase.txt');
load('EX_PDH_TFOpenLoop_mag.txt');
EX_PDH_TFOpenLoop_phase(:,2) =unwrap(EX_PDH_TFOpenLoop_phase(:,2)*pi/180)*180/pi;

% alog 10227
% PDH Servo Board Settings (differ from above)
%   Input 1 Gain:  7dB
%   Boost 2: On
% Mod Freq: 24.407363 MHz, Demod phase: 120.7 deg
load('EX_PDH_OLTF_mag.txt');
load('EX_PDH_OLTF_phase.txt');


% Calibration: Using PDH error signal 370mV peak to peak; units in
slope_X = 7.8972e3; % Hz/Volts !! slope and optical gain should be the same; they
    are off by factor of 5.465
%slope = 1/EX_PDH_OpGain;
EX_PDH_OpGain = 1/slope_X * 5.465;

%Transfer function of REFL Servo loop
f=logspace(0,6,3000);
D_REL = 0; % AO path off
GainFast =0;
GainSlow =0;
IMCTEST = 0;
ALScontrol_X;

EX_REFL_SERVO_1 =mybodesys(sys(2,3),f);
EX_REFL_SERVO_2 =mybodesys(sys(1,3),f);
TF_EX_REFL_SERVO = EX_REFL_SERVO_1./EX_REFL_SERVO_2;

% clean up of phase
for i=300:length(EX_PDH_OLTF_phase(:,2))
    if EX_PDH_OLTF_phase(i,2) >  80
        EX_PDH_OLTF_phase(i,2)= EX_PDH_OLTF_phase(i,2) 360;
    end
end

figure(103)
clf;
```

```
set(gcf, 'color', 'w');
st = suptitle('X arm Pound Drever Hall Open Loop Transfer Function');
set(st, 'fontSize',20);
subplot(3,1,[1 2])
sl=semilogx(f, mag2db(abs(TF_EX_REFL_SERVO)), EX_PDH_OLTF_mag(:,1), EX_PDH_OLTF_mag
    (:,2));
set(sl, 'LineWidth', 3);
ylabel('Magnitude [dB]','fontSize', 18)
ll=legend('Model', 'Data', 'Location', 'SouthWest');
set(ll, 'fontSize',18);
set(gca, 'FontSize', 18);
grid on;
ylim([ 50 30]);
xlim([5e2 4e4]);
subplot(3,1,3)
sl=semilogx(f, angle(TF_EX_REFL_SERVO)/pi*180,EX_PDH_OLTF_phase(:,1),
    EX_PDH_OLTF_phase(:,2)+180);
set(sl, 'LineWidth', 3);
ylabel('Phase [Deg]','fontSize', 18)
xlabel('Frequency [Hz]','fontSize', 18)
set(gca, 'FontSize', 18);
grid on;
xlim([5e2 4e4]);
ylim([ 100 100])
set(findall(gcf, 'Type', 'text'), 'FontSize', 18, 'FontWeight','bold');
set(findall(gcf, 'Type', 'axes'), 'FontSize', 18,'FontWeight','bold');


tf_closed = mybodesys(sys(1,3),f);
tf_blah = mybodesys(sys(2,3),f);
tf_open = tf_blah./tf_closed;
figure(21);
clf;
suptitle('Pound Drever Hall Locking Loop Transfer Functions')
subplot(3,1,[1 2]);
ll=loglog(f,abs(tf_blah),f,abs(tf_closed),f,abs(tf_open));
set(ll,'LineWidth',3);
ylabel('Magnitude [abs]');
ylim([10^ 6 10^5]);
set(gca,'Ytick',10.^( 6:2:5))
grid on
%legend('G/1 G', 'Closed Loop','Open Loop');
legend('Closed Loop', 'Sensitivity Function','Open Loop');
subplot(3,1,3)
sl = semilogx(f,angle(tf_blah)*180/pi,f,angle(tf_closed)*180/pi,f,angle(tf_open)
    *180/pi);
set(sl,'LineWidth',3);
ylabel('Phase [deg]');
xlabel('Frequency [Hz]');
set(gcf,'Color','w');
grid on;
set(gca,'Ytick',100*( 6:1))
set(findall(gcf, 'Type', 'text'), 'FontSize', 18, 'FontWeight','bold');
set(findall(gcf, 'Type', 'axes'), 'FontSize', 18,'FontWeight','bold');
```

```

%% EX PDH Error Signal Power Spectrum (reflection cav poles removed!)

load('EX_PDH_Noise.TXT');
load('EX_PDH_Noise_High.TXT');
load('EX_PDH_Noise_Low.TXT');
load('EX_PDH_NoiseSpectrum.txt');
load('EX_PDH_NoiseSpectrum_BoostOff_02202014.TXT');
load('EX_PDH_NoiseSpectrum_BoostOn_02202014.TXT');
load('EX_PDH_NoiseSpectrum_BoostOn_Low.TXT');

% alog 10286
% PLL boost 1 ON/OFF, PDH Boost 2 ON/Off
load('EX_PDH_NoiseSpecV_PLLBoost1Off_PDHBoost2Off.txt');
load('EX_PDH_NoiseSpecV_PLLBoost1Off_PDHBoost2On.txt');
load('EX_PDH_NoiseSpecV_PLLBoost1On_PDHBoost2Off.txt');
load('EX_PDH_NoiseSpecV_PLLBoost1On_PDHBoost2On.txt');

data_2(:,:,1) = EX_PDH_NoiseSpecV_PLLBoost1Off_PDHBoost2Off;
data_2(:,:,2) = EX_PDH_NoiseSpecV_PLLBoost1Off_PDHBoost2On;
data_2(:,:,3) = EX_PDH_NoiseSpecV_PLLBoost1On_PDHBoost2Off;
data_2(:,:,4) = EX_PDH_NoiseSpecV_PLLBoost1On_PDHBoost2On;

% alog 9574 w/ HEPA fan on
load('EX_PDH_ShotNoise.TXT');
% w/ hepa fan off
load('EX_PDH_ShotNoise_FanOff.txt');
%load('EX_PDH_ShotNoiseSpectrum.txt');

% alog 10611
load('EX_PDH_ShotNoiseAmpSpec.txt');
EX_PDH_ShotNoiseSpectrum(:,:) = EX_PDH_ShotNoiseAmpSpec(:,:);

% dark noise
% measured with ITM misaligned, PD blocked, out of IMON, HEPA fan off
%(alog 9574)
load('EX_PDH_DarkNoise.txt')

% shot noise
% measured with ITM misaligned out of IMON
% green REFL A PD reads 6.28mW, 3V at 30dB gain setting (nominally read
% 9.44mW when ITM alinged)
elec = 1.6e 19; % charge of electron
LegPD_power = 6.2e 3; % watts
LegPD_trans = 50;  % 1kOhm at RF
LegPD_curr = sqrt(LegPD_power*LegPD_trans);
shot_noise_temp = sqrt(2*elec*LegPD_curr)/Carrier_curr; % shot noise in 1/SqrtHz ?? !! same carrier current as before??
shot_noise_2 = shot_noise_temp * ones(size(f));




% Data from Daniel     measured from ALS COMM VCO so there is a factor of 10
% for FDD and a factor of 2 for double pass AOM. This only holds up until
```

```
% MCL MCF crossover when length path suppresed the VCO ~20Hz)
load('VCO_FDD_ssb_phase_noise_140415_F.txt'); % data units: dBc/sqrtHz
load('VCO_FDD_freq_noise_140415.txt'); % data units: Hz/sqrtHz
f_VCO = VCO_FDD_freq_noise_140415(:,1);
VCO_noise_Hz = VCO_FDD_freq_noise_140415(:,2);
VCO_noise_rad = VCO_noise_Hz ./ f_VCO; % data units: rad/sqrtHz

for i=1:4
    f_temp = data_2(:,1,i);
    data_rad_2(:,2,i) = data_2(:,2,i) ./EX_PDH_OpGain ./f_temp;
    data_3(:,2,i) = data_2(:,2,i) ./EX_PDH_OpGain;
end
% to get rid of cavity pole precense in measurements of PHD error signal;
% note we do not handle the notches at the FSR

for i=1:4;
    f_temp = data_2(:,1,i);
    AntiCav_TF = mybodesys(EX_REFL_CAVITY_REFL.sys, f_temp);
    data_rad_2(:,2,i) = abs(data_rad_2(:,2,i) ./ AntiCav_TF);
    data_3(:,2,i) = abs(data_3(:,2,i) ./ AntiCav_TF);
end

% converts shot and dark noise from V to rad (below calib doesnt have
% cavity pole)
% TF_PDH = mybodesys(sys(2,5),EX_PDH_DarkNoise(:,1));
% EX_PDH_DarkNoiseRad(:,2) = abs(EX_PDH_DarkNoise(:,2) .* TF_PDH)./EX_PDH_DarkNoise
    (:,1);
% TF_PDH = mybodesys(sys(2,5),EX_PDH_ShotNoiseSpectrum(:,1));
% EX_PDH_ShotNoiseSpectrumRad(:,2)=abs(EX_PDH_ShotNoiseSpectrum(:,2) .* sqrt
    (9.44/6.28).* TF_PDH)./EX_PDH_ShotNoiseSpectrum(:,1);

% convert V to Hz
EX_PDH_ShotNoiseSpectrum(:,2) = 1/EX_PDH_OpGain .* EX_PDH_ShotNoiseSpectrum(:,2) .*
    sqrt(9.44/6.28); %also scale for the power
EX_PDH_DarkNoise(:,2) = 1/EX_PDH_OpGain .* EX_PDH_DarkNoise(:,2);

% conver to rad/sqrtHz
EX_PDH_ShotNoiseSpectrumRad(:,2) = EX_PDH_ShotNoiseSpectrum(:,2) ./
    EX_PDH_ShotNoiseSpectrum(:,1);
EX_PDH_DarkNoiseRad(:,2) = EX_PDH_DarkNoise(:,2) ./EX_PDH_DarkNoise(:,1);


% interpolation to same frequency:
f_temp = EX_PDH_ShotNoiseSpectrum(:,1);
[b, i, j] = unique(f_temp);
EX_PDH_ShotNoiseSpectrum_Int = interp1(b, EX_PDH_ShotNoiseSpectrum(i,2), f, 'linear'
    , 'extrap');
EX_PDH_ShotNoiseSpectrum_Int(2501:3000) = EX_PDH_ShotNoiseSpectrum_Int(2500);

f_temp = EX_PDH_DarkNoise(:,1);
[b, i, j] = unique(f_temp);
EX_PDH_DarkNoise_Int = interp1(b, EX_PDH_DarkNoise(i,2), f, 'linear', 'extrap');
EX_PDH_DarkNoise_Int(2501:3000) = EX_PDH_DarkNoise_Int(2500);
```

```


% PLL stuff supressed by loop gain of PDH
TF_loopsup = mybodesys(sys(1,3),f);
EX_PLL_2_PDH_TF_ShotNoise_Rad = abs(EX_PLL_TF_ShotNoise_Rad .* TF_loopsup' );
EX_PLL_2_PDH_TF_PFDNoise_Rad = abs(EX_PLL_TF_PFDNoise_Rad .* TF_loopsup');
EX_2_PDH_LaserFreqNoise_rad = abs(EX_LaserFreqNoise_rad .* TF_loopsup');
EX_2_PDH_fiber = abs(EX_fiber .* TF_loopsup');
Sum_EX_2_PDH_Laser = abs(Sum_EX_Laser .* TF_loopsup');
f_temp = EX_PLL_NoiseRad_BoostOff(:,1);
TF_loopsup = mybodesys(sys(1,3),f_temp);
EX_PLL_2_PDH_NoiseSpecRad_BoostOff = abs(EX_PLL_NoiseSpecRad_BoostOff .* TF_loopsup);


% Compute RMS
for i=1:4
    rms_PDH(:, i)=[( 1.*cumtrapz(flipud(data_2(:,1, i)), flipud(data_rad_2(:, 2,i)).^2)).^(0.5)]';
end
rms_PDH=flipud(rms_PDH);
freq=data_2(:,1,1);

figure(611)
clf;
set(gcf, 'color', 'w');
ll=loglog(data_2(:,1,2), data_rad_2(:,2,2) ,...
    EX_PDH_ShotNoiseSpectrum(:,1),EX_PDH_ShotNoiseSpectrumRad(:,2) ,...
    EX_PDH_DarkNoise(:,1),EX_PDH_DarkNoiseRad(:,2) ,...
    EX_PLL_NoiseRad_BoostOff(:,1), EX_PLL_2_PDH_NoiseSpecRad_BoostOff, ...
    f_VCO,VCO_noise_rad,...
    f,EX_PLL_2_PDH_TF_ShotNoise_Rad,...
    f,EX_PLL_2_PDH_TF_PFDNoise_Rad, ...
    f, EX_2_PDH_LaserFreqNoise_rad, ...
    f, EX_2_PDH_fiber, 'g',...
    freq, rms_PDH(:,2),'b *');
legend('Measured PDH noise','PDH shot noise','PDH dark noise','PLL noise ','VCO noise', 'PLL shot noise', 'PLL PFD noise','Free running laser noise', ...
    'Fiber noise','RMS PDH','Location','SouthWest');
xlabel('Frequency [Hz]')
ylabel('Amplitude Spectrum [rad/SqrtHz]')
set(ll,'LineWidth',3);
title('X arm in loop PDH Noise');
xlim([1 10^6]);
ylim([10^ 12 1]);
set(gca, 'Ytick', 10.^( 12:5));
grid on;
set(findall(gcf, 'Type', 'text'), 'FontSize', 18, 'FontWeight','bold');
set(findall(gcf, 'Type', 'axes'), 'FontSize', 18,'FontWeight','bold');

figure(612)
clf;
set(gcf, 'color', 'w');
ll=loglog(data_2(:,1,2), data_rad_2(:,2,2) ,...
```

```
    EX_PDH_ShotNoiseSpectrum(:,1),EX_PDH_ShotNoiseSpectrumRad(:,2),...
    EX_PDH_DarkNoise(:,1),EX_PDH_DarkNoiseRad(:,2),...
    f_VCO,VCO_noise_rad,...
    f, Sum_EX_2_PDH_Laser, 'g',...
    freq, rms_PDH(:,2),'b*');
legend('PDH error signal','PDH shot noise','PDH dark noise','VCO noise','Laser noise', ...
    'RMS PDH Error Sig');
set(ll,'LineWidth',1.5);
xlabel('Frequency [Hz]')
ylabel('Amplitude Spectrum [rad/SqrtHz]')
title('X arm in loop PDH Noise');
xlim([1 10^5]);
ylim([10^ 8 1]);
set(gca, 'Ytick', 10.^( 8:5));
grid on;
set(findall(gcf, 'Type', 'text'), 'FontSize', 18, 'FontWeight','bold');
set(findall(gcf, 'Type', 'axes'), 'FontSize', 18,'FontWeight','bold');


% figure(612)
% clf;
% set(gcf, 'color', 'w');
% loglog(data_2(:,1,2), data_3(:,2,2),...
%      f, EX_PDH_ShotNoiseSpectrum_Int,...
%      f, EX_PDH_DarkNoise_Int,...
%      EX_PLL_NoiseRad_BoostOff(:,1), EX_PLL_NoiseSpecHz_BoostOff, ...
%      f, EX_PLL_TF_ShotNoise,...
%      f, EX_PLL_TF_PFDNoise, ...
%      f, EX_LaserFreqNoise_Hz,...
%      f,Fiber_noise_Hz,'g')
% legend('PDH error signal','PDH shot noise','PDH Dark noise','EX PLL noise ', 'EX PLL shot noise', 'EX PLL PFD noise','Free Running Laser Noise', ...
%     'Fiber Noise');
% xlabel('Frequency [Hz]')
% ylabel('Amplitude Spectrum [Hz/SqrtHz]')
% title('EX PDH Noise');
% grid on;



%% Projection to Corner Noise (includes green arm cavity poles in trans)
f=logspace(0,6,3000);
wCavX = 2*pi*2000;
wCavY =  2*pi*600;
EX_PDH_OpGain = 1/slope_X * 5.465;
D_REL = 0; % AO path off
GainFast =0;
GainSlow =0;
IMCTEST = 0;
ALScontrol_X;

f_temp = EX_PLL_NoiseRad_BoostOff(:,1);
EX_2_C_PLL_TF_noise = mybodesys(sys(5,1),f_temp);
```

```matlab
EX_2_C_PLL_Noise = abs(EX_PLL_NoiseSpecRad_BoostOff.* EX_2_C_PLL_TF_noise); % units: rad/SqrtHz
EX_2_C_PLL_TF_noise = mybodesys(sys(5,1),f);
EX_2_C_PLL_TF_ShotNoise = abs(EX_PLL_TF_ShotNoise_Rad .* EX_2_C_PLL_TF_noise'); % units: rad/SqrtHz
EX_2_C_PLL_TF_PFDNoise = abs(EX_PLL_TF_PFDNoise_Rad .* EX_2_C_PLL_TF_noise');   % units: rad/SqrtH

TF_endlaserfreq = mybodesys(sys(5,1),f);
EX_2_C_LaserFreqNoise = abs(EX_LaserFreqNoise_rad .* TF_endlaserfreq'); % rad/sqrtHz, supressed laser noise due to locking
TF_C_Fiber = mybodesys(EX_REFL_CAVITY_TR.sys,f);
EX_2_C_FiberNoise = abs(EX_2_PDH_fiber .* TF_C_Fiber');
EX_2_C_Sum_Laser = abs(Sum_EX_2_PDH_Laser .* TF_C_Fiber');

% mytery gain btwn optical gain and slope
mysterygain = (1/slope_X)/EX_PDH_OpGain;
f_temp_2 = data_2(:,1,2);
%EX_2_C_PDH_TF_noise = mybodesys(sys(5,5),f_temp_2);
EX_2_C_PDH_TF_noise = mybodesys(sys(36,5)/EX_REFL_CAVITY_REFL.sys * EX_REFL_CAVITY_TR.sys ,f_temp_2);
EX_2_C_PDH_NoiseSpectrum = abs(data_3(:,2,2) .* EX_2_C_PDH_TF_noise)./f_temp_2;  % not exactly correct...??
%EX_2_C_PDH_TF_noise = mybodesys(sys(5,5),f);
EX_2_C_PDH_TF_noise = mybodesys(sys(36,5)*EX_REFL_CAVITY_TR.sys,f);
EX_2_C_PDH_ShotNoiseSpectrum = abs(EX_PDH_ShotNoiseSpectrum_Int.* EX_2_C_PDH_TF_noise')./f;
EX_2_C_PDH_DarkNoise = abs(EX_PDH_DarkNoise_Int.* EX_2_C_PDH_TF_noise')./f;
EX_2_C_PDH_TF = mybodesys(sys(5,22),f_VCO);
EX_2_C_PDH_VCONoise = abs(VCO_noise_rad .* EX_2_C_PDH_TF);

rms_Corner(:, i)=[( 1.*cumtrapz(flipud(data_2(:,1, 2)), flipud(EX_2_C_PDH_NoiseSpectrum).^2)).^(0.5)]';
rms_Corner=flipud(rms_Corner);


figure(614)
clf;
set(gcf, 'color', 'w');
ll=loglog(f_temp_2, EX_2_C_PDH_NoiseSpectrum, f, EX_2_C_PDH_ShotNoiseSpectrum, f, EX_2_C_PDH_DarkNoise,...
     f_temp, EX_2_C_PLL_Noise, ...
     f, EX_2_C_PLL_TF_ShotNoise,...
     f,EX_2_C_PLL_TF_PFDNoise,...
     f, EX_2_C_LaserFreqNoise,...
     f, EX_2_C_FiberNoise,'g',...
     f_VCO, VCO_noise_rad,...
     f_temp_2, rms_Corner,'b*');
legend('PDH error signal','PDH shot noise','PDH dark noise','EX PLL noise ', 'EX PLL shot noise', 'EX PLL PFD noise','Free Running Laser Noise','Fiber noise','EX PDH VCO unsuppressed','EX PDH Error RMS','Location','SouthWest');
xlabel('Frequency [Hz]')
ylabel('Amplitude Spectrum [rad/SqrtHz]')
title('X arm Out of Loop PDH Noise');
```

```
set(ll,'LineWidth',3);
grid on;
xlim([1 10^6]);
ylim([1e 15 10^1]);
set(gca,'Xtick',10.^(0:2:6));
set(gca, 'Ytick', 10.^( 15:1));
set(findall(gcf, 'Type', 'text'), 'FontSize', 18, 'FontWeight','bold');
set(findall(gcf, 'Type', 'axes'), 'FontSize', 18,'FontWeight','bold');


figure(615)
clf;
set(gcf, 'color', 'w');
ll=loglog(f_temp_2, EX_2_C_PDH_NoiseSpectrum, f, EX_2_C_PDH_ShotNoiseSpectrum, f,
    EX_2_C_PDH_DarkNoise,f_VCO,VCO_noise_rad,...
     f, EX_2_C_Sum_Laser,...
     f_temp_2,rms_Corner,'b*');
legend('PDH error signal','PDH shot noise','PDH dark noise','PDH VCO Noise
    unsuppressed','EX Laser Noise','EX PDH Error RMS','Location','SouthWest');
xlabel('Frequency [Hz]')
ylabel('Amplitude Spectrum [rad/SqrtHz]')
title('X arm Out of Loop PDH Noise');
set(ll,'LineWidth',3);
grid on;
xlim([1 10^5]);
ylim([10^ 11 10^1]);
set(gca, 'Ytick', 10.^( 11:3));
set(gca,'Xtick',10.^(0:1:5));
set(findall(gcf, 'Type', 'text'), 'FontSize', 18, 'FontWeight','bold');
set(findall(gcf, 'Type', 'axes'), 'FontSize', 18,'FontWeight','bold');

%% ALS COMM TF
% COMM PLL to VCO Board (alog 9559)
%     Input enable: ON
%     Polarity: OFF
%     Gain: 31 dB  !!! DIFFERENT BY +4db In current settings
%     Comm filter 1: ON
%     Comm filter 2: ON
%     Boost: OFF
%     Filter: OFF
%     VCO Compensation: ON
%     Low pass: ON
%     Daughter board: OFF
%     Internal VCO path: OFF

f=logspace(0,6,3000);
wCavX = 2*pi*2000;
wCavY =  2*pi*600;
EX_PDH_OpGain = 0;
D_REL = 0; % AO path off

GainFast =0;
GainSlow =0;
IMCTEST = 0;
```

```
ALScontrol_X;

COMM_PLL_OLT_mag = load('COMM_PLL_OLT_MAG.TXT');
COMM_PLL_OLT_phase = load('COMM_PLL_OLT_PHASE.TXT');
COMM_PLL_OLT_sys = MakeSYS(COMM_PLL_OLT_mag(:,2), COMM_PLL_OLT_phase(:,2),
    COMM_PLL_OLT_mag(:,1));
% from model
COMM_PLL_OLT_model = COMM_PLL_VCO.sys  * CORNER_PFD.sys * CORNER_VCO.sys *
    COMM_PLL_VCO_DCgain.sys; %model is limited by VOC BW which is difficult to
    measure    explains phase diff from data
TF_COMM_PLL_OLTF_model = mybodesys(COMM_PLL_OLT_model,f);



figure(108)
clf;
st = suptitle('Common Mode PLL Open Loop Transfer Function');
set(st ,'fontSize', 18);
subplot(2,1,1)
sl = semilogx(COMM_PLL_OLT_mag(:,1),COMM_PLL_OLT_mag(:,2) 4,f,mag2db(abs(
    TF_COMM_PLL_OLTF_model)));
grid on;
xlim([1e3 1e5]);
ll=legend('Data', 'Model');
set(ll ,'fontSize', 18);
set(gca ,'fontSize', 18);
ylabel('Magnitude [dB]','fontSize', 18);
set(sl,'LineWidth',3);
subplot(2,1,2)
sl = semilogx(COMM_PLL_OLT_phase(:,1),COMM_PLL_OLT_phase(:,2),f,angle(
    TF_COMM_PLL_OLTF_model)*180/pi);
ylabel('Phase [degree]','fontSize', 18);
xlabel('Frequency [Hz]','fontSize', 18);
xlim([1e3 1e5]);
set(sl,'LineWidth',3);
set(gcf, 'color', 'w');
set(gca ,'fontSize', 18);
grid on;
set(findall(gcf, 'Type', 'text'), 'FontSize', 18, 'FontWeight','bold');
set(findall(gcf, 'Type', 'axes'), 'FontSize', 18,'FontWeight','bold');




tf_closed = mybodesys(sys(10,18),f);
tf_blah = mybodesys(sys(11,18),f);
tf_open = tf_blah./tf_closed;
figure(23);
clf;
suptitle('Corner Phase Locking Loop Transfer Functions')
subplot(3,1,[1 2]);
ll=loglog(f,abs(tf_blah),f,abs(tf_closed),f,abs(tf_open));
set(ll,'LineWidth',3);
ylabel('Magnitude [abs]');
xlim([1e0 1e6])
ylim([10^ 9 10^9]);
```

```
set(gca,'Ytick',10.^( 9:2:9))
grid on
%legend('G/1 G', 'Closed Loop','Open Loop');
legend('Closed Loop', 'Sensitivity Function','Open Loop');
subplot(3,1,3)
sl = semilogx(f,angle(tf_blah)*180/pi,f,angle(tf_closed)*180/pi,f,angle(tf_open)
    *180/pi);
xlim([1e0 1e6])
ylim([ 180 180])
set(gca,'Ytick',180*( 1:0.5:1))
set(sl,'LineWidth',3);
ylabel('Phase [deg]');
xlabel('Frequency [Hz]');
set(gcf,'Color','w');
grid on;
set(findall(gcf, 'Type', 'text'), 'FontSize', 18, 'FontWeight','bold');
set(findall(gcf, 'Type', 'axes'), 'FontSize', 18,'FontWeight','bold');

%% ALS COMM Noise
% PFD Noise
% ~460nV/SqrtHz at 140Hz, assume flat for freq we care
PFD_noise = 500e 9*ones(size(f));
PFD_noise = 36 * pi/180 .* PFD_noise; % convert to rad/SqtHz

% shot noise
% COMM BBPD read 88uW alog 9558
% beatnote of 28mBpp, PFD RF power 35dbm
elec = 1.6e 19; % charge of electron
CommPD_power = 88e 6; % watts
CommPD_trans = 1e3;  % 1kOhm at RF ??
CommPD_curr = sqrt(CommPD_power*CommPD_trans);
Carrier_curr = 4e 3 / CommPD_trans ; %??
shot_noise_temp = sqrt(2*elec*CommPD_curr); % shot noise in A/SqrtHz
shot_noise_temp = shot_noise_temp .* CommPD_trans * 36 * pi/180; % shot noise in rad
    /SqrtHz
shot_noise_2 = shot_noise_temp * ones(size(f));

% BBPD noise    taken from EX
BBPD_noise =  119*ones(size(f)); %  119 dBm, at 100Hz Bw
beatnote =   35*ones(size(f)); %  35 dBm, at 100Hz BW (for COMM BBPD)
dBc_BBPD = BBPD_noise   beatnote;
dBc_BBPD_Hz = dBc_BBPD   20; % dividing by 100Hz BW is the same as  20dB
BBPD_noise =  10.^(dBc_BBPD_Hz./20); % dBc to rad/sqrtHz

%BBPD_noise = abs(BBPD_noise .* mybodesys(sys(10,18),f)');

% alog 10231/10243
% COMM PLL gain: 27dB (not 31dB), Boost: ON
% With handoff, amplitude spectrum was taken out of output 2 of CM board
% (i.e. Common path green error signal)

load('Comm_Path_NoiseSpec_Gain9.txt')
load('COMM_PLL_Noise.txt') % ** not the same settings exactly ...

```

```
% PLL Error signal power spectrum measured out of PFD IMON
load('COMM_PLL_Noise.txt')
COMM_PLL_Noise(:,2) = 36 * pi/180 .* COMM_PLL_Noise(:,2); % convert to rad/sqrtHz
% alog 10292
load('COMM_PLL_NoiseSpecRad_PLLBoost1Off_PDHBoost2Off.txt');
load('COMM_PLL_NoiseSpecRad_PLLBoost1Off_PDHBoost2On.txt');
load('COMM_PLL_NoiseSpecRad_PLLBoost1On_PDHBoost2Off.txt');
load('COMM_PLL_NoiseSpecRad_PLLBoost1On_PDHBoost2On.txt');

% alog 10628
% PLL locked, no handoff
% compensation filters engaged and input gain 27dB
load('CommPLL_NoiseSpecV.txt');
load('CommPLL_NoHand_NoiseSpecV.txt');
CommPLL_NoiseSpecRad(:,2) = 36 * pi/180 .* CommPLL_NoHand_NoiseSpecV(:,2); % convert to rad/sqrtHz
% limited by SR785 noise to about 500Hz

f=logspace(0,6,3000);
wCavX = 2*pi*2000;
wCavY =  2*pi*600;
EX_PDH_OpGain = 0;
GainFast = 0;
GainSlow = 0;
IMCTEST = 0;
ALScontrol_X;

% all in rad/sqrtHz, convert in EX_2_C
f_temp = EX_PLL_NoiseRad_BoostOff(:,1);
EX_2_Comm_PLL_TF_noise = mybodesys(sys(10,18),f_temp);
EX_2_Comm_PLL_Noise = abs(EX_2_C_PLL_Noise.* EX_2_Comm_PLL_TF_noise); % units: rad/SqrtHz

Comm_PLL_TF = mybodesys(sys(10,18),f);
EX_2_Comm_Sum_laser = abs(EX_2_C_Sum_Laser.* Comm_PLL_TF');

f_temp_2 = data_2(:,1,2);
EX_2_Comm_PDH_TF_noise = mybodesys(sys(10,18),f_temp_2);
EX_2_Comm_PDH_NoiseSpectrum = abs(EX_2_C_PDH_NoiseSpectrum.* EX_2_Comm_PDH_TF_noise);
AntiCav_TF = mybodesys(EX_REFL_CAVITY_REFL.sys, f_temp_2);
AntiCav_TF2 = mybodesys(EX_REFL_CAVITY_TR.sys, f_temp_2);
EX_PDH_OpGain =1/slope_X * 5.465;
ALScontrol_X;
remove = mybodesys(sys(36,5),f_temp_2); % data is already loop suppressed; need to remove before inject
EX_2_Comm_PDH_NoiseSpectrum = abs(EX_PDH_NoiseSpecV_PLLBoost1Off_PDHBoost2On(:,2).* mybodesys(sys(10,5),EX_PDH_NoiseSpecV_PLLBoost1Off_PDHBoost2On(:,1))./remove)./ EX_PDH_NoiseSpecV_PLLBoost1Off_PDHBoost2On(:,1);

EX_2_Comm_PDH_TF_noise = mybodesys(sys(10,18),f);
EX_2_Comm_PDH_ShotNoiseSpectrum = abs(EX_2_C_PDH_ShotNoiseSpectrum.* EX_2_Comm_PDH_TF_noise');
EX_2_Comm_PDH_DarkNoise = abs(EX_2_C_PDH_DarkNoise.* EX_2_Comm_PDH_TF_noise');
```

```
%EX_2_Comm_PDH_ShotNoiseSpectrum = abs(EX_PDH_ShotNoiseSpectrum(:,2).*EX_PDH_OpGain
    .*mybodesys(sys(10,5),EX_PDH_ShotNoiseSpectrum(:,1)))./EX_PDH_ShotNoiseSpectrum
    (:,1);
%EX_2_Comm_PDH_DarkNoise = abs(EX_PDH_DarkNoise(:,2).*EX_PDH_OpGain.*mybodesys(sys
    (10,5),EX_PDH_DarkNoise(:,1)))./EX_PDH_DarkNoise(:,1);


EX_2_Comm_VCO_TF = mybodesys(sys(10,22),f_VCO);
EX_2_Comm_VCO_rad = abs(VCO_noise_rad .* EX_2_Comm_VCO_TF);

% Optic Displacement L = 1, T = 2, V = 3, R = 4, P = 5, Y = 6
% From Jeff's prediction using alive spectra of the BSC (stage 2) and
% propagate through the sus model.
load('dampingfilters_QUAD_2014 01 30 _Level2p1_RealSeismic_model.mat')
f_disp = freq;
disp_noise = opticDisp(1).total; % units: m/sqrtHz
disp_noise_Hz = sqrt(2) * disp_noise * d2f;
disp_noise_rad = disp_noise_Hz ./ f_disp;
EX_2_Comm_disp_TF = mybodesys(sys(10,18),f_disp);
EX_2_Comm_disp_rad = abs(disp_noise_rad .* EX_2_Comm_disp_TF); % !! Check !!


% sensor noise with loop suppression
tf_sup = mybodesys(sys(10,18),f);
tf_supVCO = mybodesys(sys(10,18),f_VCO);
PFD_noise = abs(PFD_noise .* tf_sup');
shot_noise_2 = abs(shot_noise_2 .* tf_sup');
BBPD_noise = abs(BBPD_noise .* tf_sup');
VCO_noise_rad = abs(VCO_noise_rad .* tf_supVCO);

% reducing COMM PLL input gain to  3dB, and turning off second common
% filter: (not convinced fully locked)
load('COMM_PLL_CTRL_LOWBW.txt');
load('COMM_PLL_CTRL_NOM.txt');

%alog 11654
load('COMMPLLErrorSpecV_wMixer.txt');  % error signal from SR785
load('COMM_PLL_CTRL_HZ.txt'); % from DTT; second column is ref 4 nominal setting,
    third column is ref 6 with input gain of 9dB
f_mix = COMM_PLL_CTRL_HZ(:,1);
tf_loopsup = mybodesys(sys(10,18),COMM_PLL_CTRL_HZ(:,1));
test = abs(COMM_PLL_CTRL_HZ(:,2) .* tf_loopsup) ./COMM_PLL_CTRL_HZ(:,1) ;
% Compute RMS
COMM_PLL_rms_Hz = flipud(sqrt(cumtrapz(flipud(COMM_PLL_CTRL_HZ(:,1)), flipud(
    COMM_PLL_CTRL_HZ(:,2)).^2) .*  1));


figure(500)
clf;
ll=loglog(CommPLL_NoHand_NoiseSpecV(:,1), CommPLL_NoiseSpecRad(:,2), 'r',...
    f, PFD_noise, 'g*',...
    f, shot_noise_2, 'r',...
    f, BBPD_noise, 'k  ',...
    f_VCO, VCO_noise_rad./10,'g  ', ...
```

```
    f_VCO, EX_2_Comm_VCO_rad, ...
    f, EX_2_Comm_PDH_DarkNoise, 'y',...
    f, EX_2_Comm_PDH_ShotNoiseSpectrum, 'c', ...
    f_temp_2, EX_2_Comm_PDH_NoiseSpectrum, 'm',...
    f, EX_2_Comm_Sum_laser, 'b  ',...
    f_disp, EX_2_Comm_disp_rad, 'k  ');
    %COMM_PLL_CTRL_HZ(:,1), test,'r',...
    %COMM_PLL_CTRL_HZ(:,1), testhold,'g');
 %  f_temp, EX_2_Comm_PLL_Noise, 'k',...
legend('Error Sig','PFD noise','PD shot noise', 'PD dark noise','COMM VCO noise','
    PDH VCO','PDH dark Noise', 'PDH shot noise', 'PDH error signal', 'End station
    laser noise','Supressed displacement noise',...
     'Location', 'SouthEast')
xlabel('Frequency [Hz]');
ylabel('Amplitude Spectrm [rad/SqrtHz]');
title('PLL Common Mode in loop Noise');
set(gcf, 'color', 'w');
set(ll,'LineWidth',3);
grid on;
xlim([3e 1 1e5]);
ylim([1e 15 1e 4]);
set(gca,'Ytick',10.^( 15: 4))
set(gca,'Xtick',10.^( 1:2:5))
set(findall(gcf, 'Type', 'text'), 'FontSize', 18, 'FontWeight','bold');
set(findall(gcf, 'Type', 'axes'), 'FontSize', 18,'FontWeight','bold');



% alog 10998
% PLL locked, no handoff
% compenstation filters engaged, input gain 27dB, VCO comp and low pass on
% measured out of Output 2 of CM Board (not PFD IMON)
% CM Board input 1 gain 0dB
load('CommPLL_NoiseSpecV_Out2.txt');
CommPLL_NoiseSpecRad_Out2(:,2) = 36 * pi/180 .* CommPLL_NoiseSpecV_Out2(:,2); %
    convert to rad/sqrtHz

TF_adjust = mybodesys(COMM_PLL_CM.sys * CORNER_PFD.sys * COMM_PLL_VCO.sys *
    COMM_PLL_VCO_DCgain.sys, f_temp_2);
EX_2_Comm_PDH_NoiseSpectrum_Adjust = abs(EX_2_Comm_PDH_NoiseSpectrum .* TF_adjust) *
     180/pi;% .* f_temp_2 / slope;

TF_adjust = mybodesys(COMM_PLL_CM.sys * CORNER_PFD.sys * COMM_PLL_VCO.sys *
    COMM_PLL_VCO_DCgain.sys,CommPLL_NoHand_NoiseSpecV(:,1));
Test = abs(CommPLL_NoiseSpecRad(:,2).* TF_adjust) * 180/pi;



%% COMM Handoff TFs
% alog 9947
%common
load('SCRN0121.txt')
load('SCRN0122.txt')
%cf/1 cs
```

```
load('SCRN0123.txt')
load('SCRN0124.txt')
%cs/1 cf
load('SCRN0119.txt')
load('SCRN0120.txt')

% COMM PLL Servo Board
%      Input gain: 27dB
%      Common Fitler 1: ON
%      Common Filter 2: ON
%      VCO Comp: ON
%      Low Pass: ON
% CM Servo Board
%      Input 1 gain: 11dB
%      Input 1 pol: POS
%      Input 2 gain: 6dB
%      Input 2 pol: NEG
%      Common Comp: ON
%      Fast Gain: 6dB
%      Fast pol: POS
% LSC CARM Filter
%      Gain: 80
%      FM1, FM4, FM5, FM8
% LSC REFL SERVO SLOW
%      Gain:1
%      FM1
% MC2_M3_LOCK_L
%      Gain:  300
%      FM9
% MC2_M2_LOCK_L
%      Gain: 0.10
%      FM3, FM4, FM10
% MC2_M1_LOCK_L
%      Gain:  1
%      FM1, FM2
% MC2_M3_ISCINF
%      Gain: 1
%      Filters OFF
f=logspace(0,6,3000);
wCavX = 2*pi*2000;
wCavY =  2*pi*600;
EX_PDH_OpGain = 1/slope_X * 5.465;
D_REL = 0; % AO path off
GainFast =1;
GainSlow =1;
IMCTEST = 0;
ALScontrol_X;

MC2_M3_ISCINF_FM.swstat = 5120; % to remove R, V notches
[systm, flexTfs] = linFlexTf('ALS_SIMULINK_X');
systm = prescale(systm);
sys = linFlexTfFold(systm, flexTfs);


```

```
% crossover using LSCCARM inputs
load('CommCrossOver_04012014.txt');
TF_CARM_crossover = mybodesys(sys(55,26),f) ./ mybodesys(sys(54,26),f);

% Common Path
TF_CARM_OpenLoop = mybodesys(sys(21,14),f) ./ mybodesys(sys(20,14),f);
load('Handoff_comm_OLTF_mag.txt');
load('Handoff_comm_OLTF_phase.txt');

% CF/1 CS
TF_CARM_cfast = mybodesys(sys(42,30),f) ./ mybodesys(sys(4,30),f);
load('Handoff_cfast_OLTF_mag.txt');
load('Handoff_cfast_OLTF_phase.txt');

% CS/1 CF      zero indicated crossover (too low)
TF_CARM_cslow = mybodesys(sys(43,31),f) ./ mybodesys(sys(27,31),f);
load('Handoff_cslow_OLTF_mag.txt');
load('Handoff_cslow_OLTF_phase.txt');


%fast
GainFast =1;
GainSlow =0;
IMCTEST = 0;
ALScontrol_X;
MC2_M3_ISCINF_FM.swstat = 5120;
[systm, flexTfs] = linFlexTf('ALS_SIMULINK_X');
systm = prescale(systm);
sys = linFlexTfFold(systm, flexTfs);

TF_CARM_fast = mybodesys(sys(42,30),f) ./ mybodesys(sys(4,30),f);

%slow
GainFast =0;
GainSlow =1;
IMCTEST = 0;
ALScontrol_X;MC2_M3_ISCINF_FM.swstat = 5120;
[systm, flexTfs] = linFlexTf('ALS_SIMULINK_X');
systm = prescale(systm);
sys = linFlexTfFold(systm, flexTfs);


TF_CARM_slow = mybodesys(sys(43,31),f) ./ mybodesys(sys(27,31),f);


figure(321)
suptitle('ALS Common Mode Open Loop TF')
subplot(2,1,1)
sl=semilogx(f,mag2db(abs(TF_CARM_OpenLoop)),Handoff_comm_OLTF_mag(:,1),
    Handoff_comm_OLTF_mag(:,2));
xlim([10^2 10^5])
set(gca,'Xtick',10.^(2:1:5))
ylim([ 40 60]);
```

```
legend('Model', 'Data')
ylabel('Magnitude [dB]');
set(sl, 'LineWidth',3);
grid on;
subplot(2,1,2)
sl=semilogx(f, angle(TF_CARM_OpenLoop)*180/pi,Handoff_comm_OLTF_phase(:,1),
    Handoff_comm_OLTF_phase(:,2)+180);
xlim([10^2 10^5])
set(gca,'Xtick',10.^(2:1:5))
ylim([0 200])
set(gca,'Ytick',1.*(0:50:200))
grid on
set(sl, 'LineWidth',3);
xlabel('Frequency [Hz]');
ylabel('Phase [deg]');
set(gcf,'Color','w');
set(findall(gcf, 'Type', 'text'), 'FontSize', 18, 'FontWeight','bold');
set(findall(gcf, 'Type', 'axes'), 'FontSize', 18,'FontWeight','bold');
% c(s+f); at low freq match slow path until cross over (13Hz), after which
% matches fast path; data loses coherence at low freq
% difference above 10^4 is due to vco in comm pll loop not being modeled
% properly...


figure(323)
suptitle('Injection in CM Fast Path (cf/1 cs)');
subplot(2,1,1)
sl = semilogx(f,mag2db(abs(TF_CARM_cfast)),Handoff_cfast_OLTF_mag(:,1),
    Handoff_cfast_OLTF_mag(:,2));
legend('Model','Data','Location','SouthEast');
set(sl,'LineWidth', 3);
xlim([1 10^5])
set(gca,'Xtick',10.^(0:1:5))
ylabel('Magnitude [dB]');
grid on;
subplot(2,1,2)
sl= semilogx(f, angle(TF_CARM_cfast)*180/pi,Handoff_cfast_OLTF_phase(:,1), unwrap(
    Handoff_cfast_OLTF_phase(:,2).*pi/180).*180/pi+180);
xlim([1 10^5])
ylim([ 200 200])
set(gca,'Ytick',1.*( 200:100:200))
set(gca,'Xtick',10.^(0:1:5))
set(sl,'LineWidth', 3);
grid on
xlabel('Frequency [Hz]');
ylabel('Phase [deg]');
set(gcf,'Color','w');
set(findall(gcf, 'Type', 'text'), 'FontSize', 18, 'FontWeight','bold');
set(findall(gcf, 'Type', 'axes'), 'FontSize', 18,'FontWeight','bold');
% at high freq cs <<1, so this is just fast past * comm path (includes comm pll)

figure(324)
suptitle('Injection in CM Slow Path (cs/1 cf)');
subplot(2,1,1)
```

```
sl = semilogx(f,mag2db(abs(TF_CARM_cslow)),Handoff_cslow_OLTF_mag(:,1), Handoff_cslow_OLTF_mag(:,2));
legend('Model','Data');
set(sl,'LineWidth', 3);
xlim([1 10^3])
ylim([ 50 100])
set(gca,'Xtick',10.^(0:1:3))
set(gca,'Ytick',10.*( 5:2:10))
ylabel('Magnitude [dB]');
grid on;
subplot(2,1,2)
sl= semilogx(f, angle(TF_CARM_cslow)*180/pi,Handoff_cslow_OLTF_phase(:,1), unwrap(Handoff_cslow_OLTF_phase(:,2).*pi/180).*180/pi 180);
xlim([1 10^3])
ylim([ 200 200])
set(gca,'Ytick',1.*( 200:100:200))
set(gca,'Xtick',10.^(0:1:3))
set(sl,'LineWidth', 3);
grid on
xlabel('Frequency [Hz]');
ylabel('Phase [deg]');
set(gcf,'Color','w');
set(findall(gcf, 'Type', 'text'), 'FontSize', 18, 'FontWeight','bold');
set(findall(gcf, 'Type', 'axes'), 'FontSize', 18,'FontWeight','bold');
% at high freq cs <<1, so this is just fast past * comm path (includes comm pll)

figure(341)
suptitle('ALS Common Mode Transfer Functions')
subplot(2,1,1)
sl=semilogx(f, mag2db(abs(TF_CARM_fast)),f,mag2db(abs(TF_CARM_slow)),f,mag2db(abs(TF_CARM_OpenLoop)),'r  ');
xlim([1 10^5])
ylim([ 300 200])
set(gca,'Xtick',10.^(0:1:5))
set(gca,'Ytick',1.*( 300:100:200))
ylabel('Magnitude [dB]');
legend('fast','slow','c(s+f)','Location','SouthWest')
set(sl, 'LineWidth',3);
grid on;
subplot(2,1,2)
sl=semilogx(f, angle(TF_CARM_fast)*180/pi,f,angle(TF_CARM_slow)*180/pi,f, angle(TF_CARM_OpenLoop)*180/pi,'r  ');
xlim([1 10^5])
ylim([ 200 200])
set(gca,'Ytick',1.*( 200:100:200))
set(gca,'Xtick',10.^(0:1:5))
grid on
set(sl, 'LineWidth',3);
xlabel('Frequency [Hz]');
ylabel('Phase [deg]');
set(gcf,'Color','w');
set(findall(gcf, 'Type', 'text'), 'FontSize', 18, 'FontWeight','bold');
set(findall(gcf, 'Type', 'axes'), 'FontSize', 18,'FontWeight','bold');
```

```
figure(342)
suptitle('COMM Crossover')
subplot(2,1,1)
sl=semilogx(f,mag2db(abs(TF_CARM_crossover)),CommCrossOver_04012014(:,1),mag2db(abs(
    CommCrossOver_04012014(:,2) + 1i*CommCrossOver_04012014(:,3))));
xlim([1 10^3])
ylabel('Magnitude [dB]');
set(sl, 'LineWidth',2);
grid on;
subplot(2,1,2)
sl=semilogx(f, angle(TF_CARM_crossover)*180/pi,CommCrossOver_04012014(:,1), angle(
    CommCrossOver_04012014(:,2) + 1i*CommCrossOver_04012014(:,3))*180/pi);
xlim([1 10^3])
grid on
set(sl, 'LineWidth',2);
xlabel('Frequency [Hz]');
ylabel('Phase [deg]');
legend('Model', 'Data')
set(gcf,'Color','w');

% % !!!! DIFFERENT SETTINGS FROM ABOVE !!!!
% % alog 10439
% % COMM PLL gain to 27dB
% % CM Servo board: Input 1 gain 18dB, boost 1 and common comp ON
% % UGF at 35kHz with 40 deg phase margin
% % Common path c(f+s)
% load('COMM_OLTF_phase.txt');
% load('COMM_OLTF_mag.txt');
% % cf/1+cs path
% load('Comm_Handoff_Fast_OLTF_mag.TXT');
% load('Comm_Handoff_Fast_OLTF_phase.TXT');
%

%% IMC Open Loop TF
% alog 9928
%  IMC Servo Board
%      Input 1 enable: ON
%      Input 1 pol: POS
%      Input 2 enable: OFF
%      Input 2 pol: POS
%      Input 2 gain: 16 dB
%      Input 1 gain: 9 dB
%      Common Compensation: ON
%      Boost 1: ON
%      Generic filter: ON
%      Fast Gain:  6dB
%      Fast enable: ON
%      Fast Pol: POS
%      Bypass: ON
% IMC L
%      FM1 (antiwhitening) ON
%      Gain 1
% LSC MC
%      All Off
```

```
%      Gain 1
% MC2_M3_ISCINF Filter
%      FM6, FM7 On
%      Gain 1
% MC2_M3_LOCK Filter
%      FM3, FM9 ON
%      Gain  300
% MC2_M2_LOCK Filter
%      FM3, FM4, FM10 On
%      Gain 0.1
% MC3_M1_LOCK Filter
%      FM1, FM2 On
%      Gain 1
load('IMC_OpenLoop_mag.txt')
load('IMC_OpenLoop_phase.txt')
load('IMC_Comm_OLTF_mag_Low.TXT')  %    off by 41dB because of stupid auto range
load('IMC_Comm_OLTF_phase_Low.TXT')
% draft alog...
% magnitude off by factor of 2 due to some weird burt restore (alog 10071)
load('IMC_Comm_OLTF_mag.txt') % ugf is 28kHz, but should be 53kHz
load('IMC_Comm_OLTF_phase.txt')
load('IMC_Fast_OLTF_mag.txt')
load('IMC_Fast_OLTF_phase.txt')
load('IMC_Slow_OLTF_mag.txt')
load('IMC_Slow_OLTF_phase.txt')


GainFast =0;
GainSlow =0;
IMCTEST = 1;
ALScontrol_X;
TF_IMC_Comm = mybodesys(sys(14,17),f) ./ mybodesys(sys(26,17),f);
TF_IMC_Fast = mybodesys(sys(23,23),f) ./ mybodesys(sys(44,23),f);

IMC_MODEL_SYS = IMC_CAVITY.sys * IMC_REFL_SERVO_COMMPATH.sys * IMC_REFL_SERVO_FAST.
    sys * IMC_VCO.sys * IMC_In1_Gain * IMC_OpGain *2;
TF_IMC_MODEL = mybodesys(IMC_MODEL_SYS,f);
IMC_SYS = MakeSYS(IMC_OpenLoop_mag(:,2), IMC_OpenLoop_phase(:,2), IMC_OpenLoop_mag
    (:,1));

figure(105);
clf;
suptitle('Input Mode Cleaner Open Loop Transfer Function')
subplot(2,1,1)
sl=semilogx(IMC_OpenLoop_mag(:,1),IMC_OpenLoop_mag(:,2), f, mag2db(abs(TF_IMC_Comm))
    ,IMC_Comm_OLTF_mag_Low(:,1),IMC_Comm_OLTF_mag_Low(:,2)+41,'b');
ylim([ 20,100]);
set(gca,'Ytick',10.*( 2:2:10))
grid on;
legend('Data','Model','Location','SouthWest');
set(sl, 'LineWidth',3);
ylabel('Magnitude [dB]');
xlim([50 2e5])
set(gca,'Xtick',10.^(1:1:5))
```

```
subplot(2,1,2)
sl=semilogx(IMC_OpenLoop_mag(:,1),IMC_OpenLoop_phase(:,2)+180, f, angle(TF_IMC_Comm)
    *180/pi,IMC_Comm_OLTF_phase_Low(:,1),IMC_Comm_OLTF_phase_Low(:,2) + 180,'b');
grid on;
ylabel('Phase [deg]');
xlabel('Frequency [Hz]');
set(sl, 'LineWidth',3);
xlim([50 2e5])
ylim([0 180])
set(gca,'Xtick',10.^(1:1:5))
set(gca,'Ytick',1.*(0:36:180))
set(gcf, 'Color','w');
set(findall(gcf, 'Type', 'text'), 'FontSize', 18, 'FontWeight','bold');
set(findall(gcf, 'Type', 'axes'), 'FontSize', 18,'FontWeight','bold');

tf_closed = mybodesys(sys(26,17),f);
tf_blah = mybodesys(sys(14,17),f);
tf_open = tf_blah./tf_closed;
figure(24);
clf;
suptitle('Input Mode Cleaner Loop Transfer Functions')
subplot(3,1,[1 2]);
ll=loglog(f,abs(tf_blah),f,abs(tf_closed),f,abs(tf_open));
set(ll,'LineWidth',3);
ylabel('Magnitude [abs]');
xlim([20 1e6])
ylim([10^ 6 10^6]);
set(gca,'Xtick',10.^(2:1:6))
set(gca,'Ytick',10.^( 6:2:6))
grid on
%legend('G/1 G', 'Closed Loop','Open Loop');
legend('Closed Loop', 'Sensitivity Function','Open Loop');
subplot(3,1,3)
sl = semilogx(f,angle(tf_blah)*180/pi,f,angle(tf_closed)*180/pi,f,angle(tf_open)
    *180/pi);
xlim([20 1e6])
ylim([0 180]);
set(gca,'Ytick',10.^( 6:2:6))
set(gca,'Ytick',180*(0:0.5:1))
set(sl,'LineWidth',3);
ylabel('Phase [deg]');
xlabel('Frequency [Hz]');
set(gcf,'Color','w');
grid on;
set(findall(gcf, 'Type', 'text'), 'FontSize', 18, 'FontWeight','bold');
set(findall(gcf, 'Type', 'axes'), 'FontSize', 18,'FontWeight','bold');


%% MC2 Stage crossover
% mystery gain of 6!!!
f=logspace(2,6,3000);
wCavX = 2*pi*2000;
wCavY =  2*pi*600;
EX_PDH_OpGain = 1/slope_X * 5.465;
```

```
D_REL = 0; % AO path off
GainFast =0;
GainSlow =0;
IMCTEST = 1;
ALScontrol_X;

% adjust switches so MC2 filters are not when COMM is handed off
MC2_M3_FM.swstat = 13572;
MC2_M2_FM.swstat = 13836;
MC2_M1_FM.swstat = 5123;
MC2_M3_ISCINF_FM.swstat = 5216;
[systm, flexTfs] = linFlexTf('ALS_SIMULINK_X');
systm = prescale(systm);
sys2 = linFlexTfFold(systm, flexTfs);


MCL_MCF=load('2014 02 11_H1IMC_MCL MCF_Crossover_OLGTF_tf.txt');
MCL_MCF_Long = load('MCL_MCF_Long.txt');
M2_M3 =load('2014 02 11_H1IMC_M2 M3_Crossover_OLGTF_tf.txt');
M1_M2 =load('2014 02 11_H1IMC_M1 M2_Crossover_OLGTF_tf.txt');
M2_M3_noM1 =load('2014 03 13_H1IMC_M2 M3_noM1_Crossover_OLGTF_tf.txt'); % with M1 stage switched off


f_temp= MCL_MCF(:,1);
f_temp_2 = M2_M3(:,1);
f_temp_3 = M1_M2(:,1);
TF_MCL_MCF_CrossOver = mybodesys(sys2(37,19),f_temp) ./ mybodesys(sys2(13,19),f_temp);
TF_M2_M3_CrossOver = mybodesys(sys2(38,28),f_temp_2) ./ mybodesys(sys2(39,28),f_temp_2);
TF_M2_M1_CrossOver = mybodesys(sys2(40,29),f_temp_3) ./ mybodesys(sys2(41,29),f_temp_3);

TF_M2_M3_CrossOver_2 = mybodesys(sys2(38,28),f) ./ mybodesys(sys2(39,28),f);
TF_MCL_MCF_CrossOver_2 = mybodesys(sys2(37,19),f) ./ mybodesys(sys2(13,19),f);


ratio_MCL_MCF_mag = abs(TF_MCL_MCF_CrossOver) ./ abs(MCL_MCF(:,2)+ 1i.*MCL_MCF(:,3));
ratio_MCL_MCF_phase = angle(TF_MCL_MCF_CrossOver)   angle(MCL_MCF(:,2)+ 1i.*MCL_MCF(:,3));

ratio_M2_M3_mag = abs(TF_M2_M3_CrossOver) ./ abs(M2_M3(:,2)+ 1i.*M2_M3(:,3));
ratio_M2_M3_phase = angle(TF_M2_M3_CrossOver)   angle(M2_M3(:,2)+ 1i.*M2_M3(:,3));

figure(601)
clf;
suptitle('MCL/MCF Crossover')
subplot(2,1,1)
ll=loglog(f,abs(TF_MCL_MCF_CrossOver_2),MCL_MCF_Long(:,1), abs(MCL_MCF_Long(:,2)+ 1i.*MCL_MCF_Long(:,3)));
set(ll, 'LineWidth', 3);
ylabel('Magnitude [abs]');
```

```
ylim([1e 4 1e2])
set(gca,'Ytick',10.^( 4:2:2))
xlim([4 1000])
grid on;
subplot(2,1,2)
sl=semilogx(f,angle(TF_MCL_MCF_CrossOver_2)*180/pi,MCL_MCF_Long(:,1), angle(
    MCL_MCF_Long(:,2)+ 1i.*MCL_MCF_Long(:,3))*180/pi);
set(sl, 'LineWidth', 3);
xlim([4 1000])
set(gca,'Ytick',200*( 1:0.5:1))
xlabel('Frequency [Hz]');
ylabel('Phase [deg]');
legend('Model', 'Data');
grid on;
set(gcf, 'Color', 'w');
set(findall(gcf, 'Type', 'text'), 'FontSize', 18, 'FontWeight','bold');
set(findall(gcf, 'Type', 'axes'), 'FontSize', 18,'FontWeight','bold');


figure(602)
clf;
suptitle('M2/M3 Crossover')
subplot(2,1,1)
ll=loglog(M2_M3(:,1), abs(M2_M3(:,2)+1i.*M2_M3(:,3)),f_temp_2,abs(TF_M2_M3_CrossOver
    ));
set(ll, 'LineWidth', 3);
set(gca,'Ytick',10.^( 2:1:2))
xlim([1 50])
ylabel('Magnitude [abs]');
grid on;
subplot(2,1,2)
sl=semilogx(M2_M3(:,1), angle(M2_M3(:,2)+1i.*M2_M3(:,3))*180/pi,f_temp_2,angle(
    TF_M2_M3_CrossOver)*180/pi);
set(sl, 'LineWidth', 3);
xlim([1 50])
set(gca,'Ytick',200*( 1:0.5:1))
xlabel('Frequency [Hz]');
ylabel('Phase [deg]');
legend('Data', 'Model');
grid on;
set(gcf, 'Color', 'w');
set(findall(gcf, 'Type', 'text'), 'FontSize', 18, 'FontWeight','bold');
set(findall(gcf, 'Type', 'axes'), 'FontSize', 18,'FontWeight','bold');

figure(603)
clf;
suptitle('M1/M2 Crossover');
subplot(2,1,1)
ll=loglog(M1_M2(:,1), abs(M1_M2(:,2)+1i.*M1_M2(:,3)),f_temp_3,abs(TF_M2_M1_CrossOver
    ));
set(ll, 'LineWidth', 3);
ylabel('Magnitude [abs]');
set(gca,'Ytick',10.^( 2:1:2))
xlim([.04 1])
```

```
grid on;
subplot(2,1,2)
sl = semilogx(M1_M2(:,1), angle((M1_M2(:,2)+1i.*M1_M2(:,3)))*180/pi,f_temp_3,angle(
    TF_M2_M1_CrossOver)*180/pi);
xlabel('Frequency [Hz]');
ylabel('Phase [deg]');
set(sl, 'LineWidth', 3);
xlim([.04 1])
legend('Data', 'Model');
grid on;
set(gcf, 'Color', 'w');
set(findall(gcf, 'Type', 'text'), 'FontSize', 18, 'FontWeight','bold');
set(findall(gcf, 'Type', 'axes'), 'FontSize', 18,'FontWeight','bold');

% ab=load('MC2_2_IMCSlow_04032014.txt');
% tf_test=mybodesys(sys2(37,34),ab(:,1));
% figure(123);clf;subplot(2,1,1),semilogx(ab(:,1),mag2db(abs(tf_test)),ab(:,1),
    mag2db(abs(ab(:,2) +1i*ab(:,3))));grid on;subplot(2,1,2);semilogx(ab(:,1),180/pi
    *(angle(tf_test)),ab(:,1), 180/pi*(angle(ab(:,2) +1i*ab(:,3))));grid on;



%%
% % slow path tests
% f=logspace( 2,6,3000);
% wCavX = 2*pi*2000;
% wCavY =  2*pi*600;
% EX_PDH_OpGain = 1/slope * 5.465;
% D_REL = 0; % AO path off
% GainFast =0;
% GainSlow =1;
% IMCTEST = 0;
% ALScontrol_X;
%
%
% % inject into ALS C_REFL_DC_BIAS_EXC (through input 2 w/ neg pol of CM board w/
    everything zeroed) (this includes a DAC conversion not present in model since
    usually use analog) and read out at MC2_M3_LOCK_L_OUT
% tf_test2 = mybodesys(sys(48,36),f);
% ac = load('SlowPathTest_04032014.txt');
% figure(124);clf;subplot(2,1,1);semilogx(f,mag2db(abs(tf_test2)*20/2^16),ac(:,1),
    mag2db(abs(ac(:,2)+1i*ac(:,3))));xlim([1 1e3]);grid on;subplot(2,1,2);semilogx(f
    ,180/pi*angle(tf_test2),ac(:,1),180/pi*angle(ac(:,2)+1i*ac(:,3)) 180);grid on;
    xlim([1 1e3]);
%
% % inject into LSC REFL_SERVO_SLOW_EXC and read out at MC2_M3_LOCK_L_OUT
% tf_test3 = mybodesys(sys(48,21),f);
% ad = load('SlowPathTest2_04032014.txt');
% figure(125);clf;subplot(2,1,1);semilogx(f,mag2db(abs(tf_test3)),ad(:,1),mag2db(abs
    (ad(:,2)+1i*ad(:,3))));xlim([5 1e3]);grid on;subplot(2,1,2);semilogx(f,180/pi*
    angle(tf_test3),ad(:,1),180/pi*angle(ad(:,2)+1i*ad(:,3)));grid on;xlim([5 1e3]);
% legend('model','data');
```

/ligo/svncommon/NbSvn/aligonoisebudget/trunk/HIFO/H1/ALS˙TFtest˙NB˙X.m

```
%close all
%clear all
% clc

% Various Transfer Functions

 f_all = logspace( 1, 3.7, 3000);
 f=logspace(0,6,3000);

 addpath('simulink');
 addpath('util');
 addpath('data')


 ALS_TFtest_NB_X; % currently running under comm handoff state
 clear Fiber_noise_Hz

 xfeedback = 0;
 yfeedback = 0;
 handoffstate = 'diffstate'; % for ey and diff measurements, we run under diff handoff state

 f=logspace(0,6,3000);

%% End Y PLL Measurements
% PLL Servo Board Settings
%   Input 1 Pol: NEG
%   Input 1 Gain: 0dB
%   Common Compensation: ON
%   Generic Filter: ON
%   Fast Option: ON
%   Fast Pol: POS
%   Fast Gain:  8dB
%   Boost 1: Off
%   Rest: Off/Zero
% UGF: 23kHz with phase margin of 52 deg
% alog 11440, 11180

%% Noise of In Loop PLL
% load model
 EY_PDH_OpGain = 0;
 GainFast =0;
 GainSlow =0;
 IMCTEST = 0;
 ALScontrol_FULL;

% PFD Noise
% ~460nV/SqrtHz at 140Hz, assume flat for freq we care
 PFD_noise_V = 500e 9*ones(size(f));
 PFD_noise = 36 * pi/180 .* PFD_noise_V; % convert to rad

% Free Running Laser Noise
 NPRO_freqfluc_zpk = makeZPK([1e4],[1e 5],1,Inf);
```

```
tf_temp = mybodesys(NPRO_freqfluc_zpk.sys, f);
NPRO_freqfluc_Hz = abs(tf_temp)';
NPRO_freqfluc = NPRO_freqfluc_Hz./f; % rad/sqrtHz
TF_endlaserfreq = mybodesys(sys(66,40),f);
EY_LaserFreqNoise_rad = abs(NPRO_freqfluc .* TF_endlaserfreq'); % rad/sqrtHz, supressed laser noise due to locking

% Fiber noise (see LIGO T0900376 v1)
Fiber_noise_zpk = makeZPK([],[1e3],3,0);
tf_temp = mybodesys(Fiber_noise_zpk.sys, f);
Fiber_noise_Hz = abs(tf_temp)';
Fiber_noise_rad = Fiber_noise_Hz./f;
EY_FiberNoise_rad = abs(Fiber_noise_rad .* TF_endlaserfreq'); % supressed fiber noise


% BBPD noise   measured out of preamplifier direct ( 1dB), with BBPD
% blocked
BBPD_noise =  115*ones(size(f)); %  116 dBm, at 100Hz Bw
beatnote =   18*ones(size(f)); %  21 dBm, at 100Hz BW
dBc_BBPD = BBPD_noise   beatnote;
dBc_BBPD_Hz = dBc_BBPD   20; % dividing by 100Hz BW is the same as  20dB
BBPD_noise =  10.^(dBc_BBPD_Hz./20); % dBc to rad/sqrtHz


% shot noise   measured out of preamplifier direct ( 1dB)
shot_noise =  107*ones(size(f)); %  108 dBm, at 100Hz Bw
beatnote =   18*ones(size(f)); %  21 dBm, at 100Hz BW
dBc = shot_noise   beatnote;
dBc_Hz = dBc   20; % dividing by 100Hz BW is the same as  20dB
shot_noise =  sqrt((10.^(dBc_Hz./20)).^2   10.^(dBc_BBPD_Hz/20).^2); % dBc to rad/sqrtHz, subtracting out the dark noise of the BBPD


%alternate method to calculate shot noise (confirmed to match)
% Power onto BBPD is almost all laser; no fiber (FIBR_A_DC)
elec = 1.6e 19; % charge of electron
BBPD_power = 18e 3; % watts: 2kOhm trans, .055A/W responsivity
BBPD_curr = BBPD_power * .055;
Carrier_curr = 28.5e 3/2e3; % carrier  18dbm to current
shot_noise_temp = sqrt(2*elec*BBPD_curr)/Carrier_curr; % shot noise in 1/SqrtHz
shot_noise_2 = shot_noise_temp * ones(size(f));

% PLL loop suppressed error signal out of PFD IMON
% alog 11440
load('EY_PLL_NoiseSpecV.txt');
% Convert data from V to rad
EY_PLL_NoiseSpecRad(:,2) = 36 *pi/180 .* EY_PLL_NoiseSpecV(:,2);

Y_rms_PLL = flipud(sqrt(cumtrapz(flipud(EY_PLL_NoiseSpecV(:,1)), flipud(EY_PLL_NoiseSpecRad(:,2)).^2) .* 1));


figure(2)
```

```
clf;
set(gcf, 'color', 'w');
ll=loglog(EY_PLL_NoiseSpecV(:,1), EY_PLL_NoiseSpecRad(:,2), ...
    f, shot_noise,...
    f, PFD_noise,...
    f, EY_LaserFreqNoise_rad, ...
    f, EY_FiberNoise_rad,...
    f, shot_noise_2 ,...
    f, BBPD_noise,...
    EY_PLL_NoiseSpecV(:,1), Y_rms_PLL,'b*');
legend('Measured PLL Noise',' Measured Shot Noise', ...
    'PFD Noise', ...
    'Suppressed Laser Frequency Noise','Suppressed Fiber Noise', 'Calculated Shot
    Noise', 'BBPD Dark Noise',...
    'RMS','Location', 'SouthOutside');
xlabel('Frequency [Hz]');
ylabel('Amplitude Spectrum [rad/SqrtHz]');
set(ll,'LineWidth',1.5);
ylim([10^ 7 3e 2]);
set(gca, 'Ytick', 10.^( 7:2));
xlim([1 10^6]);
title('EY PLL Noise at Error Point');
grid on;


%% Out of Loop PLL Noise
% load model
EY_PDH_OpGain = 0;
GainFast =0;
GainSlow =0;
IMCTEST = 0;
ALScontrol_FULL;

% Convert data from rad to V
shot_noise_V = shot_noise .* 180/pi/36;

EY_PLL_TF_noise = mybodesys(sys(66,51),f); %G/1+G
EY_PLL_TF_PFDNoise = abs(PFD_noise_V .* EY_PLL_TF_noise');   % units: Hz/SqrtHz
EY_PLL_TF_PFDNoise_Rad = EY_PLL_TF_PFDNoise./f;   % units: rad/SqrtHz
EY_PLL_TF_ShotNoise = abs(shot_noise_V .* EY_PLL_TF_noise'); % units: Hz/SqrtHz
EY_PLL_TF_ShotNoise_Rad = EY_PLL_TF_ShotNoise./f; % units: rad/SqrtHz


TF_endlaserfreq = mybodesys(sys(66,40),f); %1/1+G
EY_LaserFreqNoise_rad = abs(NPRO_freqfluc .* TF_endlaserfreq'); % rad/sqrtHz,
    supressed laser noise due to locking
EY_LaserFreqNoise_Hz = f .* EY_LaserFreqNoise_rad; % convert to Hz/sqrtHz

TF_fiber = mybodesys(sys(72,40),f); %G/1+G
EY_fiber = abs(Fiber_noise_rad .* TF_fiber'); % rad/sqrtHz


f_temp = EY_PLL_NoiseSpecV(:,1);
EY_PLL_TF_noise = mybodesys(sys(72,51),f_temp); %G/1+G
```

```
EY_PLL_NoiseSpecHz = abs( EY_PLL_NoiseSpecV(:,2).* EY_PLL_TF_noise); % units: Hz/
    SqrtHz
EY_PLL_NoiseSpec_Rad = EY_PLL_NoiseSpecHz ./f_temp; % units: rad/SqrtHz

% interpolation to same frequency:
f_temp = EY_PLL_NoiseSpecV(:,1);
[b, i, j] = unique(f_temp);
EY_PLL_NoiseSpecRad_Int = interp1(b, EY_PLL_NoiseSpecRad(i), f, 'linear', 'extrap');

Sum_EY_Laser = sqrt(EY_PLL_NoiseSpecRad_Int.^2 + EY_PLL_TF_ShotNoise_Rad.^2 +
    EY_PLL_TF_PFDNoise_Rad.^2 + EY_LaserFreqNoise_rad.^2 + EY_fiber.^2);

figure(5)
clf;
set(gcf, 'color', 'w');
ll=loglog(EY_PLL_NoiseSpecV(:,1), EY_PLL_NoiseSpec_Rad, ...
    f, EY_PLL_TF_ShotNoise_Rad,...
    f, EY_PLL_TF_PFDNoise_Rad, ...
    f, EY_LaserFreqNoise_rad, ...
    f, EY_fiber, 'g',...
    f, Sum_EY_Laser,'  ');
legend('EY PLL noise ', 'EY PLL shot noise', 'EY PLL PFD noise','Free Running Laser
    Noise', ...
    'Estimated Fiber Noise','Sum EY Laser Noise');
xlabel('Frequency [Hz]')
ylabel('Amplitude Spectrum [rad/SqrtHz]')
set(ll, 'LineWidth',3);
title('EY laser Frequency Noise');
xlim([1 10^6]);
ylim([10^ 12 5]);
set(gca,'Ytick',10.^( 12:5));
grid on;
%% Open Loop Transfer Function of PLL
% alog 11180
load('EY_PLL_OLTF_mag.txt');
load('EY_PLL_OLTF_phase.txt');
load('EY_PLL_OLTF_mag_High.txt');
load('EY_PLL_OLTF_phase_High.txt');

EY_PLL_OLTF = mybodesys(sys(75,51),f)./mybodesys(sys(33,27),f);


figure(3);
clf;
subplot(2,1,1)
sl=semilogx(EY_PLL_OLTF_mag(:,1), EY_PLL_OLTF_mag(:,2),...
    f, mag2db(abs(EY_PLL_OLTF)));
hold on;
sl2 = semilogx(EY_PLL_OLTF_mag_High(:,1), EY_PLL_OLTF_mag_High(:,2),'b');
grid on;
legend([sl],{'Data', 'Model'});
xlim([5e3 4e5]);
ylabel('Magnitude [dB]');
set(sl, 'LineWidth', 3);
```

```
set(sl2, 'LineWidth', 3);
subplot(2,1,2)
sl = semilogx(EY_PLL_OLTF_phase(:,1),unwrap(EY_PLL_OLTF_phase(:,2).*pi/180).*180/pi + 180, ...
     f, angle(EY_PLL_OLTF)*180/pi);
hold on;
sl2 = semilogx(EY_PLL_OLTF_phase_High(:,1),unwrap(EY_PLL_OLTF_phase_High(:,2).*pi/180).*180/pi + 180,'b');
xlim([5e3 4e5]);
ylim([ 200 200])
set(sl, 'LineWidth', 3);
set(sl2, 'LineWidth', 3);
hold on;
grid on;
xlabel('Frequency [Hz]');
ylabel('Phase [deg]');
suptitle('Y arm PLL Open Loop Transfer Function');
set(gcf, 'color', 'w');
set(findall(gcf, 'Type', 'text'), 'FontSize', 18, 'FontWeight','bold');
set(findall(gcf, 'Type', 'axes'), 'FontSize', 18,'FontWeight','bold');


tf_closed = mybodesys(sys(76,51),f);
tf_blah = mybodesys(sys(75,51),f);
tf_open = tf_blah./tf_closed;

figure(19);
clf;
suptitle('EY PLL TFs')
subplot(3,1,[1 2]);
ll=loglog(f,abs(tf_blah),f,abs(tf_closed),f,abs(tf_open));
set(ll,'LineWidth',3);
ylabel('Magnitude [db]');
ylim([10^ 8 10^8]);
set(gca,'Ytick',10.^( 8:8))
grid on
%legend('G/1 G', 'Closed Loop','Open Loop');
legend('Closed Loop', 'Sensitivity Function','Open Loop');
subplot(3,1,3)
sl = semilogx(f,angle(tf_blah)*180/pi,f,angle(tf_closed)*180/pi,f,angle(tf_open)*180/pi);
set(sl,'LineWidth',3);
ylabel('Phase [deg]');
xlabel('Frequency [Hz]');
set(gcf,'Color','w');
grid on;
set(gca,'Ytick',100*( 6:1))



%% EY PDH Open Loop TF
% alog 11516 and April 23,2014 tbd
% PLL Servo Board Settings
%   Input 1 Pol: NEG
```

```
%   Input 1 Gain: 0dB
%   Common Compensation: ON
%   Generic Filter: ON
%   Fast Option: ON
%   Fast Gain:  8dB
%   Boost 1: Off
%   Rest: Off/Zero
% PDH Servo Board Settings
%   Input 1 Pol; POS
%   Input 1 Gain:  7dB
%   Common Compensation: ON
%   Boost 1: On
%   Boost 2: On
%   Slow Option: On
%   Rest: off/zero
% ** April 23, 2013 Stefan adjusted the input gain to  13dB and the fast
% gain to 6dB to deal with an offset problem; UGF of loop is the same.

load('EY_PDH_OLTF_mag.txt');
load('EY_PDH_OLTF_phase.txt');


% Calibration: Using PDH error signal 816mV peak to peak; units in
slope_Y = 6.9753e 4; % Volts/Hz !! slope and optical gain should be the same

% load model stuff
f=logspace(0,6,3000);
EY_PDH_OpGain = slope_Y;
GainFast =0;
GainSlow =0;
IMCTEST = 0;
ALScontrol_FULL;

%Transfer function of REFL Servo loop
EY_REFL_SERVO_1 =mybodesys(sys(60,39),f);
EY_REFL_SERVO_2 =mybodesys(sys(59,39),f);
TF_EY_REFL_SERVO = EY_REFL_SERVO_1./EY_REFL_SERVO_2;

% clean up of phase
for i=143:length(EY_PDH_OLTF_phase(:,2))
    if EY_PDH_OLTF_phase(i,2) > 100
        EY_PDH_OLTF_phase(i,2)= EY_PDH_OLTF_phase(i,2) 360;
    end
end

figure(4)
clf;
set(gcf, 'color', 'w');
suptitle('Y arm PDH Open Loop Transfer Function')
subplot(3,1,[1 2])
sl=semilogx(f, mag2db(abs(TF_EY_REFL_SERVO)), EY_PDH_OLTF_mag(:,1), EY_PDH_OLTF_mag
    (:,2));
set(sl, 'LineWidth', 3);
ylabel('Magnitude [dB]')
```

```
legend('Model', 'Data', 'Location', 'SouthWest');
grid on;
xlim([5e2 4e4]);
subplot(3,1,3)
sl=semilogx(f, angle(TF_EY_REFL_SERVO)/pi*180,EY_PDH_OLTF_phase(:,1),
    EY_PDH_OLTF_phase(:,2)+180);
set(sl, 'LineWidth', 3);
ylabel('Phase [Deg]')
xlabel('Frequency [Hz]')
grid on;
xlim([5e2 4e4]);
ylim([ 100 100])
set(findall(gcf, 'Type', 'text'), 'FontSize', 18, 'FontWeight','bold');
set(findall(gcf, 'Type', 'axes'), 'FontSize', 18,'FontWeight','bold');


tf_closed = mybodesys(sys(59,39),f);
tf_blah = mybodesys(sys(60,39),f);
tf_open = tf_blah./tf_closed;
figure(18);
clf;
suptitle('EY PDH TFs')
subplot(3,1,[1 2]);
ll=loglog(f,abs(tf_blah),f,abs(tf_closed),f,abs(tf_open));
set(ll,'LineWidth',3);
ylabel('Magnitude [db]');
ylim([10^ 7 10^5]);
set(gca,'Ytick',10.^( 7:5))
grid on
%legend('G/1 G', 'Closed Loop','Open Loop');
legend('Closed Loop', 'Sensitivty Function','Open Loop');
subplot(3,1,3)
sl = semilogx(f,angle(tf_blah)*180/pi,f,angle(tf_closed)*180/pi,f,angle(tf_open)
    *180/pi);
set(sl,'LineWidth',3);
ylabel('Phase [deg]');
xlabel('Frequency [Hz]');
set(gcf,'Color','w');
grid on;
set(gca,'Ytick',100*( 6:1))





%% EY PDH Error Signal Power Spectrum (w/o reflection cavity pole)

% Data from Daniel   measured from ALS COMM VCO so there is a factor of 10
% for FDD and a factor of 2 for double pass AOM. This only holds up until
% MCL MCF crossover when length path suppresed the VCO ~20Hz)
load('VCO_FDD_ssb_phase_noise_140415_F.txt'); % data units: dBc/sqrtHz
load('VCO_FDD_freq_noise_140415.txt'); % data units: Hz/sqrtHz
f_VCO = VCO_FDD_freq_noise_140415(:,1);
VCO_noise_Hz = VCO_FDD_freq_noise_140415(:,2);
```

```
VCO_noise_rad = VCO_noise_Hz ./ f_VCO; % data units: rad/sqrtHz


% PDH error signal measured out of IMON
load('EY_PDH_NoiseSpecV.txt'); % units in vplts;
EY_PDH_NoiseSpecRad(:,1) = EY_PDH_NoiseSpecV(:,1);
EY_PDH_NoiseSpecRad(:,2) = EY_PDH_NoiseSpecV(:,2) ./slope_Y ./ EY_PDH_NoiseSpecRad
    (:,1); % units: rad/sqrtHz
TF_anticav = mybodesys(EY_REFL_CAVITY_REFL.sys, EY_PDH_NoiseSpecRad(:,1));
EY_PDH_NoiseSpecRad(:,2) = abs(EY_PDH_NoiseSpecRad(:,2) ./ TF_anticav);

% shot noise measured out of IMON with ITMY misaligned
load('EY_PDH_ShotNoiseSpecV.txt'); % units in vplts;
EY_PDH_ShotNoiseSpecRad(:,1) = EY_PDH_ShotNoiseSpecV(:,1);
TF_PDH = mybodesys(sys(60,41),EY_PDH_ShotNoiseSpecRad(:,1));
EY_PDH_ShotNoiseSpecRad(:,2) = EY_PDH_ShotNoiseSpecV(:,2) ./slope_Y./
    EY_PDH_ShotNoiseSpecRad(:,1);


% dark noise measured out of IMON with REFL A blocked (this is all SR785
% noise)
load('EY_PDH_DarkNoiseSpecV.txt'); % units in vplts;
EY_PDH_DarkNoiseSpecRad(:,1) = EY_PDH_DarkNoiseSpecV(:,1);
TF_PDH = mybodesys(sys(60,41),EY_PDH_DarkNoiseSpecRad(:,1));
EY_PDH_DarkNoiseSpecRad(:,2) = EY_PDH_DarkNoiseSpecV(:,2) ./slope_Y./
    EY_PDH_DarkNoiseSpecRad(:,1);

% PLL stuff supressed by loop gain of PDH
TF_loopsup = mybodesys(sys(59,39),f);
EY_PLL_2_PDH_PFDNoise_Rad = abs(EY_PLL_TF_PFDNoise_Rad .* TF_loopsup');
EY_PLL_2_PDH_ShotNoise_Rad = abs(EY_PLL_TF_ShotNoise_Rad .* TF_loopsup');
EY_PLL_2_PDH_LaserFreqNoise_rad = abs(EY_LaserFreqNoise_rad .* TF_loopsup');
EY_PLL_2_PDH_fiber = abs(EY_fiber .* TF_loopsup');
Sum_EY_2_PDH_Laser = abs(Sum_EY_Laser .* TF_loopsup');
TF_loopsup = mybodesys(sys(59,39),EY_PLL_NoiseSpecV(:,1));
EY_PLL_2_PDH_Noise_Rad = abs(EY_PLL_NoiseSpec_Rad .* TF_loopsup);


% Compute RMS
Y_rms_PDH = flipud(sqrt(cumtrapz(flipud(EY_PDH_NoiseSpecRad(:,1)), flipud(
    EY_PDH_NoiseSpecRad(:,2)).^2) .* 1));


figure(89)
clf;
set(gcf, 'color', 'w');
ll=loglog(EY_PDH_NoiseSpecRad(:,1) , EY_PDH_NoiseSpecRad(:,2) ,...
     EY_PDH_ShotNoiseSpecRad(:,1),EY_PDH_ShotNoiseSpecRad(:,2),...
     EY_PDH_DarkNoiseSpecRad(:,1),EY_PDH_DarkNoiseSpecRad(:,2),...
     EY_PLL_NoiseSpecV(:,1),EY_PLL_2_PDH_Noise_Rad, ...
     f,EY_PLL_2_PDH_ShotNoise_Rad,...
     f,EY_PLL_2_PDH_PFDNoise_Rad, ...
     f, EY_PLL_2_PDH_LaserFreqNoise_rad, ...
     f, EY_PLL_2_PDH_fiber, 'g',...
```

```
    EY_PDH_NoiseSpecRad(:,1), Y_rms_PDH,'b*');
legend('PDH error signal','PDH shot noise','PDH Dark noise','EY PLL noise ', 'EY PLL
     shot noise', 'EY PLL PFD noise','Free Running Laser Noise', ...
    'Fiber Noise','RMS PDH Error Sig');
xlabel('Frequency [Hz]')
ylabel('Amplitude Spectrum [rad/SqrtHz]')
set(ll,'LineWidth',1.5);
title('EY PDH Noise (in Loop w/o cavity pole)');
xlim([1 10^6]);
ylim([10^ 12 5]);
set(gca, 'Ytick', 10.^( 12:5));
grid on;

figure(600)
clf;
set(gcf, 'color', 'w');
ll=loglog(EY_PDH_NoiseSpecRad(:,1) , EY_PDH_NoiseSpecRad(:,2) ,...
    EY_PDH_ShotNoiseSpecRad(:,1),EY_PDH_ShotNoiseSpecRad(:,2),...
    EY_PDH_DarkNoiseSpecRad(:,1),EY_PDH_DarkNoiseSpecRad(:,2),...
    f_VCO,VCO_noise_rad,...
    f, Sum_EY_2_PDH_Laser, 'g',...
    EY_PDH_NoiseSpecV(:,1), Y_rms_PDH,'b*');
legend('PDH error signal','PDH shot noise','PDH Dark noise','VCO Noise','EX Laser
    Noise', ...
    'RMS PDH Error Sig');
set(ll,'LineWidth',1.5);
xlabel('Frequency [Hz]')
ylabel('Amplitude Spectrum [rad/SqrtHz]')
title('EY PDH Noise (in Loop w/o cavity pole)');
xlim([1 10^5]);
ylim([10^ 8 5]);
set(gca, 'Ytick', 10.^( 8:5));
grid on;


%% DIFF PLL Noise
% load model stuff
f=logspace(0,6,3000);
EY_PDH_OpGain = slope_Y;
EX_PDH_OpGain = 1/slope_X * 5.465;
GainFast =0;
GainSlow =0;
IMCTEST = 0;
ALScontrol_FULL;

% alog 11579    not loop suppressed; the way this data is calibrated we
% need to divide by G to get the error signal; I have divided by 1/1 G, but
% this is okay since data doesn't go above the DIFF PLL UGF
%load('DIFF_PLL_CTRL_04252014.txt');

DIFF_PLL_Err = load('DIFF_PLL_CTRL_05012014_v2.txt'); % in meters
TF_loop = mybodesys(sys(64,47),DIFF_PLL_Err(:,1));
DIFF_PLL_Err(:,2) = abs(DIFF_PLL_Err(:,2) .* TF_loop ./ 7e 12)./DIFF_PLL_Err(:,1);

```

```
% measured out of IMON of the PFD for DIFF (low data not right .. ?)
load('DIFF_PLL_NoiseSpecV.txt'); % units in Volts
DIFF_PLL_NoiseSpecRad(:,1) = DIFF_PLL_NoiseSpecV(:,1);
DIFF_PLL_NoiseSpecRad(:,2) = DIFF_PLL_NoiseSpecV(:,2) .* 36 * pi/180;


% alog 11759    Measured the IR noise spectrum out of DIFF PLL CTRL out
% with the DARM feedback to ETMY only
load('DIFF_PLL_CTRL_wY_05072014.txt'); % units in Hz for IR

% alog 11877. In loop IR noise budget with IR in both arms
load('DIFF_PLL_CTRL_redinloop.txt'); % in umeters
DIFF_PLL_CTRL_redinloop_Hz = DIFF_PLL_CTRL_redinloop(:,2) .* 1e 6/ 7e 12;
DIFF_PLL_CTRL_redinloop_rms_Hz = DIFF_PLL_CTRL_redinloop(:,3) .* 1e 6/ 7e 12;
load('COMM_PLL_CTRL_inloop.txt'); % in for green Hz, at same time as DIFF
    measurement column 2, a few min after column 1
COMM_PLL_CTRL_rms_Hz = flipud(sqrt(cumtrapz(flipud(COMM_PLL_CTRL_inloop(:,1)),
    flipud(COMM_PLL_CTRL_inloop(:,2)).^2) .*  1));


% alog 11877 VCO noise with 2 dividers (??)
load('VCO_w2dividers.txt');

%EY PDH Error signal projected:
TF_anticav = mybodesys(EY_REFL_CAVITY_REFL.sys, EY_PDH_NoiseSpecV(:,1));
TF_remove = mybodesys(sys(79,41),EY_PDH_NoiseSpecV(:,1)); % data is already loop
    suppressed; need to remove before inject
TF_proj = mybodesys(sys(64,41),EY_PDH_NoiseSpecV(:,1));
TF_loop = mybodesys(sys(64,47),EY_PDH_NoiseSpecV(:,1));
EY_2_Diff_PDH_NoiseSpecRad = abs(EY_PDH_NoiseSpecV(:,2) .* TF_proj ./ TF_remove)./
    EY_PDH_NoiseSpecV(:,1);
%EY_2_Diff_PDH_NoiseSpecRad = abs(EY_PDH_NoiseSpecRad(:,2) .* TF_loop .* TF_anticav)
    ;

%EY PDH VCO projected:
TF_proj  = mybodesys(sys(64,49),f_VCO);
EY_2_Diff_PDH_VCONoiseRad = abs(VCO_noise_rad .* TF_proj);

%EY PDH Shot noise projected:
TF_proj  = mybodesys(sys(64,41),EY_PDH_ShotNoiseSpecV(:,1));
EY_2_Diff_PDH_ShotNoiseRad = abs(EY_PDH_ShotNoiseSpecV(:,2) .* TF_proj)./
    EY_PDH_ShotNoiseSpecV(:,1);

%EY PDH Dark noise projected:
TF_proj  = mybodesys(sys(64,41),EY_PDH_DarkNoiseSpecV(:,1));
EY_2_Diff_PDH_DarkNoiseRad = abs(EY_PDH_DarkNoiseSpecV(:,2) .* TF_proj)./
    EY_PDH_DarkNoiseSpecV(:,1);

%EY Sum laser noise projected:
TF_cav = mybodesys(EY_REFL_CAVITY_TR.sys, f);
TF_loop = mybodesys(sys(64,47),f);
EY_2_Diff_Sum_Laser = abs(Sum_EY_2_PDH_Laser .* TF_loop' .* TF_cav');
```

```
% EX PDH noises projected:
remove = mybodesys(sys(36,5),EX_PDH_NoiseSpecV_PLLBoost1Off_PDHBoost2On(:,1)); % data is already loop suppressed; need to remove before inject
EX_2_Diff_PDH_NoiseSpectrum = abs(EX_PDH_NoiseSpecV_PLLBoost1Off_PDHBoost2On(:,2).*mybodesys(sys(64,5),EX_PDH_NoiseSpecV_PLLBoost1Off_PDHBoost2On(:,1))./remove)./EX_PDH_NoiseSpecV_PLLBoost1Off_PDHBoost2On(:,1);
EX_2_Diff_PDH_ShotNoiseSpectrum = abs(EX_PDH_ShotNoiseSpectrum(:,2).*EX_PDH_OpGain.*mybodesys(sys(64,5),EX_PDH_ShotNoiseSpectrum(:,1)))./EX_PDH_ShotNoiseSpectrum(:,1);
EX_2_Diff_PDH_DarkNoise = abs(EX_PDH_DarkNoise(:,2).*EX_PDH_OpGain.*mybodesys(sys(64,5),EX_PDH_DarkNoise(:,1)))./EX_PDH_DarkNoise(:,1);
EX_2_Diff_PDH_VCONoiseRad = abs(VCO_noise_rad .* mybodesys(sys(64,22),f_VCO));

% Optic Displacement L = 1, T = 2, V = 3, R = 4, P = 5, Y = 6
% From Jeff's prediction using alive spectra of the BSC (stage 2) and
% propagate through the sus model.
load('dampingfilters_QUAD_2014 01 30_Level2p1_RealSeismic_model.mat')
f_disp = freq;
disp_noise = opticDisp(1).total; % units: m/sqrtHz
disp_noise_Hz = sqrt(2) * disp_noise * d2f;
disp_noise_rad = disp_noise_Hz ./ f_disp;
EX_2_Comm_disp_TF = mybodesys(sys(64,47),f_disp);
EX_2_Comm_disp_rad = abs(disp_noise_rad .* EX_2_Comm_disp_TF);


tf_loopsup = mybodesys(sys(64,47),f);
% PFD Noise
% ~460nV/SqrtHz at 140Hz, assume flat for freq we care
PFD_noise = 500e 9*ones(size(f));
PFD_noise = 36 * pi/180 .* PFD_noise; % convert to rad/SqtHz
PFD_noise = abs(PFD_noise .* tf_loopsup');

% shot noise from first principles
% DIFF BBPD read 166uW alog 11519
% beatnote of  20dbm
elec = 1.6e 19; % charge of electron
CommPD_power = 116e 6; % watts
CommPD_trans = 1e3;  % 1kOhm at RF ??
CommPD_curr = sqrt(CommPD_power*CommPD_trans);
Carrier_curr = 22.5e 3 / CommPD_trans ;
shot_noise_temp = sqrt(2*elec*CommPD_curr); % shot noise in A/SqrtHz
shot_noise_temp = shot_noise_temp .* CommPD_trans * 36 * pi/180; % shot noise in rad/SqrtHz
shot_noise_2 = shot_noise_temp * ones(size(f));
shot_noise_2 = abs(shot_noise_2 .* tf_loopsup');


% BBPD noise    taken from EX
BBPD_noise =  119*ones(size(f)); %  119 dBm, at 100Hz Bw
beatnote =   35*ones(size(f)); %  35 dBm, at 100Hz BW (for COMM BBPD)
dBc_BBPD = BBPD_noise   beatnote;
dBc_BBPD_Hz = dBc_BBPD   20; % dividing by 100Hz BW is the same as  20dB
BBPD_noise =  10.^(dBc_BBPD_Hz./20); % dBc to rad/sqrtHz
BBPD_noise = abs(BBPD_noise .* tf_loopsup');
```

```
% Data from Daniel    measured from ALS COMM VCO so there is a factor of 10
% for FDD and a factor of 2 for double pass AOM. This only holds up until
% MCL MCF crossover when length path suppresed the VCO ~20Hz)
load('VCO_FDD_ssb_phase_noise_140415_F.txt'); % data units: dBc/sqrtHz
load('VCO_FDD_freq_noise_140415.txt'); % data units: Hz/sqrtHz
f_VCO = VCO_FDD_freq_noise_140415(:,1);
VCO_noise_Hz = VCO_FDD_freq_noise_140415(:,2);
VCO_noise_rad = VCO_noise_Hz ./ f_VCO; % data units: rad/sqrtHz
tf_sup = mybodesys(sys(64,47),f_VCO);
VCO_noise_rad = abs(VCO_noise_rad .* tf_sup);

DIFF_PLL(:,1) = vertcat(DIFF_PLL_Err(1:9917,1), DIFF_PLL_NoiseSpecRad(1527:2903,1));
DIFF_PLL(:,2) = vertcat(DIFF_PLL_Err(1:9917,2), DIFF_PLL_NoiseSpecRad(1527:2903,2));

figure(88);
clf;
ll=loglog(DIFF_PLL(:,1), DIFF_PLL(:,2),...
    EY_PDH_NoiseSpecRad(:,1),EY_2_Diff_PDH_NoiseSpecRad,...
    f_VCO, EY_2_Diff_PDH_VCONoiseRad,'y',....
    EY_PDH_ShotNoiseSpecV(:,1),EY_2_Diff_PDH_ShotNoiseRad,...
    EY_PDH_DarkNoiseSpecV(:,1),EY_2_Diff_PDH_DarkNoiseRad,...
    f,EY_2_Diff_Sum_Laser,...
    f_disp, EX_2_Comm_disp_rad,...
    f,PFD_noise,'r  ',...
    f,BBPD_noise,'m  ',...
    f,shot_noise_2,'b  ',...
    EX_PDH_NoiseSpecV_PLLBoost1Off_PDHBoost2On(:,1),EX_2_Diff_PDH_NoiseSpectrum,'r'
    ,...
    EX_PDH_DarkNoise(:,1),EX_2_Diff_PDH_DarkNoise,...
    EX_PDH_ShotNoiseSpectrum(:,1),EX_2_Diff_PDH_ShotNoiseSpectrum,...
    f_VCO, EX_2_Diff_PDH_VCONoiseRad,'k  ',...
    f_VCO, VCO_noise_rad);
legend('DIFF PLL Error sig','EY PDH Error Sig', 'EY PDH VCO','EY PDH Shot Noise','EY
    PDH Dark Noise','EY Laser Sum','Quad Disp Noise Suppressed','PFD Noise','Dark
    Noise','Shot Noise',...
    'EX PDH Error Sig','EX PDH Dark noise','EX PDH Shot Noise','EX PDH VCO','DIFF
    VCO suppressed','Location','SouthEast');
set(ll,'LineWidth',1.5);
xlabel('Frequency [Hz]')
ylabel('Amplitude Spectrum [rad/SqrtHz]')
title('DIFF PLL Noise');
xlim([1 1e5]);
ylim([1e 14 3e 5]);
set(gca, 'Ytick', 10.^( 14: 5));
grid on;
set(gcf, 'Color','w');




%% Compare DIFF and COMM
% PLL CTRL signals in IR for both comm and diff with IR resonant in arms
f=logspace(0,6,3000);
```

```
EY_PDH_OpGain = slope_Y;
EX_PDH_OpGain = 1/slope_X * 5.465;
GainFast =1;
GainSlow =1;
IMCTEST = 0;
ALScontrol_FULL;

aa=load('NoiseSpecIR_04022014.txt'); % includes the red cavity pole, red noise (
    sheila.dwyer/ALS/COMM/HIFOX/COMM_Noise_march31_SideOfFringe.xml) alog (11106)
f_noise_3 = aa(:,1);
IRNoise_3 = aa(:,2);
rm_IRCavPol = makeZPK([42],[],1,0);
TF_rm_IRCavPol = mybodesys(rm_IRCavPol.sys, f_noise_3);
IRNoise_rmpol_3 = abs(IRNoise_3 .* TF_rm_IRCavPol);
tf_inloop = mybodesys(sys(8,11),f_noise_3);
test = abs(IRNoise_rmpol_3 ./ tf_inloop);


figure(2342);
clf;
ll=loglog(DIFF_PLL_CTRL_redinloop(:,1), DIFF_PLL_CTRL_redinloop_Hz, 'b',...
    DIFF_PLL_CTRL_redinloop(:,1), DIFF_PLL_CTRL_redinloop_rms_Hz,'b  ', ...
    COMM_PLL_CTRL_inloop(:,1), COMM_PLL_CTRL_inloop(:,3)./2,'r',...
    COMM_PLL_CTRL_inloop(:,1), COMM_PLL_CTRL_rms_Hz./2,'r  ');
set(ll, 'LineWidth', 2);
title('In Loop Noise Budget for IR');
legend('DIFF', 'DIFF RMS', 'COMM', 'COMM RMS');
xlim([3e 2 8e3]);
ylim([1e 2 5e3]);
xlabel('Frequency [Hz]');
ylabel('Frequency Fluctuations [Hz/SqrtHz]');
grid on;
set(gcf, 'Color', 'w');
```

/ligo/svncommon/NbSvn/aligonoisebudget/trunk/HIFO/H1/ALS˙TFtest˙NB˙FULL.m

B.3 Noise Budget

```
% ultra cool noise budget script
%
% $Id: noisebudget_X.m 511 2014 02 26 13:26:22Z alexan.staley@LIGO.ORG $
%
% location: /ligo/svncommon/NbSVN/aligonoisebudget/trunk/HIFO/HI


 f_all = logspace( 1, 5, 3000);
names = {};

%% Path set up
addpath('simulink');
addpath('util');
addpath('data');
```

```
svnDir.anb = '/ligo/svncommon/NbSVN/aligonoisebudget/trunk/';
addpath(genpath([svnDir.anb 'Common/Utils']));
clear svnDir


%% load the control model
slope = 7.8972e3;
EX_PDH_OpGain = 1/slope * 5.465;
D_REL = 0;
GainFast =1;
GainSlow =1;
IMCTEST = 0;
ALScontrol_X;

%% Free Running Laser Noise
NPRO_freqfluc_zpk = makeZPK([1e4],[1e 5],1,Inf);
tf_temp = mybodesys(NPRO_freqfluc_zpk.sys, f_all);
NPRO_freqfluc_Hz = abs(tf_temp)';

EndXLaserFreqNoise = NPRO_freqfluc_Hz;
TF_EndXLaserFreqNoise = mybodesys(sys(8,4),f_all);
EX_laserfreq_noise_Hz = abs(NPRO_freqfluc_Hz .* TF_EndXLaserFreqNoise');
%% Fiber phase noise (see LIGO T0900376 v1)
Fiber_noise_zpk = makeZPK([],[1e3],3,0);
tf_temp = mybodesys(Fiber_noise_zpk.sys, f_all);
Fiber_noise_Hz = abs(tf_temp)';

FiberPhaseNoise = Fiber_noise_Hz;
TF_EndXFiberNoise = mybodesys(sys(8,15),f_all);
EX_fiber_noise_Hz = abs(Fiber_noise_Hz .* TF_EndXFiberNoise');


%% End SHG noise in Hz/rtHz    suffeciently low
% D. Yeaton Massey et al., ”A new bound on excess frequency noise in second
% harmonic generation in PPKTP at the 10 19 level”, Opt Express,
% 20(19):21019 20124
EndXSHGNoise = 1e 5 * f_all; % for detail see equation 6.13 in Kiwamu's thesis

%% End PLL PFD noise in unit of V/rtHz    suffeciently low
% noise from PFD test procedure; assumed flat
EndXFIBRPFD = 500e 9*ones(size(f_all));

TF_EndXPFD = mybodesys(sys(8,27),f_all);
EX_PLL_PFDnoise_Hz = abs(500e 9*ones(size(f_all)) .* TF_EndXPFD');

%% END X PLL BBPD Dark Noise
BBPD_noise =  119*ones(size(f_all)); %  119 dBm, at 100Hz Bw
beatnote =   33*ones(size(f_all)); %  33 dBm, at 100Hz BW
dBc_BBPD = BBPD_noise   beatnote;
dBc_BBPD_Hz = dBc_BBPD   20; % dividing by 100Hz BW is the same as  20dB
BBPD_noise =  10.^(dBc_BBPD_Hz./20); % dBc to rad/sqrtHz
BBPD_noise_Hz = BBPD_noise.* 1/36 *180/pi; % conversion through PFD since inject
    after from rad to V

```

```
% !! need to create injection
%EndXBBPDNoise = BBPD_noise_Hz;
TF_EndXBBPD = mybodesys(sys(8,27),f_all);
EX_PLL_darknoise_Hz = abs(BBPD_noise_Hz .* TF_EndXBBPD');

%% End X PLL Shot Noise
shot_noise =  114*ones(size(f_all)); %  114 dBm, at 100Hz Bw
beatnote =   32*ones(size(f_all)); %  33 dBm, at 100Hz BW
dBc = shot_noise   beatnote;
dBc_Hz = dBc   20; % dividing by 100Hz BW is the same as  20dB
shot_noise =  sqrt((10.^(dBc_Hz./20)).^2   10.^(dBc_BBPD_Hz/20).^2); % dBc to rad/sqrtHz, subtracting out the dark noise of the BBPD
shot_noise_Hz = shot_noise.* 1/36 *180/pi; % conversion through PFD since inject after from rad to V

EndXPLL_ShotNoise = shot_noise_Hz;
TF_EndXShotNoise = mybodesys(sys(8,27),f_all);
EX_PLL_shotnoise_Hz = abs(shot_noise_Hz .* TF_EndXShotNoise');





%% PDH demod electronics + dark noise in unit of V/rtHz
% measured with ITM misaligned, PD blocked, out of IMON, HEPA fan off
%(alog 9574)
load('EX_PDH_DarkNoise.txt')
f_temp = EX_PDH_DarkNoise(:,1);
EndXREFLElectronics = EX_PDH_DarkNoise(:,2);

% noise_old = ConvertPS('data/PDH_dark_electronics_070313', 17);
% f = noise_old(:,1);


[b, i, j] = unique(f_temp);
EndXREFLElectronics = interp1(b, EndXREFLElectronics(i), f_all, 'linear', 'extrap');
TF_EndXDarkNoise = mybodesys(sys(8,5),f_temp);
EX_PDH_darknoise_Hz = abs( EX_PDH_DarkNoise(:,2) .* TF_EndXDarkNoise);
%EX_PDH_darknoise_Hz = abs( noise_old(:,2) .* TF_EndXDarkNoise);

%% PDH shot noise
% alog 10611
load('EX_PDH_ShotNoiseAmpSpec.txt');
EX_PDH_ShotNoiseSpectrum(:,:) = EX_PDH_ShotNoiseAmpSpec(:,:);
EX_PDH_ShotNoiseSpectrum(:,2) = EX_PDH_ShotNoiseSpectrum(:,2) .* sqrt(9.44/6.28); % also scale for the power
f_temp = EX_PDH_ShotNoiseSpectrum(:,1);
EndXPDH_ShotNoise = EX_PDH_ShotNoiseSpectrum(:,2);

[b, i, j] = unique(f_temp);
EndXPDH_ShotNoise = interp1(b, EndXPDH_ShotNoise(i), f_all, 'linear', 'extrap');

TF_EndXShotNoise = mybodesys(sys(8,5),f_temp);
EX_PDH_shotnoise_Hz = abs( EX_PDH_ShotNoiseSpectrum(:,2).* TF_EndXShotNoise);
```

```



%% END X PDH ERROR SIGNAL
load('EX_PDH_NoiseSpecV_PLLBoost1Off_PDHBoost2On.txt');
f_temp = EX_PDH_NoiseSpecV_PLLBoost1Off_PDHBoost2On(119:2802,1);
noise = EX_PDH_NoiseSpecV_PLLBoost1Off_PDHBoost2On(119:2802,2);
AntiCav_TF_REFL = mybodesys(EX_REFL_CAVITY_REFL.sys, f_temp);
AntiCav_TF_TR = mybodesys(EX_REFL_CAVITY_TR.sys, f_temp);

GainFast = 0;
GainSlow = 0;
IMCTEST = 0;
ALScontrol_X;
remove = mybodesys(sys(36,5),f_temp); % data is already loop suppressed; need to remove before inject

GainFast = 1;
GainSlow = 1;
IMCTEST = 0;
ALScontrol_X;
TF_EX_PDH = mybodesys(sys(8,5),f_temp);
EX_PDH_error_Hz = abs(noise .* TF_EX_PDH ./remove);



%% Corner PLL PFD noise in unit of V/rtHz
CornerPLLPFD = 500e 9*ones(size(f_all));

TF_COMMPLL = mybodesys(sys(8,24),f_all);
Corner_PFD_Hz = abs(500e 9*ones(size(f_all)) .* TF_COMMPLL');


%% COMM PLL shot noise
% COMM BBPD read 88uW alog 9558
% COMM BBPD read 88uW alog 9558
% beatnote of 28mBpp, PFD RF power  35dbm
elec = 1.6e 19; % charge of electron
CommPD_power = 88e 6; % watts
CommPD_trans = 1e3;  % 1kOhm at RF ??
CommPD_curr = sqrt(CommPD_power*CommPD_trans);
Carrier_curr = 4e 3 / CommPD_trans ; %??
shot_noise_temp = sqrt(2*elec*CommPD_curr); % shot noise in A/SqrtHz
shot_noise_2 = shot_noise_temp * ones(size(f_all));

COMMPLL_ShotNoise = shot_noise_2;

TF_COMMPLL_shot = mybodesys(sys(8,24),f_all);
Corner_shotnoise_Hz = abs(shot_noise_2 .* TF_COMMPLL_shot');


%% COMM BBPD Dark noise
% BBPD noise    taken from EX
BBPD_noise =  119*ones(size(f_all)); %  119 dBm, at 100Hz Bw
```

```
beatnote =  35*ones(size(f_all)); %  35 dBm, at 100Hz BW (for COMM BBPD)
dBc_BBPD = BBPD_noise   beatnote;
dBc_BBPD_Hz = dBc_BBPD   20; % dividing by 100Hz BW is the same as  20dB
BBPD_noise =  10.^(dBc_BBPD_Hz./20); % dBc to rad/sqrtHz
BBPD_noise_Hz = BBPD_noise.* f_all;

TF_COMMPLL_BBPD = mybodesys(sys(8,7),f_all);
Corner_BBPDnoise_Hz = abs(BBPD_noise_Hz .* TF_COMMPLL_BBPD');

%% COMM PLL RF Pick up noise
% alog 11221
% RF_noise =  73*ones(size(f_all)); %  46 dBm, at 100Hz Bw
% beatnote =  33*ones(size(f_all)); %  17 dBm, at 100Hz BW
% dBc_RF = RF_noise   beatnote;
% dBc_RF_Hz = dBc_RF   20; % dividing by 200Hz BW is the same as  20dB
% RF_noise =  10.^(dBc_RF_Hz./20); % dBc to rad/sqrtHz
% RF_noise_Hz = RF_noise.* 1/36 *180/pi; % conversion through PFD since inject after from rad to V

load('RFNoise_04082014.txt');
% units: Vrms/sqrtHz; this data is suppressed by the modified comm pll loop (might not be proper measurement...)
% this will depend on where we lock and how far from carrier the pickups are


% COMM PLL to VCO
GainFast = 0;
GainSlow = 0;
IMCTEST = 0;
COMM_PLL_VCO = makeZPK([],[],1,0);
COMM_PLL_VCO_DCgain = makeZPK([],[],db2mag( 25),0);
clear systm flexTfs
[systm, flexTfs] = linFlexTf('ALS_SIMULINK_X');
systm = prescale(systm);
sys_rf = linFlexTfFold(systm, flexTfs);

rm_modCommPLL = mybodesys(sys_rf(10,18), RFNoise_04082014(:,1));

GainFast = 1;
GainSlow = 1;
IMCTEST = 0;
ALScontrol_X;
TF_COMMPLL = mybodesys(sys(8,24), RFNoise_04082014(:,1));
Corner_COMMPLL_RFnoise = abs(RFNoise_04082014(:,2) .* TF_COMMPLL ./ rm_modCommPLL);

%% COMM PLL Error Sign
load('CommPLL_NoiseSpecV.txt');
f_temp2 = CommPLL_NoiseSpecV(:,1);

load('CommPLL_NoHand_NoiseSpecV.txt');
load('CommPLL_Hand_NoiseSpecV.txt');
f_temp2_1 = CommPLL_NoHand_NoiseSpecV(240:1654,1);
f_temp2_2 = CommPLL_Hand_NoiseSpecV(:,1);

```

```
GainFast = 0;
GainSlow = 0;
IMCTEST = 0;
ALScontrol_X;
remove = mybodesys(sys(10,18),f_temp2); % data is already loop suppressed; need to remove before inject
remove_1 = mybodesys(sys(10,18),f_temp2_1); % data is already loop suppressed; need to remove before inject

GainFast = 1;
GainSlow = 1;
IMCTEST = 0;
ALScontrol_X;
TF_COMMPLL = mybodesys(sys(8,24),f_temp2);
TF_COMMPLL_1 = mybodesys(sys(8,24),f_temp2_1);
TF_COMMPLL_2 = mybodesys(sys(8,24),f_temp2_2);
remove_2 = mybodesys(sys(58,24),f_temp2_2); % data is already loop suppressed; need to remove before inject
Corner_COMMPLL_error_Hz = abs(CommPLL_NoiseSpecV(:,2) .* TF_COMMPLL ./remove);
Corner_COMMPLL_error_Hz_1 = abs(CommPLL_NoHand_NoiseSpecV(240:1654,2) .* TF_COMMPLL_1 ./remove_1);
Corner_COMMPLL_error_Hz_2 = abs(CommPLL_Hand_NoiseSpecV(:,2) .*TF_COMMPLL_2 ./ remove_2);

%% Intensity ISS on Noise
% alog 10821
data = load('PDB_DC_HZ_ISSon.txt');
names = {names{:}, 'Itensity ISS off Noise'};
data(:,2) = data(:,2) ./ 2.818e14 .* 1.36e3;
f = data(:,1);

IntensityISSOnNoise = interp1(f, data(:,2), f_all, 'linear', 'extrap');

TF_Int = mybodesys(sys(8,9),f);
IMC_IntensityNoise_Hz = abs(data(:,2) .* TF_Int);

%% ADC Noise
load('PureADCNoise_03252014.txt');
load('ADCNoiseAntiWhit_03252014.txt');
test = abs(ADCNoiseAntiWhit_03252014(:,2) .* mybodesys(WHITENING.sys, ADCNoiseAntiWhit_03252014(:,1)) );
TF_ADC = mybodesys(sys(8,26), ADCNoiseAntiWhit_03252014(:,1) );
ADCNoise = abs(ADCNoiseAntiWhit_03252014(:,2) .* TF_ADC .* mybodesys(WHITENING.sys, ADCNoiseAntiWhit_03252014(:,1)));
ADCNoiseNoSignal = interp1(PureADCNoise_03252014(:,1), PureADCNoise_03252014(:,2), f_all, 'linear', 'extrap');


%% IMC Shot Noise
load('IMC_PD_Noise.txt');
f_IMC_PD_Noise = IMC_PD_Noise(:,1);
IMC_PD_shot_noise_V = IMC_PD_Noise(:,2) .* 20/2^16 / 100; % cnts to Vrms/sqrtHz

```

```
TF_IMC = mybodesys(sys(8,13),f_IMC_PD_Noise);

IMC_shotnoise_Hz = abs(IMC_PD_shot_noise_V .* TF_IMC);


%% IMC Dark Noise
IMC_PD_dark_noise_V = IMC_PD_Noise(:,3) .* 20/2^16 / 100; % cnts to Vrms/sqrtHz
IMC_darknoise_Hz = abs(IMC_PD_dark_noise_V .* TF_IMC);


%% IMC VCO  (see LIGO T0900451 v1)
% num = xlsread('data/VCOphasenoise.xls', 1, 'A4:B2402'); % data in dBc/Hz
% f_VCO = num(:,1);
% Srad = 10.^(num(:,2)./20);
% IMCVCO_Hz = sqrt(2) .* Srad .* f_VCO; % phase noise in Hz/SqrtHz

% better data from mevans
% https://awiki.ligo wa.caltech.edu/aLIGO/RfDesign plot 3
%load('VCOphasenoise.txt');

% Data from Daniel    measured from ALS COMM VCO so there is a factor of 10
% for FDD and a factor of 2 for double pass AOM. This only holds up until
% MCL MCF crossover when length path suppresed the VCO ~20Hz)
% alog 11385
load('VCO_FDD_ssb_phase_noise_140415_F.txt'); % data units: dBc/sqrtHz
load('VCO_FDD_freq_noise_140415.txt'); % data units: Hz/sqrtHz
f_VCO = VCO_FDD_freq_noise_140415(:,1);
IMCVCO_dBc = VCO_FDD_ssb_phase_noise_140415_F(:,2);
IMCVCO_rad = db2mag(IMCVCO_dBc);
IMCVCO_Hz = VCO_FDD_freq_noise_140415(:,2) .* 10;

[b, i, j] = unique(f_VCO);
IMCVCO = interp1(b, IMCVCO_Hz(i), f_all, 'linear', 'extrap');

TF_IMCVCO = mybodesys(sys(8,23),f_VCO);
IMCVCO_noise_Hz = abs(IMCVCO_Hz .* TF_IMCVCO);


%% CMM PLL VCO

% Data from Daniel    measured from ALS COMM VCO so there is a factor of 10
% for FDD and a factor of 2 for double pass AOM. This only holds up until
% MCL MCF crossover when length path suppresed the VCO ~20Hz)
load('VCO_FDD_ssb_phase_noise_140415_F.txt'); % data units: dBc/sqrtHz
load('VCO_FDD_freq_noise_140415.txt'); % data units: Hz/sqrtHz
f_VCO = VCO_FDD_freq_noise_140415(:,1);
COMMVCO_Hz = VCO_FDD_freq_noise_140415(:,2);

TF_COMMVCO = mybodesys(sys(8,18),f_VCO);
COMMVCO_noise_Hz = abs(COMMVCO_Hz .* TF_COMMVCO);


%% PDH VCO

```

```
% Data from Daniel    measured from ALS COMM VCO so there is a factor of 10
% for FDD and a factor of 2 for double pass AOM. This only holds up until
% MCL MCF crossover when length path suppresed the VCO ~20Hz)
load('VCO_FDD_ssb_phase_noise_140415_F.txt'); % data units: dBc/sqrtHz
load('VCO_FDD_freq_noise_140415.txt'); % data units: Hz/sqrtHz
f_VCO = VCO_FDD_freq_noise_140415(:,1);
PDHVCO_Hz = VCO_FDD_freq_noise_140415(:,2);

TF_COMMVCO = mybodesys(sys(8,22),f_VCO);
PDHVCO_noise_Hz = abs(PDHVCO_Hz .* TF_COMMVCO);


%% Quad Displacement noise
load('dampingfilters_QUAD_2014 01 30_Level2p1_RealSeismic_model.mat')
f_disp = freq;
disp_noise = opticDisp(1).total; % units: m/sqrtHz

COMM_2_IR_TF2 = mybodesys(sys(8,2),f_disp);
disp_noise_Hz = abs(disp_noise .* COMM_2_IR_TF2) .* f_disp;

%% Corner SHG noise in Hz/rtHz
% D. Yeaton Massey et al., "A new bound on excess frequency noise in second
% harmonic generation in PPKTP at the 10 19 level", Opt Express,
% 20(19):21019 20124
CornerSHG = 1e 5 * f_all; % for detail see equation 6.13 in Kiwamu's thesis

%%
% %% DAC & CD Noise for MC2_M3 in m/SqrtHz    suffeciently low
% % load data measured by Jeff (LLO log 4751 3rd attachment cyan line)
% f = logspace(1,3, 100);
% DACandCDNoiseMC2M3 = 2.389e 17.*f.^( 0.7927); % estimated a line from the loglog
    plot
%
% DACandCDNoiseMC2M3 = interp1(f, DACandCDNoiseMC2M3, f_all, 'linear', 'extrap');
%
DACandCDNoiseMC2M3 = 0;
% %% DAC & CD Noise for MC2_M2 in m/SqrtHz    suffeciently low
% % load data measured by Jeff (LLO log 4751 3rd attachment green line)
% f = logspace(1,3, 100);
% DACandCDNoiseMC2M2 = 1.66e 14.*f.^( 3.3187); % estimated a line from the loglog
    plot
%
% DACandCDNoiseMC2M2 = interp1(f, DACandCDNoiseMC2M2, f_all, 'linear', 'extrap');
%
 DACandCDNoiseMC2M2 = 0;
% %% Beat note dark noise in Hz/rtHz
% f = logspace( 2, 4, 256);
% sig = 14e 3; %  24dBm
% floor = 22e 9; % At 80MHz the floor noise of the beat note PD was  139dbm/Hz with
    300KHz BW resolution
% BeatnoteDarkNoise= f.* sqrt(2) * floor/sig; % for detail see equation 6.13 in
    Kiwamu's thesis
%
% BeatnoteDarkNoise = interp1(f, BeatnoteDarkNoise, f_all, 'linear', 'extrap');
```

```
 BeatnoteDarkNoise = 0;
% %% Beat note electronic noise (includes ADC noise)
% % load data measured July 25, 2013   alog 7216 black line
% names = {names{:}, 'ADC noise with signal'};
% noise = importdata('data/H1LSC REFL_SERVO_SLOW_OUT_07252013.0');
% f = noise.data(:,1);
% ADCNoiseWithSignal = noise.data(:,2);
%
% ADCNoiseWithSignal = interp1(f, ADCNoiseWithSignal, f_all, 'linear', 'extrap');
 ADCNoiseWithSignal = 0;
% %% Electronic Noise Measurements of IMC    suffeciently low
% IMC_ENOISE_FASTOUT = ConvertPS('data/IMC_ENOISE_FASTOUT_062713', 17);
% f = IMC_ENOISE_FASTOUT(:,1);
% IMCElectronicsNoise = IMC_ENOISE_FASTOUT(:,2);
%
% IMCElectronicsNoise = interp1(f, IMCElectronicsNoise, f_all, 'linear', 'extrap');
 IMCElectronicsNoise = 0;
% %% IMC Seismic ** Terminate at 3Hz for pure IMC seismic
% % Import Noise spectrum
% load data/H1IMC_X_DQ
% f = H1IMC_X_DQ(:,1);
% % Inverse whitening filter
% filter = makeZPK([1000 1000], [0.2 0.2], 1/2.5e7,Inf);
% filter = squeeze(freqresp(filter.sys,2*pi*f));
%
% MCSeismic = abs(filter).*H1IMC_X_DQ(:,2);
%
% MCSeismic = interp1(f(1:180), MCSeismic(1:180), f_all, 'linear', 'extrap');
% MCSeismic(181:3000) = 0.* MCSeismic(181:3000); % remove negative data
%
 MCSeismic = 0;
% %% Seismic ETMY (nm)    should be same for ITMY
% load /ligo/svncommon/SeiSVN/seismic/BSC ISI/H1/ETMY/Data/Spectra/Isolated/H1_ISI_ETMY_Y_Direction_Perf_For_ISC_Noise_Budget_20130806.mat
% f = H1_ISI_Stage_2_Best_Perf_Y_Direction_20130614.Frequency;
% ETMYITMYSeismic = H1_ISI_Stage_2_Best_Perf_Y_Direction_20130614.Spectra_Isolated .* 1e 9;
%
% ETMYITMYSeismic = interp1(f, ETMYITMYSeismic, f_all, 'linear', 'extrap');
% ETMYITMYSeismic(2108:3000) = 0.* ETMYITMYSeismic(2108:3000); % remove negative data
%
 ETMYITMYSeismic = 0;
% %% CM electronic noise
% % With a terminator after the SR560
% Noise1 = load ('data/TermAfterSR560_AnalogElecNoiseCMB_08082013.TXT');
% CMBoardAnalogElectronics = Noise1(:,2) * 3276.8; % convert V to cnts
% f = Noise1(:,1);
%
% CMBoardAnalogElectronics = interp1(f, CMBoardAnalogElectronics, f_all, 'linear', 'extrap');
 CMBoardAnalogElectronics = 0;
%

```

```
%% PSL Noise (taken from free running laser noise T0900649)
NPRO_freqfluc_zpk = makeZPK([1e4],[1e5],1,Inf);
tf_temp = mybodesys(NPRO_freqfluc_zpk.sys, f_all);
NPRO_freqfluc_Hz = abs(tf_temp)';

TF_PSLNoise = mybodesys(sys(8,8),f_all);
PSL_noise_Hz = abs(NPRO_freqfluc_Hz .* TF_PSLNoise');



%% IMC Length Fluct
% Measured with H1IMC_F: FM1,2,3,4 ON (rest off)
% see /ligo/home/alexan.staley/Public/IMC_Meas/IMC_LengthNoise_05012014.xml
% see G1300236 pg 4 (measurements are consistent)
load('IMC_LengthNoise.txt');
f_IMC = IMC_LengthNoise(:,1);
IMCLengthFluc_MCF_m = IMC_LengthNoise(:,2);
IMCLengthFluc_MCL_cnts = IMC_LengthNoise(:,3);

TF_IMCLength_MCL = mybodesys(sys(8,19),f_IMC);
TF_IMCLength_MCF = mybodesys(sys(8,9),f_IMC);
IMCLengthNoise_MCL_Hz = abs(IMCLengthFluc_MCL_cnts .* TF_IMCLength_MCL);
IMCLengthNoise_MCF_Hz = abs(IMCLengthFluc_MCF_m .* TF_IMCLength_MCF);

%% Length difference btwn ALS trans beam and PSL doubled beam cauese phase noise
    that is not suppressed
load('Delay.txt');
Delay2green(:,1) = 2*Delay(:,1); % for twice fringe speed for green
Delay2green(:,2) = 2*Delay(:,2); % from red to green
Delay2red(:,2) = 1/2 * Delay2green(:,2); % green to red since NB is for red
delay2red_Hz(:,2) = Delay2red(:,2) .* Delay2green(:,1);

%% Measured out of loop infared sensor
aa=load('NoiseSpecIR_04022014.txt'); % includes the red cavity pole, red noise (
    sheila.dwyer/ALS/COMM/HIFOX/COMM_Noise_march31_SideOfFringe.xml) alog (11106)
f_noise_3 = aa(:,1);
IRNoise_3 = aa(:,2);
rm_IRCavPol = makeZPK([42],[],1,0);
TF_rm_IRCavPol = mybodesys(rm_IRCavPol.sys, f_noise_3);
IRNoise_rmpol_3 = abs(IRNoise_3 .* TF_rm_IRCavPol);

% Compute RMS
RMS = flipud(sqrt(cumtrapz(flipud(f_noise_3), flipud(IRNoise_rmpol_3).^2) .*  1));


%% Plot (modern way)
% [noises, sys2] = nbFromSimulink('ALS_SIMULINK_X', f_all);
%
%
% disp('Noise Budget for HIFOX')
% nb = nbGroupNoises('ALS_SIMULINK_X', noises, sys2);
% nb.sortModel();
% measuredNoise.f = f_noise_3;
% measuredNoise.asd = IRNoise_rmpol_3;
% measuredNoise.name = 'Measured Residual Noise from IR REFL';
```

```
% measuredRMSNoise.f = f_noise_3;
% measuredRMSNoise.asd = RMS;
% measuredRMSNoise.name = 'RMS from IR REFL';
% requirementsNoise.f = f_all;
% requirementsNoise.asd = 8*ones(size(f_all));
% requirementsNoise.name = 'Noise Requirement';
% nb.referenceNoises = {measuredNoise,requirementsNoise,measuredRMSNoise};
% %matlabNoisePlot(nb);
% set(gcf, 'color', 'w');
% xlim([1e 1 1e4]);
% ylim([1e 10 1e3]);


%% Plot (manual)

figure(3824);
clf;
title('Noise IR Out of Loop');
ylabel('Hz/SqrtHz');
xlabel('Freq Hz');
loglog(f_noise_3,IRNoise_rmpol_3,...
    f_noise_3, RMS,...
    f_IMC_PD_Noise,IMC_darknoise_Hz,...
    f_IMC_PD_Noise,IMC_shotnoise_Hz,...
    ADCNoiseAntiWhit_03252014(:,1),ADCNoise,...
    data(:,1), IMC_IntensityNoise_Hz,...
    CommPLL_NoHand_NoiseSpecV(240:1654,1),Corner_COMMPLL_error_Hz_1,'k',...
    f_all, Corner_BBPDnoise_Hz,...
    f_all, Corner_PFD_Hz,'b  ',...
    EX_PDH_NoiseSpecV_PLLBoost1Off_PDHBoost2On(119:2802,1),EX_PDH_error_Hz,'g  ',...
    EX_PDH_ShotNoiseSpectrum(:,1), EX_PDH_shotnoise_Hz,'m  ',...
    EX_PDH_DarkNoise(:,1),EX_PDH_darknoise_Hz,'k  ',...
    f_all, EX_PLL_shotnoise_Hz,'r o',...
    f_all, EX_PLL_darknoise_Hz,'b *',...
    f_all, EX_fiber_noise_Hz,'r *',...
    f_all, EX_laserfreq_noise_Hz,'g *',...
    f_disp, disp_noise_Hz,'k *',...
    f_VCO, COMMVCO_noise_Hz,'c *',...
    f_IMC, IMCLengthNoise_MCL_Hz,'r  ',...
    f_IMC, IMCLengthNoise_MCF_Hz,...
    Delay2green(1:167,1), delay2red_Hz(1:167,2));
%    f_VCO, IMCVCO_noise_Hz,'c  ',...
%   CommPLL_Hand_NoiseSpecV(:,1),Corner_COMMPLL_error_Hz_2,'r',...
%   RFNoise_04082014(:,1), Corner_COMMPLL_RFnoise
%   f_all, EX_PLL_PFDnoise_Hz,...
%   f_all, Corner_shotnoise_Hz,
grid on;
legend('IR Noise',....
    'RMS',...
    'IMC PD Dark Noise',...
    'IMC PD Shot Noise',...
    'ADC Noise',...
    'IMC Intensity Noise',...
    'Comm PLL error sig',...
```

```
    'COMM PLL BBPD Dark Noise',...
    'COMM PLL PFD Noise',...
    'EX PDH Error Sig',...
    'EX PDH Shot Noise',...
    'EX PDH Dark Noise',...
    'EX PLL Shot Noise',...
    'EX PLL Dark Noise',...
    'Fiber Noise',...
    'Laser Noise',...
    'Disp Noise',...
    'Suppressed COMM VCO',...
    'IMC Length Fluc MCL Control',...
    'IMC Length Fluc MCF Control',...
    'Noise from Length diff',...
    'Location', 'NorthEastOutside');
%    'Suppressed IMC VCO',...
%   'Comm PLL error sig w/ hand',...
%   'Corner RF pickup noise Estimate',...
%   'EX PLL PFD Noise',...
%   'COMM PLL BBPD Shot Noise',...
xlabel('Frequency [Hz]');
ylabel('Freq Fluctuations [Hz/SqrtHz]');
xlim([1e 2 1e5]);
ylim([1e 7 1e2]);
set(gca,'Ytick',10.^( 7:2))
set(gcf, 'Color', 'w');

figure(3826);
clf;
title('Noise IR Out of Loop');
ylabel('Hz/SqrtHz');
xlabel('Freq Hz');
loglog(f_noise_3,IRNoise_rmpol_3,...
    f_noise_3, RMS,...
    CommPLL_NoHand_NoiseSpecV(240:1654,1),Corner_COMMPLL_error_Hz_1,'k',...
    f_all, Corner_BBPDnoise_Hz,...
    EX_PDH_NoiseSpecV_PLLBoost1Off_PDHBoost2On(119:2802,1),EX_PDH_error_Hz,'g  ',...
    f_all, EX_PLL_shotnoise_Hz,'m o',...
    f_all, EX_PLL_darknoise_Hz,'b *',...
    f_all, EX_fiber_noise_Hz,'r *',...
    f_all, EX_laserfreq_noise_Hz,'g *',...
    f_disp, disp_noise_Hz,'k *',...
    f_VCO, COMMVCO_noise_Hz,'c *',...
    f_IMC, IMCLengthNoise_MCL_Hz,'r  ',...
    f_IMC, IMCLengthNoise_MCF_Hz,...
    Delay2green(1:167,1), delay2red_Hz(1:167,2));
grid on;
legend('IR Noise',....
    'RMS',...
    'Comm PLL error sig',...
    'COMM PLL BBPD Dark Noise',...
    'EX PDH Error Sig',...
    'EX PLL Shot Noise',...
    'EX PLL Dark Noise',...
```

```
    'Fiber Noise',...
    'Laser Noise',...
    'Disp Noise',...
    'Suppressed COMM VCO',...
    'IMC Length Fluc MCL Control',...
    'IMC Length Fluc MCF Control',...
    'Noise from Length diff',...
    'Location', 'NorthEastOutside');
xlabel('Frequency [Hz]');
ylabel('Freq Fluctuations [Hz/SqrtHz]');
xlim([1e 2 1e5]);
ylim([1e 4 1e2]);
set(gca,'Ytick',10.^( 4:2))
set(gcf, 'Color', 'w');

figure(3826);
clf;
title('Noise IR Out of Loop');
ylabel('Hz/SqrtHz');
xlabel('Freq Hz');
ll  = loglog(f_noise_3,IRNoise_rmpol_3,...
    f_noise_3, RMS,...
    EX_PDH_NoiseSpecV_PLLBoost1Off_PDHBoost2On(119:2802,1),EX_PDH_error_Hz,...
    f_all, EX_fiber_noise_Hz,...
    f_all, EX_laserfreq_noise_Hz,...
    CommPLL_NoHand_NoiseSpecV(240:1654,1),Corner_COMMPLL_error_Hz_1,...
    Delay2green(1:167,1), delay2red_Hz(1:167,2),...
    f_disp(651:2001), disp_noise_Hz(651:2001));
set(ll, 'LineWidth', 2.5);
set(ll(1),'Color',[1, 0, 0]);
set(ll(2),'Color',[1, 0, 0],'LineStyle','  ');
set(ll(3),'Color',[0, 0, 1]);
set(ll(4),'Color',[0, 0, 0],'LineStyle',' .');
set(ll(5),'Color',[0, .907, 0.907],'LineStyle',' .');
set(ll(6),'Color',[0, 0.5, 0]);
set(ll(7),'Color',[0, 0.6, 0.6]);
set(ll(8),'Color',[0, 0, 0]);

%set(ll(5),'Color',[0.453, 0.453, 0.453]);
%set(ll(5),'Color',[0.42, 0.259, 0.149]);
%set(ll(6),'Color',[0.453, 0, 0.907]);
%set(ll(6),'Color',[.298, 0, 0.6]);
%set(ll(7),'Color',[0.7, 0, 0]);

grid on;
% leg = legend('IR out of Loop Noise',....
%     'RMS',...
%     'EX PDH Error Signal',...
%     'Fiber Noise',...
%     'Laser Noise',...
%     'Comm PLL Error Signal',...
%     'Noise from Length Variations',...
%     'Displacement Noise',...
%     'Location', 'NorthEastOutside');
```

```
xlim([1e 1 1e5]);
ylim([1e 3 1e2]);
set(gca,'Ytick',10.^( 3:2))
set(gca,'Xtick',10.^( 1:5))
set(gca, 'FontSize', 20);
set(gcf, 'Color', 'w');
%set(leg, 'FontSize', 15);
xlabel('Frequency [$Hz$]','Interpreter','Latex','fontSize', 20);
ylabel('Frequency Fluctuations [$Hz/\sqrt{Hz}$]','Interpreter','Latex','fontSize', 20);

%% Compare to HIFOY
% Measured out of loop infared sensor
% import power spectrum (measured July 25, 2013)    alog 7216, Brown
H1LSC_REFLAIR_A_RF9_I_ERR = importdata('data/H1LSC_REFLAIR_A_RF9_I_ERR.0');
% names = {names{:}, 'HIFOY noise from IR REFL'};
% loglog(f, H1LSC_REFLAIR_A_RF9_I_ERR.data(:,2)/2, 'Color', 'r', 'LineWidth',2);  % factor of 1/2 comes from green to red conversion

% Compute RMS
RMS_Y = flipud(sqrt(cumtrapz(flipud(H1LSC_REFLAIR_A_RF9_I_ERR.data(:,1)), flipud((H1LSC_REFLAIR_A_RF9_I_ERR.data(:,2)./2)).^2) .*  1));
% names = {names{:}, 'RMS form IR REFL at high BW'};
% loglog(H1LSC_REFLAIR_A_RF9_I_ERR.data(:,1), RMS, 'Color', 'r', 'LineStyle', '  ', 'Linewidth', 2);

figure(4567);
clf
ll=loglog(f_noise_3,IRNoise_rmpol_3,'b',...
     f_noise_3, RMS, 'b  ',...
     H1LSC_REFLAIR_A_RF9_I_ERR.data(:,1),H1LSC_REFLAIR_A_RF9_I_ERR.data(:,2)./2,'r',...
     H1LSC_REFLAIR_A_RF9_I_ERR.data(:,1), RMS_Y,'r  ');
legend('HIFOX', 'HIFOX RMS', 'HIFOY', 'HIFOY RMS','Location','SouthWest');
xlabel('Frequency [Hz]');
ylabel('Frequency Fluctuations [Hz/SqrtHz]');
grid on;
set(gcf, 'Color', 'w');
set(ll, 'LineWidth',2);
```

/ligo/svncommon/NbSvn/aligonoisebudget/trunk/HIFO/H1/noisebudget˙X.m

```
% ultra cool noise budget script
%
% $Id: noisebudget_X.m 511 2014 02 26 13:26:22Z alexan.staley@LIGO.ORG $
%
% location: /ligo/svncommon/NbSVN/aligonoisebudget/trunk/HIFO/HI


f_all = logspace( 1, 5, 3000);
names = {};

%% Path set up
addpath('simulink');
```

```
addpath('util');
addpath('data');
svnDir.anb = '/ligo/svncommon/NbSVN/aligonoisebudget/trunk/';
addpath(genpath([svnDir.anb 'Common/Utils']));
clear svnDir


%% load the control model
slope_Y = 6.9753e 4; % Volts/Hz !! slope and optical gain should be the same
slope_X = 7.8972e3;
EX_PDH_OpGain = 1/slope_X * 5.465;
EY_PDH_OpGain = slope_Y;
GainFast =1;
GainSlow =1;
IMCTEST = 0;
xfeedback = 1;
yfeedback = 1;
handoffstate = 'diffstate'; % for ey and diff measurements, we run under diff handoff state
ALScontrol_FULL;

%% Free Running Laser Noise
NPRO_freqfluc_zpk = makeZPK([1e4],[1e 5],1,Inf);
tf_temp = mybodesys(NPRO_freqfluc_zpk.sys, f_all);
NPRO_freqfluc_Hz = abs(tf_temp)';

EndXLaserFreqNoise = NPRO_freqfluc_Hz;
TF_EndXLaserFreqNoise = mybodesys(sys(65,4),f_all);
EX_laserfreq_noise_Hz = abs(NPRO_freqfluc_Hz .* TF_EndXLaserFreqNoise');

TF_EndYLaserFreqNoise = mybodesys(sys(65,40),f_all);
EY_laserfreq_noise_Hz = abs(NPRO_freqfluc_Hz .* TF_EndYLaserFreqNoise');

%% Fiber phase noise (see LIGO T0900376 v1)
Fiber_noise_zpk = makeZPK([],[1e3],3,0);
tf_temp = mybodesys(Fiber_noise_zpk.sys, f_all);
Fiber_noise_Hz = abs(tf_temp)';

FiberPhaseNoise = Fiber_noise_Hz;
TF_EndXFiberNoise = mybodesys(sys(65,15),f_all);
EX_fiber_noise_Hz = abs(Fiber_noise_Hz .* TF_EndXFiberNoise');

TF_EndYFiberNoise = mybodesys(sys(65,46),f_all);
EY_fiber_noise_Hz = abs(Fiber_noise_Hz .* TF_EndYFiberNoise');

%% End SHG noise in Hz/rtHz    suffeciently low
% D. Yeaton Massey et al., "A new bound on excess frequency noise in second
% harmonic generation in PPKTP at the 10 19 level", Opt Express,
% 20(19):21019 20124
EndXSHGNoise = 1e 5 * f_all; % for detail see equation 6.13 in Kiwamu's thesis

%% End PLL PFD noise in unit of V/rtHz    suffeciently low
% noise from PFD test procedure; assumed flat
EndXFIBRPFD = 500e 9*ones(size(f_all));
```

```

TF_EndXPFD = mybodesys(sys(65,27),f_all);
EX_PLL_PFDnoise_Hz = abs(500e 9*ones(size(f_all)) .* TF_EndXPFD');

TF_EndYPFD = mybodesys(sys(65,51),f_all);
EY_PLL_PFDnoise_Hz = abs(500e 9*ones(size(f_all)) .* TF_EndYPFD');

%% END X PLL BBPD Dark Noise
BBPD_noise =  119*ones(size(f_all)); %  119 dBm, at 100Hz Bw
beatnote =   33*ones(size(f_all)); %  33 dBm, at 100Hz BW
dBc_BBPD = BBPD_noise   beatnote;
dBc_BBPD_Hz = dBc_BBPD   20; % dividing by 100Hz BW is the same as  20dB
BBPD_noise =  10.^(dBc_BBPD_Hz./20); % dBc to rad/sqrtHz
BBPD_noise_Hz = BBPD_noise.* 1/36 *180/pi; % conversion through PFD since inject after from rad to V

TF_EndXBBPD = mybodesys(sys(65,27),f_all);
EX_PLL_darknoise_Hz = abs(BBPD_noise_Hz .* TF_EndXBBPD');

%% END Y PLL BBPD Dark Noise
% BBPD noise    measured out of preamplifier direct ( 1dB), with BBPD
% blocked
BBPD_noise =  115*ones(size(f_all)); %  116 dBm, at 100Hz Bw
beatnote =   18*ones(size(f_all)); %  21 dBm, at 100Hz BW
dBc_BBPD = BBPD_noise   beatnote;
dBc_BBPD_Hz = dBc_BBPD   20; % dividing by 100Hz BW is the same as  20dB
BBPD_noise =  10.^(dBc_BBPD_Hz./20); % dBc to rad/sqrtHz
BBPD_noise_Hz = BBPD_noise.* 1/36 *180/pi; % conversion through PFD since inject after from rad to V


TF_EndYBBPD = mybodesys(sys(65,51),f_all);
EY_PLL_darknoise_Hz = abs(BBPD_noise_Hz .* TF_EndYBBPD');

%% End X PLL Shot Noise
shot_noise =  114*ones(size(f_all)); %  114 dBm, at 100Hz Bw
beatnote =   32*ones(size(f_all)); %  33 dBm, at 100Hz BW
dBc = shot_noise   beatnote;
dBc_Hz = dBc   20; % dividing by 100Hz BW is the same as  20dB
shot_noise =  sqrt((10.^(dBc_Hz./20)).^2   10.^(dBc_BBPD_Hz/20).^2); % dBc to rad/sqrtHz, subtracting out the dark noise of the BBPD
shot_noise_Hz = shot_noise.* 1/36 *180/pi; % conversion through PFD since inject after from rad to V

EndXPLL_ShotNoise = shot_noise_Hz;
TF_EndXShotNoise = mybodesys(sys(65,27),f_all);
EX_PLL_shotnoise_Hz = abs(shot_noise_Hz .* TF_EndXShotNoise');

%% END Y PLL Shot Noise
shot_noise =  107*ones(size(f_all)); %  108 dBm, at 100Hz Bw
beatnote =   18*ones(size(f_all)); %  21 dBm, at 100Hz BW
dBc = shot_noise   beatnote;
dBc_Hz = dBc   20; % dividing by 100Hz BW is the same as  20dB
```

```
shot_noise =  sqrt((10.^(dBc_Hz./20)).^2   10.^(dBc_BBPD_Hz/20).^2); % dBc to rad/sqrtHz, subtracting out the dark noise of the BBPD
shot_noise_Hz = shot_noise.* 1/36 *180/pi; % conversion through PFD since inject after from rad to V


TF_EndYShotNoise = mybodesys(sys(65,51),f_all);
EY_PLL_shotnoise_Hz = abs(shot_noise_Hz .* TF_EndYShotNoise');


%% EX PDH demod electronics + dark noise in unit of V/rtHz
% measured with ITM misaligned, PD blocked, out of IMON, HEPA fan off
%(alog 9574)
load('EX_PDH_DarkNoise.txt')
f_temp = EX_PDH_DarkNoise(:,1);
EndXREFLElectronics = EX_PDH_DarkNoise(:,2);

% noise_old = ConvertPS('data/PDH_dark_electronics_070313', 17);
% f = noise_old(:,1);


[b, i, j] = unique(f_temp);
EndXREFLElectronics = interp1(b, EndXREFLElectronics(i), f_all, 'linear', 'extrap');
TF_EndXDarkNoise = mybodesys(sys(65,5),f_temp);
EX_PDH_darknoise_Hz = abs( EX_PDH_DarkNoise(:,2) .* TF_EndXDarkNoise);

%% EY PDH Dark Noise
load('EY_PDH_DarkNoiseSpecV.txt'); % units in vplts;
f_temp = EY_PDH_DarkNoiseSpecV(:,1);
TF_EndYDarkNoise = mybodesys(sys(65,41),f_temp);
EY_PDH_darknoise_Hz = abs( EY_PDH_DarkNoiseSpecV(:,2) .* TF_EndYDarkNoise);


%% EX PDH shot noise
% alog 10611
load('EX_PDH_ShotNoiseAmpSpec.txt');
EX_PDH_ShotNoiseSpectrum(:,:) = EX_PDH_ShotNoiseAmpSpec(:,:);
EX_PDH_ShotNoiseSpectrum(:,2) = EX_PDH_ShotNoiseSpectrum(:,2) .* sqrt(9.44/6.28); % also scale for the power
f_temp = EX_PDH_ShotNoiseSpectrum(:,1);
EndXPDH_ShotNoise = EX_PDH_ShotNoiseSpectrum(:,2);

[b, i, j] = unique(f_temp);
EndXPDH_ShotNoise = interp1(b, EndXPDH_ShotNoise(i), f_all, 'linear', 'extrap');

TF_EndXShotNoise = mybodesys(sys(65,5),f_temp);
EX_PDH_shotnoise_Hz = abs( EX_PDH_ShotNoiseSpectrum(:,2).* TF_EndXShotNoise);

%% EY Shot Noise
load('EY_PDH_ShotNoiseSpecV.txt'); % units in volts;
f_temp = EY_PDH_ShotNoiseSpecV(:,1);
TF_EndYShotNoise = mybodesys(sys(65,41),f_temp);
EY_PDH_shotnoise_Hz = abs( EY_PDH_ShotNoiseSpecV(:,2).* TF_EndYShotNoise);
```

```


%% EX PDH VCO

% Data from Daniel    measured from ALS COMM VCO so there is a factor of 10
% for FDD and a factor of 2 for double pass AOM. This only holds up until
% MCL MCF crossover when length path suppresed the VCO ~20Hz)
load('VCO_FDD_ssb_phase_noise_140415_F.txt'); % data units: dBc/sqrtHz
load('VCO_FDD_freq_noise_140415.txt'); % data units: Hz/sqrtHz
f_VCO = VCO_FDD_freq_noise_140415(:,1);
PDHVCO_Hz = VCO_FDD_freq_noise_140415(:,2);

TF_DIFFVCO = mybodesys(sys(65,22),f_VCO);
EX_PDHVCO_noise_Hz = abs(PDHVCO_Hz .* TF_DIFFVCO);

%% EY PDH VCO

% Data from Daniel    measured from ALS COMM VCO so there is a factor of 10
% for FDD and a factor of 2 for double pass AOM. This only holds up until
% MCL MCF crossover when length path suppresed the VCO ~20Hz)
load('VCO_FDD_ssb_phase_noise_140415_F.txt'); % data units: dBc/sqrtHz
load('VCO_FDD_freq_noise_140415.txt'); % data units: Hz/sqrtHz
f_VCO = VCO_FDD_freq_noise_140415(:,1);
PDHVCO_Hz = VCO_FDD_freq_noise_140415(:,2);

TF_DIFFVCO = mybodesys(sys(65,49),f_VCO);
EY_PDHVCO_noise_Hz = abs(PDHVCO_Hz .* TF_DIFFVCO);

%% END X PDH ERROR SIGNAL
load('EX_PDH_NoiseSpecV_PLLBoost1Off_PDHBoost2On.txt');
f_temp = EX_PDH_NoiseSpecV_PLLBoost1Off_PDHBoost2On(119:2802,1);
noise = EX_PDH_NoiseSpecV_PLLBoost1Off_PDHBoost2On(119:2802,2);

GainFast = 0;
GainSlow = 0;
IMCTEST = 0;
ALScontrol_FULL;
remove = mybodesys(sys(36,5),f_temp); % data is already loop suppressed; need to
    remove before inject

GainFast = 1;
GainSlow = 1;
IMCTEST = 0;
ALScontrol_FULL;
TF_EX_PDH = mybodesys(sys(65,5),f_temp);
EX_PDH_error_Hz = abs(noise .* TF_EX_PDH ./remove);


%% END Y PDH ERROR SIGNAL
load('EY_PDH_NoiseSpecV.txt'); % units in vplts;
f_temp = EY_PDH_NoiseSpecV(:,1);
noise = EY_PDH_NoiseSpecV(:,2);

xfeedback = 0;
```

```
yfeedback = 0;
ALScontrol_FULL;
remove = mybodesys(sys(79,41),f_temp); % data is already loop suppressed; need to remove before inject



xfeedback = 0;
yfeedback = 0;
ALScontrol_FULL;
TF_EY_PDH = mybodesys(sys(65,51),f_temp);
EY_PDH_error_Hz = abs(noise .* TF_EY_PDH ./remove);

%% Corner PLL PFD noise in unit of V/rtHz
CornerPLLPFD = 500e 9*ones(size(f_all));

TF_COMMPLL = mybodesys(sys(65,50),f_all);
Corner_PFD_Hz = abs(500e 9*ones(size(f_all)) .* TF_COMMPLL');


%% DIFF PLL shot noise
% shot noise from first principles
% DIFF BBPD read 166uW alog 11519
% beatnote of  20dbm
elec = 1.6e 19; % charge of electron
CommPD_power = 116e 6; % watts
CommPD_trans = 1e3;  % 1kOhm at RF ??
CommPD_curr = sqrt(CommPD_power*CommPD_trans);
Carrier_curr = 22.5e 3 / CommPD_trans ;
shot_noise_temp = sqrt(2*elec*CommPD_curr); % shot noise in A/SqrtHz
shot_noise_temp = shot_noise_temp .* CommPD_trans * 36 * pi/180; % shot noise in rad/SqrtHz
shot_noise_2 = shot_noise_temp * ones(size(f_all));


COMMPLL_ShotNoise = shot_noise_2;

TF_DIFFPLL_shot = mybodesys(sys(65,50),f_all);
Corner_shotnoise_Hz = abs(shot_noise_2 .* TF_DIFFPLL_shot');


%% DIFF BBPD Dark noise
% BBPD noise    taken from EX
BBPD_noise =  119*ones(size(f)); %  119 dBm, at 100Hz Bw
beatnote =   35*ones(size(f)); %  35 dBm, at 100Hz BW (for COMM BBPD)
dBc_BBPD = BBPD_noise   beatnote;
dBc_BBPD_Hz = dBc_BBPD   20; % dividing by 100Hz BW is the same as  20dB
BBPD_noise =  10.^(dBc_BBPD_Hz./20); % dBc to rad/sqrtHz

TF_DIFFPLL_BBPD = mybodesys(sys(65,43),f_all);
Corner_BBPDnoise_Hz = abs(BBPD_noise_Hz .* TF_DIFFPLL_BBPD');



%% DIFF PLL VCO
```

```
% Data from Daniel    measured from ALS COMM VCO so there is a factor of 10
% for FDD and a factor of 2 for double pass AOM. This only holds up until
% MCL MCF crossover when length path suppresed the VCO ~20Hz)
load('VCO_FDD_ssb_phase_noise_140415_F.txt'); % data units: dBc/sqrtHz
load('VCO_FDD_freq_noise_140415.txt'); % data units: Hz/sqrtHz
f_VCO = VCO_FDD_freq_noise_140415(:,1);
DIFFVCO_Hz = VCO_FDD_freq_noise_140415(:,2);

TF_DIFFVCO = mybodesys(sys(65,47),f_VCO);
DIFFVCO_noise_Hz = abs(DIFFVCO_Hz .* TF_DIFFVCO);


%% Quad Displacement noise
load('dampingfilters_QUAD_2014 01 30_Level2p1_RealSeismic_model.mat')
f_disp = freq;
disp_noise = opticDisp(1).total; % units: m/sqrtHz

X_2_DIFF_TF2 = mybodesys(sys(65,2),f_disp);
dispX_noise_Hz = abs(disp_noise .* X_2_DIFF_TF2);

Y_2_DIFF_TF2 = mybodesys(sys(65,38),f_disp);
dispY_noise_Hz = abs(disp_noise .* Y_2_DIFF_TF2);

%% DIFF CTRL SIGNAL
% alog 11791 GPS time: 1083657316
%DIFF=load('DIFF_PLL_CTRL_05092014.txt');

% alog 11877. In loop IR noise budget with IR in both arms
% GPS time: May 14, 2014 08:55 UTC  1084092948
load('DIFF_PLL_CTRL_redinloop.txt'); % in umeters
DIFF_PLL_CTRL_redinloop_Hz = DIFF_PLL_CTRL_redinloop(:,2) .* 1e 6/ 7e12;
DIFF_PLL_CTRL_redinloop_rms_Hz = DIFF_PLL_CTRL_redinloop(:,3) .* 1e 6/ 7e12;

%%

DACandCDNoiseMC2M3 = 0;
DACandCDNoiseMC2M2 = 0;
BeatnoteDarkNoise = 0;
ADCNoiseWithSignal = 0;
IMCElectronicsNoise = 0;
MCSeismic = 0;
ETMYITMYSeismic = 0;
CMBoardAnalogElectronics = 0;


%% Plot (manual)

figure(3829);
clf;
title('DIFF Noise Green In Loop');
ylabel('Hz/SqrtHz');
xlabel('Freq Hz');
loglog(DIFF_PLL_CTRL_redinloop(:,1),DIFF_PLL_CTRL_redinloop_Hz.*2,...
```

```
    DIFF_PLL_CTRL_redinloop(:,1),DIFF_PLL_CTRL_redinloop_rms_Hz.*2,...
    EX_PDH_NoiseSpecV_PLLBoost1Off_PDHBoost2On(119:2802,1),EX_PDH_error_Hz,'g  ',...
    EY_PDH_NoiseSpecV(:,1),EY_PDH_error_Hz,...
    f_all, EX_PLL_shotnoise_Hz,'r',...
    f_all, EX_PLL_darknoise_Hz,'b*',...
    f_all, EX_fiber_noise_Hz,'r*',...
    f_all, EX_laserfreq_noise_Hz,'g*',...
    f_all, EY_PLL_shotnoise_Hz,'m',...
    f_all, EY_PLL_darknoise_Hz,'c*',...
    f_disp, dispY_noise_Hz,'k*',...
    f_VCO, DIFFVCO_noise_Hz,'c*');
%   f_all, EX_PLL_PFDnoise_Hz,...
%   f_all, Corner_shotnoise_Hz,
grid on;
legend('Green Noise',....
    'RMS',...
    'EX PDH Error Sig',...
    'EY PDH Error Sig',...
    'EX PLL Shot Noise',...
    'EX PLL Dark Noise',...
    'Fiber Noise',...
    'Laser Noise',...
    'EY PLL Shot Noise',...
    'EY PLL Dark Noise',...
    'Disp Noise',...
    'Suppressed COMM VCO',...
    'Location', 'NorthEastOutside');
%   'EX PLL PFD Noise',...
%   'DIFF PLL BBPD Shot Noise',...
xlabel('Frequency [Hz]');
ylabel('Freq Fluctuations [Hz/SqrtHz]');
xlim([1e 2 1e5]);
ylim([1e 4 1e2]);
set(gca,'Ytick',10.^( 4:2))
set(gcf, 'Color', 'w');
```

/ligo/svncommon/NbSvn/aligonoisebudget/trunk/HIFO/H1/noisebudget˙DIFF.m

Appendix C

Suspension Hierarchy Loop Algebra

Currently both the triple and quadruple suspensions of Advanced LIGO are in an offloaded hierarchy. The suspension model is designed to allow for both offloaded and distributed configurations. Figure C.1 is an example of a triple suspension in the offloaded configuration. This can be generalized to more suspension stages.

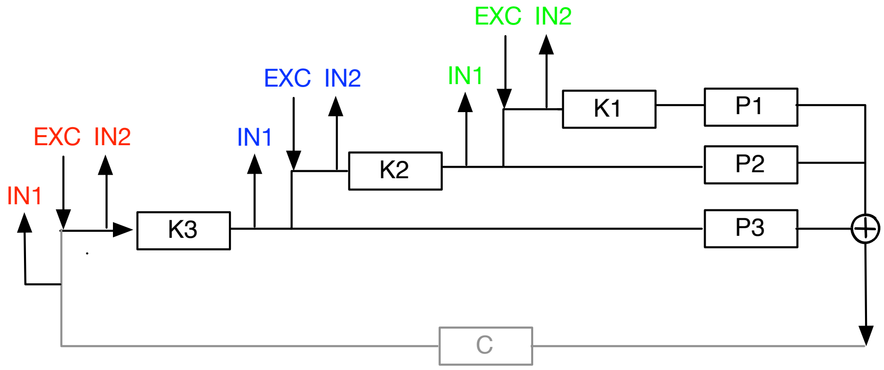

Figure C.1: Triple suspension in an offloaded hierarchy where P_1, P_2, P_3 are the plants, K_1, K_2, K_3 are the digital filters, and C is the control.

Several transfer functions can be taken to determine the stability of the suspension dynamics. In this Appendix, I provide the loop algebra for such a system. For the red, blue, and green excitations, the three transfer functions are:

$$\begin{aligned} IN2 &= EXC + IN1 \\ &= EXC + C(P_3K_3 + P_2K_2K_3 + P_1K_1K_2K_3)IN2 \\ \frac{IN1}{IN2} &= C(P_3K_3 + P_2K_2K_3 + P_1K_1K_2K_3) \end{aligned} \tag{C.1}$$

$$\begin{aligned} IN2 &= EXC + IN1 \\ &= EXC + K_3C(P_3IN1 + (P_2K_2 + P_1K_1K_2)IN2) \\ \frac{IN1}{IN2} &= \frac{C(P_2K_2K_3 + P_1K_1K_2K_3)}{1 - P_3K_3C} \end{aligned} \tag{C.2}$$

$$\begin{aligned} IN2 &= EXC + IN1 \\ &= EXC + K_2K_3C(P_3IN1 + P_1K_1IN2) \\ \frac{IN1}{IN2} &= \frac{C(P_1K_1K_2K_3)}{1 - P_2K_2K_3C} \end{aligned} \tag{C.3}$$

Notice, Equation C.3 is similar to the transfer function discussed in Section 5.8 Figure 5.33, but with $P_1, K_1 = 0$. At low frequencies, this equation approaches $\frac{IN1}{IN2} = \frac{P_2K_2}{P_3}$, which is sufficient to approximate the crossover of the two suspension stages.

Meanwhile, Figure C.2 is an example of a triple suspension in the distributed configuration. This can also be generalized to more suspension stages.

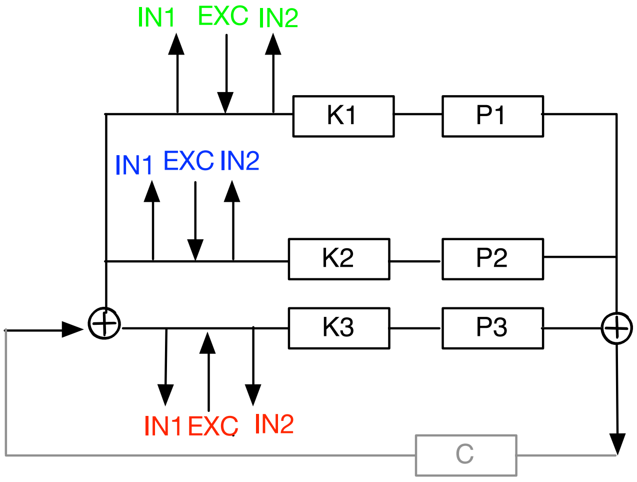

Figure C.2: Triple suspension in an distributed hierarchy where P_1, P_2, P_3 are the plants, K_1, K_2, K_3 are the digital filters, and C is the control.

The transfer functions are now as follows:

$$\begin{aligned} IN2 &= EXC + IN1 \\ &= EXC + C(P_3K_3)IN2 \\ \frac{IN1}{IN2} &= C(P_3K_3) \end{aligned} \tag{C.4}$$

$$\begin{aligned} IN2 &= EXC + IN1 \\ &= EXC + C(P_2K_2)IN2 \\ \frac{IN1}{IN2} &= C(P_2K_2) \end{aligned} \tag{C.5}$$

$$\begin{aligned} IN2 &= EXC + IN1 \\ &= EXC + C(P_1K_1)IN2 \\ \frac{IN1}{IN2} &= C(P_1K_1) \end{aligned} \tag{C.6}$$

Crossovers can be taken with the ratio of these transfer functions.

Appendix D

List of Publications

The publications directly related to the results presented in this thesis are highlighted. Paper number 9 was highlighted in CQG + [9].

— **2015** —

1.— **Staley, A.**, Hoak, D., Effler, A., Izumi, K., Dwyer, S., Kawabe, K., King, E. J., Rakhmanov, M., Savage, R. L., Sigg, S., "High Precision Optical Cavity Length and Width Measurements Using Double Modulation," *Optics Express* **23(15)**:19417-19431 (2015).

2.— Evans, Matt,. … **Staley, A.**, … Zhao, C., "Observation of Parametric Instabilities in Advanced LIGO," *Physics Review Letters* **114** 161102 (2015).

3.— **Staley, A.**, "The Status of the Advanced LIGO Gravitational-Wave Detectors," *Proceedings for the Rencontres de Moriond Conference* (2015).

4.— Aasi, J., …, **Staley, A.**, …, Zweizig, J., "Advanced LIGO," *Classical and Quantum Gravity* **32** 074001 (2015).

5.— Aasi, J., …, **Staley, A.**, …, Zweizig, J., "Directed search for gravitational waves from Scorpis X-1 with initial LIGO data," *Phys. Rev. D.* **91** 062008 (2015).

6.— Aasi, J., …, **Staley, A.**, …, Zweizig, J., "Narrow-band search of continuous gravitational-wave signals from Crab and Vela pulsars in Virgo VSR4 data," *Phys. Rev. D.* **91** 022004 (2015).

7.— Aasi, J., …, **Staley, A.**, …, Zweizig, J., "Characterization of the LIGO detectors during their sixth science run," *Classical and Quantum Gravity* **32** 115012 (2015).

8.— Aasi, J., …, **Staley, A.**, …, Zweizig, J., “Searching for stochastic gravitational waves using data from the two collocated LGO Hanford detectors,” *Phys. Rev. D.* **91** 022003 (2015).

— **2014** —

9.— **Staley, A.** *et al*, “Achieving Resonance in the Advanced LIGO Gravitational-wave Interferometer,” *Classical and Quantum Gravity* **31** 245010 (2014)

10.— Aartsen, M. G., …, **Staley, A.**, …, Zweizig, J., “Multimessenger search for sources of gravitational waves and high-energy neutrinos: Initial results for LIGO-Virgo and IceCube,” *Phys. Rev. D.* **90** 102002 (2014).

11.— Aasi, J., …, **Staley, A.**, …, Zweizig, J., “Improved Upper Limits on the Stochastic Gravitational-Wave Background from 2009-2010 LIGO and Virgo Data,” *Phys. Rev. Lett.* **113** 231101 (2014).

12.— Aasi, J., …, **Staley, A.**, …, Zweizig, J., “First all-sky search for continuous gravitational waves from unknown sources in binary systems,” *Phys. Rev. D.* **90** 062010 (2014).

13.— Aasi, J., …, **Staley, A.**, …, Zweizig, J., “Methods and results of a search for gravitational waves associated with gamma-ray bursts using the GEO 600, LIGO, and Virgo detectors,” *Phys. Rev. D.* **89** 122004 (2014).

14.— Aasi, J., …, **Staley, A.**, …, Zweizig, J., “Search for gravitational radiation from intermediate mass black hole binaries in data from second LIGO-Virgo joint science run,” *Phys. Rev. D.* **89** 122003 (2014).

15.— Aasi, J., …, **Staley, A.**, …, Zweizig, J., “Search for gravitational waves associated with Gamma-ray bursts detected by interplanetary network,” *Phys. Rev. Lett.* **113** 011102 (2014).

16.— Aasi, J., …, **Staley, A.**, …, Zweizig, J., “Search for gravitational wave ring downs from perturbed intermediate mass black holes in LIGO-Virgo data from 2005-2010,” *Phys. Rev. D.* **89** 102006 (2014).

17.— Aasi, J., …, **Staley, A.**, …, Zweizig, J., “Implementation of an F-static all-sky search for continuous gravitational waves in Virgo VSR1 data,” *Classical and Quantum Gravity* **31** 165014 (2014).

18.— Aasi, J., …, **Staley, A.**, …, Zweizig, J., “The NINJA-2 project:detecting and characterizing gravitational waveforms modelled using numerical binary black hole simulations,” *Classical and Quantum Gravity* **31** 115004 (2014).

19.— Aasi, J., …, **Staley, A.**, …, Zweizig, J., “Application of a Hough search for continuous gravitational waves on data from the fifth LIGO science run,” *Classical and Quantum Gravity* **31** 085014 (2014).

20.— Aasi, J., . . ., **Staley, A.**, . . ., Zweizig, J., "Constraints on Cosmic Strings from the LIGO-Virgo Gravitational-Wave Detectors," *Phys. Rev. Lett.* **112** 131101 (2014).

21.— Aasi, J., . . ., **Staley, A.**, . . ., Zweizig, J., "First searches for optical counterparts to gravitational-wave candidate events," *Astrophysical Journal, Supplement Series* **211** 7 (2014).

22.— Aasi, J., . . ., **Staley, A.**, . . ., Zweizig, J., "Gravitational waves from known pulsars: results from the initial detector era," *Astrophysical Journal* **785** 119 (2014).

— 2013 —

23.— Aasi, J., . . ., **Staley, A.**, . . ., Zweizig, J., "Search for long-lived gravitational wave transients coincident with long gamma-ray bursts," *Phys. Rev. D.* **88** 122004 (2013).

24.— Aasi, J., . . ., **Staley, A.**, . . ., Zweizig, J., "Search for long-lived gravitational wave transients coincident with long gamma-ray bursts," *Phys. Rev. D.* **88** 122004 (2013).

25.— Aasi, J., . . ., **Staley, A.**, . . ., Zweizig, J., "Directed search for continuous gravitational waves from the Galactic center," *Phys. Rev. D.* **88** 102002 (2013).

— 2012 —

26.— **Staley, A.** *et al*, "Oppenheimer-Synder Collapse in Moving-Puncture Coordinates ," *Classical and Quantum Gravity* **29** 015003 (2012)